

ASPECTS OF FLOW AND COMPACTION
OF LAMINATED COMPOSITE SHAPES DURING CURE

by

PASCAL HUBERT

B. Ing., Ecole Polytechnique de Montréal, 1988

M. Sc. A., Ecole Polytechnique de Montréal, 1991

A THESIS SUBMITTED IN PARTIAL FULFILLMENT OF

THE REQUIREMENTS FOR THE DEGREE OF

DOCTOR OF PHILOSOPHY

in

THE FACULTY OF GRADUATE STUDIES

Department of Metals and Materials Engineering

We accept this thesis as confirming
to the required standard

THE UNIVERSITY OF BRITISH COLUMBIA

July 1996

© Pascal Hubert, 1996

In presenting this thesis in partial fulfilment of the requirements for an advanced degree at the University of British Columbia, I agree that the Library shall make it freely available for reference and study. I further agree that permission for extensive copying of this thesis for scholarly purposes may be granted by the head of my department or by his or her representatives. It is understood that copying or publication of this thesis for financial gain shall not be allowed without my written permission.

Department of Metals and Materials Engineering
The University of British Columbia
Vancouver, Canada

Date 15/7/96

Abstract

Cost-effective manufacturing has become the primary objective for many industries using composite materials in primary structures. To realize this objective, it is often desired to use process modelling, as it helps understand the interaction between the parameters affecting the product quality. Among the multitude of phenomena occurring during composites processing, resin flow is a critical issue. It affects the fibre volume fraction distribution, the mechanical properties of the laminate and the final dimensions of the part. For thermoset matrix composites, the percolation flow approach is typically used to model flow and compaction. In this approach, the resin flows relative to the fibres and the flow has to be coupled with the fibre bed compaction behaviour to obtain the final shape of the laminate.

In the present work, a percolation flow-compaction model is implemented in a two-dimensional finite element processing model for complex shapes such as angles or hat sections. Material properties required for the flow-compaction model, such as resin viscosity and the fibre bed compaction curve are measured for two carbon-epoxy composites: AS4/3501-6 and AS4/8552. An experimental technique to measure the fibre bed compaction curve directly from the prepreg is presented. The fibre bed compaction curves are validated with results from uniaxial compaction tests. The flow-compaction model is used to study the effect of a variation of the material properties on the compaction of angle laminates. The results from this sensitivity analysis show that the compaction curve significantly affects the final laminate thickness while the fibre bed shear modulus controls the ability of the fibres to conform to a curvilinear shape.

A series of angle laminates were cured to study the effect of fibre orientation, bagging conditions, material and tool type on compaction behaviour. Simulations of the angle laminates

in bleed conditions are in good agreement with the experiments. However, the model does not predict the experimentally observed magnitude of the deformation at the corner of the $[90^\circ]$ lay-up. This behaviour is attributed to shear flow, where the fibres and the resin move together as a very viscous anisotropic fluid.

Direct observations of the compaction behaviour during transverse flow are presented. They confirm the kinematic relations used in shear flow theory and show that friction is present at the plate-laminate interface. Next, the conditions required to produce percolation or shear flow are investigated in a simple uniaxial compaction experiment. Fibre orientation and resin viscosity are the primary variables determining the dominant flow mechanism. Shear flow is primarily affected by the fibre orientation and occurs essentially in the direction perpendicular to the fibres. Percolation flow depends on the resin viscosity and occurs mainly in the direction where shear flow is not possible.

Sommaire

L'optimisation des coûts de fabrication est le principal objectif des compagnies qui veulent concevoir des structures mécaniques primaires en utilisant des matériaux composites. Cet objectif peut être atteint en effectuant l'analyse des procédés de fabrication à l'aide de modèles mathématiques. Ces modèles permettent d'étudier l'écoulement de la résine qui est un des mécanismes importants de la mise en forme des composites. En effet, ce mécanisme influence la distribution du pourcentage volumique des fibres dans le stratifié, les propriétés du stratifié et les dimensions de la pièce. Pour les composites à matrice thermodurcissable, on suppose que la résine s'écoule relativement aux fibres. Ainsi, la déformation du stratifié est obtenue en couplant l'écoulement de la résine à la compressibilité du réseau de fibres.

Dans ce travail, pour tenter de répondre à la modélisation mathématique des procédés de fabrication, un modèle d'écoulement est incorporé à un programme d'éléments finis 2-D. Ce modèle s'applique à l'analyse de stratifiés à forme complexe, par exemple des profilés en L. Une nouvelle méthode est développée pour mesurer la courbe de compaction directement à partir du pré-imprégné. Cette méthode est appliquée à deux types de composites carbone-époxy: les composites AS4/3501-6 et AS4/8552. Les courbes de compaction obtenues sont validées grâce à des essais uniaxes de compression. Une étude paramétrique est ensuite effectuée afin de vérifier l'effet de la variation des propriétés du matériau sur la compaction de profilés en L. A partir de ces études, nous avons trouvé que : i) la courbe de compaction est le paramètre principal contrôlant l'épaisseur du stratifié et ii) le module de cisaillement du réseau de fibres influence la facilité avec laquelle le stratifié se déforme dans le coin du profilé.

Des profilés en L sont fabriqués afin d'étudier l'effet : i) de l'orientation des fibres, ii) des conditions de moulage, iii) du matériau et iv) du type de moule sur la compaction du stratifié. Les simulations utilisant le modèle d'éléments finis donnent des résultats qui concordent bien avec ceux des expériences. Par contre, le modèle développé ne peut prédire l'amplitude des déformations observées au coin des stratifiés ayant les fibres orientées à 90°. Cette déformation est plutôt causée par un mode d'écoulement appelé écoulement par cisaillement. Dans ce cas, les fibres et la résine s'écoulent ensemble à la manière d'un liquide anisotrope très visqueux.

L'observation de la déformation de stratifiés soumis à un écoulement transversal a permis de vérifier la validité des hypothèses formulées à partir des modèles développés pour ce type d'écoulement. Cette expérience indique la présence de frottement à l'interface entre le stratifié et le moule. Les conditions favorisant un type d'écoulement par rapport à un autre sont étudiées grâce à un essai simple de compression uniaxe. L'orientation des fibres et la viscosité de la résine sont les variables qui influencent le mécanisme d'écoulement observé. L'écoulement par cisaillement est principalement influencé par l'orientation des fibres et se produit perpendiculairement aux fibres. L'écoulement de la résine dépend essentiellement de sa viscosité et a principalement lieu dans la direction où l'écoulement par cisaillement est impossible.

Table of contents

ABSTRACT	ii
SOMMAIRE	iv
TABLE OF CONTENTS	vi
LIST OF TABLES	xi
LIST OF FIGURES	xiii
NOMENCLATURE	xxiv
ACKNOWLEDGMENTS	xxxix
CHAPTER 1 INTRODUCTION	1
1.1 FIGURES	7
CHAPTER 2 LITERATURE REVIEW AND RESEARCH OBJECTIVES	10
2.1 RESIN BEHAVIOUR DURING CURE	10
2.2 FIBRE BED BEHAVIOUR	13
2.2.1 Fibre bed elasticity	14
2.2.2 Fibre bed permeability	18
2.3 FLOW-COMPACTION MODELS	22
2.3.1 Percolation flow models	23
2.3.1.1 Darcy's Law	23
2.3.1.2 Sequential compaction	25
2.3.1.3 Effective stress formulation	26
2.3.2 Shear flow models	31
2.3.2.1 Intraply	31
2.3.2.2 Interply	35
2.4 LITERATURE REVIEW SUMMARY AND RESEARCH OBJECTIVES	35
2.5 TABLES	39
2.6 FIGURES	40

CHAPTER 3 PERCOLATION FLOW-COMPACTION FINITE ELEMENT MODEL.....	47
3.1 COMPOSITE PROCESS MODELLING APPROACH	47
3.2 FLOW-COMPACTION MODEL DEVELOPMENT.....	49
3.2.1 Model assumptions	50
3.2.2 Governing equations.....	50
3.2.3 Boundary and initial conditions	52
3.2.4 Composite constitutive law	53
3.2.5 Finite element formulation.....	56
3.2.5.1 Weighted residual method.....	57
3.2.5.2 Galerkin finite element equations.....	59
3.2.5.3 Method of solution	61
3.2.5.4 Time integration	62
3.2.5.5 Non-linear solution technique	64
3.2.6 Program algorithm	67
3.3 Flow-compaction model verification	69
3.3.1 Static solution	69
3.3.2 TRANSIENT SOLUTION	70
3.3.3 MESH DENSITY	73
3.4 Summary.....	75
3.5 TABLES	76
3.6 FIGURES.....	78
CHAPTER 4 MATERIAL PROPERTIES AND FIBRE BED COMPACTION CURVE	
CHARACTERIZATION	88
4.1 MATERIALS STUDIED.....	88
4.2 COMPACTION CURVE CHARACTERIZATION APPROACH	90
4.2.1 Load-hold method description.....	92
4.2.2 Testing procedure	92
4.3 RESULTS OF COMPACTION CURVE CHARACTERIZATION	94
4.4 COMPACTION CURVE VALIDATION	97
4.4.1 Compaction test model	98

4.4.2 <i>Results and discussion</i>	98
4.4.2.1 <i>Temperature effect</i>	100
4.4.2.2 <i>Complete cure</i>	102
4.5 SUMMARY	102
4.6 TABLES	104
4.7 FIGURES	106
CHAPTER 5 COMPACTION OF ANGLE LAMINATES: A NUMERICAL AND EXPERIMENTAL STUDY	116
5.1 PERCOLATION FLOW MODEL SENSITIVITY ANALYSIS	116
5.1.1 <i>Finite element model and runs definition</i>	117
5.1.2 <i>Results of the sensitivity analysis</i>	119
5.2 EXPERIMENTAL INVESTIGATION	122
5.2.1 <i>Testing procedure</i>	123
5.2.2 <i>Measurements and data analysis</i>	125
5.2.3 <i>Temperature profiles</i>	127
5.2.4 <i>Defects and problems induced by the experimental method</i>	127
5.2.5 <i>Resin mass loss</i>	129
5.2.6 <i>Thickness profiles</i>	130
5.2.7 <i>Strains</i>	133
5.2.8 <i>Discussion</i>	135
5.3 NUMERICAL INVESTIGATION	136
5.3.1 <i>Finite element models definition</i>	137
5.3.2 <i>Resin mass losses and laminate thickness predictions</i>	138
5.3.3 <i>Final shape of the laminates</i>	139
5.3.4 <i>Compaction of the laminates during cure</i>	140
5.3.5 <i>Resin pressure variation during cure</i>	141
5.3.6 <i>Corner compaction behaviour</i>	142
5.3.7 <i>Resin flow behaviour during cure</i>	143

5.3.8 Discussion.....	144
5.4 SUMMARY	145
5.5 TABLES	147
5.6 FIGURES.....	150
CHAPTER 6 ASPECTS OF SHEAR FLOW AND THE INTERACTION WITH PERCOLATION	
FLOW	188
6.1 SHEAR FLOW EXPERIMENTAL INVESTIGATION.....	188
6.1.1 Experimental procedure	190
6.1.2 Resin percolation.....	193
6.1.3 Displacement profiles	194
6.1.4 Condition at the plate-laminate interface.....	194
6.2 Experimental investigation of flow mechanisms.....	197
6.2.1 EXPERIMENTAL PROCEDURE	198
6.2.2 EXTRACTION OF THE RESULTS	200
6.2.3 General observations.....	202
6.2.4 Percolation and shear strain analysis	203
6.2.5 Flow mechanisms contribution.....	204
6.2.6 Discussion.....	205
6.2.7 Flow mechanism map	206
6.3 SUMMARY	207
6.4 TABLES.....	209
6.5 FIGURES.....	210
CHAPTER 7 CONCLUSIONS AND FURTHER WORK.....	225
7.1 FURTHER WORK	226
REFERENCES	228
APPENDIX A FLOW-COMPACTION MODEL DETAILS	234
A.1 COMPOSITE CONTINUITY EQUATION.....	234
A.2 RESIDUAL EQUATIONS DEVELOPMENT.....	236
A.3 ELEMENT SHAPE FUNCTIONS AND THEIR DERIVATIVES.....	239
A.4 ELEMENT SPATIAL INTEGRATION AND LOAD VECTOR CALCULATION	241
A.5 ELEMENT FIBRE BED PROPERTIES CALCULATION.....	243

<i>A.5.1 Fibre bed permeability matrix</i>	243
<i>A.5.2 Fibre bed tangent modulus matrix</i>	244
A.6 ELEMENT STATE VARIABLES COMPUTATION	246
<i>A.6.1 Fibre bed effective stresses and element strains</i>	246
<i>A.6.2 Fibre volume fraction</i>	247
<i>A.6.3 Resin velocity</i>	248
<i>A.6.4 Laminate mass loss</i>	249
<i>A.6.5 Stresses and strains coordinate transformation</i>	249
A.7 FIGURES	251
APPENDIX B MATERIAL PROPERTIES AND CHARACTERIZATION	254
B.1 RESIN CURE KINETICS	254
B.2 RESIN VISCOSITY	256
<i>B.2.1 Viscosity model for 3501-6 resin</i>	257
<i>B.2.2 Viscosity model for 8552 resin</i>	259
B.2.2.1 Testing procedure	259
B.2.2.2 Experimental results	260
B.2.2.3 Viscosity model	261
B.3 FIBRE BED PERMEABILITY	263
B.4 COMPACTION CURVE CHARACTERIZATION WITH THE LOAD-UNLOAD METHOD	264
<i>B.4.1 Results</i>	266
<i>B.4.2 Comparison with load-hold method</i>	267
B.5 TABLES.....	269
B.6 FIGURES.....	272
APPENDIX C RESULTS OF ANGLE LAMINATE COMPACTION EXPERIMENTS	280
C.1 TABLES.....	281
C.2 FIGURES.....	283
APPENDIX D RESULTS OF SHEAR FLOW EXPERIMENTS	284
D.1 TABLES.....	286
D.2 FIGURES	292
APPENDIX E RESULTS FOR FLOW MECHANISMS TEST	293
E.1 TABLES	295
E.2 FIGURES.....	298

List of tables

Table 2.1	Summary of flow-compaction theoretical and experimental work.....	39
Table 3.1	Summary of the initial and boundary conditions for the flow-compaction model.	76
Table 3.2	Run matrix for the flow-compaction model verification.	76
Table 3.3	Results from patch test runs for undrained (S1, S2) and drained (S3, S4) conditions..	77
Table 4.1	Typical fibre and resin properties for the materials studied: AS4/3501-6 (material A) and AS4/8552 (material B).....	104
Table 4.2	Prepreg properties for AS4/3501-6 (material A) and AS4/8552 (material B).....	104
Table 4.3	Total in-plane strains and volumetric strain measured after the compaction tests.	104
Table 4.4	Total in-plane strains, volumetric strain and ratio of volumetric to total vertical deformation measured after the validation compaction tests.....	105
Table 4.5	Comparison between predicted and measured specimen volumetric strains for the validation compaction tests.....	105
Table 5.1	Run definition and results for the sensitivity analysis.	147
Table 5.2	Sample definition for angle processing experiments and test matrix.	147
Table 5.3	Type of defects observed after cure of the angles. Typical defects are shown in Fig. 5.20.	148
Table 5.4	Level of voids in the flat section and at the corner of the laminates. Obtained from the visual inspection of the angles after the cure. The void level is ranked on a scale of 0 to 3 corresponding to no voids (0) to large number of voids (3).	148
Table 5.5	Resin mass loss ratio calculated from the mass of the laminates before and after cure (Equation 5.1).....	148
Table 5.6	Finite element model dimensions and material input used for the simulations of the angle laminates. The models and the material input are defined in Figure 5.35...	149
Table 5.7	Comparison of the resin mass loss ratio obtained from the experiments and the predictions with the finite element program (COMPRO).....	149
Table 6.1	Shear flow experiments loading increments (u_{plate}) with corresponding peak and relaxed load. The peak load corresponds to the load measured as the loading is stopped. The relaxed load corresponds to the stable load measured after the load is stopped.	209
Table 6.2	Flow mechanisms test matrix and sample definition. The variable n corresponds to the specimen number tested in the condition specified.	209
Table B.1	Constants for the cure kinetics models of the resins.	269
Table B.2	Constants for the viscosity models of the resins.	269

Table B.3	Test matrix for material B resin 8552 viscosity characterization.....	270
Table B.4	Summary of the fibre bed permeability variations for unidirectional fibre beds available from the literature.	270
Table B.5	Test definition and measurement results for the determination of the fibre bed compaction curve tests.	271
Table B.6	Test definition and measurement results for the fibre bed compaction curve validation tests.	271
Table C.1	Thickness and laminate mass measurements on the angle laminates before and after the cure.....	281
Table C.2	Laminate normal strains, total strain and percolation strain.	282
Table D.1	Sample dimensions before the test.....	286
Table D.2	Marker positions for sample 10_1.	287
Table D.3	Marker positions for sample 10_2.	288
Table D.4	Marker positions for sample 20_1.	289
Table D.5	Marker positions for sample 20_2.	290
Table D.6	Position of the plates and the sample edges for the sample tested and all load increments.	291
Table E.1	Flow mechanism tests, sample measurement results and strains calculated for material A at 100°C.	295
Table E.2	Flow mechanism tests, sample measurement results and strains calculated for material B at 100°C.....	295
Table E.3	Flow mechanism tests, sample measurement results and strains calculated for material A at 140°C.	296
Table E.4	Flow mechanism tests, sample measurement results and strains calculated for material B at 140°C.....	296
Table E.5	Flow mechanism tests, average strains (ϵ_x and ϵ_v) and vertical strains caused by shear flow (e_z^S) and percolation flow (e_z^P).....	297

List of figures

Figure 1.1 Application of composites for large aircraft structures. (Courtesy of the Boeing Company).	7
Figure 1.2 Autoclave processing steps, (a) lay-up, (b) cure with a controller loop.	8
Figure 1.3 Typical autoclave cure cycle.	9
Figure 1.4 Processing defects induced by flow and compaction, (1) warpage, (2) resin rich region, (3) resin poor region, (4) voids, (5) surface dimpling and (6) core buckling. .9	
Figure 2.1 Typical resin degree of cure evolution during cure. The resin changes from a liquid state (Phase I), to a gel state (Phase II) and finally to a solid state (Phase III).....	40
Figure 2.2 Typical resin viscosity evolution during cure. The resin is fluid during Phase I before it reaches the gel point in Phase II.....	40
Figure 2.3 Ideal fibre packing arrangements, (a) square and (b) hexagonal.....	41
Figure 2.4 Actual fibre beds pore geometries, (a) intraply, (b) resin rich regions between individual plies and (c) non-uniform fabric arrangement.....	41
Figure 2.5 Typical fibre bed compaction curves. V_a is the maximum fibre volume fraction possible which is related to the fibres alignment in the fibre bed.	42
Figure 2.6 3-D fibre bundle stress state (Cai and Gutowski, 1992a).....	42
Figure 2.7 Typical fibre bed axial and transverse permeability variation with fibre volume fraction.....	43
Figure 2.8 Type of flow mechanisms during processing (Ó Brádaigh et al., 1993).	43
Figure 2.9 Sequential compaction behaviour, (a) transverse flow and (b) axial flow (Loos and Springer, 1983).	44
Figure 2.10 Effective stress compaction analogy (Davé et al., 1987a).....	44
Figure 2.11 Resin pressure sensor response during compaction of a flat carbon-epoxy laminate (Mackenzie, 1993). The pressure sensors where distributed through the thickness from the top (S1) to the tool (S5).	45
Figure 2.12 Resin pressure from 1-D compaction simulation of the experiment of Fig. 2.11 assuming a bag pressure equivalent to the measured pressure for the top sensor (S1).	45
Figure 2.13 Composite laminate idealization for shear flow models (Ó Brádaigh et al., 1993). .46	
Figure 2.14 Flow chart of the research presented in this thesis.	46
Figure 3.1 Present modelling approach.	78
Figure 3.2 Processing model flowchart showing the different modules.....	78
Figure 3.3 Laminate representative volume and plane strain composite element.	79

Figure 3.4	Stress state on a representative element of a unidirectional ply.	79
Figure 3.5	Bilinear quadrilateral element and degrees of freedom (i.e. displacements u_{xn} , u_{zn} and pressure P_n where n is the node number).	80
Figure 3.6	Finite element mesh and boundary conditions for patch test runs, (a) axial stress state, (b) transverse stress state. The fibre bed properties are also given.	80
Figure 3.7	Model definition for the exact solution transient run (T1), (a) boundary conditions and material property inputs, (b) finite element mesh used (20 elements).	81
Figure 3.8	Results from transient run T1 compared to the exact solution showing the vertical pressure profile evolution with time.	81
Figure 3.9	Boundary conditions and material property inputs for the non-linear permeability transient runs, (a) 1-D flow (T2), (b) 2-D flow (T3).	82
Figure 3.10	Finite element meshes used for the transient runs, (a) T2 (10 elements), (b) T3 (100 elements).	82
Figure 3.11	Results from transient run T2 compared to ABAQUS solution showing the vertical pressure profile evolution with time.	83
Figure 3.12	Results from transient run T2 compared to ABAQUS solution showing the variation of vertical displacement at the top of the model with time. Also shown is a simulation assuming a constant permeability (dashed line).	83
Figure 3.13	Results from transient run T3 compared to ABAQUS solution showing the vertical pressure profile evolution with time at $x=0$	84
Figure 3.14	Results from transient run T3 compared to ABAQUS solution showing the horizontal pressure profile evolution with time at $z=0$	84
Figure 3.15	Results from transient run T3 compared to ABAQUS solution showing the variation of vertical displacement at the top of the model with time. Also shown is a simulation assuming a constant permeability (dashed line).	85
Figure 3.16	Boundary conditions and cure cycle for the composite consolidation runs (T4 and T5).	85
Figure 3.17	Fibre bed compaction curves for the composite consolidation runs ($V_{f0}=0.48$ for T4 and $V_{f0}=0.57$ for T5).	86
Figure 3.18	Results from transient runs T4 and T5 compared to LAMCURE solution showing the variation of vertical displacement at the top of the model with time.	86
Figure 3.19	Boundary conditions and material property inputs for the study of the effect of the mesh size on the model predictions. For the meshes, the domain is divided in 4 and 40 elements of equal sizes.	87
Figure 3.20	Vertical pressure profile evolution with time obtained by COMPRO compared to the exact solution showing the effect of the mesh density.	87
Figure 4.1	Experimental setup for the fibre bed compaction test.	106

Figure 4.2	Compaction test data analysis, (a) simple viscoelastic model and (b) schematic of compaction specimen loading and dimensions.	106
Figure 4.3	Compaction curve computation for the load-hold test method. From the master loading curve (a), the fibre bed load is directly obtained from the load-displacement value when the total load has fully relaxed (b).....	107
Figure 4.4	Photograph of the compaction test setup, (a) the fixture as installed in the temperature controlled chamber and (b) a close-up view of the compaction fixture.	107
Figure 4.5	Compaction test sample dimensions: before the test (L_0, W_0, H_0) and after the test (L', W', H'). The definition of the fibre orientation direction is also shown.	108
Figure 4.6	Compaction test sample preparation, where the sample is wrapped in a teflon film.	108
Figure 4.7	Plan view photograph of typical specimens after a compaction test. Resin can be seen at the edges of the specimen.	109
Figure 4.8	Applied load and displacement variation with time for load-hold compaction test (material A, 7A01) showing the load relaxation at the different loading increments (1 to 8).	109
Figure 4.9	Load-displacement curve for the load-hold test method (material A, 7A01) showing the points (1 to 8) extracted to build the fibre bed compaction curve.....	110
Figure 4.10	Compaction curves obtained for material A obtained with the load-hold method for samples 7A01 and 7A02. A comparison with Gutowski's model (Equation 2.3) is presented with $\beta=350$, $V_a=0.81$, $V_{f0}=0.558$ and $E_f=230$ GPa.....	110
Figure 4.11	Applied load and displacement variation with time for load-hold compaction test (material B, 7B01) showing the load relaxation at the different loading increments (1 to 6).	111
Figure 4.12	Compaction curves obtained for material B. A comparison with Gutowski's model (Equation 2.3) is presented with $\beta=350$, $V_a=0.68$, $V_{f0}=0.574$ and $E_f=230$ GPa. The experimental result for sample 7B02 is shown as a reference.....	111
Figure 4.13	Comparison of the compaction curves for the materials studied.....	112
Figure 4.14	Finite element model used for the compaction curve validation runs.....	112
Figure 4.15	Flow-compaction model prediction of the load-displacement behaviour compared with the experimental results of a load controlled compaction test of material A at 100°C (sample 4A01). The fibre bed elastic compaction curve is shown for reference.	113
Figure 4.16	Flow-compaction model prediction of the load-displacement behaviour compared with the experimental results of a load controlled compaction test of material A at 140°C (sample 5A01). The fibre bed elastic compaction curve is shown for reference.	113

Figure 4.17	Flow-compaction model prediction of the load-displacement behaviour compared with the experimental results of a load controlled compaction test of material B at 100°C (sample 4B02). The fibre bed elastic compaction curve and the onset of resin flow are also shown for reference.	114
Figure 4.18	Flow-compaction model prediction of the load-displacement behaviour compared with the experimental results of a load controlled compaction test of material B at 140°C (sample 5B02). The fibre bed elastic compaction curve and the onset of resin flow are also shown for reference.	114
Figure 4.19	Flow-compaction model prediction of the stress-strain behaviour compared with the experimental data of a load controlled compaction test of material A and material B at 170°C (samples 9A01 and 9B01).....	115
Figure 5.1	Angle laminate geometric definition for modelling.	150
Figure 5.2	Finite element model dimensions, boundary conditions and material properties input for the nominal case of the sensitivity analysis (SANOM).....	150
Figure 5.3	Finite element mesh used for the sensitivity analysis. The location for the normal displacement (u_n) outputs is shown.....	151
Figure 5.4	Compaction curves used for the sensitivity analysis to investigate the effect of shifting the fibre bed effective stress in the stiffening region ($0.1 < e_3 < 0.25$).	151
Figure 5.5	Effect of the variation of the transverse permeability on the angle compaction behaviour. The viscosity profile is also shown indicating the gel time of the resin.	152
Figure 5.6	Effect of the compaction curve shape on the angle compaction behaviour.	152
Figure 5.7	Effect of the fibre bed longitudinal modulus (E_1) on the angle compaction behaviour.	153
Figure 5.8	Effect of the fibre bed shear modulus (G_{13}) variation on the angle compaction behaviour.	153
Figure 5.9	Effect of the fibre bed shear modulus (G_{13}) on the final shape of the angle. The deformation behaviour at the corner is enlarged.	154
Figure 5.10	Effect of the fibre bed shear modulus (G_{13}) on the final shear deformation (γ_{13}) distribution in the laminate, (a) SANOM, (b) SAG131 and (c) SAG132.....	155
Figure 5.11	Angle laminate compaction experiments, (a) laminate dimensions and fibre orientation definition, (b) tool dimensions.	156
Figure 5.12	Typical bagging configurations for no-bleed and bleed conditions. Configuration for the convex tool is shown in this figure.	157
Figure 5.13	Photograph of the tools with the bagging elements before the installation of the breather and the vacuum bag.	158
Figure 5.14	Photograph of the autoclave and the computer controlling the cure cycle.....	158

Figure 5.15	Definition of the processing parameters measured for the autoclave and the bag (top) and typical location of the thermocouples on the tool and in the part (bottom). The part thermocouples are embedded about 5 mm inside the part.	159
Figure 5.16	Cure cycle used and segment definition for the autoclave control system for the angle compaction experiment.	160
Figure 5.17	Laminate trimming after the cure.	161
Figure 5.18	Angle thickness measurement stations.	161
Figure 5.19	Temperature and pressure variation recorded during the cure showing the temperature gradients between the autoclave, tool and part temperatures. The tool and part temperatures shown are representative of the results for all thermocouples located in similar areas.	162
Figure 5.20	Photographs of the cross-section of samples showing the aspect of the defects found. The defects distribution is presented in Table 5.3.	162
Figure 5.21	Photographs of the samples after removal of the bagging elements. Resin can be seen at the edges of the samples.	163
Figure 5.22	Photographs showing the exterior aspect of the bags after cure. Resin is seen mainly with material A.	164
Figure 5.23	Thickness measurements after cure for material A with convex tool. The top of the error bar corresponds to the initial thickness of the laminate. The symbol * indicates the presence of minor defect at the corner.	165
Figure 5.24	Thickness measurements after cure for material B with convex tool. The top of the error bar corresponds to the initial thickness of the laminate.	165
Figure 5.25	Thickness measurements after cure for material A with concave tool. The top of the error bar corresponds to the initial thickness of the laminate. The symbols * and ** indicate the presence of minor and major defects at the corner respectively.	166
Figure 5.26	Thickness measurements after cure for material B with concave tool. The top of the error bar corresponds to the initial thickness of the laminate. The symbols * and ** indicate the presence of minor and major defects at the corner respectively.	166
Figure 5.27	Angle profiles obtained from image analysis of photographs of the specimen cross-sections. Good quality samples are shown on the left (5AM3 and 5CF3). On the right, thickness gradients at the corner for [90] samples (5BM7 and 5DF7) are exemplified by corner thinning and thickening.	167
Figure 5.28	Microphotographs of the cross-section of samples with defect at the corner for convex tool ((a) and (b)) and concave tool ((c) and (d)), (a) [0] sample (5BM11), (b) [Q] sample (5BM12), (c) [0] sample (5DF8) and (d) [Q] sample (5DF9).	168

Figure 5.29	Laminate strains for material A with convex tool. The strains at the measuring points are shown by the white bars. The total strain (ϵ_{total}) and the percolation strain ($\epsilon_{percolation}$) are also shown. The symbol * indicates the presence of minor defect at the corner. The strain sign is inverted so that positive indicates compression.	169
Figure 5.30	Laminate strains for material B with convex tool. The strains at the measuring points are shown by the white bars. The total strain (ϵ_{total}) and the percolation strain ($\epsilon_{percolation}$) are also shown. The strain sign is inverted so that positive indicates compression.	169
Figure 5.31	Laminate strains for material A with concave tool. The strains at the measuring points are shown by the white bars. The total strain (ϵ_{total}) and the percolation strain ($\epsilon_{percolation}$) are also shown. The symbols * and ** indicate the presence of minor and major defects at the corner respectively. The strain sign is inverted so that positive indicates compression.	170
Figure 5.32	Laminate strains for material B with concave tool. The strains at the measuring points are shown by the white bars. The total strain (ϵ_{total}) and the percolation strain ($\epsilon_{percolation}$) are also shown. The symbols * and ** indicate the presence of minor and major defects at the corner respectively. The strain sign is inverted so that positive indicates compression.	170
Figure 5.33	Finite element mesh including the tool and the laminate used for temperature predictions.	171
Figure 5.34	Temperature profiles predicted by COMPRO compared to the experiments. The viscosity profiles predicted for the two materials are also shown indicating the gel time of the resin.	171
Figure 5.35	Finite element models definition and material properties for angle laminate simulations.	172
Figure 5.36	Finite element meshes for convex tool specimens (464 elements) and concave tool specimens (448 elements).	173
Figure 5.37	Location of node outputs of COMPRO simulations for the normal displacement and the resin pressure.	173
Figure 5.38	Comparison between the predicted and measured final thickness for the convex tool laminates. The top of the error bar corresponds to the initial thickness of the laminate. The symbol * indicates the presence of a minor defect at the corner.	174
Figure 5.39	Comparison between the predicted and measured final thickness for the concave tool laminates. The top of the error bar corresponds to the initial thickness of the laminate. The symbols * and ** indicate the presence of minor and major defects at the corner respectively.	174

Figure 5.40	Comparison between the experimental (ϵ_{total}) and predicted (ϵ_n) normal strain for convex tool laminates. The symbol * indicates the presence of a minor defect at the corner. The strain sign is inverted so that positive indicates compression. ...	175
Figure 5.41	Comparison between the experimental (ϵ_{total}) and predicted (ϵ_n) normal strain for concave tool laminates. The symbols * and ** indicate the presence of minor and major defects at the corner respectively. The strain sign is inverted so that positive indicates compression.	175
Figure 5.42	Predicted deformed shape at the end of the compaction for material A laminates. The original shape of the laminate is shown by the solid line.....	176
Figure 5.43	Photograph of the edge profile of the laminates after cure for sample moulded with concave tool. The cross-sections shown are in the x-z plane (Figure 5.11 (a)).....	176
Figure 5.44	Angle laminate compaction behaviour predicted by COMPRO for material A, convex tool. The viscosity profile for the resin is also shown.	177
Figure 5.45	Angle laminate compaction behaviour predicted by COMPRO for material B, convex tool. The viscosity profile for the resin is also shown.	177
Figure 5.46	Angle laminate compaction behaviour predicted by COMPRO for material A, concave tool. The viscosity profile for the resin is also shown.	178
Figure 5.47	Angle laminate compaction behaviour predicted by COMPRO for material B, concave tool. The viscosity profile for the resin is also shown.	178
Figure 5.48	Resin pressure variation at the tool surface (Figure 5.37) predicted by COMPRO for material A, convex tool.....	179
Figure 5.49	Resin pressure variation at the tool surface (Figure 5.37) predicted by COMPRO for material B, convex tool.....	179
Figure 5.50	Resin pressure variation at the tool surface (Figure 5.37) predicted by COMPRO for material A, concave tool.	180
Figure 5.51	Resin pressure variation at the tool surface (Figure 5.37) predicted by COMPRO for material B, concave tool.	180
Figure 5.52	Contours for the normal strain ϵ_3 at the end of compaction predicted by COMPRO for laminates with material A.	181
Figure 5.53	Longitudinal and shear stresses generated by the compaction of a curvilinear fibre bed for convex and concave tool configurations. The original shape is shown by the dotted lines. The fibres are oriented along s and are assumed to be very stiff in that direction.....	182
Figure 5.54	Photograph of a wrinkle at the corner of a [0] lay-up with material A on a convex tool. The fibres are bridging at the corner creating voids (dark lines).....	182
Figure 5.55	Reaction stress at the corner (σ^*) for the different tool configuration, convex and concave. σ is the applied pressure, s_p is the surface exposed to the pressure and s_t is the surface exposed to the tool.	183

Figure 5.56 Resin velocity vector plot predicted by COMPRO during the compaction of the laminates at t=50 minutes for material A.	184
Figure 5.57 Resin pressure (kPa) contours predicted by COMPRO during the compaction of the laminates at t=50 minutes for material A.	185
Figure 5.58 Fibre volume fraction contours predicted by COMPRO during the compaction of the laminates at t=50 minutes for material A.	186
Figure 5.59 Photograph of a wrinkle at the corner of a [90] lay-up with material A on concave tool. The bag wedged the laminate at the corner. The bleeder stayed included in the laminate as shown.....	187
Figure 6.1 Dimensions and variables definition for the shear flow model.	210
Figure 6.2 Effect of the tool-laminate interface boundary conditions on the predicted longitudinal velocity (v_x) profile shape with Equation 6.1.....	210
Figure 6.3 Shear flow test configuration.....	211
Figure 6.4 Photograph of the loading jig for the shear flow experiments showing the principal components.....	211
Figure 6.5 Definition of the marker positions before the test.	212
Figure 6.6 Micrographs (50X) of sample 10_2 (markers 2, 3,4,5 - Row C) at different load increment, (a) no load, (b) Load 1, (c) Load 2 and (d) Load 3. The percolation of the resin becomes visible as the load applied increases.	213
Figure 6.7 Micrographs (50X) comparing the specimen edge surface profile after Load 1 for (a) thin sample 10_2, (b) thick sample 20_2.	214
Figure 6.8 Markers displacement (u_x) profiles of a thick sample 20_1, Load 1 (Rows A, B and C) compared with the displacement profile using the function for u_x in Equation 6.5 to fit the experimental points.	214
Figure 6.9 Markers displacement (u_x) profiles along the length of a thick sample 20_1, Load 1 (Rows A, B and C) compared with the displacement profile using the function for u_x in Equation 6.5 to fit the experimental points.	215
Figure 6.10 Markers displacement (u_z) profiles of a thick sample 20_1, Load 1 (Rows A, B and C) compared with the displacement profile using the function for u_z in Equation 6.5 to fit the experimental points.	215
Figure 6.11 Micrographs (50X) taken from a video recording showing the plate-laminate interface at different time intervals during Load 2 increment of sample 10_2 (Row C). Images on the left are untouched, images on the right are overlaid to illustrate the deformation of a surface patch of resin as the specimen is loaded.....	216
Figure 6.12 Variation of the marker displacements (u_x and u_z) with time during and after loading for sample 20_1, Load 1 (markers 1,2 and surface - Row C).....	217

Figure 6.13	Markers displacement (u_x) profiles of thin sample 10_2, Load 1 (Row C). The final displacement profile is compared with the displacement profile using the function for u_x in Equation 6.5 to fit the experimental points. The transient markers displacement are obtained from a video tape recording taken during compaction.	217
Figure 6.14	Markers displacement (u_x) profiles of a thick sample 20_1, Load 1 (Row C). The final displacement profile is compared with the displacement profile using the function for u_x in Equation 6.5 to fit the experimental points. The transient markers displacement are obtained from a video tape recording taken during compaction.	218
Figure 6.15	Variation of the slip velocity at the plate-laminate interface (V_{xwall}) and the shear strain rate close to the surface ($\partial v_x/\partial z$) with time for a thin specimen (10_2).	218
Figure 6.16	Variation of the slip velocity at the plate-laminate interface (V_{xwall}) with the shear strain rate close to the sample surface ($\partial v_x/\partial z$) for a thin and thick sample. The critical shear strain rate $(\partial v_x/\partial z)_0$ is shown which correspond to a critical shear stress $(\tau_{xz})_0$ after which the sample starts to slip.	219
Figure 6.17	Specimen configuration for the flow mechanisms experiments.....	219
Figure 6.18	Possible flow mechanisms, (a) percolation and (b) shear. The initial sample dimension is indicated by the dashed line.	220
Figure 6.19	Flow number variation with curing temperature for material A and B.	220
Figure 6.20	Plane view photograph of typical specimens after testing.....	221
Figure 6.21	Effect of ply orientation on e_x (shear) and ε_v (percolation). The results shown are the average for three samples and the error bars represent the standard variation. The strain sign is inverted so that positive indicates compression.	222
Figure 6.22	Effect of ply orientation on e_z^P (percolation) and e_z^S (shear). The results shown are the average of three samples. The strain sign is inverted so that positive indicates compression. The strains are added to obtain the total strain of the sample e_z	223
Figure 6.23	Flow mechanisms map for a uniaxial loading condition. The range of viscosity and laminate elastic modulus (E_x) in the flow direction for material A and B is shown as a reference. For $[0^\circ]$ and $[90^\circ]$, the fibres are oriented in the x and y direction respectively.....	224
Figure A.1	Bilinear quadrilateral element: isoparametric transformation and Gauss points location.	251
Figure A.2	Computation of equivalent nodal load vectors due to the applied external pressure.	251
Figure A.3	Element coordinate system.	252
Figure A.4	Tangent modulus and effective stress calculation from the fibre bed compaction curve.	253

Figure B.1	Parallel plate viscosity test setup, torsional oscillation ($\theta(t)$) is applied to the specimen and the torque $T(t)$ is measured by a load cell.....	272
Figure B.2	Dynamic cure viscosity results (start temperature: 50°C) for material A resin (3501-6) and comparison with model predictions (Equation B.6) using constants from Table B.2 and constants in Lee et al. (1982).	272
Figure B.3	Variation of $\ln m$ versus $1/T$ (Equation B.7 with $\alpha \approx 0$) for material A resin (3501-6) over a range of 50°C to 90°C. A linear regression leads to a value of 114477 J/mol for the activation energy U	273
Figure B.4	Isothermal viscosity results for material B resin (8552) and comparison with model predictions (Equation B.8) using constants from Table B.2.....	273
Figure B.5	Dynamic viscosity results (start temperature: 60°C) for material B resin (8552) and comparison with model predictions (Equation B.8) using constants from Table B.2.	274
Figure B.6	Typical cure cycle viscosity results (start temperature: 60°C) for material B resin (8552) and comparison with model predictions (Equation B.8) using constants from Table B.2.....	274
Figure B.7	Variation of $\ln m$ versus $1/T$ (Equation B.10) for material B resin (8552) over a range of 60°C to 145°C. A linear regression leads to a value of 76536 J/mol for the activation energy E_{μ}	275
Figure B.8	Longitudinal permeability prediction for a unidirectional fibre bed from different sources (Table B.4) as a function of the fibre volume fraction.	275
Figure B.9	Transverse permeability prediction for a unidirectional fibre bed from different sources (Table B.4) as a function of the fibre volume fraction.	276
Figure B.10	Compaction curve computation for the load-unload test method, (a) master loading curve built from load-unload cycles, (b) resin pressure is computed, (c) the fibre bed load is calculated by subtracting (b) from (a).....	276
Figure B.11	Load-displacement curves for different load-unload cycles (1 to 5) for load-unload compaction test (material A, 6A01).....	277
Figure B.12	Load-displacement curves for load-unload compaction test (material A, 6A01) showing the different components of the total load: the resin pressure load calculated from Equation B.13 and the fibre bed elastic load.	277
Figure B.13	Compaction curve for material A obtained with the load-unload method for samples 6A01 and 6A02. A comparison with Gutowski's model (Equation 2.3) is presented with $\beta=350$, $V^a=0.81$, $V_{f0}=0.558$ and $E_f=230$ GPa.....	278
Figure B.14	Comparison of the compaction curves for the materials studied. For the material A, the curve obtained by both testing methods are shown.	278
Figure B.15	Comparison of the load-displacement behaviour predictions using the compaction curves obtained by the load-unload and load-hold method respectively. The results are compared with specimen 9A01 (material A) experimental results.	279

Figure C.1 Angle thickness measurement stations.283

Figure D.1 Coordinate definitions for the computation of the marker position, (a) measurements from the ESEM and (b) marker position definition in the sample coordinate system.292

Figure E.1 Flow mechanisms test sample dimensions: before the test (L_0, W_0, H_0) and after the test (L', W', H'). The definition of the fibre orientation direction is also shown. ...298

Nomenclature

a_j^u	displacement degree of freedom
a_j^p	resin pressure degree of freedom
a_i	unit vector for fibre direction
A	constant for composite velocity function
A	constant for resin viscosity model (Appendix B)
A_μ	constant for resin viscosity model
A_1, A_2, A_3	constants for resin cure kinetics model
A_c	element area
A_i	ply area
A^*	constant for composite displacement function
B	constant for composite velocity function
B	constant for resin cure kinetics model (Appendix B)
B	constant for resin viscosity model (Appendix B)
B^*	constant for composite displacement function
\mathbf{B}	shape function derivatives matrix
c	constant for permeability model
C	constant for permeability model
C	constant for resin cure kinetics model (Appendix B)
C_1, C_2, C_3	constants for resin cure kinetics model
\mathbf{C}	damping matrix
C_c	fibre bed compression index
d_{ij}	strain rate vector
\mathbf{D}	stiffness matrix
D_{ijkl}	composite viscosity constitutive matrix
\mathbf{D}_T	tangent material stiffness matrix
\mathbf{D}_T^c	element tangent material stiffness matrix
e	composite void ratio
e_{ij}	large strain vector
e_z^p	vertical strain caused by percolation flow

e_z^s	vertical strain caused by shear flow
E	fibre bed Young's modulus
E_μ	constant for resin viscosity model
E_a	constants for resin cure kinetics model
E_1	fibre bed longitudinal modulus
E_3	fibre bed transverse modulus
E_3^c	fibre bed transverse modulus in compression
E_3^t	fibre bed transverse modulus in tension
E_f	fibre flexural modulus
E_{fb}	fibre bed effective stiffness matrix
F	constant for composite viscosity model
\mathbf{F}	load vector
\mathbf{F}^{ext}	vector of applied loads
\mathbf{F}^{int}	vector of internal loads
\mathbf{F}^g	gravity forces vector
F_i^{eq}	equivalent nodal forces due to applied external pressure
F_i	internal body forces
F_p	resin pressure load
F_z	applied load for compaction experiments
FN	flow number
g	acceleration due to gravity
g_z	gravitational acceleration
G_{13}	fibre bed shear modulus
\mathbf{G}	shape function derivatives matrix
h	height above a reference point
h^j	ply thickness
H	laminate thickness (Chapter 2, Chapter 4 and Chapter 5)
H	laminate half thickness (Chapter 6 and Appendix D)
H_0	laminate initial thickness (Chapter 4 and Chapter 6)
H_{0i}	laminate initial thickness (Chapter 5)
H_i	laminate final thickness (Chapter 5)
H'	laminate final thickness (Chapter 4 and Chapter 6)

H_r	total heat of reaction
\mathbf{H}^d	matrix containing pressure head term
\mathbf{J}	Jacobian matrix
k	Kozeny constant
k'	modified Kozeny constant
K_{ij}	fibre bed permeability tensor
K	fibre bed permeability
\mathbf{K}	fibre bed permeability matrix
\mathbf{K}^e	element fibre bed permeability matrix
K_x^e	element longitudinal permeability
K_z^e	element transverse permeability
K_x^i	ply longitudinal permeability
L	laminate length (Chapter 2 and Chapter 4)
L	laminate half length (Chapter 6 and Appendix D)
L	length of the flat section for angle laminate (Chapter 5)
L_0	laminate initial length (Chapter 4 and Chapter 6)
L'	laminate final length (Chapter 4 and Chapter 6)
m	constant for resin cure kinetics model
m_{rloss}	resin mass loss
m_{c0}	initial laminate mass
m_c	final laminate mass
m_v	fibre bed coefficient of volume change
M_0	laminate initial mass
M'	laminate final mass
M_{rloss}	resin mass loss ratio
n	constant for resin cure kinetics model
n^U	Euclidean norm of the increment of the state variables
n^R	Euclidean norm of residual forces
\mathbf{N}	element shape function matrix
N_{ij}^u	element shape function
N_j^p	element shape function
P	resin pressure

P_{atm}	atmospheric pressure
P_b	bag pressure
q	heat generated during curing reaction
q^n	applied resin flux at the domain boundary
r_f	fibre radius
r_{ij}	reaction stress
R	universal gas constant
R	tool side radius (Chapter 5)
R_f	continuity equation Galerkin residual
R_{in}	angle laminate inside radius
R_{out}	angle laminate outside radius
\mathbf{R}	vector of residual forces
R_s	equilibrium of forces Galerkin residual
s	arc length at corner of a curved laminate
s_p	arc length of the laminate surface exposed to the bag
s_t	arc length of the laminate surface exposed to the tool
S	composite saturation
S_{ij}	fibre bed compliance matrix
t	time
t_{gel}	time at resin gelation
T	temperature
T	tension in fibre direction (Chapter 2)
\mathbf{T}	transformation matrix for coordinate system transformation
\mathbf{T}_e	transformation matrix for coordinate system transformation
u_i	fibre bed displacement vector
u_i	marker displacement (Chapter 6)
u_{plate}	displacement of the plates for a loading increment
\dot{u}_i	fibre bed velocity
\dot{u}_{Ri}	resin velocity
U	constant for resin viscosity model
\mathbf{U}	vector of unknown nodal variables
$\dot{\mathbf{U}}$	vector of time derivatives of the unknown nodal variables

V_f	volume of fibre
V_c	volume of composite
V_{c0}	initial volume of composite
v_i	resin velocity
v	composite velocity (Chapter 6)
V_{xwall}	longitudinal velocity at the plate-laminate interface
V	resin velocity
V_a	maximum fibre volume fraction
V_a'	maximum fibre volume fraction for permeability model
V_f	fibre volume fraction
V_{f0}	initial fibre volume fraction
V_{fmax}	constant for permeability model
V_0	initial laminate volume
w_k, w_l	Gauss point weights
W	laminate width (Chapter 4 and Chapter 5)
W_0	laminate initial width (Chapter 4 and Chapter 6)
W'	Laminate final width (Chapter 4 and Chapter 6)
W_k	Galerkin weight function
x_{ESEM}	marker position in ESEM Coordinate System
x_{frame}	marker position in picture frame Coordinate System
x_i	marker position in laminate coordinate system
x_{stage}	stage position in ESEM Coordinate System
x_{LEFT}	sample position of the left edge surface in ESEM Coordinate System
x_{RIGHT}	sample position of the right edge surface in ESEM Coordinate System
z_{ESEM}	marker position in ESEM Coordinate System
z_{frame}	marker position in picture frame Coordinate System
z_{stage}	stage position in ESEM Coordinate System
z_{BOT}	bottom plate position in ESEM Coordinate System
z_i	marker position in laminate coordinate system
z_{TOP}	top plate position in ESEM Coordinate System
α	resin degree of cure
α_g	resin degree of cure at gelation

α_0	initial resin degree of cure
α_{C0}	constant for resin cure kinetics model
α_{CT}	constant for resin cure kinetics model
α_x	slip constant
β	fibre waviness ratio
β	angle between local and global coordinate system (Appendix A)
δ_{ij}	Kronecher delta
δ	vector from Kronecher delta
$\Delta E_1, \Delta E_2, \Delta E_3$	constants for resin cure kinetics model
ε^e	element strain in local coordinate system
ε_i	fibre bed strain
ε_b	fibre bed bulk strain
ε_{ni}	laminare normal strain
$\varepsilon_{percolation}$	laminare percolation strain
ε_{total}	laminare total strain
ε_v	laminare volumetric strain
ε_v^e	element volumetric strain
ϕ	composite porosity
$\dot{\gamma}_{ij}$	fibre bed shear strain rate
$\dot{\gamma}^*$	complex strain rate
Γ	boundary of the domain
η_l	Gauss point coordinate
η_L	composite longitudinal viscosity
η_T	composite transverse viscosity
η^*	complex resin viscosity
η'	real part of complex resin viscosity
η''	imaginary part of complex resin viscosity
κ	constant for viscosity model
λ_x	slip coefficient
μ	resin viscosity
μ_∞	constant for viscosity model

ν	fibre bed Poisson's ratio
θ	fibre orientation angle
ρ_C	composite density
ρ_F	fibre density
ρ_R	resin density
ρ_R^e	element resin density
σ	autoclave pressure
σ_i^n	applied traction at the domain boundary
σ^*	reaction stress at the corner of curved laminate
σ_{ij}	total applied stress
σ^*	complex stress
τ_{ij}	composite stress
$\bar{\sigma}^e$	element strain in local coordinate system
$\bar{\sigma}_{ij}$	effective stress
$\bar{\sigma}_b$	bulk effective stress
$\bar{\sigma}_0$	effective stress at a void ratio e_0
$\bar{\tau}_{ij}$	shear effective stress
ω	oscillations frequency during resin viscosity tests
Ω	domain
ξ_k	Gauss point coordinate
Ψ	tolerance for convergence criteria

Acknowledgments

I would like to express my gratitude to all the people who helped me throughout the course of my research. I would first like to express my deepest gratitude to Dr. Anoush Poursartip and Dr. Reza Vaziri for their guidance and enthusiastic support.

My experimental work could not have been completed without the assistance of Roger Bennett and Serge Milaire. Many thanks to Andrew Johnston, co-developer of COMPRO, for all the years of collaboration and the many long discussions. I am grateful to Dr. Göran Fernlund for his valuable assistance and ideas.

I would like to express my gratitude to Dr. Larry Ilcewicz and Dr. Carl Nelson of The Boeing Company for giving me the chance to experience the real-world application of composite materials. This experience added a practical aspect to my research work.

Many thanks to Don Stobbe and Brian Coxon of Integrated Technology Inc. for their invaluable advice on composite manufacturing. Many thanks to Dr. Alan Russel of DREP for providing material which was used in this research and to Dr. William McCarvill of Hercules Inc. for all the information on the resins used in this work.

I would like to thank Dr. Walter Bradley for allowing me to carry out the very useful experiments at Texas A&M University and Catherine Wood for her advice on how to use the Environmental Scanning Electron Microscope facility.

Many thanks to Dean Carnes for his precious assistance during the manufacturing of the angle laminates.

I am very grateful to all the members of the Composites Group for their friendship and their support during my stay in Beautiful British Columbia.

Finally, I would like to acknowledge the Canadian Natural Sciences and Engineering Research Council (NSERC) and Les Fonds pour la Formation de Chercheurs et l'Aide à la Recherche (FCAR) for their financial support.

Chapter 1 Introduction

The future use of fibre reinforced polymer composites in primary structures for aerospace applications depends mainly on cost-effective manufacturing. The material cost of aerospace composites is about ten times higher than the materials currently used. However, composites permit the manufacturing of large structural panels having complex shapes with fewer fasteners and parts, as shown in Figure 1.1. For this type of structure, the different structural elements such as skin, frames and stiffeners are cured in one operation, considerably reducing the manufacturing costs. Thus the higher cost of the material is compensated by the reduction in labor costs associated with the assembly of the structural components. The success of this cost reduction depends entirely on the design of a robust manufacturing process. Such a process should produce high quality structures that meet design tolerances, since the rejection costs for structures of the size depicted in Figure 1.1 are considerable. Today, large composite parts are routinely manufactured with a high degree of quality. However, questions about the level of reproducibility, predictability and dimension tolerances need to be addressed.

A multitude of manufacturing routes are available to produce composite structures. The distinctive characteristic of composite processes is that the material is engineered simultaneously with the final part. The process used depends on the application and the number of structures to be produced. For low cost applications and small production rates, hand lay-up is the most common process used. For larger production rates, compression moulding, filament winding and pultrusion have been widely adopted by industry. More recently, resin transfer moulding allows the manufacture of high quality parts with a short process cycle, and thus has great potential for

the automotive industry. Autoclave processing is often chosen for high performance parts, and typically used in aerospace applications.

The base material used in autoclave processing is a pre-impregnated sheet, commonly called 'prepreg'¹. This prepreg contains fibres pre-impregnated with a catalyzed thermoset resin which will cure at high temperatures. The resin is partially cured to facilitate the manipulation of the prepreg.

The first step of the autoclave process is the lay-up and bagging procedure outlined in Figure 1.2 (a). The prepreg plies are laid-up, forming a laminate, on a tool having the shape of the final part. The plies can be oriented in any direction to obtain the desired mechanical properties. Layers of an absorbing material forming the bleeder can be placed around the laminate if excess resin has to be absorbed from the laminate². Dams are placed around the edges of the laminate to restrict resin flow in those directions. Inserts and honeycomb cores can be included in the laminate for moulding purposes or structural requirements. A breather cloth covers the laminate assembly to provide a path for air flow. The complete assembly consisting of tool, laminate, bleeder, breather and inserts is bagged in a plastic film (called the vacuum bag) that is sealed at the tool plate. A vacuum plug connects the interior of the bag to an external vacuum pump.

The second step is the curing of the part as shown in Figure 1.2 (b). The tool-laminate assembly is placed in an autoclave, essentially a large temperature and pressure controlled vessel, and the

¹ Typically, a prepreg ply has a thickness of 0.2 mm and a fibre volume fraction (V_f) of 50 to 60%.

² For no-bleed conditions (i.e. no resin flow), a layer of impermeable material replaces the bleeder.

bag is connected to the vacuum system. In order to cure the part, pressure and temperature are applied to the laminate in a predetermined cure cycle (Figure 1.3). The temperature (T) cycle is necessary to trigger the resin polymerization reaction. The pressure (σ) is applied to the laminate to conform the laminate to the tool surface, and to compact the laminate at the desired fibre volume fraction and collapse any voids that may develop during the resin cure. The bag pressure (P_b) is controlled to initially remove any entrapped air during lay-up and volatiles during cure. The bag pressure must be less than the autoclave pressure to ensure compaction of the laminate. Finally, the cured part is debagged and ready for secondary and finishing processes. The main challenge of the curing process is to determine the cure cycle, design the tool and define a bagging procedure that will produce a fully cured, void free and undistorted part in the shortest time and the most economical fashion.

The trial-and-error approach was the only option initially and remains a popular way to develop cure cycles (Purslow and Childs, 1986). It consists of making several test panels with different cure cycles until the desired characteristics of the part are obtained. This approach is acceptable for basic parts such as flat or low curvature thin panels (<6 mm thick). For thicker panels (≈ 25 mm), temperature gradients through the thickness can lead to non-uniform cure and flow of the resin. Such panels need extensive test programs before a suitable cure cycle is obtained.

The more modern approach to overcome the difficulty of processing complex parts is to control the autoclave using expert systems and sensors embedded in the laminate (Holl and Rehfield, 1992). Parameters such as temperature, dielectric activity (Kenny et al., 1991), degree of compaction (Ciriscioli et al., 1992; Saliba et al., 1994), and more recently resin pressure (Mackenzie, 1993) are monitored during the cure by a computer. Processing rules based on

experience or basic theoretical background are implemented in a real time control loop (Figure 1.2 (b)). As the part is processed, the cure cycle is altered in real time depending on the state of the processing variables measured by the sensors. The problem with this method is that the laminate is sometimes heavily instrumented with sensors that are permanently embedded in the final part. The sensors can also perturb the process by their presence. Finally, some sensors used are expensive and difficult to implement in a production environment.

The more fundamental approach is process modelling (Loos and Springer, 1983). Cure cycle guidelines are obtained by studying and understanding the fundamental mechanisms that occur during processing. Processing models are developed from the governing equations for the physical phenomena involved during processing (i.e. heat transfer, cure kinetics, resin flow, laminate compaction, residual stresses). Computer simulations can isolate the dominant variables that affect the cure by means of parametric or sensitivity analysis. This approach could considerably reduce the number of plant trials to achieve an adequate processing scheme for a complex part.

Among the multitude of phenomena occurring during processing, resin flow in the laminate is a critical issue. It affects the fibre volume fraction distribution, the formation of resin rich regions and the final dimensions of the part. Figure 1.4 shows typical defects related to resin movement or pressure distribution in the laminate. Residual deformations or warpage (1) are affected by residual stress development during cure. Stress calculations require the knowledge of the local elastic properties that are functions of the local fibre volume fraction. Resin rich (2) and resin poor (3) regions are a consequence of resin movements. Flow and resin pressure distributions in the laminate play an important role in void formation and migration (4). For sandwich panels,

surface dimpling (5) and core buckling (6) also depend on the pressure distribution and consequently resin flow in the laminate.

Flow of composites during cure can be separated into two major mechanisms: percolation flow and shear flow. For *percolation flow*, applying pressure to the laminate is similar to squeezing a sponge that causes the fluid to bleed out. In this case, the resin flows relative to the fibres and the flow has to be coupled with the fibre bed compaction behaviour to obtain the final shape of the laminate. For *shear flow*, the composite behaves as a very viscous fluid filled with inextensible fibres. In this case the resin and the fibres move together with the application of an external pressure. Typically, the percolation flow approach is used to model the flow and compaction of thermoset matrix composites and the shear flow approach is applied to thermoplastic matrix composites. In both cases, the flow and compaction behaviour of laminates of simple shape is well covered in the literature.

The main goal of the present research project is to build on the previous work on flow and compaction of composites. This is done by applying the current theories to study complex shape laminates such as curved panels or hat sections. To achieve this objective, the present research is organized as follows:

- 1) First, a complete literature review of the pertinent aspects related to flow during processing of composites is presented in Chapter 2. Based on the literature review, our objectives to study flow and compaction of complex shapes are formulated.

- 2) Next, a 2-D finite element flow-compaction model assuming percolation flow is developed in Chapter 3. This model is applied to laminates of complex shape in Chapter 5 to study the effect of different material properties on the compaction behaviour.
- 3) Two thermoset matrix composites are studied for this project: a low resin viscosity and a high resin viscosity system. The material properties required by the flow-compaction model are measured, or evaluated from the literature, in Chapter 4.
- 4) An experimental investigation of the compaction of curved laminates having different lay-ups and bagging conditions is conducted. The results from these experiments are compared to the numerical simulations in Chapter 5.
- 5) Next, the shear flow behaviour mechanism is observed directly during compaction. The results are compared to the current theory used for shear flow modelling in Chapter 6.
- 6) The contribution of percolation and shear flow to the compaction of simple laminates is investigated in Chapter 6. Finally, suggestions to improve the current flow-compaction model formulation and recommendations for further studies are given in Chapter 7.

1.1 Figures

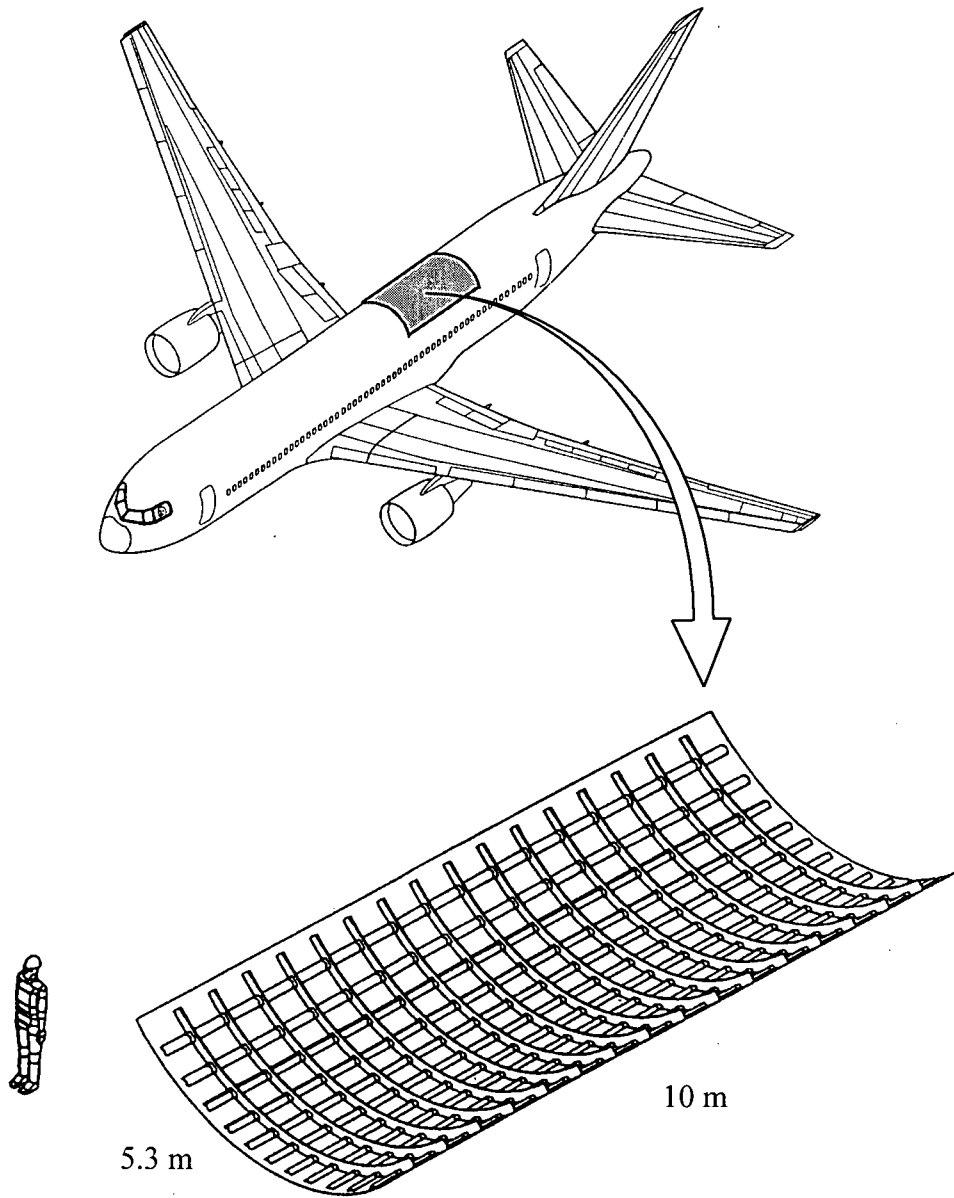
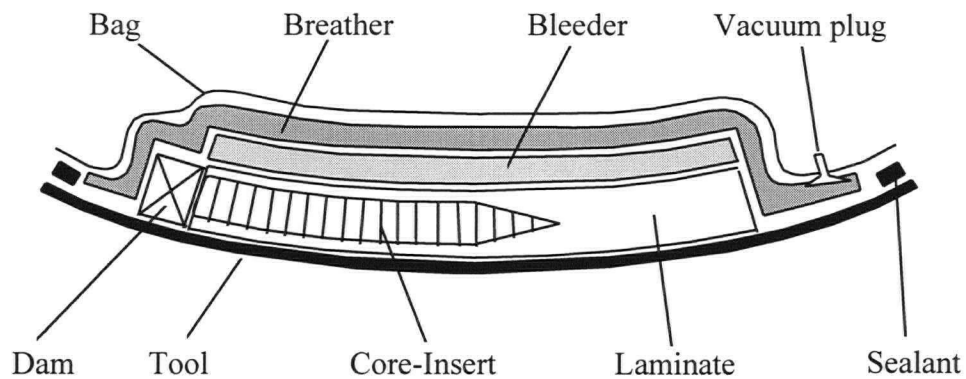
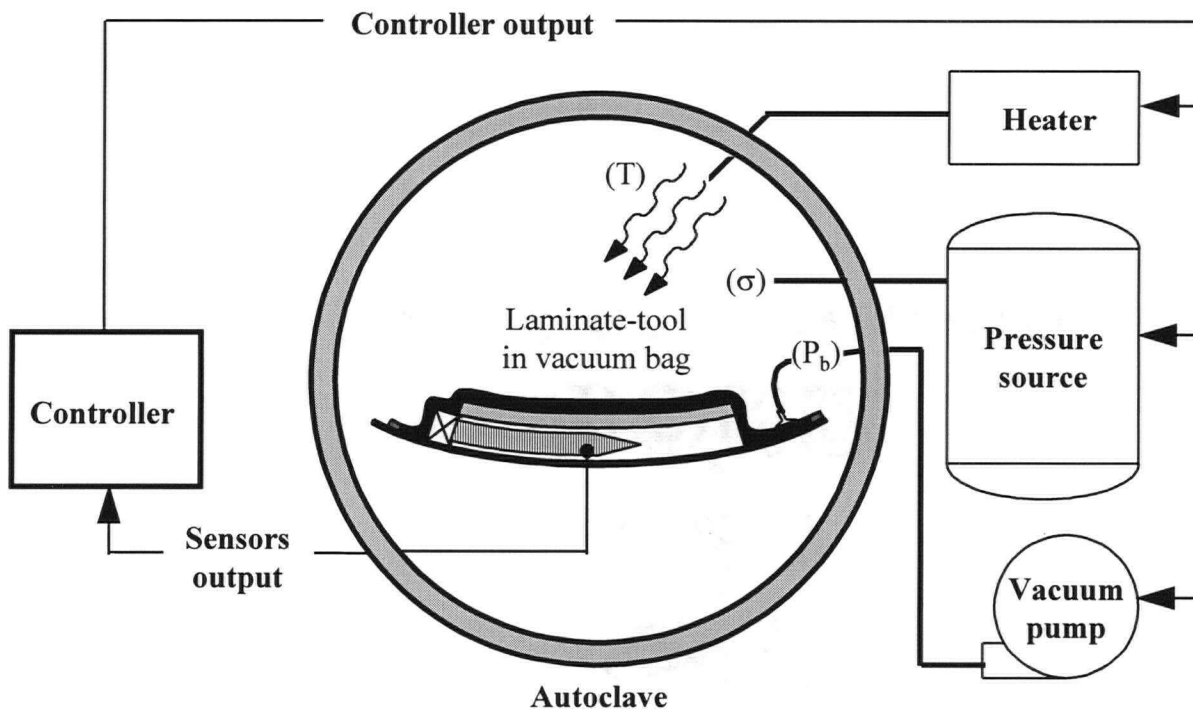


Figure 1.1 Application of composites for large aircraft structures. (Courtesy of the Boeing Company).



(a)



(b)

Figure 1.2 Autoclave processing steps, (a) lay-up, (b) cure with a controller loop.

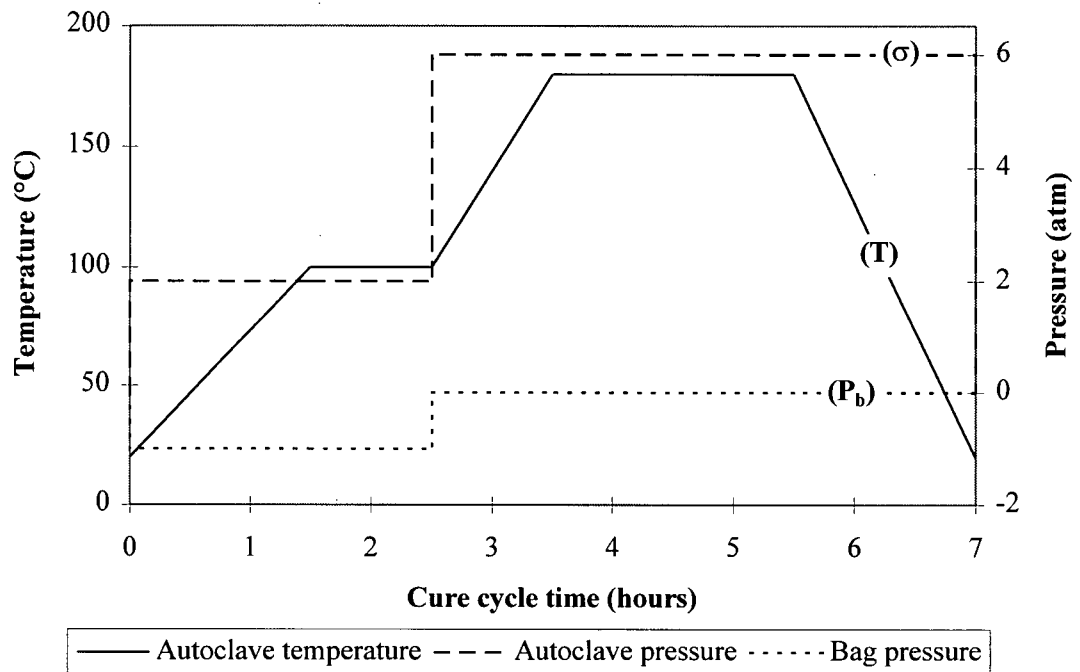


Figure 1.3 Typical autoclave cure cycle.

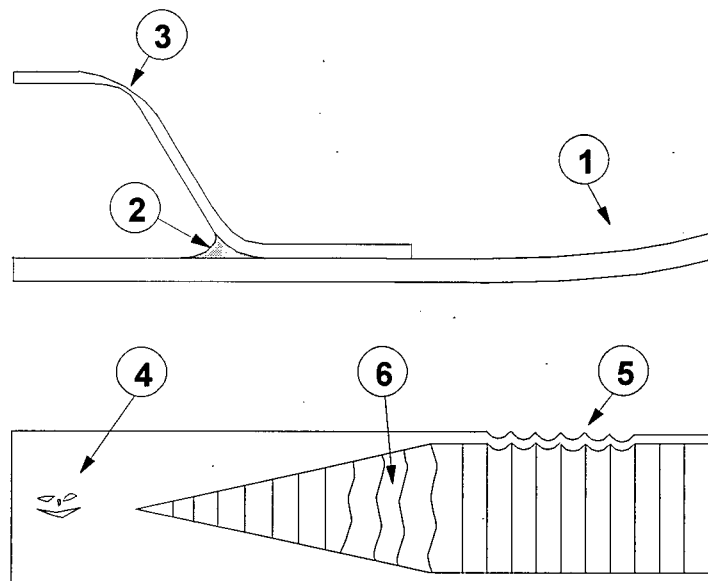


Figure 1.4 Processing defects induced by flow and compaction, (1) warpage, (2) resin rich region, (3) resin poor region, (4) voids, (5) surface dimpling and (6) core buckling.

Chapter 2 Literature Review and Research Objectives

This chapter contains a comprehensive literature review on the flow and compaction behaviour of composites during cure. In the first two sections, the characteristics of the curing resin and the fibre bed are discussed. Then the flow models for the two main flow mechanisms in composite laminates are presented. Experimental characterizations of the flow in composites are also reviewed. Finally, from the summary of the literature review, research objectives for this work are stated.

2.1 Resin behaviour during cure

Cured resins in composites are long molecular chains cross-linked in a three-dimensional network. The curing process is basically the formation of that network from the basic resin components (Berglund and Kenny, 1991). A curing agent or catalyst is added to the resin to initiate the polymerization reaction. Initially, the resin is a liquid and polymerization will result in a change from a liquid to a solid state. The degree of cure, α , represents the extent of the resin polymerization reaction. Rather than basing α on a material physical property such as molecular weight or cross-link density, a definition based on the more easily measured heat of reaction of the resin is usually used as follows:

$$\alpha = \frac{q(t)}{H_R} \quad (2.1)$$

where $q(t)$ is the heat generation up to time t and H_R is the total amount of heat that would be evolved during a 'complete' reaction. Thus, the degree of cure has a value between zero and unity ($\alpha=1$ indicates that the resin has attained full conversion). Figure 2.1 shows a typical

variation of α with curing time. When the resin and the curing agent are mixed together, the reaction starts and the epoxy molecules increase their molecular weight (Figure 2.1 Phase I). Eventually, an infinite network is formed at a stage called the gel point (Figure 2.1 Phase II). Finally, other cross-linking reactions increase the density and the stiffness of the network to form a fully cured solid polymer (Figure 2.1 Phase III). Since the resin molecular structure changes during cure, its physical and rheological properties will change as well. The initial stages of the resin curing will more likely be dominated by purely viscous effects. But as the crosslinking reaction occurs and particularly in the region of the gel point, the resin will behave increasingly as a viscoelastic material.

The rate of the curing reaction $d\alpha/dt$, is a function of the temperature, T , and α . Different expressions are found in the literature to describe $d\alpha/dt$ (Kenny et al., 1989 and 1990; Dusi et al., 1987; Mijovic and Lee, 1989). Mechanistic models are based upon a detailed knowledge of the specific chemical reactions that occur throughout the curing process. As the detailed chemical composition of many resin systems is proprietary, use of a fully mechanistic approach may not always be possible. Thus empirical or semi-empirical models are used. Empirical models are based on experimental determination of the rate of resin cure through measurement of the heat generated by the reaction. Expressions are then developed to fit experimental results. Cure kinetic constants for these semi-empirical expressions can be found experimentally with DSC (Differential Scanning Calorimeter) isothermal and dynamic tests. An accurate determination of $d\alpha/dt$ is critical for the calculation of other properties related to the curing state of the resin such as the resin viscosity.

In its liquid stage, the resin viscosity is influenced by two major phenomena. The first is the growing size of the molecules which increases the viscosity. The second is the effect of the temperature on the molecular mobility. Therefore, the resin viscosity, μ , depends on T and α . Different approaches are found in the literature to model resin viscosity. Dusi et al. (1987) proposed the following empirical relation:

$$\mu = \mu_{\infty} \exp(\kappa\alpha) \exp\left(\frac{U}{RT}\right) \quad (2.2)$$

where μ_{∞} , U , and κ are constants determined from viscometer data. More fundamental models based on the free volume concept and branching theory lead to more complicated relations for the resin viscosity (Kenny et al., 1989; Mijovic and Lee, 1989). These latter models are more accurate but need extensive epoxy and amine molecular structure characterization and require the knowledge of the reaction mechanism. Figure 2.2 shows a typical viscosity variation during cure. As the resin temperature increases, the viscosity decreases to reach a minimum. At this point most of the flow occurs until the curing reaction starts and increases the viscosity. When the resin reaches the gel point, the viscosity rises rapidly and the flow stops (the resin forms a gel).

Most flow models assume the resin is a Newtonian fluid (i.e. the viscosity is independent of the shear rate). During autoclave processing, the flow is quasi-static (creeping flow); therefore, the Newtonian fluid behaviour assumption can be assumed valid since the shear rates are low. However, because of the curing process, the resin rheological behaviour can change during cure. Bartlett (1978) measured the viscosity change during cure at different values of shear rates for an

epoxy resin and found deviation of Newtonian behaviour approaching the gel point¹. Since flow slows down considerably near the gel point, the non-Newtonian behaviour might not affect the flow significantly. Very viscous polymers like thermoplastic melts can exhibit a shear thinning behaviour or extensional flow. Shear thinning effects are more likely to appear at high shear rates. Extensional flow results in larger pressure drops than those predicted using classical Newtonian flow models. Skartsis et al. (1992a) isolated the viscous and elastic behaviour of polymer flow through porous media. The onset of elastic behaviour depends on the relaxation time of the fluid, the fluid velocity and the fibre bed geometry. As mentioned by Åström et al. (1992), elastic or viscoelastic effects will more likely occur with thermoplastic processing at high shear rates, such as in thermoplastic pultrusion.

2.2 Fibre bed behaviour

The fibre bed is assumed to be an elastic porous medium with incompressible and inextensible fibres. The fibre bed is fully saturated with the resin. In the percolation approach, the resin flows in the pores between the fibres. The fibre mass in the laminate remains constant during cure. This fibre bed idealization is the basis for the development of expressions to describe its elastic and flow behaviour. Since this thesis focuses mainly on the percolation flow mechanism, the fibre bed characteristics applied for this approach are described in more depth.

Porous media exist in numerous forms. Soils are granular (sand) or fractured (rocks) porous media. Fibre beds are more similar to textiles. The fibres can take two ideal packing

¹ The resin is in a viscoelastic regime, therefore a different material constitutive law should be considered.

arrangements: square and hexagonal (Figure 2.3), that enable a theoretical maximum fibre volume fraction (V_f) of 78.5% and 90.4% respectively. From that ideal arrangement, the fibres are assumed straight and the fibre bed is represented as a multitude of cells with an equivalent pore geometry. In reality, the pore geometry might not be constant in the laminate. Figure 2.4 shows different possible pore geometries for different fibre beds. Figure 2.4 (a) is a typical cross-section of a fully compacted unidirectional laminate. The pore geometry is relatively uniform and is represented as channels with a star cross section. Figure 2.4 (b) shows a unidirectional laminate where resin rich regions exist between the plies. This arrangement is similar to fractured rock soils where a network of channels exists between groups of uniform porous media. Figure 2.4 (c) illustrates a non-homogeneous pore geometry pattern typical of a fabric where fibre tows are woven together. Real unidirectional fibre beds contain fibres having small waviness with a length to height ratio of approximately 150 (Gutowski et al., 1986a). The typical pore cell and the fibre representation are a function of the type of fibre bed. This aspect is very important in the discretization of the fibre bed into characteristic porous media elements.

2.2.1 Fibre bed elasticity

From compaction experiments on carbon fibre beds impregnated with silicone oil, Gutowski et al. (1986a and 1986b) found that at high fibre volume fraction ($V_f > 0.5$) the fibres gradually carry an increasing portion of the applied load, defined as the effective stress ($\bar{\sigma}$). This behaviour is caused by multiple fibre-to-fibre contacts resulting from the fibre waviness. Assuming the fibres to be curved beams in bending, they derived the following expression to express the fibre bed effective stress as a function of the fibre volume fraction:

$$\bar{\sigma}(V_f) = \frac{3\pi E_f}{\beta^4} \frac{\left(1 - \sqrt{\frac{V_f}{V_{f0}}}\right)}{\left(\sqrt{\frac{V_a}{V_{f0}}} - 1\right)^4} \quad (2.3)$$

where E_f is the flexural modulus of the fibre, β is the waviness ratio, V_{f0} is the initial fibre volume fraction and V_a is the maximum fibre volume fraction achievable. Davé et al. (1987b) have fitted an empirical relation relating the void ratio² (e) to the effective stress for ($\bar{\sigma}$) ranging from 0.07 (10 psi) to 1.0 MPa (140 psi):

$$e = -C_c \log\left(\frac{\bar{\sigma}}{\bar{\sigma}_0}\right) - e_0 \quad (2.4)$$

where

$$e = \frac{1 - V_f}{V_f} \quad (2.5)$$

C_c is the compression index and ($\bar{\sigma}_0$) is the effective stress at a void ratio e_0 . Lam and Kardos (1989) and Skartsis et al. (1992c) did compression tests on unidirectional carbon fibre tows impregnated with water and silicone oil. Like Davé et al. (1987b), they observed that at low effective stresses ($0 < \bar{\sigma} < 0.07$ MPa (10 psi)), the relation between e and ($\bar{\sigma}$) is linear and highly dependent on the initial fibre volume content. This region corresponds to some initial settlement of the fibre bed.

² The void ratio is defined as the ratio of the resin volume fraction over the fibre volume fraction.

Kim et al. (1991) did numerous experiments on dry and lubricated glass and carbon fibre beds. They noted that an increase in the rate of loading causes an increase in the measured effective stress. Slower loading rates allow more time for fibre rearrangement. Gutowski and Dillon (1992) confirmed that observation by comparing all the available compaction curves from the literature. They stress the importance of rate effects on the consolidation behaviour of fibres by showing that slow loading rates lead to higher maximum fibre volume fractions (V_a). Kim et al. (1991) found that the compressibility of the fibre bed is strongly dependent on the type of fibre bed: unidirectional, roving or mat. Unlike Gutowski et al. (1986a), they measured an hysteresis effect during load/unload cycles of the fibre bed sample. The difference comes from the fact that Gutowski et al. tested lubricated fibre beds instead of dry fibre beds. The latter favors more fibre breakage caused by friction between fibres. Gutowski and Dillon (1992) propose a "universal" model using Equation 2.3 that fits all the fibre bed compaction curves found in the literature by setting $\beta=350$, $V_a - V_{f0}=0.38$ and by adjusting V_a which represents the state of the fibre bed. They insist that this model is valid only if the bundle remains in a particular state. This state depends upon equilibrium and dynamic considerations that can be altered by the condition of the experiment. As an example, Figure 2.5 shows the calculated compaction curves of two fibre beds having a V_a of 0.7 and 0.9 using Equation 2.3. V_a has a strong effect on the shape of the compaction curve as seen in Figure 2.5. According to Gutowski and Dillon (1992), a fibre bed with $V_a < 0.785$ has poorly aligned fibres.

Cai and Gutowski (1992a) developed a general 3-D deformation model of a lubricated fibre bundle subjected to a multidirectional stress state (Figure 2.6). The stresses carried by the fibre

bundle are divided into normal stresses ($\bar{\sigma}_1, \bar{\sigma}_2, \bar{\sigma}_3$) and deviatoric shear stresses ($\bar{\tau}_{12}, \bar{\tau}_{13}, \bar{\tau}_{23}$). The fibre bundle cannot support tensile stresses in the transverse directions (2 and 3). A finite compression stress can be supported by the bundle in the longitudinal direction (1) depending on how the bundle is constrained. The deviatoric stresses are pure shear stresses. It is assumed that a lubricated aligned fibre bundle will react to shear stresses primarily by viscous shearing related to the rate of deformation and a viscous function. Therefore, the deformation behaviour of a fibre bundle can be characterized with a knowledge of three elastic and two viscous functions. For the elastic part of the bundle behaviour, expressions are presented to relate the bundle strains ϵ_1 and ϵ_b to the normal stress state:

$$\begin{bmatrix} \epsilon_1 \\ \epsilon_b \end{bmatrix} = \begin{bmatrix} S_1 & S_{1b} \\ S_{b1} & S_b \end{bmatrix} \begin{bmatrix} \bar{\sigma}_1 \\ \bar{\sigma}_b \end{bmatrix} \quad (2.6)$$

where S_1, S_{1b}, S_{b1} and S_b are the fibre bundle compliances that are functions of V_a, V_{f0}, β and E_f . The transverse behaviour is given as a bulk behaviour (i.e. $\epsilon_b = \epsilon_2 + \epsilon_3$ and $\bar{\sigma}_b = (\bar{\sigma}_2 + \bar{\sigma}_3)/2$). Since unidirectional fibre bundles are transversely isotropic, the shear behaviour is governed by two material constants for the composite transverse shear η_T and the composite longitudinal shear η_L . Therefore the bundle shear stresses are related to the shear deformation rates $\dot{\gamma}_{ij}$ by:

$$\begin{bmatrix} \bar{\tau}_{12} \\ \bar{\tau}_{13} \\ \bar{\tau}_{23} \end{bmatrix} = \begin{bmatrix} 2\eta_L & 0 & 0 \\ 0 & 2\eta_L & 0 \\ 0 & 0 & 2\eta_T \end{bmatrix} \begin{bmatrix} \dot{\gamma}_{12} \\ \dot{\gamma}_{13} \\ \dot{\gamma}_{23} \end{bmatrix} \quad (2.7)$$

Little information is available on the subject of shear deformation of fibre bundles. Most of the investigations of this mode of deformation come from thermoplastic matrix composites process

(i.e. thermo-forming process) modelling where composite layers have to conform to a complex shape tool. In such processes, large shear deformations are expected and the resin rich regions between plies act as lubricant and allow large shear deformations (Kaprielian and O'Neill, 1989; Tam and Gutowski, 1989). For percolation flow models, since the plies are conformed to the tool during the lay-up, shear deformations are relatively small and are typically neglected.

Kim et al. (1991) observed some stress relaxation effects when applying a constant deformation to a dry fibre bundle. They described that phenomenon using a viscoelastic model (i.e. similar to the Maxwell model). The stress relaxation effect was greater for random mats than unidirectional fibres and it is more likely to occur for processes where deformation is imposed on the fibre bundle such as in pultrusion.

2.2.2 Fibre bed permeability

The fibre bed permeability describes the resistance of the porous media to the flow of a wetting fluid. Loos and Springer (1983) and Ciriscioli et al. (1992) assumed the fibre bed permeability perpendicular to the fibre to be constant ($K=5.8 \times 10^{-16} \text{ m}^2$), consistent with their flow-compaction model (Section 2.3.1.2). In reality, the resin flow can cause fibre volume fraction changes during laminate consolidation. Therefore, the fibre bed permeability is a function of the fibre volume fraction. The Carman-Kozeny equation is commonly used to describe the permeability of a variable porosity medium (Davé et al., 1987b). This relation was originally developed for isotropic porous media made of spherical particles of near equal size and considers the porous media as a system of parallel capillaries. For fibre beds, the Carman-Kozeny equation is

modified by substituting the hydraulic radius for a sphere bed with the hydraulic radius for a cylinder bed:

$$K = \frac{r_f^2 (1 - V_f)^3}{4k V_f^2} \quad (2.8)$$

where r_f is the fibre radius and k is the Kozeny constant. To take into account the anisotropy of the fibre bed permeability, the Kozeny constant has to be determined in the principal directions (1, 2 and 3). Gutowski et al. (1987b) measured the axial and transverse permeability of carbon fibre beds wetted with silicone oil. They found the axial and transverse Kozeny constants to be respectively $k_1=0.7$ ($0.4 < V_f < 0.8$) and $k_2=17.9$ ($0.69 < V_f < 0.72$). Lam and Kardos (1989) measured the permeability at different fibre volume fractions for a carbon fibre bed with water or silicone oil. For the transverse permeability, they found $k_2=11$ ($0.5 < V_f < 0.75$), but at higher V_f , k_2 seemed to decrease. The axial Kozeny (k_1) constant was 0.35 for silicone oil and 0.68 for water raising concern that the fluid type affects the fibre bed permeability. Williams et al. (1974) measured the axial permeability of glass, carbon and nylon fibre beds using different fluids. Their main conclusion is that non-uniform porosity, entrapped air and fluid surface tension affect the flow of the fluid and therefore the fibre bed permeability³. Ahn et al. (1991) measured a maximum capillary pressure of 37 kPa during the impregnation of graphite fibre beds. Compared to the pressure of autoclave processing (100-700 kPa), the capillary pressure is small.

³ For unsaturated fibre beds where fluid front advances like in resin transfer moulding process.

Gutowski et al. (1987b) pointed out a flaw in Equation 2.8 for the prediction of the transverse permeability. The disturbing feature of this equation is that it predicts a permeability greater than zero at fibre volume fractions higher than the theoretical maximum V_f . At this theoretical maximum V_f , the fibres are in direct contact together blocking any transverse flow. Accordingly, they propose the following expression for K_2 :

$$K_2 = \frac{r_f^2 \left(\sqrt{\frac{V_a'}{V_f}} - 1 \right)^3}{4k' \left(\frac{V_a'}{V_f} + 1 \right)} \quad (2.9)$$

where k' and V_a' are empirical parameters. For carbon fibre beds they found $k'=0.2$ and $V_a'=0.76-0.82$.

Other approaches to develop closed-form expressions for the permeability are described by Gebart (1992), Brusckke and Advani (1993). At high fibre volume fractions, Gebart (1992) and Brusckke and Advani (1993) used lubrication theory for the transverse permeability that leads to the following expression:

$$K_2 = C \left(\sqrt{\frac{V_{f\max}}{V_f}} - 1 \right)^{5/2} r_f^2 \quad (2.10)$$

where C and $V_{f\max}$ depend on the fibre bed packing arrangement. For the axial permeability, Gebart (1992) derives a relation similar to the Kozeny equation:

$$K_1 = \frac{8r_f^2 (1 - V_f)^3}{c V_f^2} \quad (2.11)$$

where c is the hydraulic radius between the fibres. This approach agrees well with the numerical simulations for $V_f > 0.4$. Figure 2.7 shows a typical permeability variation as function of V_f obtained with Equations 2.10 and 2.11.

Skartsis et al. (1992b, 1992c), Åström et al. (1992) and Gebart (1992) give a good overview on the subject of the permeability and flow through fibre beds. All agree that the capillary model (Equation 2.8) fails to predict the permeability over the total porosity range of the fibre bed. k is constant over a very small porosity range and must be experimentally evaluated for the specific fibre bed/fluid combination of the laminate studied.

Since the fibre bed is approximately transversely isotropic, the permeability is different for flow in the axial (1) and transverse (2) directions and is represented by the tensor \mathbf{K} :

$$\mathbf{K} = \begin{bmatrix} K_1 & K_{12} \\ K_{21} & K_2 \end{bmatrix} \quad (2.12)$$

For the case where the principal directions of the permeability tensor coincides with the reference coordinate system, $K_{12}=K_{21}=0$. Lam and Kardos (1989) measured the permeability of fibre beds having 10 to 15 cross plies $[0^\circ, \theta]$ for $\theta=0^\circ, 30^\circ, 45^\circ$ and 90° . The axial permeability decreases as θ increases and K_1 can be related to θ by:

$$\frac{1}{K_1} = \frac{\cos^2 \theta}{K_{0^\circ}} + \frac{\sin^2 \theta}{K_{90^\circ}} \quad (2.13)$$

where K_{0° and K_{90° are the permeabilities for $\theta=0^\circ$ and 90° respectively. Chan et al. (1993) studied the in-plane permeability tensor for isotropic, orthotropic and anisotropic preforms.

Most composite laminates contain several layers of unidirectional ply oriented in different directions. Therefore, each layer has a different permeability and when they are stacked together, the average permeability is given by Brusckhe and Advani (1990):

$$K_i = \frac{1}{H} \sum_{j=1}^n h^j K_i^j \quad (2.14)$$

where H is the total thickness of the lay-up containing n layers, and h^j and K_i^j are the thickness and permeability of the j^{th} layer respectively. Chan et al. (1992) noted that at $V_f > 0.5$, Equation 2.14 deviates from experimental results. Adams and Rebenfeld (1991) concluded from experiments on preforms having different layer orientation that the weighted average approach is only valid when the permeability of the layers are relatively equivalent. For laminates containing layers of very different permeability, the flow is governed by the layer having the highest permeability.

An important issue in the permeability modelling of fibre beds is the assumption that the material is homogeneous. In practice this assumption is not true, as some non-homogeneities are present, such as fibres of different diameter, gaps between fibre tows and non-uniform fibre distribution. Lunstrom and Gebart (1995) found analytically that the permeability was affected by both fibre size and position perturbations. Cai and Berdichevsky (1994) showed analytically that flow occurs in the layers between the fibre tows in both axial and transverse directions.

2.3 Flow-compaction models

The different flow mechanisms found in composite materials are presented in Figure 2.8. Percolation flow is characterized by the motion of the resin relative to the fibre bed which leads

to resin-poor or resin-rich areas in the laminate. For shear flow, the composite flows like a very viscous fluid containing stiff fibres where the deformation occurs within a ply (intraply) or between the plies (interply).

Typically, the percolation flow approach is used to describe the flow of the resin in thermoset matrix composites. For thermoplastic matrix composites, the shear flow approach is used to represent the flow behaviour of the laminate.

2.3.1 Percolation flow models

The percolation flow approach predicts resin migration within or out of the laminate. The resin movements in the laminate are obtained by solving the appropriate governing equations for flow through porous media. Darcy's law is the most popular equation used. The following section describes the approaches commonly used to calculate resin flow during composites processing.

2.3.1.1 Darcy's Law

The fundamental equation that describes flow through porous media is the Darcy's law:

$$V = -\frac{K \Delta P}{\mu L} \quad (2.15)$$

where V , μ are the resin velocity and viscosity, K , L are the fibre bed permeability and thickness and ΔP is the pressure gradient. This law was originally developed for the flow of Newtonian fluids through porous media made of granular particles (Darcy, 1856). Gebart (1992) validated Darcy's law for low flow rate composite processes. For non-Newtonian (shear-thinning) fluids, Darcy's law can be used, but few experimental verifications are available (Åström et al., 1992).

Loos and Springer (1983) used Equation 2.15 to calculate resin mass losses of a flat laminate normal to the tool plate. Equation 2.15 can be generalized for a two dimensional problem:

$$\begin{bmatrix} V_x \\ V_y \end{bmatrix} = -\frac{1}{\mu} \mathbf{K} \begin{bmatrix} \partial P / \partial x \\ \partial P / \partial y \end{bmatrix} \quad (2.16)$$

where \mathbf{K} is the permeability tensor of the fibre bed (Equation 2.12).

Davé (1990) derived the general flow equation applicable to all composite processes. Solving the continuity equation for the resin and assuming Darcy's law leads to the following continuity equation for the flow of resin through an orthotropic fibre bed ($K_{xy}=K_{yx}=0$):

$$\frac{\partial(\rho S \phi)}{\partial t} - \frac{1}{\mu \phi} \left\{ K_x \frac{\partial P}{\partial x} \left[\frac{\partial}{\partial x} (\rho S \phi) \right] + K_y \frac{\partial P}{\partial y} \left[\frac{\partial}{\partial y} (\rho S \phi) \right] \right\} = \rho S \phi \left[\frac{\partial}{\partial x} \left(\frac{K_x}{\phi \mu} \frac{\partial P}{\partial x} \right) + \frac{\partial}{\partial y} \left(\frac{K_y}{\phi \mu} \frac{\partial P}{\partial y} \right) \right] \quad (2.17)$$

where ϕ is the fibre bed porosity ($\phi=1-V_f$) and S is the saturation of the resin ($S=1$: fibre bed fully saturated with resin). The assumptions for Equation 2.17 are:

- 1) the porous medium contains both air and resin
- 2) the resistance to resin flow due to air is negligible
- 3) the individual fibres are assumed incompressible
- 4) the body forces are neglected
- 5) the process is quasi-static (i.e. resin velocity is small).

For autoclave processing, Equation 2.17 is simplified by assuming that the spatial variation in the resin density, viscosity and porosity are negligible. Also, the composite is assumed to be fully saturated with resin ($S=1$). Therefore, the resin flow equation for autoclave processing is reduced to (Davé et al., 1987a; Gutowski et al., 1987a):

$$\frac{\partial\phi}{\partial t} = -\frac{\phi}{\mu} \left[\frac{\partial}{\partial x} \left(K_x \frac{\partial P}{\partial x} \right) + \frac{\partial}{\partial y} \left(K_y \frac{\partial P}{\partial y} \right) \right] \quad (2.18)$$

One important aspect of Equation 2.18 is that it accounts for resin mass loss due to resin flow out of the laminate (i.e. $\partial\phi/\partial t$), since autoclave processing involves a non constant volume flow problem.

The resin flow behaviour alone is not sufficient to fully describe laminate consolidation during processing. The actual flow and compaction behaviour is impossible to observe directly during a real cure cycle. Springer (1982) studied the compaction of thin porous plates in a constant viscous liquid. His observations lead to a flow-compaction model called the sequential compaction model. Gutowski (1985) described the compaction behaviour of composite laminates by applying the effective stress formulation used in soil mechanics.

2.3.1.2 Sequential compaction

The sequential compaction model was developed based on experimental observations of the compaction of racks of metal rods in a viscous fluid (Springer, 1982). When the resin flow is only in the normal direction, the compaction process starts from the top to the bottom of the laminate in a wave like, cascading manner (Figure 2.9 (a)). When resin flow is parallel to the plies, the laminate compacts almost uniformly (Figure 2.9 (b)). During compaction, the resin pressure is equal to the applied pressure in the uncompacted zone of the laminate. In the perpendicular direction, a pressure gradient exists only across the compacted plies where resin flows according to Equation 2.15. In the direction parallel to the plies, flow is characterized as squeezing flow between two parallel plates. This flow model assumes no resin mixing between

the different plies of the laminate. The model predicts the laminate mass loss and the thickness variation during the cure cycle. Loos and Springer (1983) solved numerically the flow equations with a thermochemical model (resin behaviour) for different flat laminates. Model results were compared to experiments where resin mass losses normal and parallel to the tool were measured as function of the processing time. Good agreement was found and the authors concluded that their model predicts accurately the resin flow and can be used as a cure cycle design tool (Ciriscioli et al., 1992). Loos and William (1985) measured the resin flow from laminates with different ply thicknesses, dimensions and ply-stacking sequences. They used the sequential model and found good agreement with the data. The experiments indicated that the ply-stacking sequence for flat laminates does not affect significantly the total resin mass loss.

2.3.1.3 Effective stress formulation

The effective stress theory was introduced in soil mechanics to model the consolidation of soils, Terzaghi (1943) and Biot (1941). Based on experimental data on compaction of fibre beds, Gutowski et al. (1987a) applied this theory to the consolidation of composites during cure. The effective stress formulation states that at any point in the laminate the stress is given by the following expression:

$$\sigma = \bar{\sigma} + P \quad (2.19)$$

where σ is the applied stress, P is the resin pressure and $\bar{\sigma}$ is the fibre bed effective stress. The spring and piston analogy explains the consolidation behaviour of a composite laminate (Figure 2.10). The fibre bed is assumed as an uncompressed spring (i.e. the fibre bed has an elastic behaviour, Section 2.2.1) placed in a cylinder filled with fluid (i.e. the resin). As an

external load is applied on the piston (Figure 2.10 (a)) it is totally carried by the fluid. As flow begins (Figure 2.10 (b)) because of an opening in the piston, the spring is compressed and carries a fraction of the load. As flow continues (Figure 2.10 (c)) more load is shared to the spring. Eventually, the applied load is totally carried by the spring (Figure 2.10 (d)). The rate at which the fluid bleeds out of the cylinder is dictated by the flow equation. The spring stiffness corresponds to the fibre bed elastic behaviour described in Section 2.2.1. Gutowski et al. (1987a) and Davé et al. (1987a) solved the continuity equation (Equation 2.18) with the stress equilibrium equation (Equation 2.19) to model the flow and compaction of composite laminates. Davé et al. (1987b) solved the laminate consolidation by decoupling the two governing equations. First, the resin pressure distribution is evaluated by solving the following flow equation:

$$\frac{\partial P}{\partial t} = \frac{1}{\mu m_v} \left[K_x \left(\frac{\partial^2 P}{\partial x^2} \right) + K_y \left(\frac{\partial^2 P}{\partial y^2} \right) \right] \quad (2.20)$$

where m_v is the coefficient of volume change:

$$m_v = \frac{-de/d\bar{\sigma}}{(1 + e_0)} \quad (2.21)$$

$de/d\bar{\sigma}$ is the inverse of the slope of the fibre bed stress versus void ratio curve and e_0 is the initial void ratio. Equation 2.20 assumes the external load and boundary conditions to be constant. Although two dimensional flow is addressed, consolidation occurs only in the direction normal to the tool plate (no horizontal displacements). From the pressure distribution given by Equation 2.20, the resin velocity and mass losses are calculated using Darcy's Law. The resin

loss can then be related to a new fibre volume distribution and a corresponding effective stress is given by the fibre bed compaction curve (i.e. the variation of the fibre bed stress versus the fibre bed deformation). Finally, the resin pressure is updated by solving the equilibrium equation (Equation 2.19). This solution loop is valid if appropriate time steps are chosen. Davé used a finite difference solution scheme to study the effect of laminate thickness and effect of axial versus transverse flow. In his model, the resistance to flow in the bleeder is assumed negligible and the pressure at the laminate interface is equal to the pressure in the bag. The main conclusion from his simulations was that the resin pressure falls to the bag pressure before the gel point and for any laminate thickness. For thicker laminates, the pressure decay is slower. A resin pressure gradient exists in the laminate in both the axial and transverse directions. For a thick laminate, most of the flow is axial. For a thin laminate most of the flow is transverse. Good agreement between model and experiments was found for mass losses and final ply thicknesses for different laminates with 1-D transverse flow only (Davé et al. (1987b)).

The solution proposed by Davé et al. (1987b) does not take into account the moving boundary in the thickness direction. After each time step, the computational grid size has to be updated. Gutowski et al. (1987a) solved the consolidation equations by explicitly incorporating the moving boundary normal to the tool. The equation for normal flow and 1-D consolidation becomes:

$$\frac{\partial}{\partial t} \left(\frac{1 - V_f}{V_f} \right) = \frac{1}{\mu} \left[\frac{1}{V_{f0}^2} \frac{\partial}{\partial y} \left(K_y V_f \frac{\partial P}{\partial y} \right) \right] \quad (2.22)$$

Solving Equation 2.22 with the equilibrium Equation 2.19 using the finite difference method, the model agreed with the measured resin pressure variation at the tool for constant viscosity fluid and carbon fibre beds during a constant pressure 1-D consolidation experiment (Gutowski et al., 1987b). Better agreement with experimental data was obtained using the modified Kozeny relation (Equation 2.9) for the permeability calculation. Dudukovic et al. (1990) used a similar formulation to Equation 2.22 and validated the model with a 1-D consolidation test using carbon fibre bed and constant viscosity silicone oil under isothermal conditions. Finally, Cai and Gutowski (1992b) modelled the compaction of cylindrical laminates during filament winding. They solved the problem for normal flow (Equation 2.22) and applied the fibre bundle elasticity relations (Equation 2.6). Again, good agreement was found between the predicted and measured resin pressure at the mandrel surface for a silicone oil-fibre laminate. A 3-D laminate consolidation finite element model was developed by Young (1995) using shell elements for each layer. The model is based on the effective stress compaction theory coupled with Darcy's law.

Although the sequential and the effective stress models have different assumptions, they predict essentially the same results in the regime when the fibre bed carries no load (Tang et al., 1987). Smith and Poursartip (1993) demonstrated that the sequential model is a special case of the effective stress formulation. They concluded that the effective stress model describes more accurately the entire laminate compaction process. They also calculated the compaction behaviour of laminates having different fibre bed stress-strain curves. They found that this

parameter has a major effect on the resin pressure distribution and the laminate compaction behaviour.

The major problem for the flow and compaction modelling is the lack of experimental data to validate the model. Measuring the pressure distribution and monitoring the flow in the laminate is a very difficult task. Poursartip et al. (1992) using a tagged resin to monitor the flow during cure, noticed resin mixing between successive layers. This can come from the resin pressure gradient through the thickness of the laminate, as predicted by the effective stress formulation. Frank-Susich et al. (1992) installed pressure transducers at the tool plate and filled them with uncatalyzed resin to read the resin pressure variation during the cure. For a flat laminate, they found that the edge sensor measured a pressure 10% greater than the center sensor. They noticed local resin flow at the center of the laminate that could explain the difference between the two sensors. Both sensors were reading a pressure lower by at least 10% than the applied pressure confirming that the balance of the load must be carried by the fibre bed.

Mackenzie (1993) used embedded pressure sensors to measure the hydrostatic resin pressure at different locations through the thickness of a flat carbon epoxy laminate. Figure 2.11 shows the response of the pressure sensors during the first 100 minutes of the run. As expected by the effective stress theory, a resin pressure gradient exists in the laminate from the tool to the top. A computer simulation using a 1-D cure model with the appropriate material properties and boundary conditions predicted the same resin mass loss and similar resin pressure profiles as shown in Figure 2.12.

2.3.2 Shear flow models

For this type of flow model, the resin and the fibres move together. Thus the composite material is treated as a continuum. The theory originates from the modelling of plane deformation of fibre-reinforced materials. During the forming process, the continuous fibres exhibit no extensional flow in the fibre direction. The dominant mode of deformation is the shear across or along the fibres (Figure 2.8, intraply transverse or longitudinal). The shearing response is dominated by the matrix viscous behaviour since the resin acts as a lubricant between the stiff fibres. The composite is then treated as a highly anisotropic fluid where the extensional viscosity in the plane of deformation is much greater than its shear viscosity. The idealization generally adopted is that of an ideal fibre reinforced material (IFRM). The composite is assumed to be incompressible and to flow as a Newtonian fluid. Details of the development and assumptions of the above theory can be found in Rogers (1989).

2.3.2.1 *Intraply*

The constitutive equations for the intraply flow are developed by Rogers (1989). The fibres are assumed to lie in a plane and are continuously distributed throughout the laminate. The local orientation of the fibre is represented by a unit vector \mathbf{a} that is a function of position and time (Figure 2.13). With the kinematic constraints of incompressibility and inextensibility in the fibre direction, the constitutive equation is written as follows:

$$\sigma_{ij} = -P\delta_{ij} + T a_i a_j + 2\eta_T d_{ij} + 2(\eta_L - \eta_T)(a_i a_k d_{kj} + a_j a_k d_{ki}) \quad (2.23)$$

where δ_{ij} is the Kronecker delta, $\delta_{ij} = 1 (i=j)$, $\delta_{ij} = 0 (i \neq j)$; σ_{ij} is the stress tensor, η_L is the composite longitudinal shear viscosity, η_T is the composite transverse shear viscosity, P is an arbitrary hydrostatic pressure and T is an arbitrary tension in the fibre direction and d is the Eulerian rate of strain tensor. The constraint equations (incompressibility and inextensibility) have caused two arbitrary stress terms to appear in the constitutive equation (the hydrostatic pressure P and the fibre tension T). The stress tensor is then divided into two components:

$$\sigma_{ij} = r_{ij} + \tau_{ij} \quad (2.24)$$

where r_{ij} is the reaction stress due to the kinematic constraints and τ_{ij} is the stress corresponding to the deformation rate, d_{ij} . The material constitutive relation can then be written as:

$$\sigma_{ij} = D_{ijkl} d_{kl} + r_{ij} \quad (2.25)$$

where D_{ijkl} is the composite viscosity constitutive matrix and d_{kl} is the deformation rate. For continuous fibre reinforced composites, the composite viscosity matrix has two independent material properties η_L and η_T since the material is assumed to be transversely isotropic. The practical determination of the material properties are discussed later.

The above theory has been used to model shear flow in numerous situations. Balasubramanyam et al. (1989), Barnes and Cogswell (1989) and Rogers (1989) applied the IFRM theory to study the squeezing flow or transverse intraply flow of PEEK⁴-carbon fibre composites. The equations can be significantly simplified for the forming flow involved in the compression moulding of

⁴ poly(ether ether ketone).

unidirectional composites between two parallel heated plates. Simple analytical expressions for the material deformation are developed by Rogers (1989) and Balasubramanyam et al. (1989) for different boundary conditions at the composite-tool interface. Balasubramanyam et al. (1989) found that a zero-friction boundary condition cannot match the experimental data. A no-slip boundary condition gave better agreement but like Barnes and Cogswell (1989), they found that the viscosity of the material increased dramatically as the material was compacted. Both explain the phenomena by the fact that as the material shears, the fibres move and may twist causing them to lock and prevent any further deformation. Ó Brádaigh (1993) applied the IFRM theory to the sheet forming process by solving Equation 2.23 using the finite element method under plane stress conditions. For the forming of unidirectional PEEK-carbon fibre composite plates, the model could predict the zone of high shear stresses and compression stresses that would lead to local buckling of the fibres. These local stresses were causing severe fibre buckling observed experimentally. Rogers and O'Neill (1991) developed plane strain analytical expressions to describe the forming process of unidirectional composites from a flat plate to an angle under a line load or a uniform pressure.

Efforts to characterize the shear flow behaviour of continuous fibre composites were conducted by Groves (1989) and Groves and Stocks (1991). They used a parallel plate torsion rheometer to measure the transverse and longitudinal composite viscosities under different conditions of strain, strain-rate and temperature. One of their major findings was that although the resin (in this case PEEK) would almost exhibit a Newtonian behaviour, the composite ($V_f=60\%$) appears to be very non-Newtonian. Jones and Roberts (1994) investigated the effect of the fibre volume fraction on η_T and η_L for an 'ideal' composite material made of nylon fibres and Golden Syrup

matrix (a Newtonian fluid). Using a linear oscillator apparatus, they found that η_T and η_L increase with the fibre volume fraction. The experimental results were compared with micromechanical analytical predictions of the composite viscosity as a function of the fibre volume fraction (Pipes, 1992; Christensen, 1993). The analytical predictions agreed relatively well with the data up to a fibre volume fraction of 60%. The transverse to longitudinal composite viscosity ratio (η_T/η_L) found in the literature varies significantly. Groves and Stocks (1991) reported a ratio of η_T/η_L ranging from 1 to 2 for composites tested at different temperatures and shear rates. Cogswell (1991) suggested that η_T/η_L was 0.77 and finally Wheeler and Jones (1991) concluded that no distinct differences could be made between η_T and η_L due to the large scatter in the data. Coffin et al. (1995) developed an analytical relation for η_T and η_L by considering the deformation of an assembly of rigid fibres in a linear viscous fluid subjected to a steady state pure shearing motion:

$$\eta_L = \eta_T = \frac{1}{1 - \sqrt{V_f/F}} \mu \quad (2.26)$$

where $F=\pi/4$ for a square array and $F=\pi/(2\sqrt{3})$ for a hexagonal array.

The work done to characterize the composite viscosity was conducted on thermoplastic matrix composites. For these materials, the resin viscosity in Equation 2.26 depends essentially on the temperature. For thermoset matrix composites, the resin viscosity is a function of temperature and degree of cure (Equation 2.2). Thus, the composite viscosity would be also affected by the curing state of the resin.

2.3.2.2 Interply

In practice, composite laminates consist of a stack of plies having different fibre orientations. It is often observed that a resin rich region corresponding to 5% of a ply thickness is formed between two adjacent plies. This viscous layer acts as a lubricant allowing high shear deformations of the laminate during processing. For this particular mode of deformation different modelling approaches are considered. Kaprielian and O'Neill (1989) have modelled the ply as a fibre-reinforced inextensible viscous fluid and the resin rich layer as a Newtonian viscous fluid. Tam and Gutowski (1989) adopted a similar approach but assumed the ply to be linear elastic. Finally Jones and Oakley (1990) used the interply shear mode approach to explain the composite non-Newtonian behaviour found in rheological test data from Groves (1989). They concluded that the combination of interply and intraply deformation could explain the non-linear response of the material. Scherer and Friedrich (1991) performed simple pull-out experiments to study the laminate ply-slip behaviour. They found that the major parameters influencing the interply shear behaviour was the temperature, the slip velocity and the laminate lay-up. Using simple bending forming tests, they found the presence of both interply and intraply deformation in the laminate. The stacking sequence was found to greatly influence the laminate quality.

2.4 Literature review summary and research objectives

Table 2.1 summarizes the state of research on flow and compaction of laminates during cure. From this table, the following statements can be made:

- 1) The percolation flow approach (Darcy's law) has been applied to thermoset composites.

- 2) The shear flow approach (IFRM theory) has been applied to thermoplastic composites.
- 3) Most of the theoretical and experimental work has focused on flat laminates.
- 4) Validation of the flow-compaction theories were done using 'ideal' composites (e.g. oil-fibre).
- 5) Most of the thermoset matrix composites studied to date are high flow systems (i.e. low resin viscosity).

Problem statement

A fundamental knowledge of flow and laminate compaction mechanisms has been gained by the study of laminates having simple geometries. The problem now consists of applying, evaluating and expanding this knowledge to predict the flow and compaction behaviour of complex shaped laminates which are representative of real applications of the autoclave processing of thermoset matrix laminated composites.

What has been done for this thesis

In order to solve the problem stated above, the following issues have been addressed:

- the development and application of a process model for complex shapes based on the percolation approach
- the study of actual composite materials, especially the newer materials
- the determination and investigation of the fact that shear flow is significant for both complex shapes and the newer materials.

Work presented in this thesis

Figure 2.14 presents a flow chart that outlines the organization of the present research. The work is divided into numerical and experimental parts as follows:

- *Implementation of current knowledge in a versatile process model*

A flow-compaction model based on the percolation flow approach is implemented in a 2-D finite element process model. The material properties required to run the model are evaluated from the literature or with experiments. Particularly the fibre bed compaction curve is measured directly from the prepreg supplied from the manufacturer. Then, simple uniaxial compaction tests are used to validate the model and verify that the materials are adequately characterized.

- *Application of the model to practical shapes*

Once validated, the model can be applied to study the compaction of angle laminates. The first step of this investigation consists of doing a sensitivity analysis to identify the critical material properties and their effect on compaction. Then, an experimental investigation of angle laminate compaction is conducted. These experiments are designed to cover a wide range of processing conditions. Thus the different flow mechanisms and their effect on compaction can be identified. The last step consists of comparing the experiment results with simulations using the process model. This is necessary to verify the applicability of the model to predict the compaction of complex shapes.

- *Expansion of current knowledge to improve the model developed*

Results from the angle laminate experiments indicate that shear flow is important. Thus a shear flow experimental study is performed. Finally, to understand the interaction between the different flow mechanisms, simple compaction experiments are performed.

2.5 Tables

Table 2.1 Summary of flow-compaction theoretical and experimental work.

Reference	Theory		Experiment		
	Approach	Assumptions	Geometry	Material	Parameters
Loos and Springer (1983) Loos and William (1985) Ciriscioli et al. (1992)	Sequential compac. Darcy's law	Normal compac. Normal, longitudinal flow	Flat panels	Carbon-epoxy	Resin mass losses Laminate thickness
Gutowski et al. (1987a) Gutowski et al. (1987b)	Effective stress Darcy's law	Normal compac. Normal, longitudinal flow	Flat panels	Carbon- silicone oil	Oil pressure at tool
Davé et al. (1987a) Davé et al. (1987b)	Effective stress Darcy's law	Normal compac. Normal, longitudinal flow			
Rogers (1989)	IFRM theory	Plane strain			
Barnes and Cogswell (1989)			Flat panels	Carbon-PEEK	Dimension change Force-time history
Balasubramanyam et al. (1989)	IFRM theory	Plane strain	Flat panels	Carbon-PEEK	Dimension change Force-time history
Frank-Susich et al. (1992)			Flat panels Honeycomb panels	Carbon-epoxy	Resin pressure at tool
Cai and Gutowski (1992b)	Effective stress Darcy's law	Normal, tangential compac. Normal flow	Cylinders	Carbon- silicone oil	Oil pressure at mandrel
Dudukovic et al. (1990)	Effective stress Darcy's law	Normal compac. Normal flow	Flat panels	Carbon- silicone oil	Oil pressure in laminate
Smith and Poursartip (1993)	Sequential compac. Effective stress Darcy's law	Normal compac. Normal, longitudinal flow			
Mackenzie (1993)	Effective stress Darcy's law	Normal compac. Normal flow	Flat panels	Carbon-epoxy	Resin pressure in laminate Resin mass losses Laminate Vf
O'Brádaigh (1993)	IFRM theory	Plane stress	Sheet	Carbon-PEEK	Final deformation
Saliba et al. (1994)			Flat panels	Carbon-epoxy	Panel thickness change
Young (1995)	Effective stress Darcy's law	Normal compac 3-D flow			

2.6 Figures

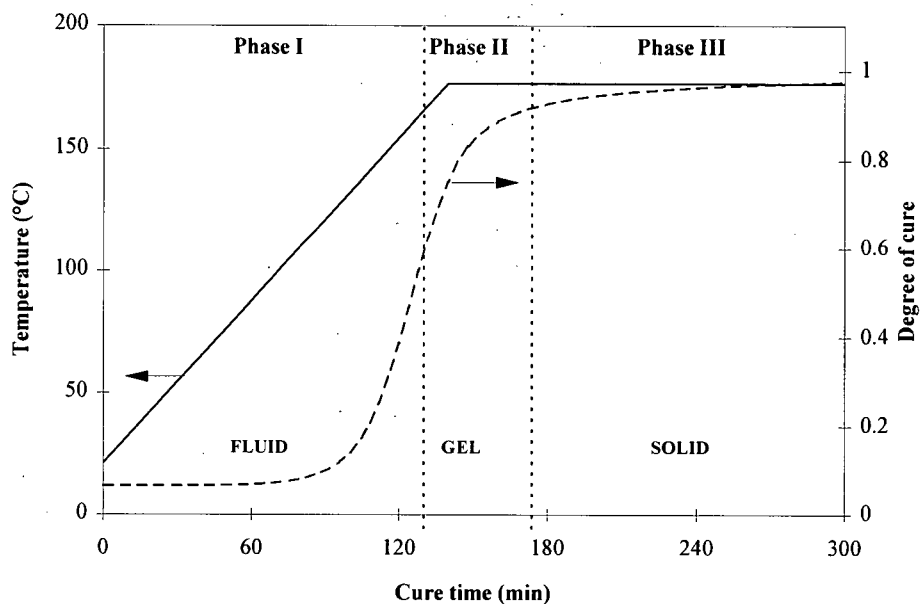


Figure 2.1 Typical resin degree of cure evolution during cure. The resin changes from a liquid state (Phase I), to a gel state (Phase II) and finally to a solid state (Phase III).

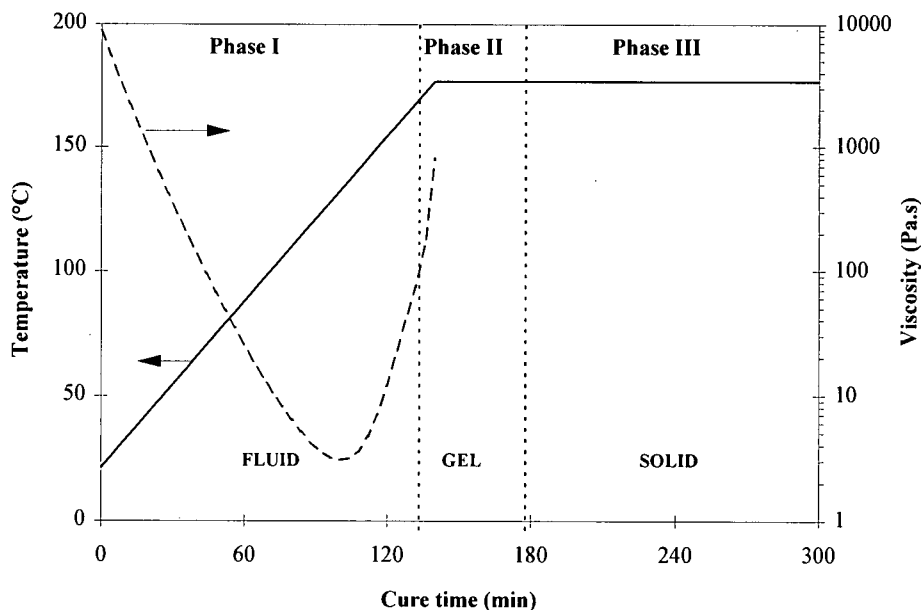


Figure 2.2 Typical resin viscosity evolution during cure. The resin is fluid during Phase I before it reaches the gel point in Phase II.

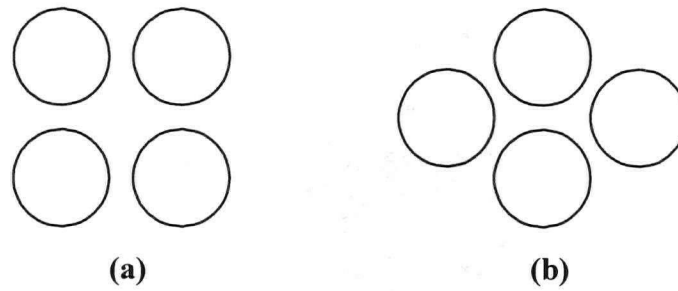


Figure 2.3 Ideal fibre packing arrangements, (a) square and (b) hexagonal.

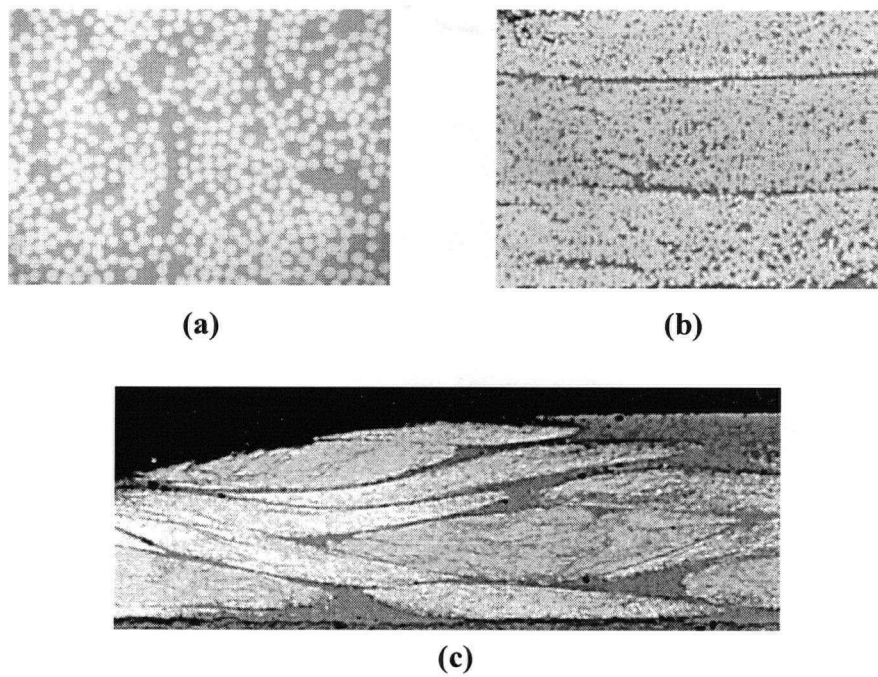


Figure 2.4 Actual fibre beds pore geometries, (a) intraply, (b) resin rich regions between individual plies and (c) non-uniform fabric arrangement.

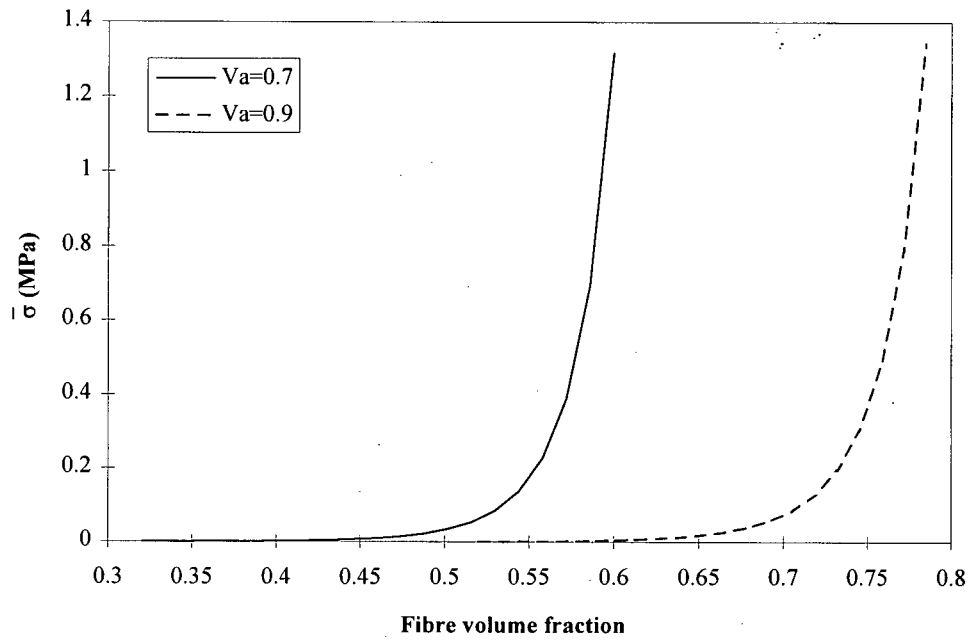


Figure 2.5 Typical fibre bed compaction curves. V_a is the maximum fibre volume fraction possible which is related to the fibres alignment in the fibre bed.

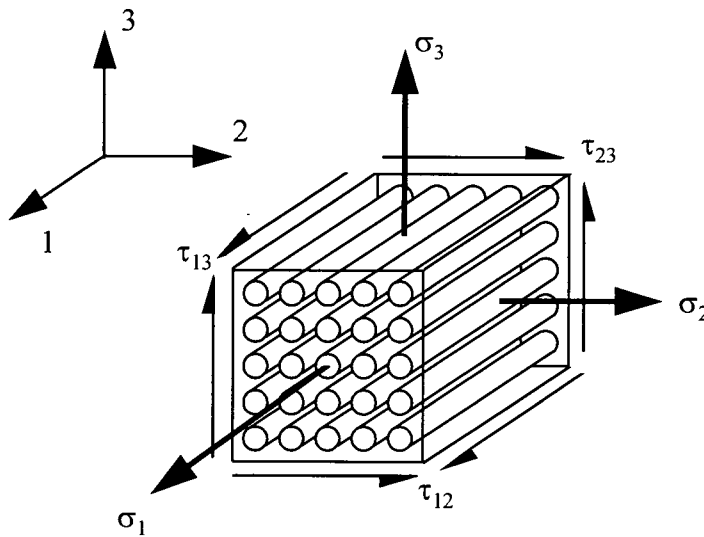


Figure 2.6 3-D fibre bundle stress state (Cai and Gutowski, 1992a).

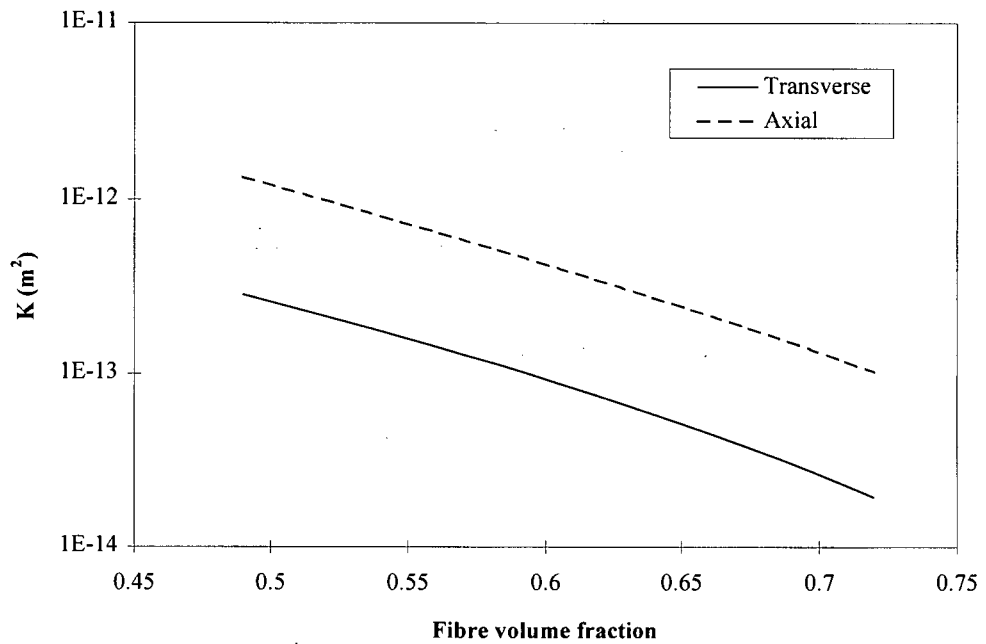


Figure 2.7 Typical fibre bed axial and transverse permeability variation with fibre volume fraction.

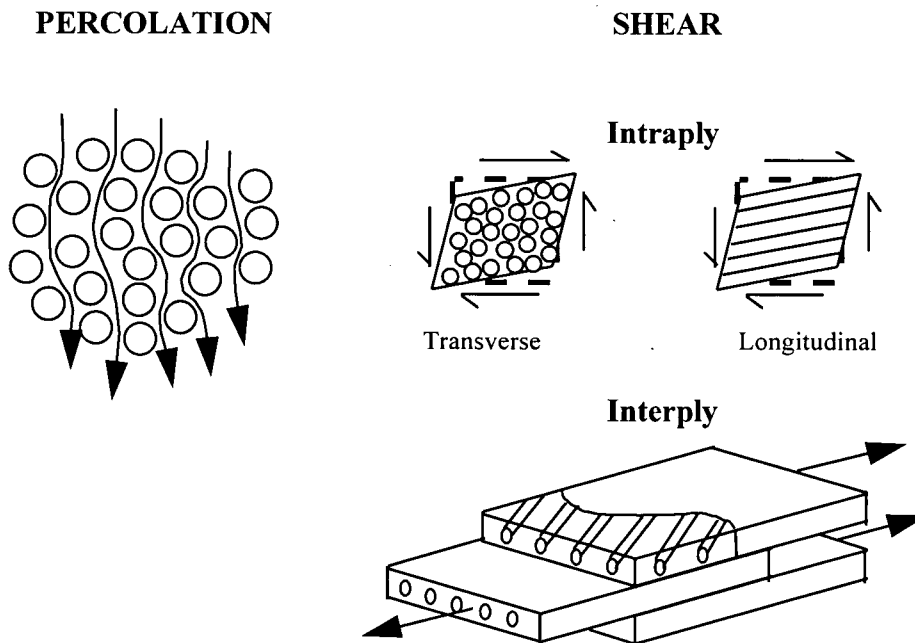


Figure 2.8 Type of flow mechanisms during processing (Ó Brádaigh et al., 1993).

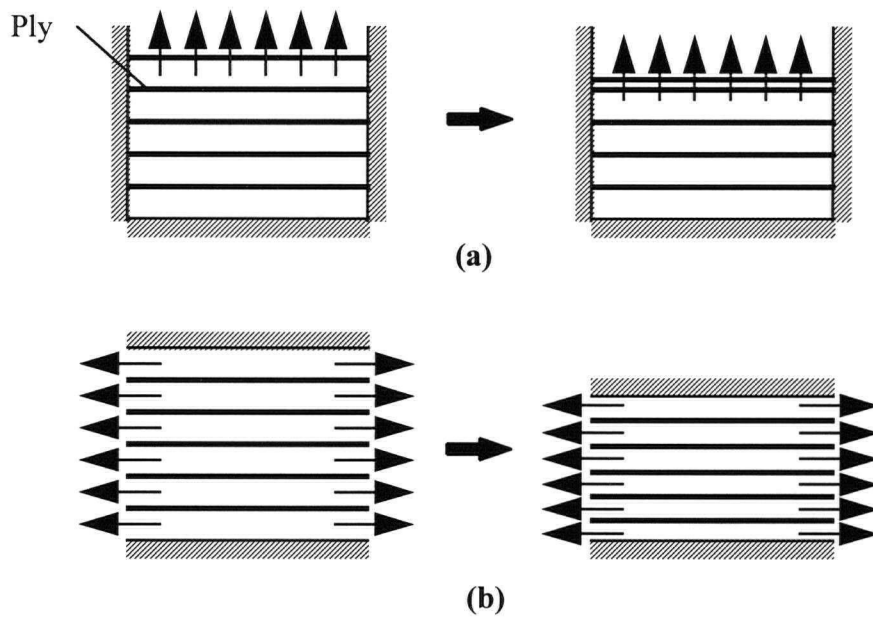


Figure 2.9 Sequential compaction behaviour, (a) transverse flow and (b) axial flow (Loos and Springer, 1983).

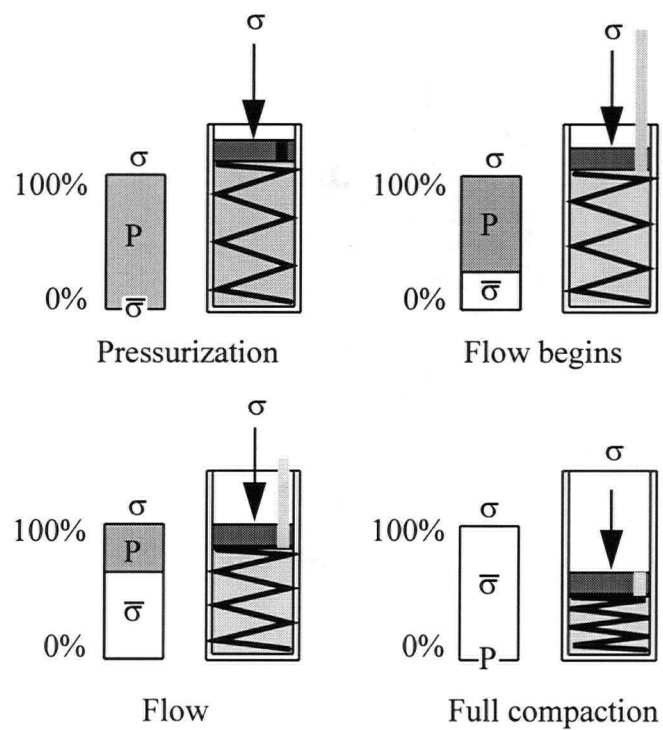


Figure 2.10 Effective stress compaction analogy (Davé et al., 1987a).

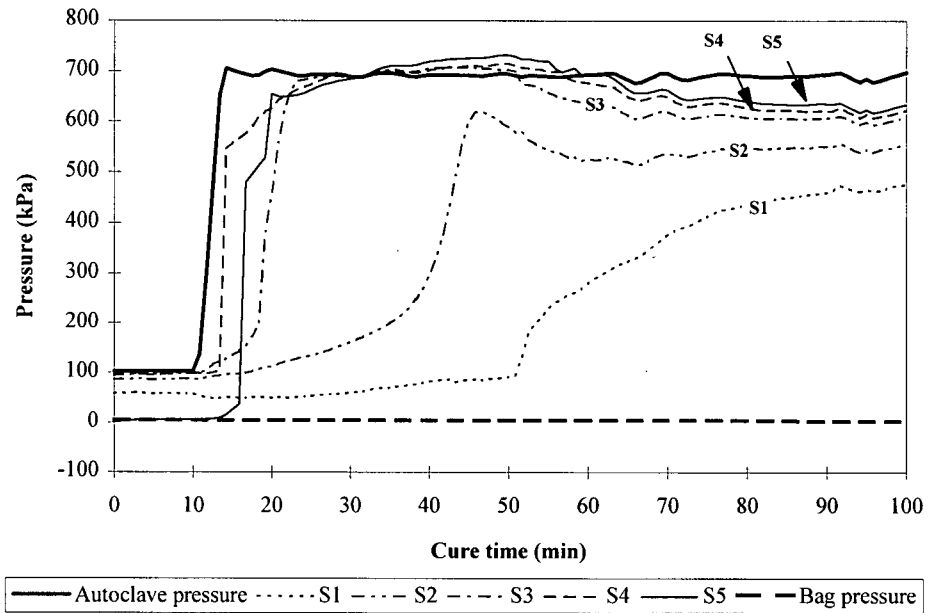


Figure 2.11 Resin pressure sensor response during compaction of a flat carbon-epoxy laminate (Mackenzie, 1993). The pressure sensors were distributed through the thickness from the top (S1) to the tool (S5).

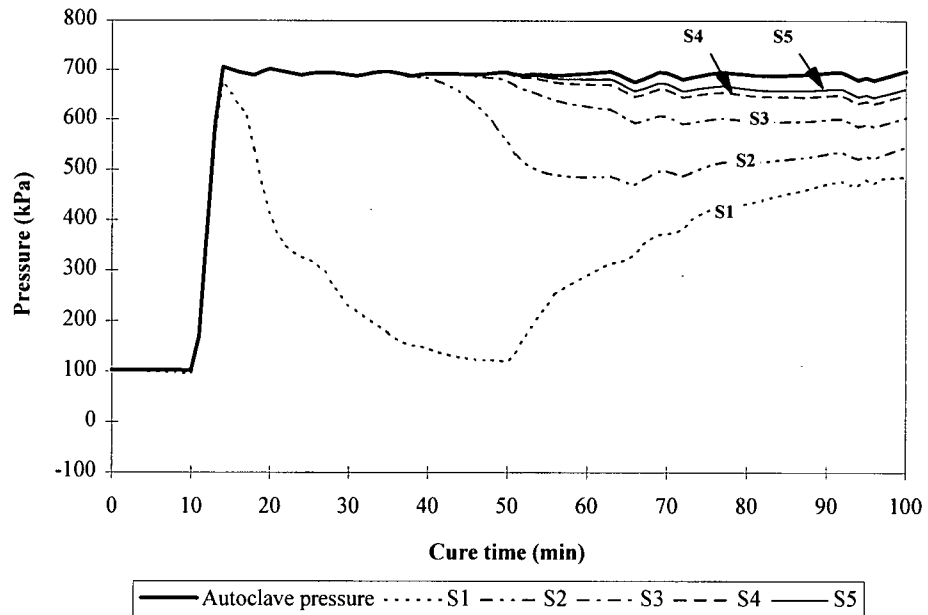


Figure 2.12 Resin pressure from 1-D compaction simulation of the experiment of Fig. 2.11 assuming a bag pressure equivalent to the measured pressure for the top sensor (S1).

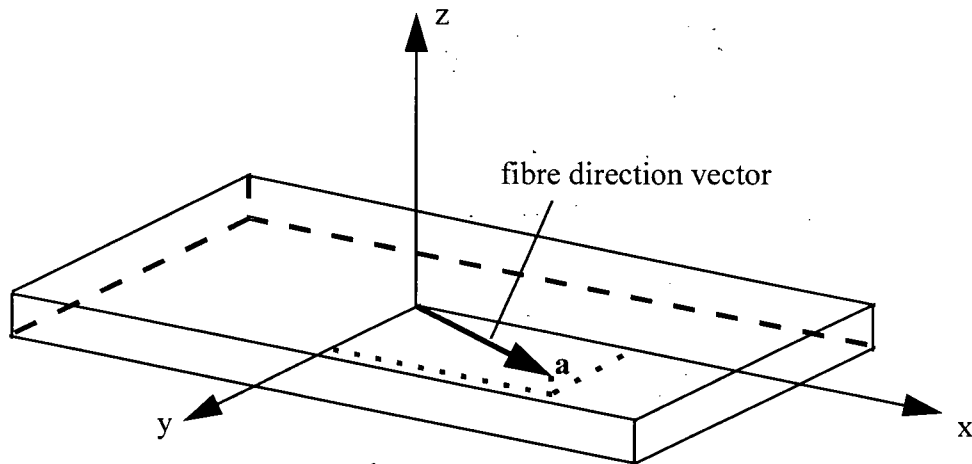


Figure 2.13 Composite laminate idealization for shear flow models (Ó Brádaigh et al., 1993).

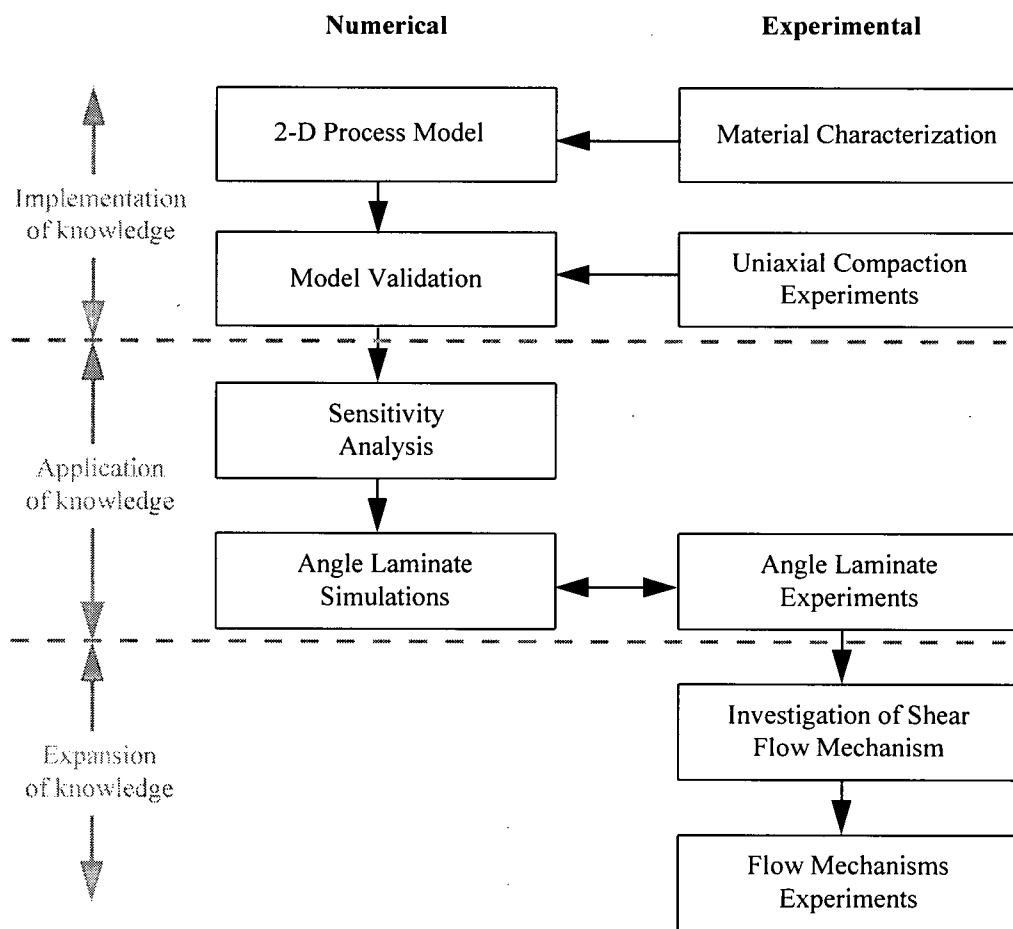


Figure 2.14 Flow chart of the research presented in this thesis.

Chapter 3 Percolation Flow-Compaction Finite Element Model

This chapter presents the details of the development of the percolation flow-compaction model. The general modelling approach is described and details of the assumptions for the flow-compaction model are discussed. Then, the governing equations for our problem are developed before applying the finite element method to solve the differential equations. The different methods of solution are described with the actual program algorithm. Finally, the present model is validated by comparing the solution of different cases with closed-form solutions or other available numerical models.

3.1 Composite process modelling approach

The optimum goal of process modelling is to predict the curing behaviour of large and complex parts. Because of the complexity of the different mechanisms occurring during processing, it is almost impossible to model directly such complex structures. The focus of the present model is on the analysis of composites processing at a 'local discretization' level as illustrated in Figure 3.1. At this level, it is possible to incorporate a relatively high degree of complexity¹ in the solution. The results from the simulation at a local level can then be used as input to larger models to predict the behaviour of a more complex structure.

A modular approach similar to that described by Loos and Springer (1983) is employed for the overall model structure. As illustrated in Figure 3.2, the main body of the program consists of a

¹ Complex geometries, tooling effects and automated autoclave control.

series of 'modules', each responsible for performing a single task such as calculating resin flow (the 'flow-compaction' module) or development of internal stresses (the 'stress-deformation' module). The various modules are called as needed by a controlling routine as the solution marches forward in time. At the beginning of each time step, an 'autoclave controller' module, simulating automated autoclave control, updates all process variables including the autoclave air temperature, the autoclave pressure and the vacuum bag pressure. A central database containing a description of the modelled components (i.e. composite, tool, inserts, etc.) is updated by each solution module as it is called. A brief description of the thermochemical, stress-deformation and autoclave controller modules is presented. The flow-compaction module which is the main topic of this chapter is described in depth in Section 3.2.

The thermochemical module is responsible for the calculation of the distribution of the component temperature and the resin degree of cure. This module consists of a combination of analyses for heat transfer and resin reaction kinetics (e.g. Bogetti and Gillespie (1991)). The composite thermophysical properties (i.e. density, heat capacity and thermal conductivity) are calculated from the local fibre volume fraction (V_f), and instantaneous resin and fibre properties. Six of the most widely used cure kinetic models are available in this module.

The stress-deformation module models the development of internal stresses and deformations within a component throughout the processing cycle. The current model incorporates analyses of the following major sources of process-induced stresses: thermal effects, resin cure shrinkage, uneven resin flow and tool-part interface. A hardening linear elastic material model is used to describe the behaviour of the curing resin. At the start of each module time step, ply mechanical

properties are determined from micromechanics models using the local fibre volume fraction (V_f) and fibre and resin properties calculated from the local temperature and degree of cure. A combined trapezoidal/Gaussian integration rule is used to smear the ply properties and strains to obtain equivalent element stiffnesses and nodal displacements.

An important concept used in the present process modelling approach is that of the 'virtual autoclave' incorporated in the controller module. Virtual sensors can be placed at element nodes and are monitored just as thermocouples would in a real part. These 'measured' temperatures are used by controller algorithms based on those used in actual autoclaves to set the air temperature and autoclave pressure for the next time step. Also, other autoclave characteristics may be simulated, such as maximum heating rates (based on maximum heater capacity and part/autoclave thermal mass) and the boundary heat transfer coefficient (as a function of autoclave temperature and pressure). The combined effect of this type of autoclave controller algorithm with the modelling of the tool affects the curing prediction considerably (Hubert et al., 1995).

3.2 Flow-compaction model development

As discussed in Chapter 2, the flow and compaction of thermoset matrix composites has been modelled previously using the percolation flow approach applied to simple cases. Our goal is to apply this approach to complex structures to investigate if it can predict their compaction behaviour adequately. Performing the analysis on only a 2-D section is believed to be adequate for most composite structures as at least one dimension is usually much larger than the other two. Gradients in this third direction are correspondingly small and can safely be ignored.

Furthermore, in practice dams are placed around the laminate to prevent resin flow from the edge of the part. This reduces considerably any in-plane resin flow out of the laminate.

3.2.1 Model assumptions

The curing composite material is idealized as a void free fibre bed fully saturated with a curing resin. A ply is composed of regular, unidirectional, very stiff and incompressible fibres. Individual plies can be oriented in any direction (in-plane orientation) (Figure 3.3). The resin is assumed to behave as an incompressible Newtonian fluid. The incompressibility of the constituents is justified here because the stress level involved during processing are much lower than the bulk modulus of the resin and the fibres². As the laminate is compacted, the resin flows relative to the fibre bed. The resin viscosity changes with temperature and degree of cure. The temperature effects on the resin and fibre physical properties (i.e. density) are not included explicitly in the governing equations. A plane strain condition is assumed since the model discretizes a slice of the part (Figure 3.3).

3.2.2 Governing equations

Figure 3.3 shows the representative element of a curved composite part defining the domain where the governing equations must be satisfied. The governing equations of the system must describe the behaviour of the composite constituents: the fibre bed and the resin. Firstly, the equilibrium of forces on the representative element is considered. Secondly, the mass

² Applied stress: 0-1.4 MPa, resin bulk modulus: ≈ 1 GPa, fibre bulk modulus: 196 GPa.

conservation for the representative element must be satisfied. For a porous medium saturated with a single phase fluid, the effective stress formulation states that the total stress σ_{ij} is separated into two parts as³:

$$\sigma_{ij} = \bar{\sigma}_{ij} - \delta_{ij}P \quad (3.1)$$

where $\bar{\sigma}_{ij}$ is the fibre bed effective stress, δ_{ij} is the Kronecker delta ($\delta_{ij}=1$ for $i=j$ and $\delta_{ij}=0$ for $i \neq j$) and P is the resin pressure. For the representative element, the equilibrium equation is:

$$\sigma_{ij,j} + F_i = 0 \quad (3.2)$$

where F_i are internal body forces. For simplicity, the following notation is adopted:

$$(*)_{,i} = \frac{\partial(*)}{\partial x_i} \quad (3.3)$$

We can replace the total stress in Equation 3.2 by Equation 3.1 to obtain the equilibrium equation for a differential element of the composite:

$$(\bar{\sigma}_{ij} - \delta_{ij}P)_{,j} + F_i = 0 \quad (3.4)$$

The resin percolates through the fibre bed according to Darcy's law. Accordingly, the resin velocity v_i relative to the fibre bed is expressed as:

$$v_i = -\frac{K_{ij}}{\mu} (P + \rho_R gh)_{,j} \quad (3.5)$$

³ Tensile stresses are by convention positive.

where K_{ij} is the fibre bed permeability tensor, μ is the resin viscosity, ρ_R is the resin density, g is the acceleration due to gravity and h is the height above a reference point. In Equation 3.5, the effect of gravity is included because we believe that it might affect the resin flow specially when a laminate contains vertical surfaces. For the composite representative element, the conservation of mass is then applied to the fibres and the resin. If the fibres and the resin are assumed to be incompressible, the conservation of mass requires (Appendix A, Section A.1):

$$(\dot{u}_i)_{,i} + (v_i)_{,i} = 0 \quad (3.6)$$

where \dot{u}_i is the fibre bed velocity. Replacing the resin relative velocity in Equation 3.6 by the expression of Equation 3.5, we obtain the final resin flow continuity equation for the curing composite:

$$(\dot{u}_i)_{,i} = \left(\frac{K_{ij}}{\mu} (P + \rho_R gh)_{,j} \right)_{,i} \quad (3.7)$$

The continuity equation (Equation 3.7) implies that the volumetric deformations of the composite are caused by the flow of the resin out of the representative element (Figure 3.3). This implies that the dimensional reference for the composite is in fact the fibre bed dimensions.

3.2.3 Boundary and initial conditions

The solution to the problem of flow and compaction involves a set of transient differential equations. We need to specify the initial conditions and the boundary conditions applied to the domain. The state variables that describe the evolution of the flow-compaction process are the fibre bed displacements u_i and the resin pressure P . All pertinent parameters can be derived from

these primary state variables. The initial and boundary conditions are summarized in Table 3.1. The composite material has an initial fibre volume fraction V_{f0} . This information is used to calculate the instantaneous fibre volume fraction at any time during the solution. The initial resin pressure is assumed to be atmospheric pressure and the fibre bed is initially stress free. Boundary conditions specify the displacements, the applied pressure and resin pressure state at the edge of the laminate. The displacement boundaries are constant during the entire solution and are separated into three categories: free, fixed and sliding⁴. The external pressure can vary during the solution. The flow boundary condition is either impermeable or permeable. The permeable boundary condition is specified by imposing a prescribed resin pressure at the boundary. The boundary pressure is the pressure of the vacuum bag and can change with time. The restriction to flow from the bleeder is neglected since the permeability of the bleeder is typically three orders of magnitude higher than that of the composite. Therefore, the assumption of a 'free flow' boundary condition is justified. The impermeability condition is equivalent to having a zero normal pressure gradient at the boundary (i.e. $\partial P / \partial n = 0$).

3.2.4 Composite constitutive law

The fibre bed constitutive law relates the fibre bed stresses to the strain or strain rate field applied to a unidirectional composite representative element (Figure 3.4). The constitutive law used for the present model considers the elastic response of the fiber bed. Cai and Gutowski (1992a) proposed a constitutive law for a fibre bundle where the stresses were divided into normal and

⁴ Only displacements normal to the surface are fixed.

deviatoric shear stresses. The normal stresses would result in the elastic response of the material and the shear stresses cause the viscous flow. In the present work, only the fibre bed elastic response is considered. In Section 2.2.1, it was shown that the fibre bed effective stresses are related to the strains and this relation in matrix form can be written as:

$$\{\bar{\sigma}\} = [E_{fb}]\{\varepsilon\} \quad (3.8)$$

where $[E_{fb}]$ is the fibre bed effective stiffness matrix. For an element of a unidirectional fibre bundle, the entries of $[E_{fb}]$ are functions of both the fibre bed state and fibre volume fraction. For plane strain conditions ($\varepsilon_2 = \gamma_{12} = \gamma_{23} = 0$, $\bar{\tau}_{12} = \bar{\tau}_{13} = 0$), Equation 3.8 can be simplified as follows:

$$\begin{Bmatrix} \bar{\sigma}_1 \\ \bar{\sigma}_3 \\ \bar{\tau}_{13} \end{Bmatrix} = [E_{fb}] \begin{Bmatrix} \varepsilon_1 \\ \varepsilon_3 \\ \gamma_{13} \end{Bmatrix} \quad (3.9)$$

where $\bar{\sigma}_1, \bar{\sigma}_3, \bar{\tau}_{13}$ and $\varepsilon_1, \varepsilon_3, \tau_{13}$ are the stresses and strains in the local coordinate system of the unidirectional fibre bundle (Figure 3.4). Cai and Gutowski (1992a) considered only the normal component of $\bar{\sigma}_{ij}$ (i.e. $i=j$) to be elastic. In their constitutive law, they separated the normal stresses into two components: the axial stress σ_1 and the bulk stress $\sigma_b = (\sigma_2 + \sigma_3)/2$. For a plane strain problem their constitutive law yields:

$$\begin{Bmatrix} \bar{\sigma}_1 \\ \bar{\sigma}_3 \\ \bar{\tau}_{13} \end{Bmatrix} = \begin{bmatrix} E_1 & E_{13} & 0 \\ E_{31} & E_3 & 0 \\ 0 & 0 & 2\eta \end{bmatrix} \begin{Bmatrix} \varepsilon_1 \\ \varepsilon_3 \\ \dot{\gamma}_{13} \end{Bmatrix} \quad (3.10)$$

Their expression for $[E_{fb}]$ includes a coupling term between $\bar{\sigma}_1$ and $\bar{\sigma}_3$ which implies that a transverse strain induces an axial strain and the fibre bundle has a Poisson's ratio. The shear

response of the material is assumed to be viscous or strain rate sensitive. In soil mechanics problems, the linear elastic response of the porous medium is assumed to be isotropic leading to the following constitutive law:

$$\begin{Bmatrix} \bar{\sigma}_1 \\ \bar{\sigma}_3 \\ \bar{\tau}_{13} \end{Bmatrix} = \frac{E}{(1+\nu)(1-2\nu)} \begin{bmatrix} 1-\nu & \nu & 0 \\ \nu & 1-\nu & 0 \\ 0 & 0 & \frac{1-2\nu}{2} \end{bmatrix} \begin{Bmatrix} \epsilon_1 \\ \epsilon_3 \\ \gamma_{13} \end{Bmatrix} \quad (3.11)$$

where E and ν are the soil Young's modulus and Poisson's ratio. In this case, the shear response is elastic as opposed to the model presented in Equation 3.10 and coupling is also included. For the present model, a constitutive law that includes elements of both of the previously discussed approaches is used. A simplified model is adopted because there is a lack of experimental evidence to support a more complex constitutive law. Consequently, the present compaction model is based on the following purely elastic constitutive relation:

$$\begin{Bmatrix} \bar{\sigma}_1 \\ \bar{\sigma}_3 \\ \bar{\tau}_{13} \end{Bmatrix} = \begin{bmatrix} E_1 & 0 & 0 \\ 0 & E_3 & 0 \\ 0 & 0 & G_{13} \end{bmatrix} \begin{Bmatrix} \epsilon_1 \\ \epsilon_3 \\ \gamma_{13} \end{Bmatrix} \quad (3.12)$$

where E_1 , E_3 and G_{13} are the elastic constants describing the fibre bundle compaction behaviour. Since the fibres are oriented in the longitudinal direction, E_1 is assumed to be a function of the fibre longitudinal elastic modulus and the fibre volume fraction. The fibre bundle transverse response is controlled by E_3 which varies with the fibre bundle transverse strain. This property is calculated from the fibre bed compaction curve obtained experimentally. The fibre bundle shear modulus G_{13} is a material property that has not been discussed previously. In soil mechanics, this property is directly derived from the elastic modulus of the porous medium with the

assumption that the material is isotropic. The actual effect of this material property on the compaction behaviour of the laminates is unknown. Therefore, a sensitivity analysis for the shear modulus G_{13} is conducted in Section 5.1. A very important aspect to note is that there is no coupling between the longitudinal and transverse behaviour (i.e. Poisson's ratio is assumed to be zero). From the Cai and Gutowski's constitutive law (Equation 3.10), the induced axial strain caused by a transverse strain is very small ($\nu \approx 0$). Uncoupling the deformation is not an exact assumption, nevertheless it is believed to be reasonable. In practice, the transverse strains (out-of-plane) are the primary mode of laminate deformation. The in-plane strains of the laminate induced by the applied out-of-plane strains can be neglected since the ratio between the in-plane dimensions and the out-of-plane dimensions is very large. Details on the implemented fibre bed constitutive law are presented in Appendix A, Section A.5.2.

3.2.5 Finite element formulation

The governing equations for flow and compaction are solved using the finite element approximation. For soil consolidation problems, this method was successfully used by Lewis and Schrefler, (1987). In composite manufacturing, the flow of resin in resin transfer moulding process was also modelled using finite elements (Bruschke and Advani, 1990; Trochu et al., 1992). For autoclave processing Young (1995) used the finite element method, although typically the finite difference method has been used in the past (Section 2.3.1.3). The finite difference method is adequate for the simple geometries typically studied before. Since the main goal of the present study is to analyze the flow and compaction of more complex geometries, the finite element method is more appropriate. The solution for a porous medium compaction-flow

model is available in the commercial code ABAQUS⁵ to model consolidation of soils. Attempts were made to use this code to solve the present problem. Unfortunately, special features such as variable viscosity and a general fibre bed constitutive law are not implemented in ABAQUS. Therefore, a new special purpose finite element code was developed. The details on the theory of the finite element technique is not discussed since numerous references are available on this subject (e.g. Cook et al., 1989). However, a complete derivation of the discretized equations along with the solution method is presented here.

3.2.5.1 Weighted residual method

The governing equations (Equations 3.4 and 3.7) form a system of differential equations that have to be discretized into a system of algebraic equations. This is accomplished with the finite element method where the domain is subdivided into a series of simple shaped elements connected together at the nodes. The unknown variables are approximated by simple polynomial functions. Each node of the finite element model has one or more degrees of freedom associated with it. Since a finite element model contains a finite number of degrees of freedom⁶, the solution is only an approximation. The first step in the finite element method is to develop the discretized equations for a single element. Several techniques are commonly used. For structural analysis, the variational method or the Rayleigh-Ritz method is typically used because the governing equations can easily be expressed in terms of the potential energy. When the

⁵Commercial non-linear implicit finite element code.

⁶The real system will have an infinite number of degrees of freedom.

differential equations are available and a variational formulation does not necessarily exist, weighted residual methods are the preferred choice. These techniques are typically used for field problems such as heat transfer or fluid flow. The weighted residual equation is:

$$\int_{\Omega} R \cdot W_k \, d\Omega = 0, \quad k = 1, \dots, n \quad (3.13)$$

where R and W_k are the residual and the weight functions. For the equilibrium of forces (Equation 3.4), the residual is:

$$R_s = (\bar{\sigma}_{ij} - \delta_{ij}P)_{,j} + F_i \quad (3.14)$$

and for the continuity equation (Equation 3.7), the residual is:

$$R_f = (\dot{u}_i)_{,i} - \left(\frac{K_{ij}}{\mu} (P + \rho_R gh)_{,j} \right)_{,i} \quad (3.15)$$

Introducing the residuals (Equations 3.14 and 3.15) into Equation 3.13 and integrating by parts (Appendix A, Section A.2) results in the following set of equations:

$$\begin{aligned} \int_{\Omega} \bar{\sigma}_{ij} W_{k,j} \, d\Omega - \int_{\Omega} \delta_{ij} P W_{k,i} \, d\Omega &= \int_{\Omega} F_i W_k \, d\Omega + \int_{\Gamma} \sigma_i^n W_k \, d\Gamma \\ - \int_{\Omega} (\dot{u}_i)_{,i} W_k \, d\Omega - \int_{\Omega} \frac{K_{ij}}{\mu} P_{,j} W_{k,i} \, d\Omega &= \int_{\Omega} \frac{K_{ij}}{\mu} (\rho_R gh)_{,j} W_{k,i} \, d\Omega - \int_{\Gamma} q^n W_k \, d\Gamma \end{aligned} \quad (3.16)$$

The integration by parts introduces the boundary integrals on the right end side of Equation 3.16.

The next step consists of choosing the appropriate weight functions and substituting them in the residual equations.

3.2.5.2 Galerkin finite element equations

The Galerkin method, which is the most popular weighted residual method, is used to produce the finite element formulations of the present model. The Galerkin finite element formulation is applied to the governing equations (Equation 3.4 and 3.7) over the domain Ω . For the Galerkin finite element method, the weight functions used are the shape functions N_i chosen for the element. The composite displacements and the resin pressure are approximated over each element with two sets of interpolation functions:

$$\mathbf{u}_i \approx \sum_{j=1}^n N_{ij}^u \mathbf{a}_j^u \quad \text{and} \quad P \approx \sum_{j=1}^n N_j^p \mathbf{a}_j^p \quad (3.17)$$

where N_{ij}^u and N_j^p are the shape functions, \mathbf{a}_j^u and \mathbf{a}_j^p are the displacement and resin pressure degrees of freedom at the nodes respectively. Matrix notation is adopted to make the equations more readable. Thus, Equation 3.17 is written as follows:

$$\mathbf{u} = \mathbf{N}^u \mathbf{a}^u \quad \text{and} \quad P = \mathbf{N}^p \mathbf{a}^p \quad (3.18)$$

The present model assumes small strains, therefore the strain is related to the displacements by:

$$\varepsilon_{ij} = \frac{1}{2} (u_{i,j} + u_{j,i}) \quad (3.19)$$

Replacing the displacements by their discretized form we obtain:

$$\boldsymbol{\varepsilon} = \mathbf{B} \mathbf{a}^u \quad (3.20)$$

where \mathbf{B} is a matrix containing the derivatives of the displacement shape functions (Appendix A, Section A.3). Substituting Equation 3.20 in the constitutive relation (Equation 3.8), the effective stress can be expressed in terms of the nodal displacements by:

$$\bar{\sigma} = \mathbf{D}_T \mathbf{B} \mathbf{a}^u \quad (3.21)$$

where \mathbf{D}_T is the tangent material stiffness matrix for the fibre bed. Replacing $\bar{\sigma}_{ij}$ in Equation 3.16 with Equation 3.21 and replacing the weight functions and their derivatives by the shape functions and their derivatives, we obtain the discretized governing equations:

$$\begin{aligned} \int_{\Omega} \mathbf{B}^T \mathbf{D}_T \mathbf{B} \mathbf{a}^u d\Omega - \int_{\Omega} \mathbf{B}^T \delta \mathbf{a}^p \mathbf{N}^p d\Omega &= \int_{\Omega} \mathbf{N}^{uT} \mathbf{F} d\Omega + \int_{\Gamma} \mathbf{N}^{uT} \sigma_i^n d\Gamma \\ - \int_{\Omega} \mathbf{N}^{pT} \delta^T \mathbf{B} \mathbf{a}^u d\Omega - \int_{\Omega} \mathbf{G}^T \frac{\mathbf{K}}{\mu} \mathbf{G} \mathbf{a}^p d\Omega &= \int_{\Omega} \mathbf{G}^T \mathbf{H}^d d\Omega - \int_{\Gamma} \mathbf{N}^{pT} q^n d\Gamma \end{aligned} \quad (3.22)$$

where \mathbf{G} is a matrix containing the derivatives of the shape functions, δ is a vector defined in Appendix A, Equation A.35 and \mathbf{H}^d is a matrix containing the pressure head term, Appendix A, Equation A.40. The domain is discretized with bilinear quadrilateral isoparametric elements (Figure 3.5). Most laminates can be meshed using quadrilateral elements. The choice of an isoparametric element enables one to apply the equations to a domain of arbitrary shape in the x-z plane. The same shape function is used for the displacements and the resin pressure (i.e. $\mathbf{N}^u = \mathbf{N}^p = \mathbf{N}$). Details on the particular form of the shape function and the procedure to get the shape function derivatives are provided in Appendix A, Section A.3. For coupled fluid flow-elasticity problems, it is recommended to use an eight noded rectangular element with quadratic functions for the displacements and linear functions for the pressure. Although the problem has been successfully solved with a four noded bilinear element, the eight noded element approach

reduces some numerical instabilities arising from the coupling of the governing equations. For simplicity and computing efficiency, the bilinear four noded element is chosen.

3.2.5.3 Method of solution

Different routes are available for solving the governing equations (Equation 3.22). One can uncouple the system of equations by alternatively solving the stress equilibrium and then the continuity (or fluid flow) equation. This technique has been used in the majority of flow-compaction models for composites. Typically, for soil mechanics applications, the solution is applied to the coupled system of equations. For the present model, the coupling approach is used even though the problem can be assumed quasi-static and the uncoupled method is justified. Coupling the governing equations is a more standard practice which simplifies the solution algorithm. From Equation 3.22, we can write the system of equations to solve:

$$\begin{bmatrix} \mathbf{S} & \mathbf{L} \\ \mathbf{0} & \mathbf{H} \end{bmatrix} \begin{bmatrix} \mathbf{a}^u \\ \mathbf{a}^p \end{bmatrix} + \begin{bmatrix} \mathbf{0} & \mathbf{0} \\ \mathbf{L}^T & \mathbf{0} \end{bmatrix} \begin{bmatrix} \dot{\mathbf{a}}^u \\ \dot{\mathbf{a}}^p \end{bmatrix} = \begin{bmatrix} \mathbf{F}^s \\ \mathbf{F}^f \end{bmatrix} \quad (3.23)$$

where

$$\mathbf{S} = \int_{\Omega} \mathbf{B}^T \mathbf{D}_T \mathbf{B} d\Omega \quad (3.24)$$

$$\mathbf{L} = - \int_{\Omega} \mathbf{B}^T \delta \mathbf{N} d\Omega \quad (3.25)$$

$$\mathbf{H} = - \int_{\Omega} \mathbf{G}^T \frac{\mathbf{K}}{\mu} \mathbf{G} d\Omega \quad (3.26)$$

$$\mathbf{L}^T = - \int_{\Omega} \mathbf{N}^T \delta^T \mathbf{B} d\Omega \quad (3.27)$$

$$\mathbf{F}^s = \int_{\Omega} \mathbf{N}^T \mathbf{F}^g d\Omega + \int_{\Gamma} \mathbf{N}^T \sigma_i^n d\Gamma \quad (3.28)$$

$$\mathbf{F}^f = \int_{\Omega} \mathbf{G}^T \mathbf{H}^d d\Omega - \int_{\Gamma} \mathbf{N}^T q^n d\Gamma \quad (3.29)$$

The solution procedure consists of performing the integration of Equations 3.24-3.27 in order to obtain the element stiffness matrix which is then assembled in the global stiffness matrix of the system. The integration of Equations 3.28-3.29 for each element leads to consistent nodal load vectors. Details for the integration of Equation 3.24-3.29 are presented in Appendix A, Section A.4. Then the appropriate essential boundary conditions (i.e. displacements and resin pressure) are applied and Equation 3.23 is solved to find the unknown nodal variables. Apart from the standard spatial element integration required, the solution of the system of equations requires two other fundamental solution strategies. The presence of a time derivative in Equation 3.23 implies that the governing equation has to be integrated in time (this solution method is presented in Section 3.2.5.4). Finally, because of the non-linear behaviour of the fibre bed elasticity and permeability, a non-linear iterative technique is required. Details of the solution procedure are discussed in Section 3.2.5.5.

3.2.5.4 Time integration

The consolidation is a transient problem and the system of equations has to be integrated in time.

The system of ordinary differential equations (Equation 3.23) can be rewritten as follows:

$$\mathbf{C} \dot{\mathbf{U}} + \mathbf{D} \mathbf{U} = \mathbf{F} \quad \text{for } t > t_0 \quad (3.30)$$

where \mathbf{U} is the vector of unknown nodal variables, $\dot{\mathbf{U}}$ is the vector of time derivatives of the unknown nodal variables, \mathbf{C} is the damping matrix, \mathbf{D} is the stiffness matrix and \mathbf{F} is the load vector. The system of equations is of the first order and a number of methods are available for its time integration. The Euler direct integration methods are probably the most popular. Among them, the implicit Euler method is unconditionally stable but not unconditionally accurate. The advantage of this method is that it is possible to use large time steps. For our problem, the total time scale is long (in the minutes range) and the process is quasi-static, therefore the time steps are necessarily long. With the implicit method, the time derivative is approximated by a backward finite difference approximation:

$$\dot{\mathbf{U}}_{t+\Delta t} \approx \frac{1}{\Delta t} (\mathbf{U}_{t+\Delta t} - \mathbf{U}_t) \quad (3.31)$$

Substituting Equation 3.31 in Equation 3.30, we obtain the following system of equations:

$$(\mathbf{C} + \Delta t \mathbf{D}) \Delta \mathbf{U} = \Delta t (\mathbf{F} - \mathbf{D} \mathbf{U}_t) \quad (3.32)$$

where Δt is the solution time step and $\Delta \mathbf{U}$ is the vector of increments of nodal variables. The solution procedure consists of providing initial values for all the unknowns (i.e. initial conditions) and then solve the system of equations in Equation 3.32. After each time step, the solution vector is updated using:

$$\mathbf{U}_{t+\Delta t} = \mathbf{U}_t + \Delta \mathbf{U} \quad (3.33)$$

The time integration solution has to be coupled with a non-linear iterative technique since the problem contains material properties that are functions of the nodal variables. Details of the non-linear solution technique are discussed in the next section.

3.2.5.5 Non-linear solution technique

As seen in Sections 2.1 and 2.2, some material properties are not constant (e.g. the fibre bed stiffness and permeability are functions of the fibre volume fraction). To account for the property change, a non-linear solution procedure is required. Several techniques are available to solve the problem and the choice of a method depends mainly on the type or the severity of the non-linearity. For our problem the non-linearities are: the resin viscosity, the fibre bed permeability and the fibre bed transverse elasticity. The resin viscosity can be assumed constant during a time step provided that the rate of change of the resin viscosity is small during the time step. After each time step, the resin viscosity will be updated based on the actual element temperature and resin degree of cure. For the permeability, a substitution method (Dhatt et al., 1984) is used where the permeability is updated at every iteration until a convergence criterion is reached. Finally, for the fibre bed elasticity, a Newton-Raphson technique (Owen and Hinton, 1980) is required to take into account the severe hardening of the effective stress-strain curve. At each time step the system of equations to be solved can be written as:

$$\mathbf{F}^{\text{ext}} - \mathbf{D}\mathbf{U} = 0 \quad (3.34)$$

where \mathbf{D} is the assembled stiffness matrix, \mathbf{U} is the vector of unknowns and \mathbf{F}^{ext} is the vector of applied external loads at a time $t+\Delta t$. For non-linear problems, during one step of the iterative

solution, Equation 3.34 is not satisfied until convergence has occurred. An unbalance exists between the applied loads and the internal load vector:

$$\mathbf{R} = \mathbf{F}^{\text{ext}} - \mathbf{D}\mathbf{U} \neq 0 \quad (3.35)$$

where \mathbf{R} is a vector of residual forces at a time $t+\Delta t$. The purpose of the non-linear solution technique is to use a series of iterations in order to minimize the residual force vector until a convergence criterion is reached. Using the residual force vector concept and the Newton-Raphson method, the system of equations to be solved at each iteration is:

$$\mathbf{D}\Delta\mathbf{U}_i = \mathbf{R} \quad (3.36)$$

where $\Delta\mathbf{U}_i$ is the vector of increment nodal variables to be determined during the i^{th} iteration. Combining the time integration (Equation 3.32) and the non-linear incremental solution (Equation 3.36) we obtain the following expressions for \mathbf{D} and \mathbf{R} :

$$\mathbf{D} = \mathbf{C} + \Delta t\mathbf{D}_{i-1} \quad (3.37)$$

where \mathbf{D}_{i-1} is the stiffness matrix calculated from the unknown values at the i^{th} iteration and

$$\mathbf{R} = \Delta t[\mathbf{F}^{\text{ext}} - \mathbf{F}^{\text{int}}] + \mathbf{C}(\mathbf{U}_0 - \mathbf{U}_{i-1}) \quad (3.38)$$

where \mathbf{F}^{int} is the internal load vector and \mathbf{U}_0 is the unknown values at the previous time step. The internal load vector is calculated from the solution state using the following relation:

$$\mathbf{F}^{\text{int}} = \begin{bmatrix} \int_{\Omega} (\mathbf{B}^T \bar{\boldsymbol{\sigma}} + \mathbf{L}\mathbf{a}^p) d\Omega \\ \int_{\Omega} \mathbf{H}\mathbf{a}^p d\Omega \end{bmatrix} \quad (3.39)$$

where $\bar{\sigma}$ is the actual updated effective stress vector obtained from the constitutive model. After each iteration, the solution is updated simply by:

$$\mathbf{U} = \mathbf{U}_{i-1} + \Delta\mathbf{U}_i \quad (3.40)$$

until a convergence criterion is reached. We use two norms to test the solution convergence:

$$\|n^U\| = \frac{\sum(\Delta\mathbf{U}_i)^2}{\sum(\mathbf{U})^2} \quad (3.41)$$

and

$$\|n^R\| = \frac{\sum(\mathbf{R})^2}{\sum(\mathbf{F}^{\text{ext}})^2} \quad (3.42)$$

Equation 3.41 is the ratio of Euclidean norm of the increment of the state variables and Equation 3.42 is the ratio of Euclidean norm of the residual forces. The summation is performed over the total active degrees of freedom. The solution is obtained when the residual or the state variable increment are ideally equal to zero. In practice, convergence is reached when the maximum of the two norms is less than a certain tolerance ψ :

$$\max(\|n^U\|, \|n^R\|) < \psi \quad (3.43)$$

The value of ψ specified by the user depends on the precision of the computer and the degree of accuracy required.

3.2.6 Program algorithm

The process model developed is called COMPRO. The finite element code is written in FORTRAN and the flow-compaction module is divided into subroutines for flexibility. As presented in Section 3.1, the flow-compaction module is part of a general processing model. At each iteration of the main program loop, the following steps are executed:

- 1) **Update** element viscosity (Section 2.1)
- 2) **If** at least one element has a viscosity below the flow limit viscosity⁷ **then RUN**
- 3) **If** all elements have reached the gel point **then STOP**⁸
- 4) **If RUN** then
 - 5) **Store** previous time step solution vector: U_t
 - 6) **Give** an initial guess for the solution vector: $U_0=U_t$
 - 7) **Update** the element external load vector F^{ext} and the gravity load vectors (Appendix A, Section A.4)
 - 8) **Loop** over the elements
 - 9) **Update** permeability matrix K (Appendix A, Section A.5.1)
 - 10) **Update** fibre bed tangent modulus matrix D_T (Appendix A, Section A.5.2)
 - 11) **Compute** element stiffness matrix D (Equation 3.37)
 - 12) **Compute** element residuals force vectors R (Equation 3.38)
 - 13) **Apply** essential boundary conditions (Section 3.2.3)
 - 14) **Assemble** D and R in global stiffness matrix and residual vector
 - 15) **Solve** the system of equations $D\Delta U_i = R$
 - 16) **Update** solution vector: $U = U_{i-1} + \Delta U_i$
 - 17) **Compute** element internal load vector F^{int} (Equation 3.39)

⁷ This value of viscosity selected by the user specifies when the solution of the flow model should start. Flow effects are not significant above a certain resin viscosity value (see discussion in Section 3.3.3).

⁸ The resin is in a rubbery state and percolation flow is impossible.

- 18) **Check** convergence (Equations 3.41-3.43)
- 19) **If converged then go to 21)**
- 20) **If not converged then go to 8)**
- 21) **Update** the state variables (Appendix A, Section A.6)
- 22) **STOP**

The implementation of the finite element method previously described is not discussed in detail. However, some explanation is given on critical aspects of the present solution method. The calculation of the material properties is very important.

The resin viscosity calculation (Step 1) is straightforward since it depends only on the element temperature and resin degree of cure. The viscosity is simply updated at each time step using empirical equations (e.g. Equation 2.2).

The fibre bed properties are given for a unidirectional ply of the composite. Laminates consist of a series of plies oriented in different directions. One finite element can contain several plies, therefore, the element properties are obtained by averaging techniques. The element permeability (Step 9) is simply obtained by a weighted averaging technique (Appendix A, Section A.5.1).

The element fibre bed elasticity (Step 10) is more difficult to evaluate when the laminate is composed of plies with different orientations. The constitutive law for the fibre bed elastic behaviour is restricted to unidirectional laminates only. Details of the approach used in the present model are discussed in Appendix A, Section A.5.2.

The computation of the effective stresses (Step 17) and other state variables (Step 22) such as the fibre volume fraction, the resin velocity and the laminate resin mass losses is presented in

Appendix A, Section A.6. Details on the coordinate system transformations are given in Appendix A, Section A.6.5.

3.3 Flow-compaction model verification

Before applying the flow-compaction model to study complex shapes, a number of verification runs were performed. The purpose of the verification runs was to test the element formulation and implementation. These runs consisted of testing the model at different levels of complexity ranging from simple static cases. (Section 3.3.1) to the full non-linear transient solution (Section 3.3.2). Several comparison sources were available to validate the results from the present model. The linear solution for a 1-D consolidation coupled with 1-D flow can be compared with an analytical solution. For the non-linear solution, ABAQUS or a previously developed 1-D composite processing model, LAMCURE, (Smith and Poursartip, 1993) was used. The verifications run were also used to define the limitations of the present model and the level of accuracy of the solution. Table 3.2 outlines the different verification runs performed. Finally, issues about the mesh density are discussed in Section 3.3.3.

3.3.1 Static solution

The main objective of the static runs was to verify if the element developed for the present model converged to the exact solution. A simple patch test was conducted for different loading cases. Since the element represents a porous material, the patch test was done for undrained and drained conditions. The undrained condition consists of applying the load to the model with impermeable boundary conditions. This loading condition results in a fluid pressure building up

in the material. The undrained condition consists of applying the load to the model with unsaturated material (i.e. no fluid). The applied stress is therefore entirely reacted by the porous material. Figure 3.6 shows the model used for the patch test with the different load cases. This model is composed of four elements that share a common node and form a patch. The model is loaded such that a uniform stress state is applied with the minimum number of displacement constraints to prevent any rigid body motion. The fibre bed is assumed linear elastic, the material properties are presented in Figure 3.6. The results from the patch test are presented in Table 3.3. The computed stresses and strains in the elements are in perfect agreement with the applied stress state. Thus, the element passes the patch test for the static conditions. This insures that the element converges to the exact solution and that the elements are compatible.

3.3.2 Transient solution

The objective of the transient runs listed in Table 3.2 was to verify the consolidation solution algorithm used in the present model. Closed-form solution for the consolidation process is given by Davé (1987a). Constant material properties are used and Figure 3.7 (a) shows the simulation model with the boundary conditions and material input data for run T1. The finite element mesh used is presented in Figure 3.7 (b). For this particular case, only the consolidation in the vertical direction is considered and the applied pressure is held constant. The result of the simulation is presented in Figure 3.8. The transient variation of the vertical pressure gradient is in good agreement with the results from the exact solution.

The previous simulation assumed linear material properties. The objective of the next simulations is to test the non-linear solution procedure of the present model. The non-linearity of

the fibre bed permeability is first considered. Figure 3.9 presents the models and the material inputs used for the simulations T2 (Figure 3.9 (a)) and T3 (Figure 3.9 (b)). The permeability is calculated from Equation 2.8 with $k_x=k_z=6$ and $r_f=4.2 \times 10^{-6}$ m. The meshes used are shown in Figure 3.10. The resin viscosity is constant and the fibre bed elasticity is assumed linear. The solution from the present model is compared with the ABAQUS results. Figures 3.11 and 3.12 present the results for a one-dimensional consolidation. As shown in Figure 3.11, the transient variation of the vertical pressure profile is in good agreement with the results from ABAQUS. The change of the laminate thickness (u_z) with time calculated with the model is identical to the results from ABAQUS (Figure 3.12). In Figure 3.12, the results for T2 are compared to a simulation where the permeability was kept constant (i.e. at the initial value of K_z given by Equation 2.8). Significant difference in the compaction behaviour of the laminate is observed showing the importance of considering the permeability non-linearity in the solution. For the two dimensional case, the results (Figures 3.13-3.15) show again a very good agreement between ABAQUS and the present model. The horizontal pressure profiles tend to disagree near the edge of the laminate (Figure 3.14). Eight noded elements were used in ABAQUS and this could account for the observed differences. Large deformations occur at the edge of the laminate. In such areas, higher order elements will predict the behaviour more accurately. Nevertheless, the two models predict similar results even though the present model uses linear elements. Again, the importance of considering permeability variation in the solution is demonstrated in Figure 3.15 where it can clearly be seen that the laminate compaction behaviour changes substantially if we assume a constant fibre bed permeability.

The next simulations tested the non-linear solution for the compaction prediction of a composite material. The results from the present model were compared with the solution from a one dimensional processing model for composites, LAMCURE (Smith and Poursartip, 1993). Figure 3.16 presents the models, the boundary conditions and the cure cycle used for the simulations. The laminate has an initial thickness of 25 mm and consists of unidirectional plies of AS4/3501-6. The curing properties for this material are available from the literature (Loos and Springer, 1983). The permeability is calculated from Equation 2.8 with $k_z=6$ and $r_f=4.2 \times 10^{-6}$ m. For the fibre bed elasticity, two compaction curves are used (Figure 3.17). They typically represent the compaction behaviour of a 'high-flow' system (i.e. $V_{f0}=0.48$) and a 'low-flow' composite (i.e. $V_{f0}=0.57$). Figure 3.18 shows that the variation of the thickness change (u_z) with time are similar for both models. Better agreement between LAMCURE and the present model is obtained for the 'low-flow' system (T5). This can be explained by the difference in the solution method between LAMCURE and COMPRO. The present model assumes small strains and therefore, non-linear geometric effects are not considered. In the solution procedure of LAMCURE, the geometric non-linearity is accounted for by updating the nodal locations at each time step. Geometric non-linearity can have an effect on the compaction prediction as seen in the simulations. When the material strains are large, the error in the predictions become more pronounced. Since the material studied in the present research is considered to fall under 'low-flow' systems, the assumption of small strains is acceptable.

3.3.3 Mesh density

The final verification was to study the effect of the mesh density on the predictions of the model. The major issue concerned is the ability of the model to predict the important resin pressure gradients at permeable boundaries observed in the initial stages of the consolidation. The problem of oscillations in the pressure profile has been reported for the finite element solution of consolidation problems (Vermeer and Verruijt, 1981). To illustrate the problem, simulations for a 1-D consolidation were conducted. The model dimensions, boundary conditions and material input data are presented in Figure 3.19. The simulations consisted of two runs with different mesh densities (i.e. 4 elements and 40 elements meshes). The predicted variations of the resin pressure profile in the vertical direction with time are compared to the exact solution in Figure 3.20. The results clearly show the oscillations of the solution in the early stages of the consolidation (i.e. 1 minute) seen for the 4 elements mesh. By increasing the mesh density, the oscillations are not present and the model results are in good agreement with the closed-form solution. As seen in Figure 3.20, the problem is limited to the initial stage of the compaction. The results for both meshes are in good agreement with the exact solution for the compaction time greater than 1 minute. Even though the oscillations eventually disappear later in the solution process, the initial stage of the solution is very critical to the convergence of the non-linear solution procedure.

Different approaches can be taken to limit these oscillations. Vermeer and Verruijt (1981) give an expression for the minimum time step $(\Delta t)_{\min}$ necessary to avoid the pressure oscillations:

$$(\Delta t)_{\min} \geq \frac{1}{6} \frac{\mu(\Delta h)^2}{K E} \quad (3.44)$$

where μ is the viscosity of the fluid, K is the permeability of the porous medium, E is the elastic modulus of the porous medium and Δh is the element size in the direction of the pressure gradient. As seen by Equation 3.44, a combination of material properties, element size and time step length can control the problem. For the consolidation of composite laminates, the material properties change during the solution. At the beginning of the solution, the resin viscosity is high (>1000 Pa.s), the fibre bed permeability is of the order of $1 \times 10^{-13} \text{ m}^2$ and the fibre bed elastic modulus can be low (≈ 0.4 MPa). The element size close to the boundary used in most of the meshes are about (0.6 mm). Thus the minimum time step according to Equation 3.44 would be about 25 minutes.

Compromises were made in order to minimize the problem of oscillations of the solution. These compromises come from the maximum number of elements possible and the convergence of the non-linear solution procedure. Most of the simulations were made with a constant time step of 1 minute. This value gave good convergence of the solution with minimum oscillations in the resin pressure profiles. To minimize the oscillation problem, the flow limit viscosity⁹ was also decreased. However, decreasing the flow limit viscosity from 10000 Pa.s to 100 Pa.s did not significantly affect the final results. A value of 1000 Pa.s is typically used for the flow limit

⁹ Viscosity value when the flow-compaction solution is started.

viscosity. When the resin viscosity is above this value, the resin flow is not significant in most processing conditions and running the flow model is not necessary.

3.4 Summary

From the verification simulations presented (Table 3.2), we have demonstrated that the present finite element model successfully calculates the compaction behaviour of an elastic porous medium. The linear element developed converged to the exact solution in static loading conditions. The transient non-linear solution algorithm is correctly implemented as shown by comparison of simulation results with closed-form predictions or ABAQUS results. The present processing model is in good agreement with previously developed models for composite materials. We note that the model predictions could be inaccurate when geometric nonlinearities are important.

3.5 Tables

Table 3.1 Summary of the initial and boundary conditions for the flow-compaction model.

Initial conditions, for $t=0$, in the domain Ω		
$V_f = V_{f0}$, $P = P_{atm}$, $\bar{\sigma} = 0$		
Boundary conditions, for $t > 0$, on the surface Γ		
Displacement	External pressure	Flow
Free	$\sigma = f(t)$	Impermeable: $\partial P / \partial n = 0$
Fixed: $u_i = 0$		Permeable: $P_b = f(t)$
Sliding: $u^n = 0$		

Table 3.2 Run matrix for the flow-compaction model verification.

Case	Geometry	Elasticity	Permeability	Viscosity	Boundary conditions
Static runs Patch test					
S1	patch	linear	constant	constant	Fig. 3.6 (a)
S2	patch	linear	constant	constant	Fig. 3.6 (b)
S3	patch	linear	constant	constant	Fig. 3.6 (a)
S4	patch	linear	constant	constant	Fig. 3.6 (b)
Transient runs					
T1	1-D	linear	constant	constant	Fig. 3.7
T2	1-D	linear	variable	constant	Fig. 3.9 (a)
T3	2-D	linear	variable	constant	Fig. 3.9 (b)
T4	1-D	non-linear	variable	variable	Fig. 3.16
T5	1-D	non-linear	variable	variable	Fig. 3.16

Table 3.3 Results from patch test runs for undrained (S1, S2) and drained (S3, S4) conditions.

Run	Stress applied	Results from COMPRO						
		P (kPa)	$\bar{\sigma}_x$ (kPa)	$\bar{\sigma}_z$ (kPa)	$\bar{\tau}_{xz}$ (kPa)	ϵ_x	ϵ_z	γ_{xz}
S1	$\sigma_x = -100$	50	-50	50	≈ 0	-0.005	0.005	≈ 0
S2	$\sigma_z = -100$	50	50	-50	≈ 0	.005	-.005	≈ 0
S3	$\sigma_x = -100$	0	-100	≈ 0	≈ 0	-0.01	≈ 0	≈ 0
S4	$\sigma_z = -100$	0	≈ 0	-100	≈ 0	≈ 0	-0.01	≈ 0

Note: ≈ 0 indicates a result $< 10^{-10}$

3.6 Figures

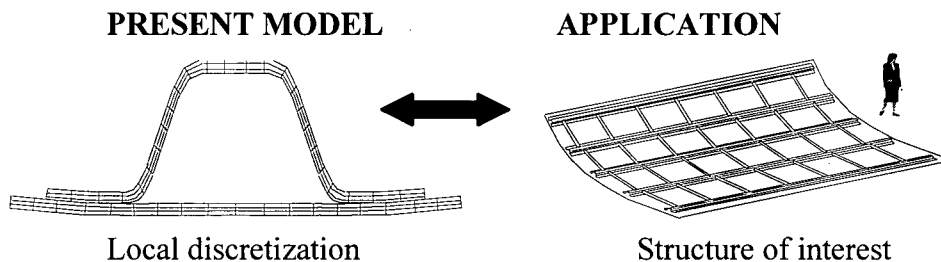


Figure 3.1 Present modelling approach.

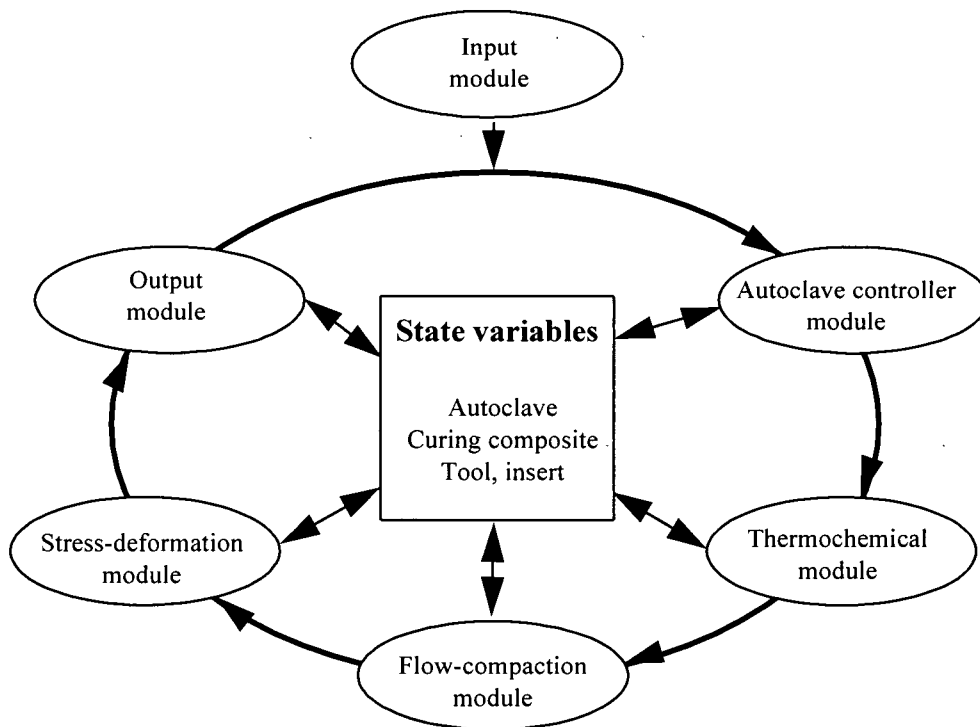


Figure 3.2 Processing model flowchart showing the different modules.

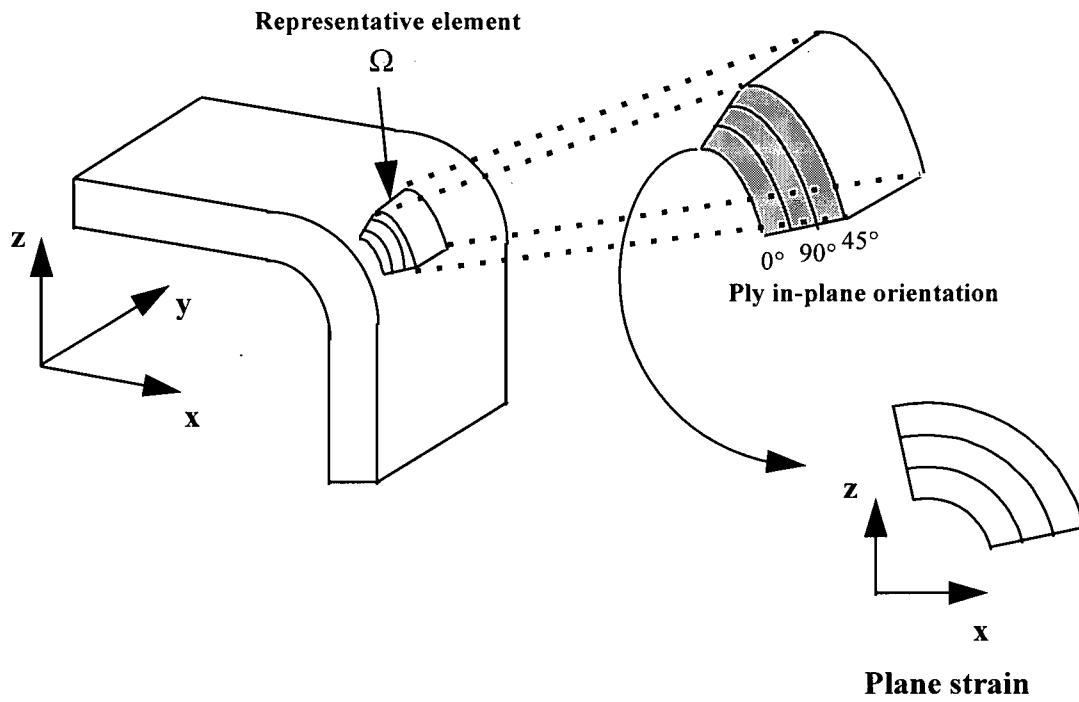


Figure 3.3 Laminate representative volume and plane strain composite element.

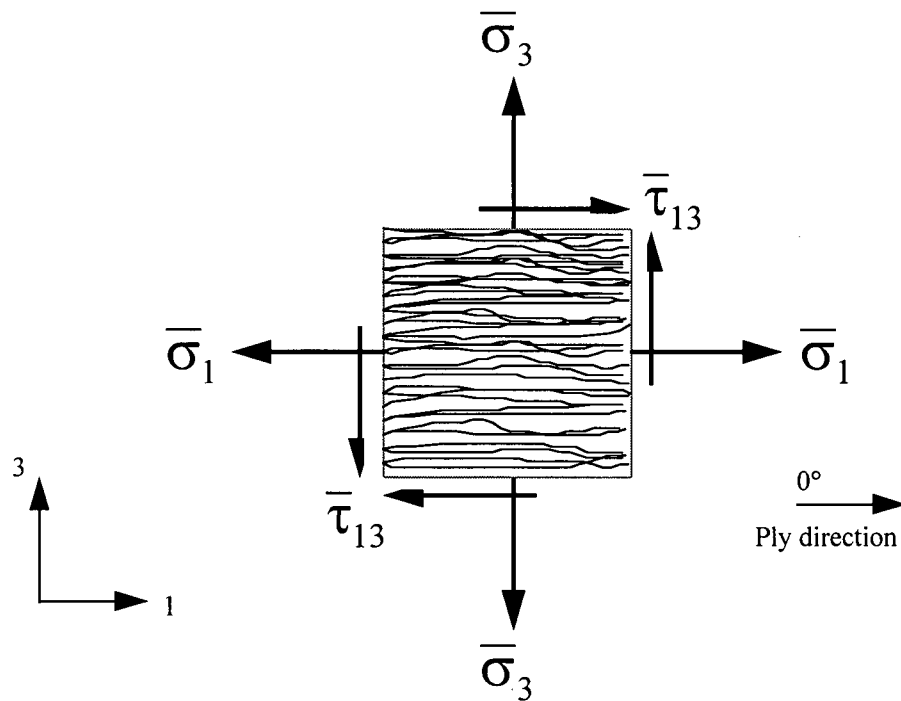


Figure 3.4 Stress state on a representative element of a unidirectional ply.

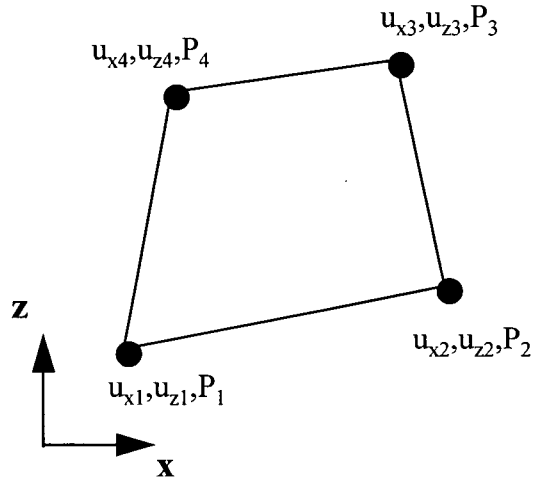


Figure 3.5 Bilinear quadrilateral element and degrees of freedom (i.e. displacements u_{xn} , u_{zn} and pressure P_n where n is the node number).

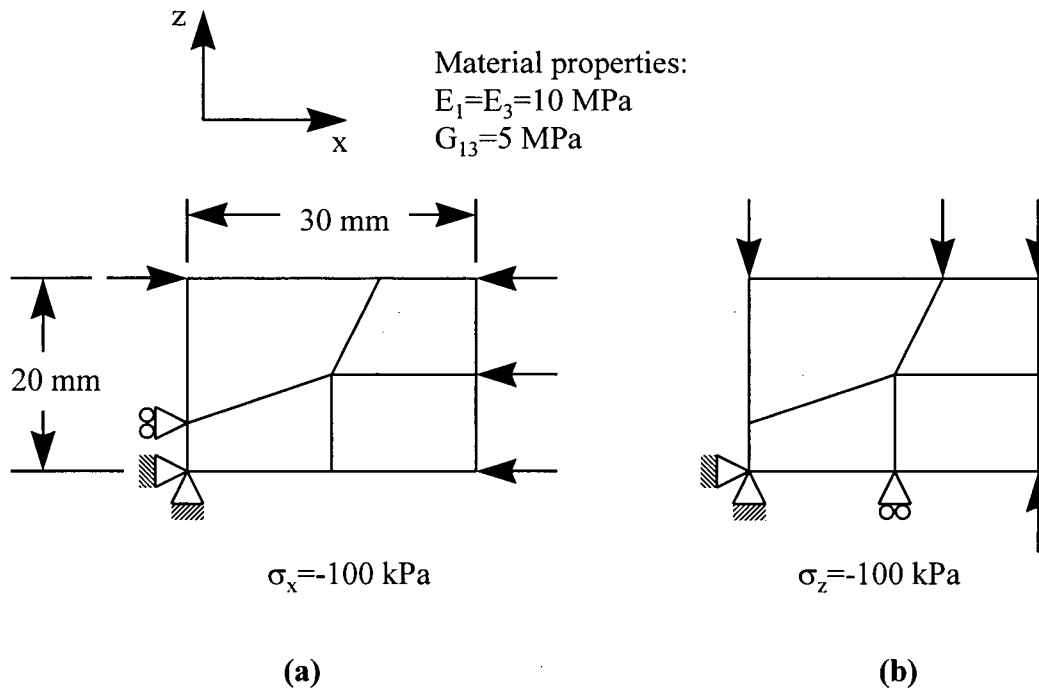


Figure 3.6 Finite element mesh and boundary conditions for patch test runs, (a) axial stress state, (b) transverse stress state. The fibre bed properties are also given.

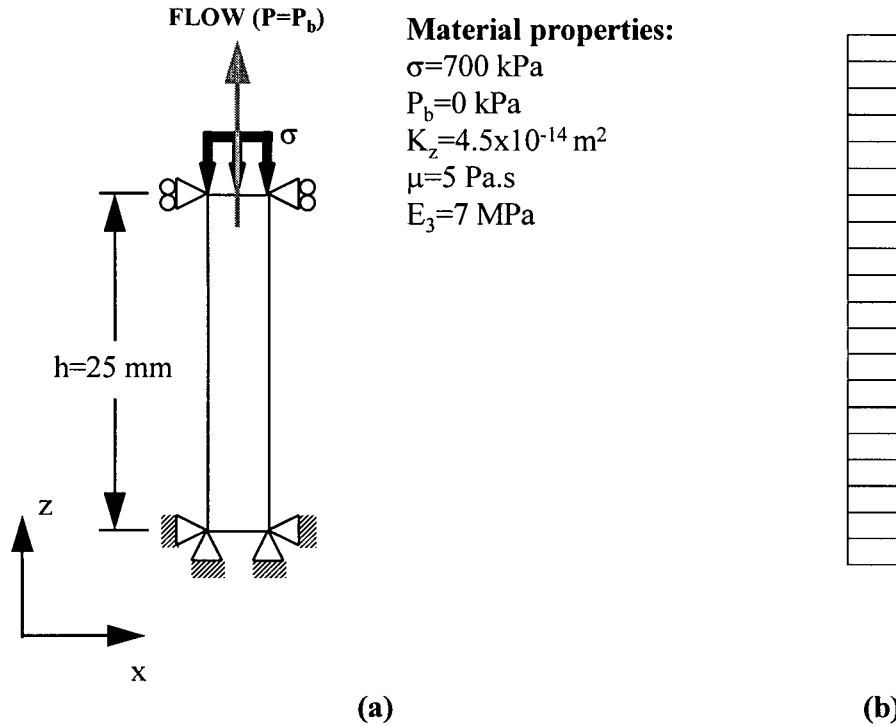


Figure 3.7 Model definition for the exact solution transient run (T1), (a) boundary conditions and material property inputs, (b) finite element mesh used (20 elements).

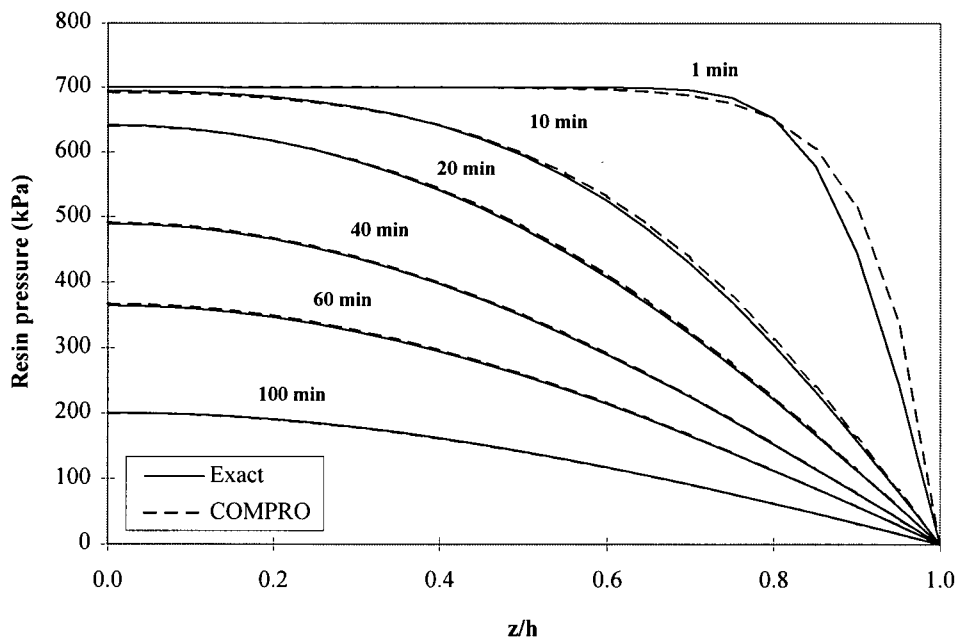


Figure 3.8 Results from transient run T1 compared to the exact solution showing the vertical pressure profile evolution with time.

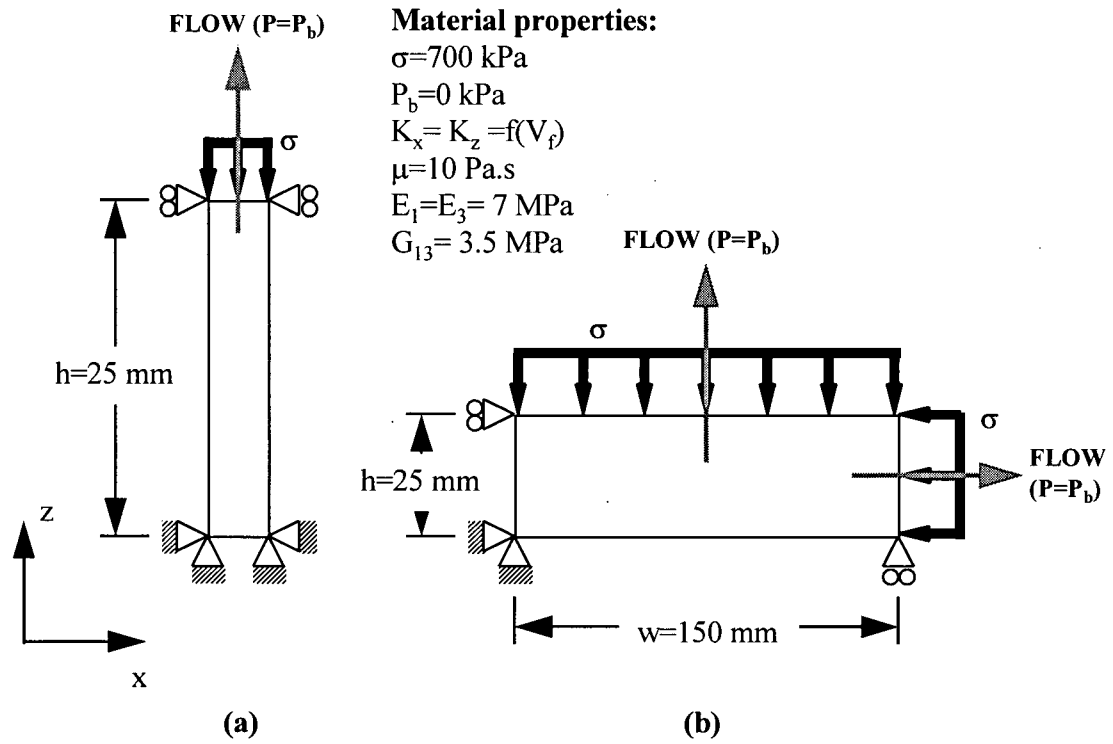


Figure 3.9 Boundary conditions and material property inputs for the non-linear permeability transient runs, (a) 1-D flow (T2), (b) 2-D flow (T3).

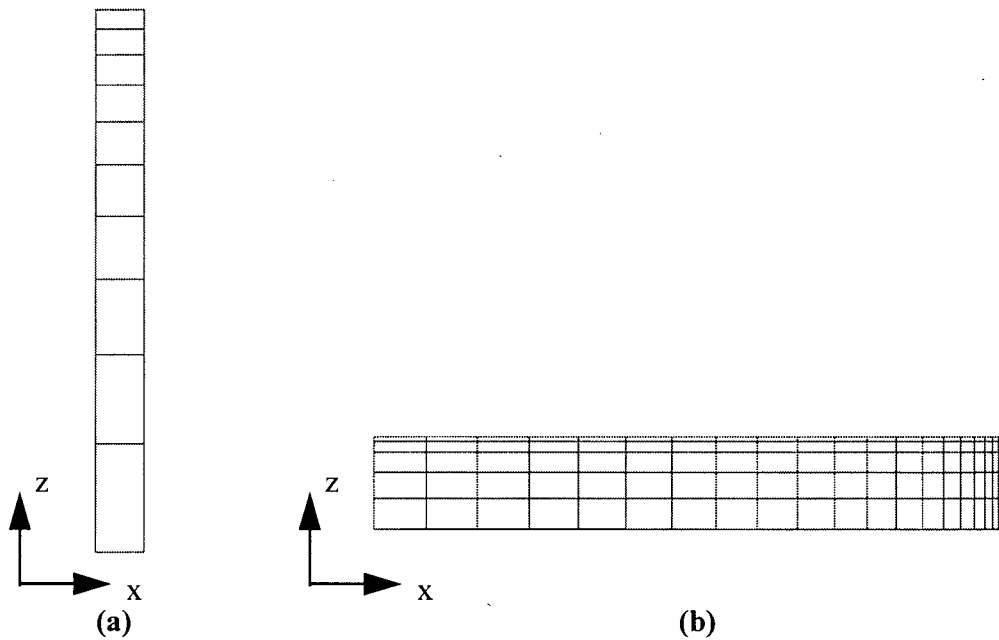


Figure 3.10 Finite element meshes used for the transient runs, (a) T2 (10 elements), (b) T3 (100 elements).

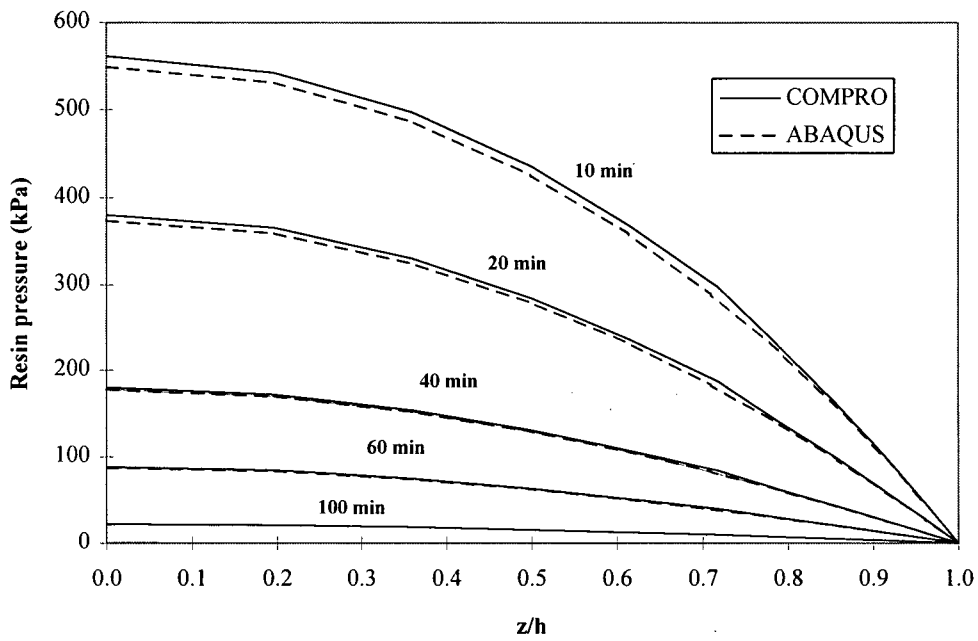


Figure 3.11 Results from transient run T2 compared to ABAQUS solution showing the vertical pressure profile evolution with time.

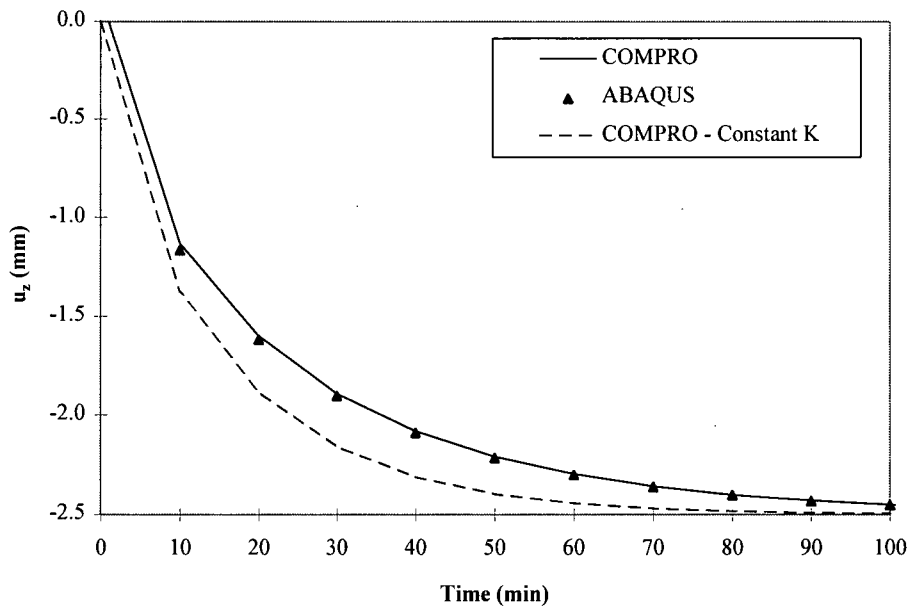


Figure 3.12 Results from transient run T2 compared to ABAQUS solution showing the variation of vertical displacement at the top of the model with time. Also shown is a simulation assuming a constant permeability (dashed line).

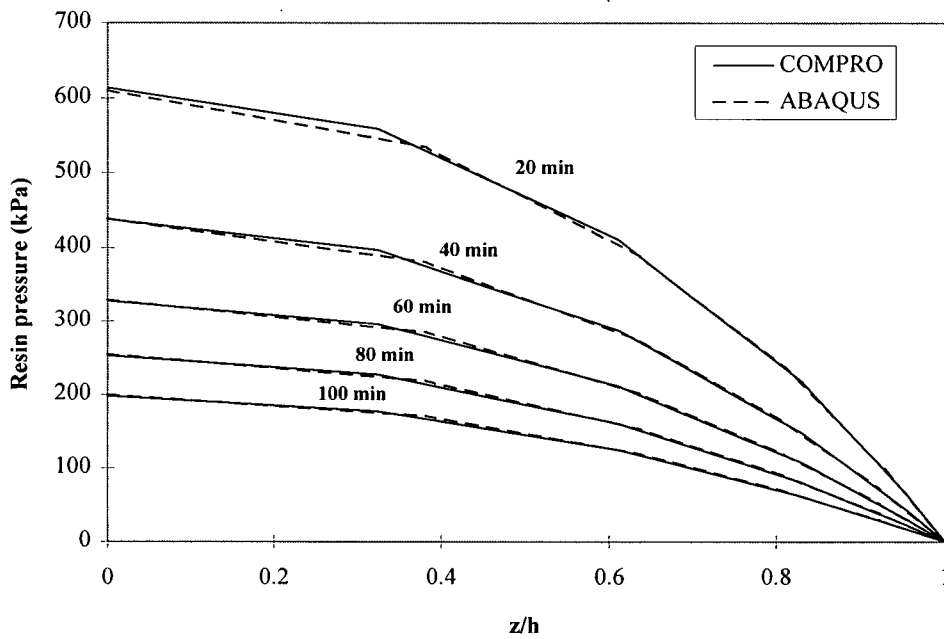


Figure 3.13 Results from transient run T3 compared to ABAQUS solution showing the vertical pressure profile evolution with time at $x=0$.

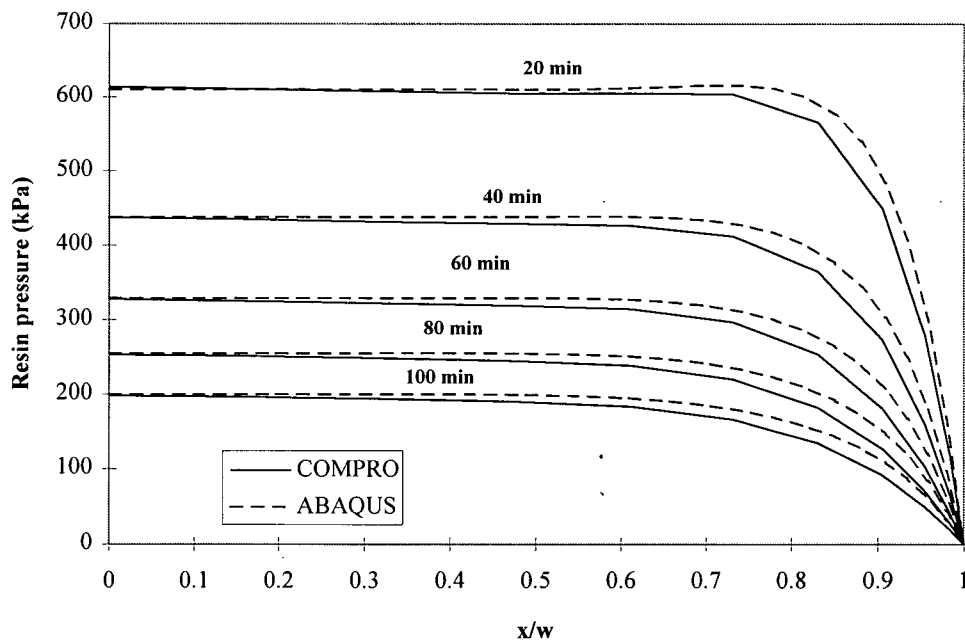


Figure 3.14 Results from transient run T3 compared to ABAQUS solution showing the horizontal pressure profile evolution with time at $z=0$.

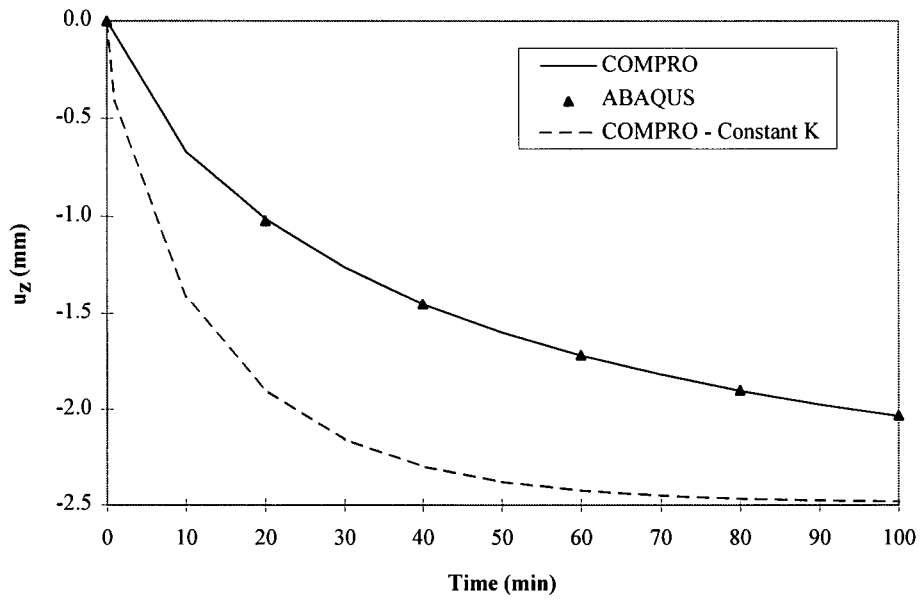


Figure 3.15 Results from transient run T3 compared to ABAQUS solution showing the variation of vertical displacement at the top of the model with time. Also shown is a simulation assuming a constant permeability (dashed line).

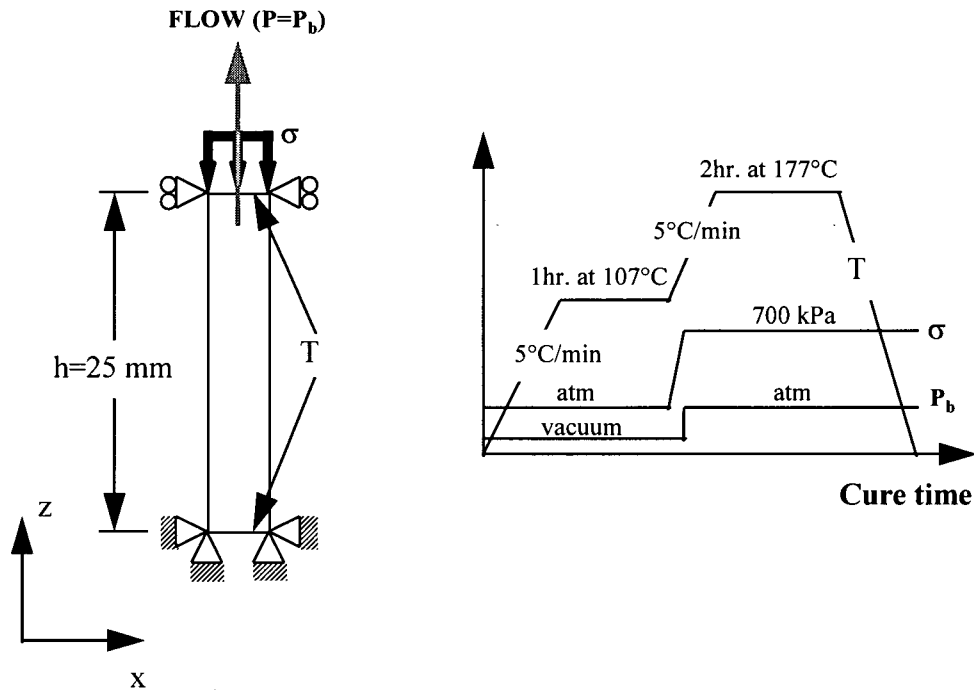


Figure 3.16 Boundary conditions and cure cycle for the composite consolidation runs (T4 and T5).

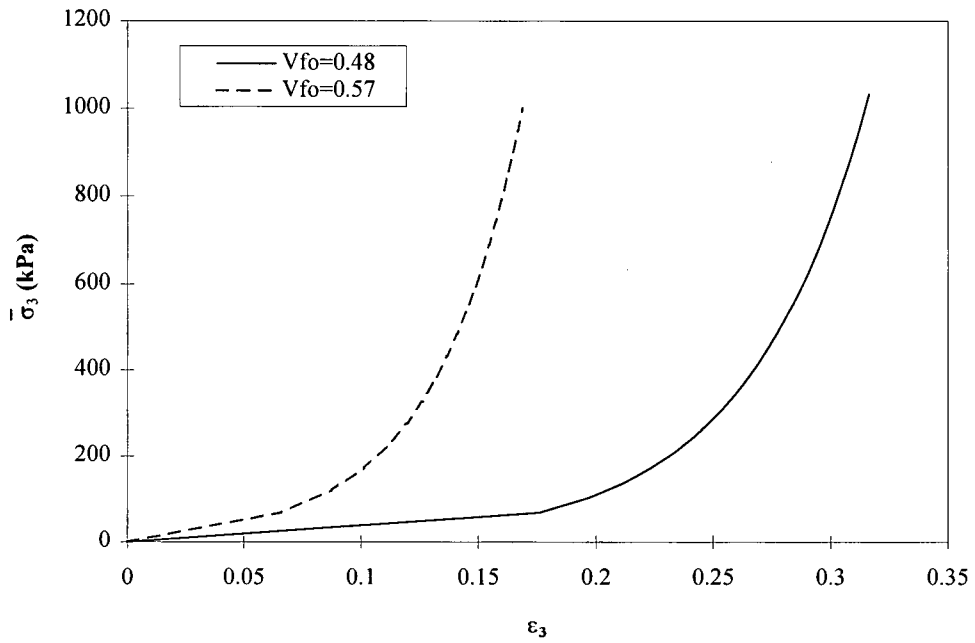


Figure 3.17 Fibre bed compaction curves for the composite consolidation runs ($V_{f0}=0.48$ for T4 and $V_{f0}=0.57$ for T5).

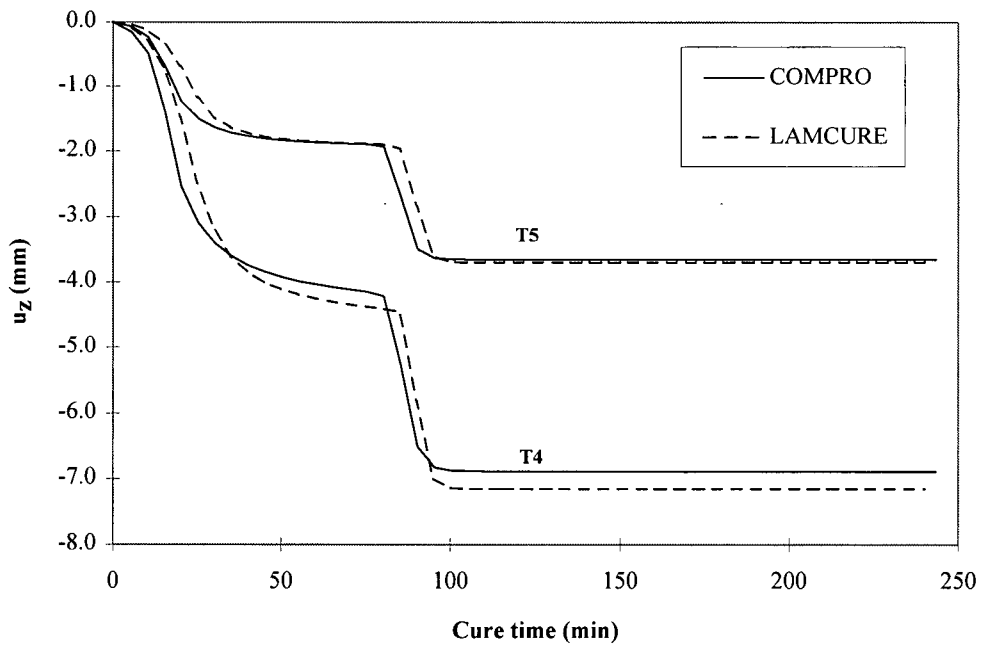


Figure 3.18 Results from transient runs T4 and T5 compared to LAMCURE solution showing the variation of vertical displacement at the top of the model with time.

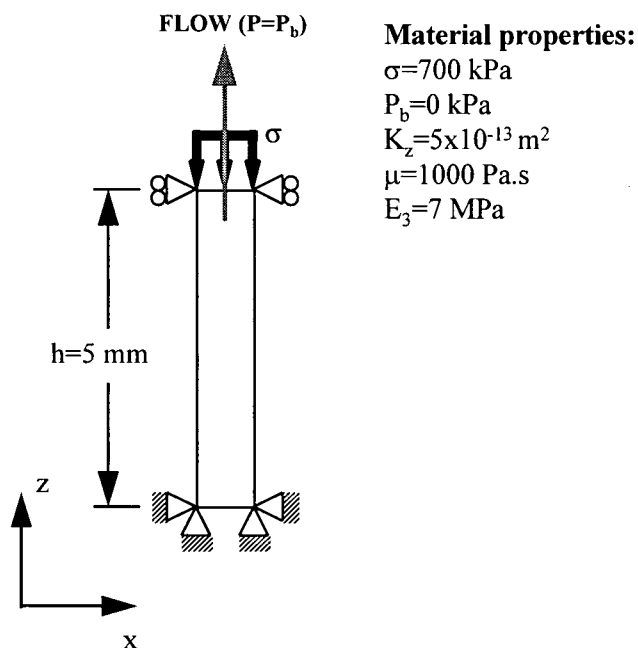


Figure 3.19 Boundary conditions and material property inputs for the study of the effect of the mesh size on the model predictions. For the meshes, the domain is divided in 4 and 40 elements of equal sizes.

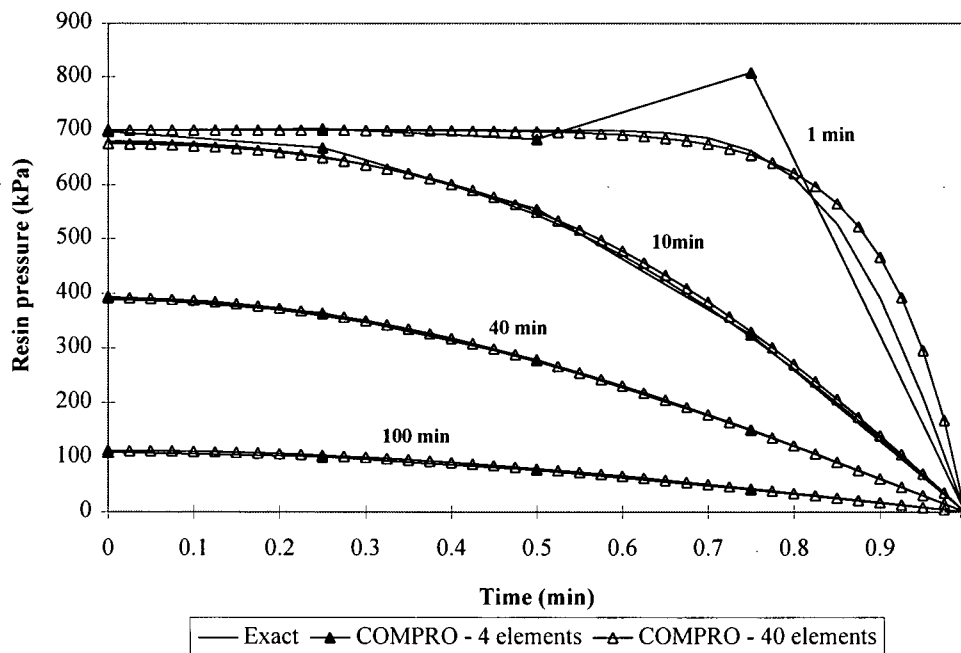


Figure 3.20 Vertical pressure profile evolution with time obtained by COMPRO compared to the exact solution showing the effect of the mesh density.

Chapter 4 Material Properties and Fibre Bed Compaction Curve Characterization

In this chapter, the materials studied in this work are first introduced. In order to use the flow-compaction model presented in Chapter 3, a number of material properties are required. Among them, the fibre bed compaction curve is a critical parameter of the fibre bed constitutive law used in this work (Section 3.2.4). Thus, this chapter focuses on the methodology used to measure and validate the fibre bed compaction curve for the material studied.

4.1 Materials studied

The materials considered for this study are two advanced carbon-epoxy composites: AS4/3501-6 and AS4/8552. Throughout this thesis, the AS4/3501-6 and AS4/8552 systems are referred to as materials A and B respectively. Both materials contain the same fibre: Hercules AS4 high strength carbon fibre. Material A is a very common system containing Hercules 3501-6 amine-cured epoxy resin. Material B is a more recently developed system based on Hercules 8552 which is an epoxy resin modified with a thermoplastic toughener. Table 4.1 presents the thermophysical properties of the fibre and the two resins. General resin curing and rheological information is also presented. The major difference between the two materials related to processing is in their resin viscosity or rheological characteristics. As shown in Table 4.1, the 3501-6 resin has a minimum viscosity which is an order of magnitude lower than 8552. This difference is caused by the addition of the thermoplastic toughener in 8552.

The materials are second generation prepregs defined as no-bleed systems (i.e. no bleeder¹ is required during the bagging process). With the first generation prepregs, excess resin had to be bled out of the composite to compact the laminate to the desired volume fraction. Typically, these prepregs had an initial V_f of 48% and had to be compacted to a final V_f of 60-70%. This operation was difficult to control accurately, leading to variations of V_f in the final part. With improvements in prepegging techniques, prepreg manufacturers are now able to develop prepregs having higher initial V_f . Therefore, the resin flow is more controlled and material processibility is improved. Table 4.2 presents the initial ply thickness and V_f for the prepreg studied. Both materials are supplied as unidirectional tape² of 30 cm width. Material A is thinner and easier to lay-up and conform to a complex shaped tool compared to material B. Using the fibre and resin density in Table 4.1, the initial fibre volume fraction of the prepregs, V_{f0} , was measured according to the ASTM D 3171-76 standard (ASTM Standards, 1994). From Table 4.2, both prepregs have a similar V_{f0} .

One general observation about the prepregs is the difference in tack: the surface of material B is dryer and rougher than material A. This is explained by the fact that AS4/8552 is designed for automated fibre placement machines and is slightly advanced in its degree of cure. This increases the room temperature viscosity so that it would be easier to handle the material during lay-up. Also, a surface inspection of the prepregs showed that material B has more twisted fibres

¹ See Figure 1.2 (a).

² The fibres are all parallel.

compared to material A. Fibre misalignments are likely introduced at the impregnation operation of the prepreg manufacturing process.

The materials chosen for this research represent typical composites used in industry. Very little work has been done on no-bleed systems. Although material A has been studied previously, no work has been reported on high viscosity thermoset matrix composites such as material B. The difference in the rheological behaviour of the two resins was a major factor in selecting the materials, and should significantly affect their flow and compaction behaviour.

The cure kinetics models used for the materials studied are presented in Appendix B, Section B.1 and details on the viscosity models are given in Appendix B, Section B.2. The fibre bed permeability are calculated from the permeability models available from the literature and presented in Appendix B, Section B.3. This information has been relegated to appendices as it involves relatively standard procedures.

4.2 Compaction curve characterization approach

As discussed in Section 2.2.1, the fibre bed elastic response is more dominant at fibre volume fractions greater than 50%. The fibre bed compaction curve (i.e. the variation of $\bar{\sigma}_3$ with ε_3) is a critical material property input for the flow-compaction model (Section 3.2.4). The main focus of this section is to present the experimental procedures that lead to the determination of the compaction curve.

The principal difficulty is to measure the response of the fibre bed alone. Typically, the fibre bed is tested in a dry form (Kim et al., 1991) or is impregnated with silicone oil after dissolving the polymer matrix (Gutowski et al., 1986a). The operation of dissolving the resin of the prepreg

can change the fibre arrangement which could affect the fibre bed compaction behaviour. Using a very low viscosity fluid (e.g. $\mu < 0.1$ Pa.s) or no fluid, and loading the specimen at a very low rate (e.g. < 0.1 mm/min.) minimizes the viscous response effects caused by the fluid flow out of the sample. When a wetting fluid was used, the fluid pressure was measured and subtracted from the total applied stress to obtain the fibre bed effective stress (Gutowski et al., 1986a).

In the present work, the compaction behaviour is determined directly with the prepreg. Since this technique is new, a complete description of the experimental technique is presented. The testing apparatus developed to obtain the compaction curve (Figure 4.1) is similar to the one used by Gutowski et al. (1986a). With this apparatus a unidirectional composite specimen is loaded in the vertical direction (z) which is the main deformation mode of the fibre bed. To obtain a uniaxial testing condition, the deformation in the (y) direction is blocked by the mould walls and the fibres are oriented in the (x) direction. Therefore, the fibre bed deformation in the longitudinal direction is negligible³ compared to the transverse vertical deformation. The composite is heated and resin is allowed to flow longitudinally (x direction) in order to get the fibre bed effective stresses at different values of strains⁴. From the measured displacement (u_z) and applied load (F_z), the compaction curve of the fibre bed is extracted.

Two testing procedures were used in this work: the load-unload method and the load-hold method. The load-unload method was tested first and it was found that this method was not adequate for accurate measurements of the fibre bed compaction curve. For reference, details on

³ The fibres are very stiff in the longitudinal direction.

⁴ The fibre bed strains are related to the resin loss by the composite during the compaction.

the load-unload method are presented in Appendix B, Section B.4. On the other hand, the load-hold method successfully measured the fibre bed compaction curve. Thus the following sections focus only on the load-hold technique.

4.2.1 Load-hold method description

The load-hold method consists of deforming the specimen to different levels where the displacement is held constant until the load measured relaxes to a stable value. Assuming the composite material as a simple viscoelastic system (Figure 4.2), the value of the relaxed load should correspond to the elastic response of the material (i.e. the fibre bed effective stress). By loading the specimen to different displacement levels, the complete fibre bed compaction curve is extracted from the displacements and the relaxed load values at each loading step.

Figure 4.3 presents the procedure used for computing the fibre bed compaction curve in the load-hold method. From the master loading curve (Figure 4.3 (a)), the relaxed load is plotted against the displacement at each holding step (Figure 4.3 (b)). The fibre bed compaction curve is directly obtained from the total load curve. This method was used for material A (specimens 7A01 and 7A02) and material B (specimens 7B01 and 7B02).

4.2.2 Testing procedure

A compaction testing fixture was designed and installed on a servo-hydraulic testing machine (Figure 4.4 (a)). The fixture consists of a top piston that applies the load to the sample, which is constrained laterally (y direction) in a mould (Figure 4.4 (b)). The gap tolerance between the mould wall and the piston was adjusted to provide a sliding fit between the two parts. The

fixture was installed in an environmental chamber where the temperature can be controlled from room temperature to 200°C. Heat was applied to the mould by air convection. The temperature of the mould was monitored by two thermocouples located at the top and lower parts of the fixture. The testing fixtures were machined from solid steel, and thus have a relatively high thermal mass. Therefore, once the target temperature was reached, the fixture temperature remained stable during the test. The load applied to the specimen was measured by the load cell of the testing machine. The displacement of the mould was monitored by the testing machine LVDT that was previously calibrated with a digital micrometer.

The specimens were prepared by laying-up 16 plies of prepreg. The specimens were debulked at room temperature in a vacuum bag. This procedure was done to remove most of the air bubbles between the individual plies. A series of measurements (i.e. sample mass and geometric dimensions) were taken before the test (Figure 4.5). The specimens were wrapped in a thin film of teflon (thickness of ≈ 0.01 mm) to prevent them from sticking to the fixture (Figure 4.6).

The tests were conducted under displacement control. This way, the compaction of the specimen was precisely controlled. The testing conditions, namely the temperature and the loading rate, were selected to minimize the viscosity of the resin and to maximize the duration of the test before the resin started to cure. Using the viscosity data for resins, a testing temperature ranging from 100°C and 140°C and a loading rate of 0.1 mm/min. was chosen.

The general testing procedure is the same for the two methods used:

1. The fixtures are heated to the target temperature
2. The specimen is placed in the mould
3. Time is allowed so that the specimen reaches the target temperature (typically 2 minutes)

4. The test is performed according to the testing method for a maximum duration of 30 minutes
5. The specimen is removed from the mould and allowed to cool down to room temperature
6. The resin that bled out of the specimen is trimmed
7. The specimen is measured (dimensions and mass)
8. The data is analyzed according to the testing method (Section 4.2.1 or Appendix B, Section B.4).

The specimen final strains (ϵ_x and ϵ_y) are determined from the measurements before and after the test. The specimen volumetric strain (ϵ_v) is computed from the resin mass loss during the test.

The following expressions are used to calculate the different specimen strains:

$$\epsilon_x = \frac{L' - L_0}{L_0} \quad \epsilon_y = \frac{W' - W_0}{W_0} \quad \epsilon_v = \frac{1}{\rho_R} \frac{(M_0 - M')}{L_0 W_0 H_0} \quad (4.1)$$

where ρ_R is the resin density. The test conditions and the sample measurements are summarized in Table B.5 of Appendix B.

4.3 Results of compaction curve characterization

The specimen final strains calculated using Equation 4.1 are presented in Table 4.3. In general, ϵ_x and ϵ_y were negligible as expected by the physical constraints of the mould and by the fact that the fibres prevented any motion in the longitudinal direction. Therefore, the volumetric strains measured were caused by the vertical deformation of the specimen (ϵ_z). The measured volumetric strains for material A (samples 7A01 and 7A02) were significantly higher than for material B (samples 7B01 and 7B02). Sample 7B01 was not considered for analysis because it did not exhibit resin flow.

Figure 4.7 shows photographs of two specimens after testing. The resin that percolated out of the specimens can be seen at the edges of the specimens. The resin front was not perfectly uniform, particularly for material A, where the resin flow was concentrated at the mould side walls. The presence of the teflon film might have disturbed the resin flow at the edges of the specimen.

A typical variation of the displacement u_z and the applied load F_z with time for the load-hold compaction test is presented in Figure 4.8. The test which consisted of eight load increments was carried out on material A. As seen in Figure 4.8, the hold times allowed sufficient load relaxation before loading to the next increment. The following observations can be made:

- 1) The load increases rapidly with the imposed displacement on the specimen. During the hold period (i.e. at a constant displacement), the load gradually relaxes to a stable level. This behaviour confirms the viscoelastic nature of the material depicted in Figure 4.2 (a).
- 2) The relaxed load increases after each load step. The increase in load was gradual for steps 1 to 4 and was more noticeable for steps 5 to 8. This confirms that the elastic load-bearing capacity of the specimen increases with increasing deformations. This behaviour supports the assumptions that the fibre bed behaves as a stiffening spring (Section 2.2.1).
- 3) The relaxation time is shorter for steps 5 to 8 compared to steps 1 to 4. This suggests that viscous effects are more important in the early stages of compaction.

As explained in Figure 4.3, the fibre bed elastic response can be constructed from the load-displacement curve. This fibre bed compaction curve is shown by the dashed line in Figure 4.9. The same procedure was repeated for sample 7A02 and the compaction curves obtained were compared with that predicted by Gutowski's model (Equation 2.3) in Figure 4.10. The curves

from the two specimens tested are similar. The experimental curves obtained have a different shape compared to the curve generated from Gutowski's model between strains of 0.16 and 0.22.

Attempts were made to extract the compaction curve for material B. The viscosity of the resin present in material B is an order of magnitude higher compared to the resin of material A. Therefore, viscous effects are expected to be more important for material B. The test was more difficult to conduct for material B. The variation of the imposed displacement and the applied load with time for sample 7B02 is presented in Figure 4.11. Six load increments were applied and the following observations can be made:

- 1) Compared to material A, the load increase for a given displacement increase is higher. This demonstrates that material B is more viscous.
- 2) It is difficult to deform the material at a level where elastic loads are carried by the fibre bed. Very important viscous effects coupled with long relaxation times made the duration of the test too long (above the 30 minutes limit).

Unlike material A, it was impossible to obtain the compaction curve directly from the test data. Instead, the compaction curve for material B was adjusted until the load-displacement curve and the resin mass losses fitted the experimental results from load controlled compaction tests (Section 4.4). A compaction curve from Gutowski's model was used as a starting point for the determination of the final compaction curve for material B that would best fit the experimental data. As seen in Figure 4.12, the points obtained from the compaction test for steps 5 and 6 do not fall on the final compaction curve. A probable cause would be that the load was not completely relaxed at these steps (Figure 4.11).

The fibre bed compaction curves obtained for materials A and B are presented in Figure 4.13. The compaction curve for material B has a lower maximum strain compared to material A. Given their respective initial fibre volume fraction (Table 4.2), the maximum achievable fibre volume fraction of the materials was calculated from their compaction curve. Values of 73% for material A and 65% for material B were obtained. From this information, the following conclusions on the fibre bed characteristics of the two materials can be drawn:

- 1) Although the composites studied contain the same fibre type, this does not guarantee that the fibre bed compaction curves are identical.
- 2) The fibres in material A have better alignment compared to material B. This is consistent with the observation of misaligned fibres on the surface of the material B prepreg.

4.4 Compaction curve validation

The constitutive model validation tests were conducted to verify the validity of the compaction curves obtained from the foregoing tests. The goal of the validation runs was also to verify if the flow-compaction model could predict the compaction behaviour of a laminate in a simple uniaxial loading configuration under different curing conditions. The tests consisted of using the compaction fixture (Figure 4.1) to load a unidirectional specimen at different temperatures. The specimens were loaded in a load controlled mode to simulate an autoclave condition where a prescribed pressure rather than a prescribed deformation is applied to the laminate. Table B.6 in Appendix B presents the test matrix and the sample measurements for the validation runs. The validation procedure consists of a comparison between the measured and predicted load-displacement curves and the resin losses.

4.4.1 Compaction test model

For each specimen tested, a finite element mesh was constructed. An example of the mesh used is shown in Figure 4.14. One half of the specimen was modelled due to the symmetry of the problem. The mesh was divided in two regions: the piston and the specimen. The piston was modelled to reproduce the uniform compaction of the specimen during a compression test. The stiffness and impermeability of the steel piston was achieved by setting the element properties accordingly. The load measured during the real compaction test was applied at the top of the piston as shown in Figure 4.14. The sliding motion of the piston was ensured by vertical sliding displacement conditions. Resin flow out of the laminate was permitted by setting the resin pressure to atmospheric at the right edge of the specimen (Figure 4.14). The temperature was assumed constant and uniform in the piston and at the boundaries of the specimen during the entire simulation. The material properties for the different regions of the model are presented in Figure 4.14. The vertical displacement (u_z) extracted from the simulation corresponds to the value at the node indicated in Figure 4.14. The predicted displacements were uniform along the length of the specimen, as in the actual compression test. The vertical load (F_z) was computed from the applied pressure and the specimen dimensions.

4.4.2 Results and discussion

The specimen final strains calculated using Equation 4.1 are presented in Table 4.4. The in-plane deformations (ϵ_x and ϵ_y) were negligible confirming that the dominant deformation mode of the specimen is in the vertical direction and that the test is essentially uniaxial. As expected, material A lost more resin compared to material B. The effect of temperature on the amount of

flow was more important for material B. A change of temperature from 100°C to 140°C produced an increase in the laminate volumetric strain of 350% for material B compared to only 6% for material A.

Table 4.4 also presents the ratio of the final volumetric strain and the maximum vertical deformation of the specimen. Assuming negligible in-plane deformations, a value of 100% for $\varepsilon_v/\varepsilon_z$ would indicate that the vertical deformation of the sample is entirely due to resin flow. A value less than 100% would suggest that other deformation mechanisms contribute to the total deformation of the specimen. For the samples of material A, the ratio $\varepsilon_v/\varepsilon_z$ was always close to 100%. However, for material B, $\varepsilon_v/\varepsilon_z$ varies from 27% to 77%. Obviously, the main deformation mechanism for material A was flow, but for material B, another deformation mechanism occurred during compaction. The deformation caused by the compaction of entrapped air bubbles from the lay-up is most likely the cause of the additional vertical strains observed, particularly with material B.

Material B was dry (Section 4.1), making the debulking of the plies during the lay-up more difficult compared to material A. The debulking of the specimen after lay-up was done at room temperature (Section 4.2.2). At this temperature, the high resin viscosity dramatically decreases the deformation capacity of the prepreg. For a system such as material B, it would imply that the specimen may contain air bubbles entrapped between the plies before the compaction test. When the sample is heated, the compaction of the voids in the laminate is then possible to complete the debulking of the laminate.

Table 4.5 compares the volumetric strains predicted by the flow-compaction model with the experimental data. The agreement is good for all material A samples. However, for material B, the flow-compaction overestimated the amount of flow except for the 140°C test (sample 5B02). Although the general trend was reproduced with the model (i.e. ε_v increased from 4B02 to 5B02 and decreased from 5B02 to 9B01), the magnitude of the variation did not correspond to the experiments.

4.4.2.1 Temperature effect

In Figures 4.15 and 4.16, the compaction predictions are compared with the experimental results for material A at 100°C and 140°C. In both cases, the agreement between the numerical and the experimental data is very good. The load predicted by the model for the test at 100°C (Figure 4.15) is slightly higher in the early stages of compaction ($u_z < 0.2$ mm). The actual fibre bed compaction curve was added to the graph for reference. As expected, the first part of the compaction, where the fibre bed elastic stiffness is very low, the behaviour is dominated by viscous effects (i.e. the difference between the compaction curve and the load-displacement curve is important). During this phase, the majority of the flow is taking place as indicated by the large displacement change. The final stage of the compaction is controlled by the fibre bed elastic response as the fibre bed stiffness increases dramatically. The displacement change is not important as the fibre bed reaches its maximum compaction deformation. By increasing the temperature, the viscous effects become less important. This is shown by the smaller difference between the compaction curve and the load-displacement curve for the 140°C test (Figure 4.16) compared to the 100°C test (Figure 4.15). The experimental results confirm that as the resin

viscosity decreases, the load-displacement curve of the sample approaches the load-displacement curve of a purely elastic fibre bed. It is clear that the present flow-compaction model adequately describes the compaction behaviour of flow dominated materials such as AS4/3501-6 composites.

In Figures 4.17 and 4.18, the compaction predictions are compared with the experimental results for material B at 100°C and 140°C. As seen in these figures, the load-displacement curve from the simulations were shifted along the displacement axis to fit the experimental results. The initial part of the experimental load-displacement curves of Figures 4.17 and 4.18 more likely corresponded to the compaction of the previously discussed air bubbles (i.e. debulking phase). The present flow-compaction model does not consider the debulking mechanism and we must therefore make a manual correction. As observed for both tests, once the load-displacement curve from the model is shifted in the region of the compaction corresponding to the resin flow regime, the numerical prediction is in relatively good agreement with the experimental results.

Again, an increase in the test temperature decreased the magnitude of the viscous effects. Compared with material A, material B exhibits more important viscous effects as shown by the difference between the load-displacement curve and the compaction curve. For material B, this difference is still important even at 140°C. Finally, as the temperature of the test is increased, the displacement corresponding to the onset of the resin flow regime decreases. At 100°C, this displacement is 0.06 mm compared to 0.04 mm at 140°C. Thus, higher loads and more time are required at 100°C to compact the voids in the specimen before the beginning of resin flow.

4.4.2.2 Complete cure

Figure 4.19 shows the compaction behaviour of the materials studied in typical compaction conditions. The load was increased to a pressure corresponding to typical autoclave pressures and held constant until the resin reached the gel point. To compare the two materials, the stress-strain curves obtained are shown in Figure 4.19. Again, the curve for material B was shifted as explained previously. Very good agreement was obtained for both materials. Thus, the compaction curves shown in Figure 4.13 describe adequately the actual compaction of the materials in typical processing conditions.

4.5 Summary

- The load-hold technique was simple and directly provided a compaction curve for material A, and for this material, the agreement with the validation runs was excellent.
- For material B, a fitting technique was required to finally obtain a compaction curve that would give good agreement with the validation run.
- The following conclusions can be drawn from the compaction experiments:
 1. The initial stage of compaction is dominated by viscous effects. Most of the flow occurs at this stage and the viscosity of the resin can significantly affect the load-displacement response of the material during the compaction. These observations are consistent with previous work from Springer (1982) and Gutowski et al. (1986a).

2. The region corresponding to the final stage of the compaction is mainly controlled by the sharp increase in the fibre bed stiffness. This behaviour confirms the assumptions stated by Gutowski et al. (1986a).
3. Material A exhibits more flow than material B. A lower initial fibre volume fraction combined with better fibre alignment and a lower viscosity resin are the major reasons.
4. For material B, the early stages of compaction correspond to the collapse of air bubbles (i.e. debulking phase) introduced during the lay-up operation.

4.6 Tables

Table 4.1 Typical fibre and resin properties for the materials studied: AS4/3501-6 (material A) and AS4/8552 (material B).

Property	AS4 fibre	3501-6 resin	8552 resin
Density (kg/m^3)	1790	1265	1300
Specific heat (J/kgK)	904	1260	1025
Thermal conductivity (W/mK)	Long. 8.02 Trans. 25	0.167	0.128
Min. viscosity at $2^\circ\text{C}/\text{min.}$ (Pa.s)	-	0.4	3
Gel time at 177°C (min.)	-	9	13

Table 4.2 Prepreg properties for AS4/3501-6 (material A) and AS4/8552 (material B).

Property	AS4/3501-6	AS4/8552
Ply thickness (μm)	155	200
Initial fibre volume fraction	55.81 (0.83)*	57.41 (0.81)*

* standard variations of the fibre volume fraction for three samples are indicated in parentheses.

Table 4.3 Total in-plane strains and volumetric strain measured after the compaction tests.

Sample	ϵ_x	ϵ_y	ϵ_v
7A01	0.00	0.00	-0.18
7A02	0.00	0.01	-0.17
7B01	0.00	-0.01	0.00
7B02	0.00	-0.01	-0.04

Table 4.4 Total in-plane strains, volumetric strain and ratio of volumetric to total vertical deformation measured after the validation compaction tests.

Sample	ϵ_x	ϵ_y	ϵ_v	ϵ_z^*	ϵ_v/ϵ_z (%)
4A01	0.00	-0.02	-0.17	-0.20	86
4B02	0.00	-0.02	-0.02	-0.07	27
5A01	0.00	-0.02	-0.18	-0.20	91
5B02	0.00	-0.01	-0.09	-0.12	77
9A01	0.00	0.00	-0.19	-0.18	103
9B01	0.01	0.00	-0.05	-0.15	33

* ϵ_z correspond to the maximum vertical strain measured during the compaction.

Table 4.5 Comparison between predicted and measured specimen volumetric strains for the validation compaction tests.

Sample	Experiment	COMPRO
4A01	-0.17	-0.19
4B02	-0.02	-0.04
5A01	-0.18	-0.19
5B02	-0.09	-0.09
9A01	-0.19	-0.19
9B01	-0.05	-0.08

4.7 Figures

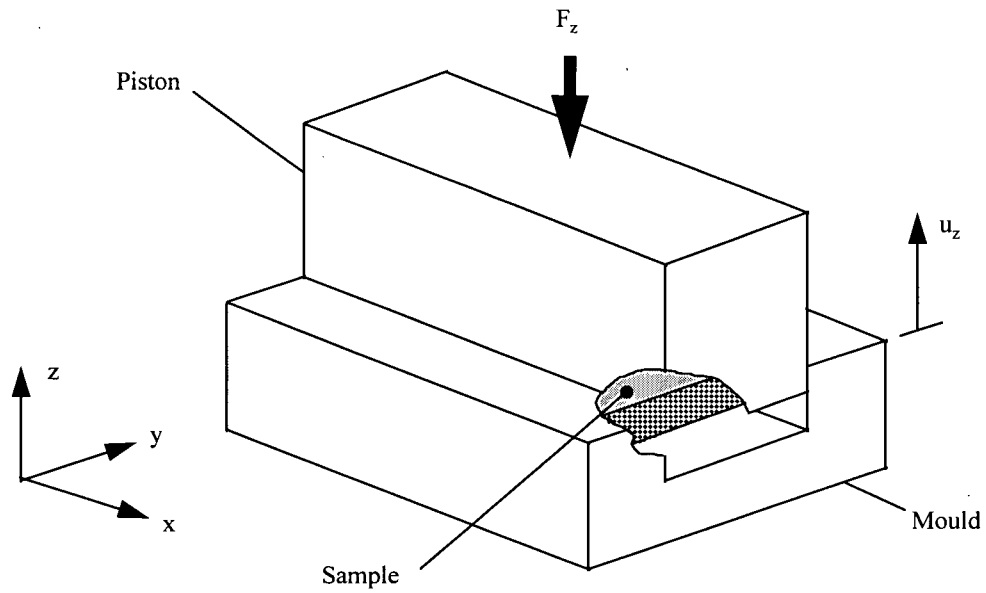


Figure 4.1 Experimental setup for the fibre bed compaction test.

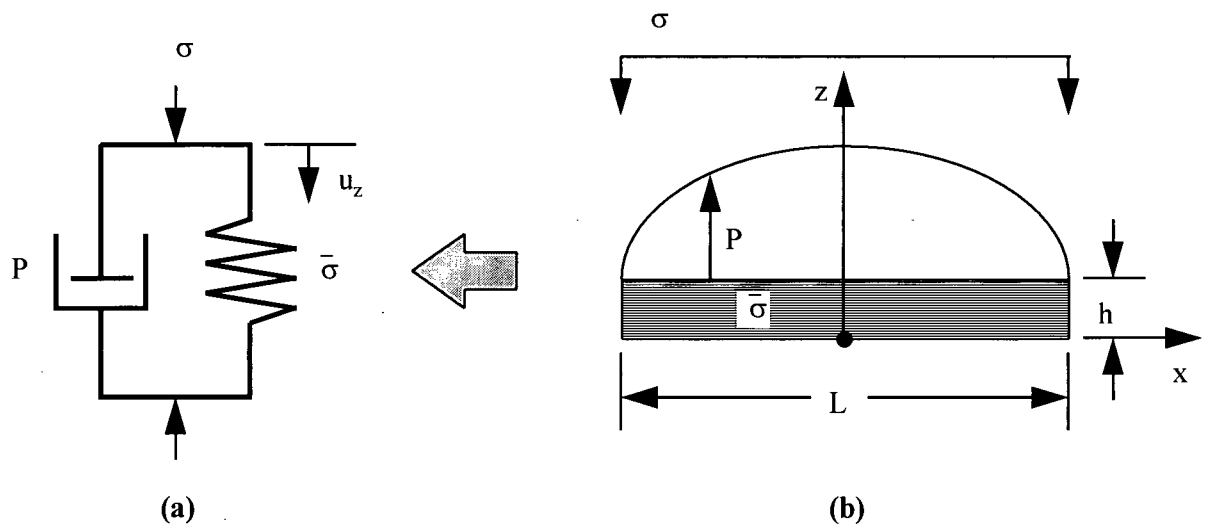


Figure 4.2 Compaction test data analysis, (a) simple viscoelastic model and (b) schematic of compaction specimen loading and dimensions.

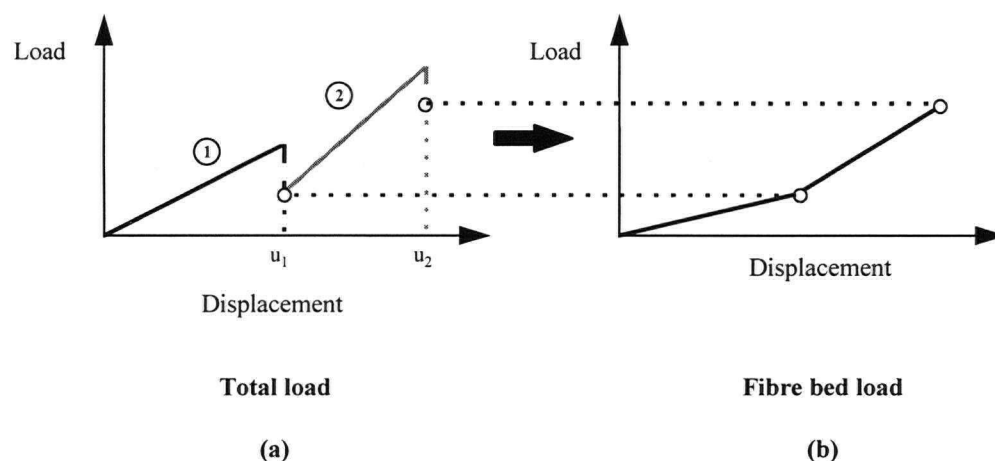


Figure 4.3 Compaction curve computation for the load-hold test method. From the master loading curve (a), the fibre bed load is directly obtained from the load-displacement value when the total load has fully relaxed (b).

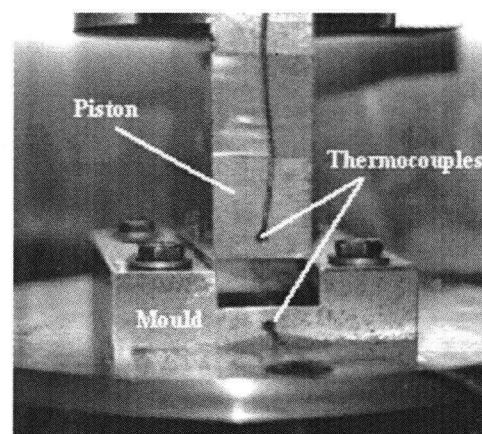
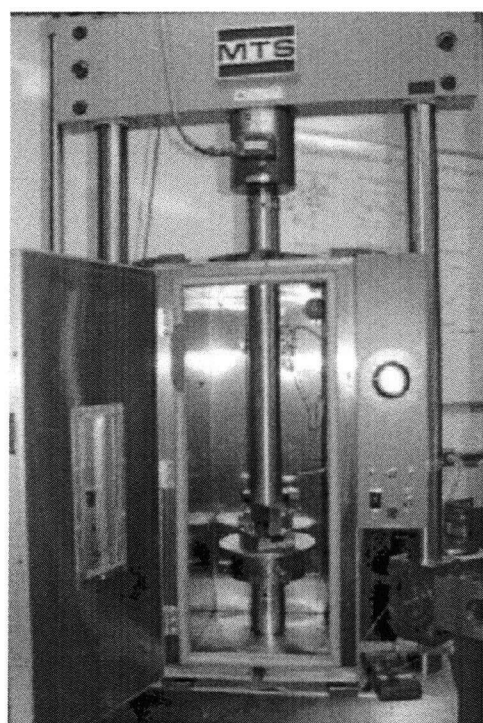


Figure 4.4 Photograph of the compaction test setup, (a) the fixture as installed in the temperature controlled chamber and (b) a close-up view of the compaction fixture.

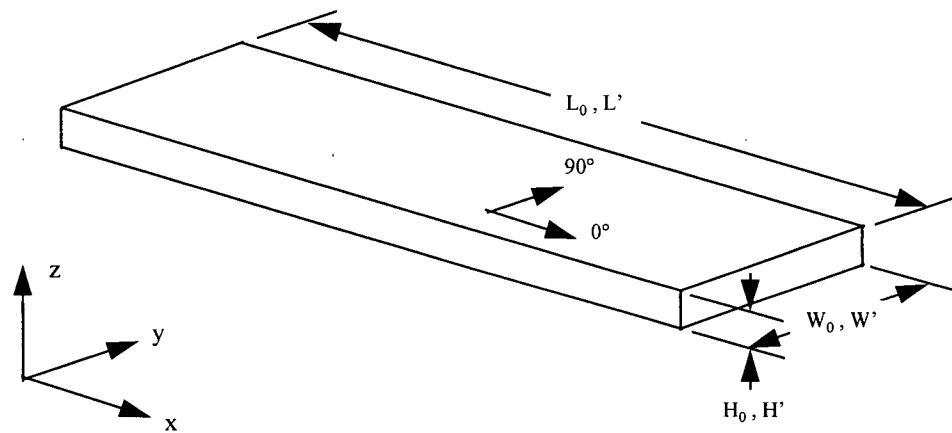


Figure 4.5 Compaction test sample dimensions: before the test (L_0, W_0, H_0) and after the test (L', W', H'). The definition of the fibre orientation direction is also shown.

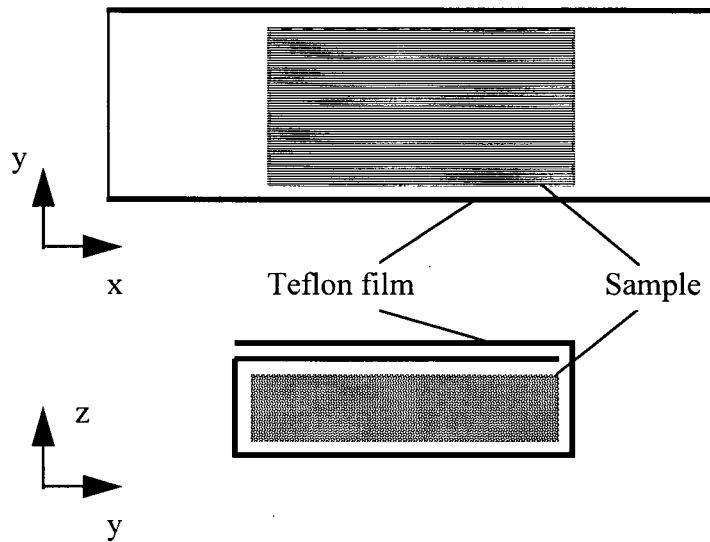


Figure 4.6 Compaction test sample preparation, where the sample is wrapped in a teflon film.

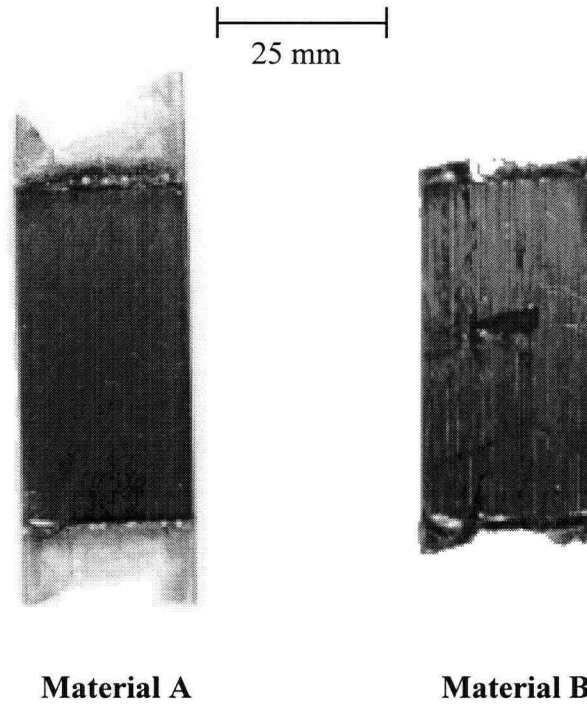


Figure 4.7 Plan view photograph of typical specimens after a compaction test. Resin can be seen at the edges of the specimen.

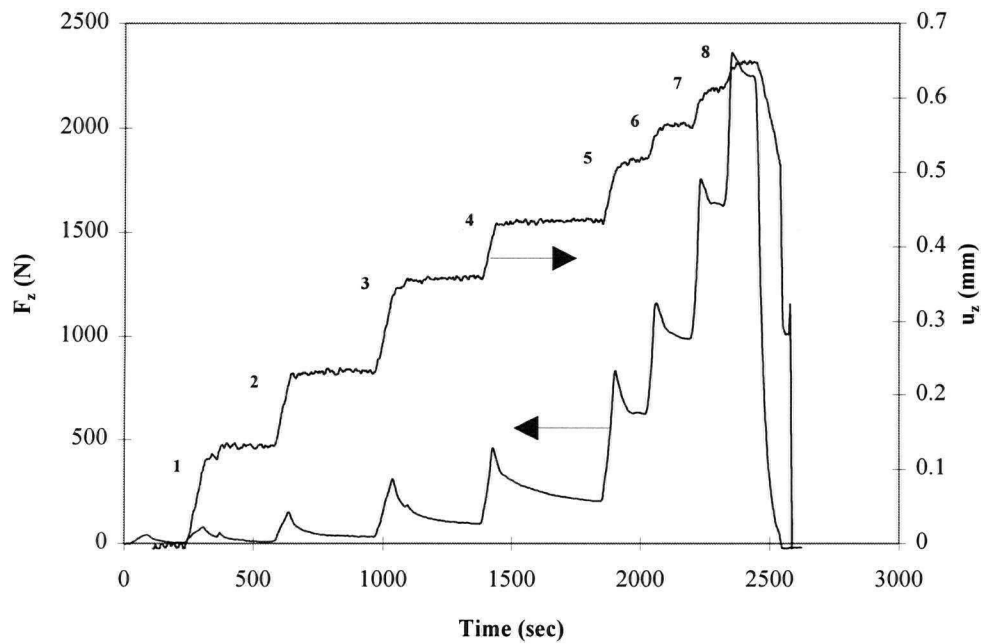


Figure 4.8 Applied load and displacement variation with time for load-hold compaction test (material A, 7A01) showing the load relaxation at the different loading increments (1 to 8).

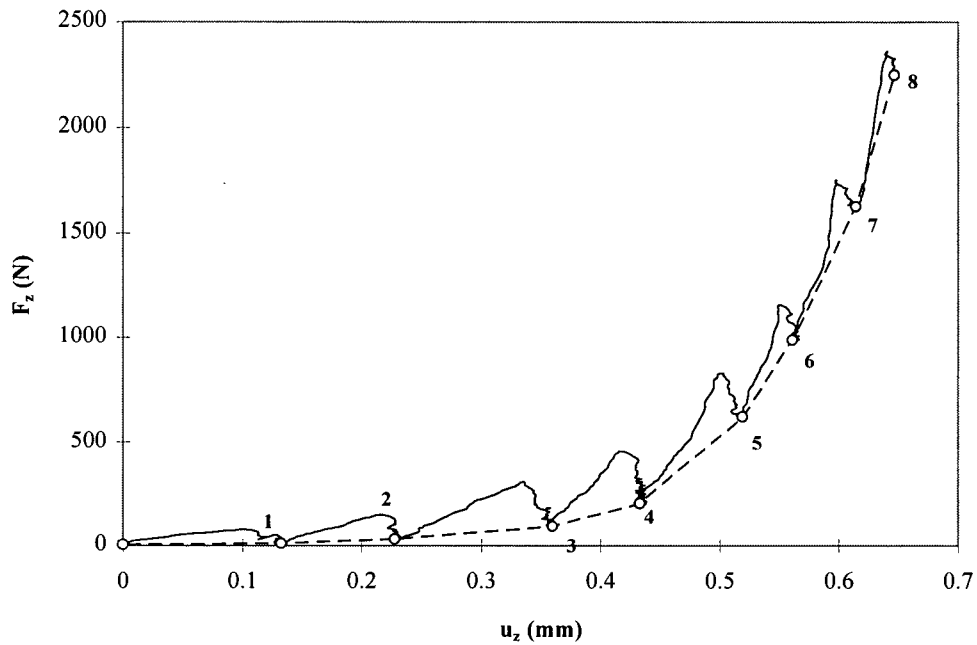


Figure 4.9 Load-displacement curve for the load-hold test method (material A, 7A01) showing the points (1 to 8) extracted to build the fibre bed compaction curve.

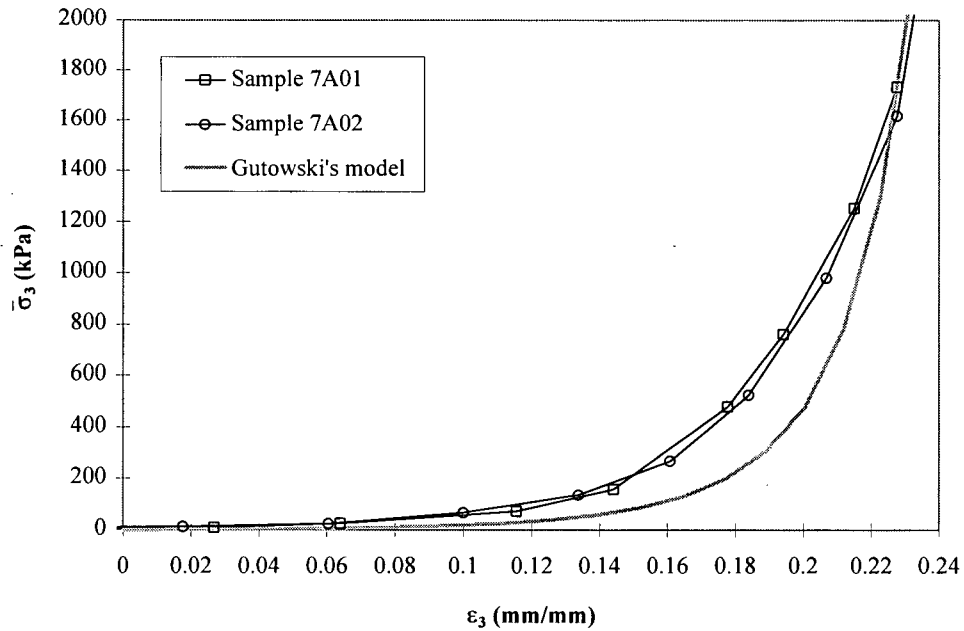


Figure 4.10 Compaction curves obtained for material A obtained with the load-hold method for samples 7A01 and 7A02. A comparison with Gutowski's model (Equation 2.3) is presented with $\beta=350$, $V_a=0.81$, $V_m=0.558$ and $E_f=230$ Gpa.

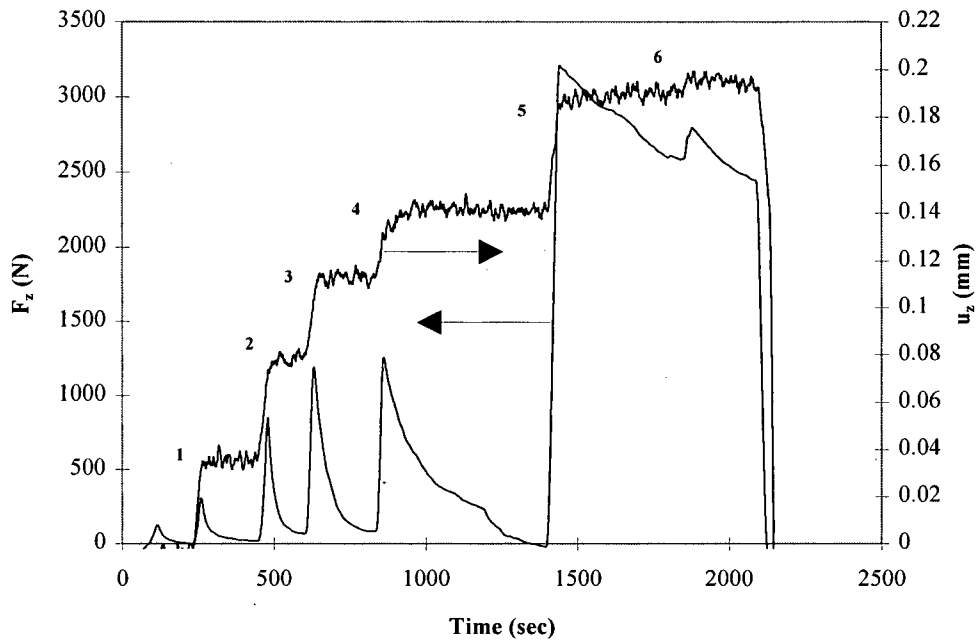


Figure 4.11 Applied load and displacement variation with time for load-hold compaction test (material B, 7B01) showing the load relaxation at the different loading increments (1 to 6).

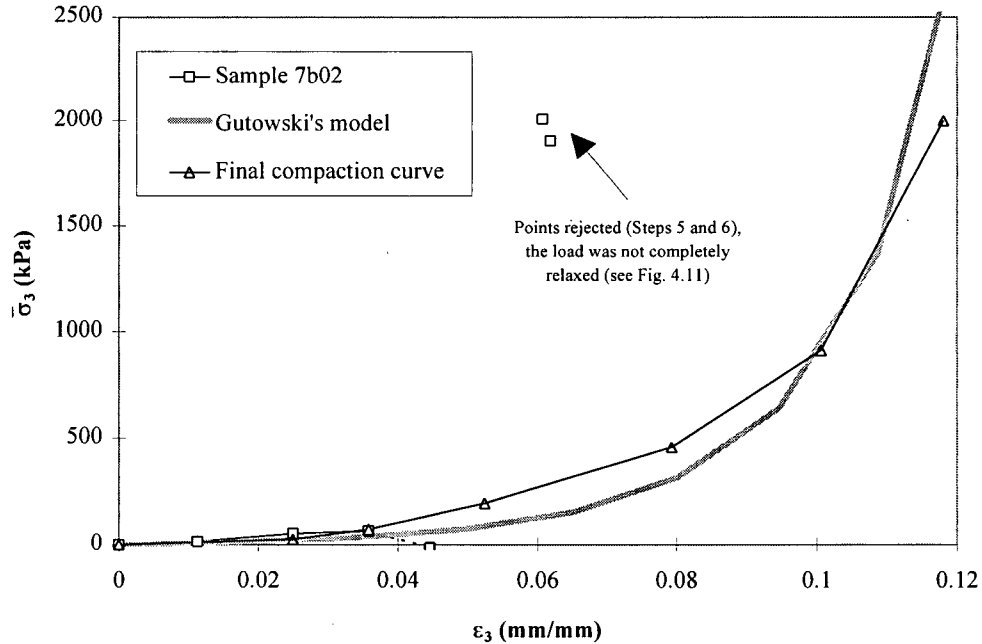


Figure 4.12 Compaction curves obtained for material B. A comparison with Gutowski's model (Equation 2.3) is presented with $\beta=350$, $V_a=0.68$, $V_0=0.574$ and $E_f=230$ GPa. The experimental result for sample 7B02 is shown as a reference.

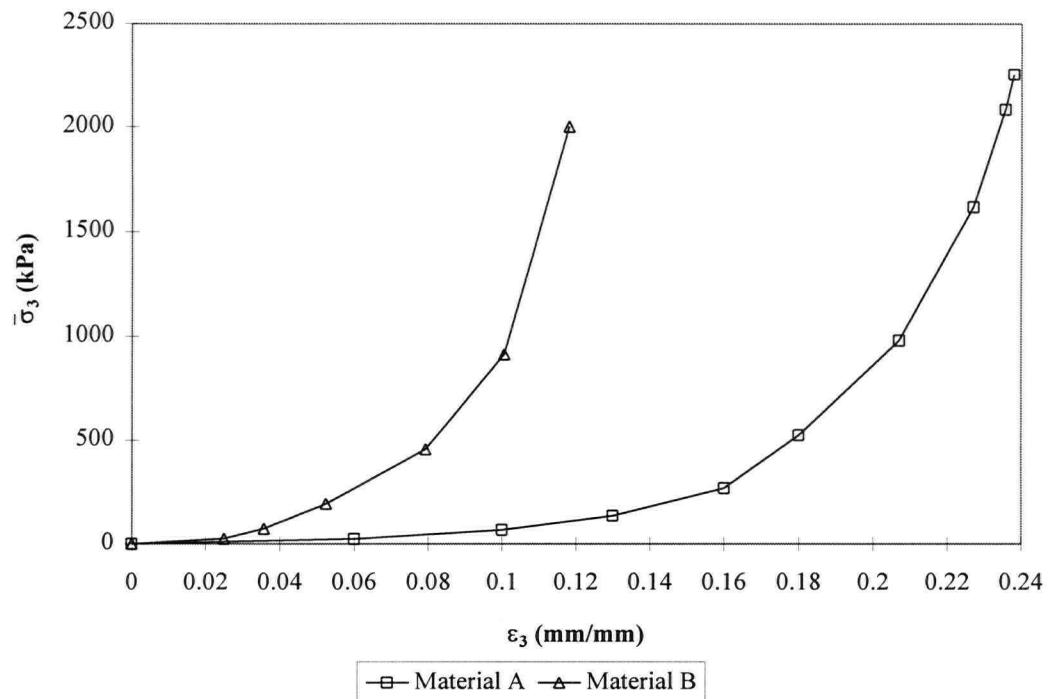


Figure 4.13 Comparison of the compaction curves for the materials studied.

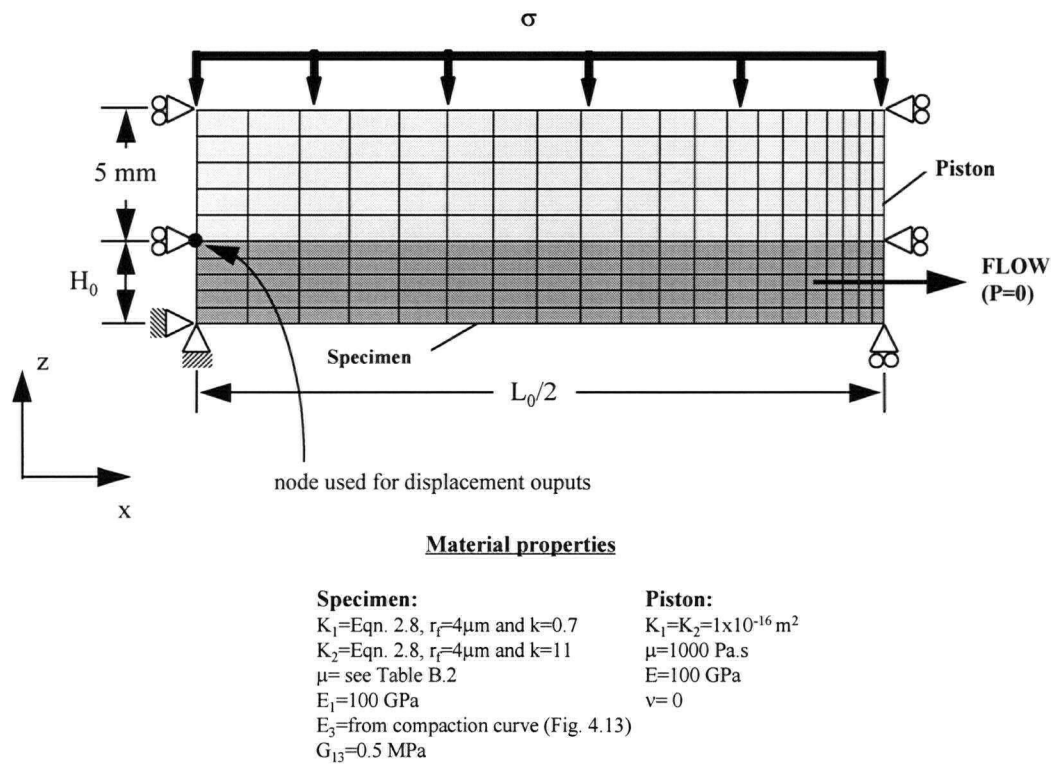


Figure 4.14 Finite element model used for the compaction curve validation runs.

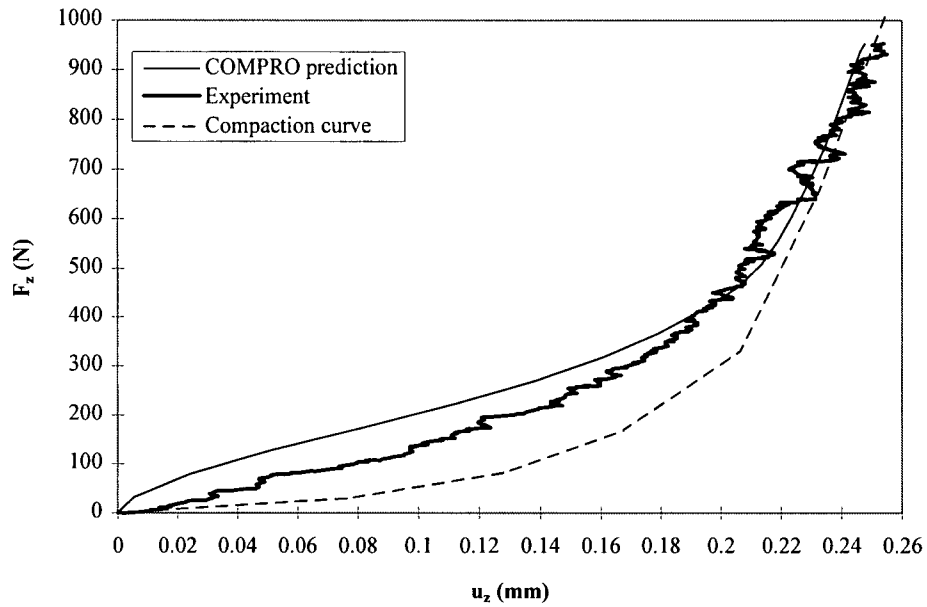


Figure 4.15 Flow-compaction model prediction of the load-displacement behaviour compared with the experimental results of a load controlled compaction test of material A at 100°C (sample 4A01). The fibre bed elastic compaction curve is shown for reference.

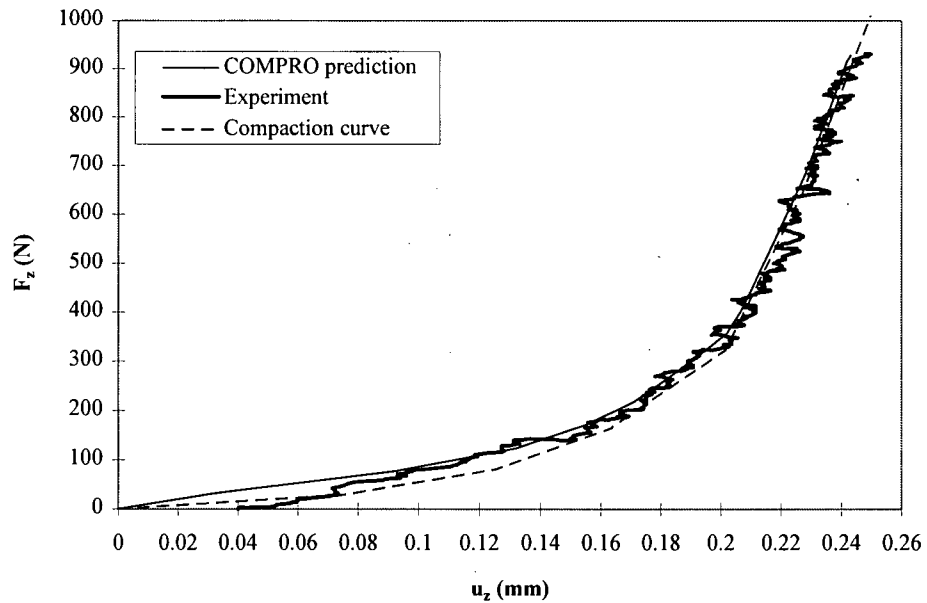


Figure 4.16 Flow-compaction model prediction of the load-displacement behaviour compared with the experimental results of a load controlled compaction test of material A at 140°C (sample 5A01). The fibre bed elastic compaction curve is shown for reference.

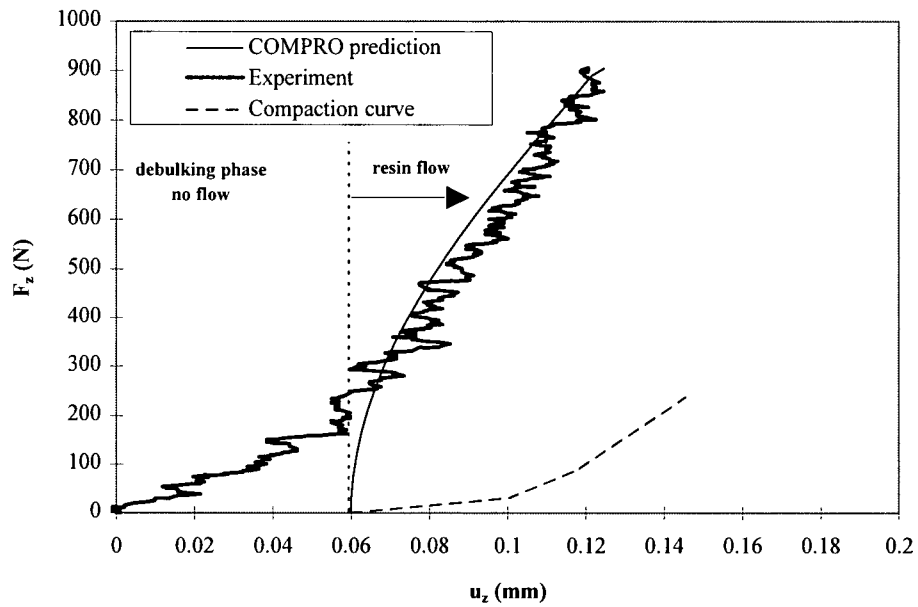


Figure 4.17 Flow-compaction model prediction of the load-displacement behaviour compared with the experimental results of a load controlled compaction test of material B at 100°C (sample 4B02). The fibre bed elastic compaction curve and the onset of resin flow are also shown for reference.

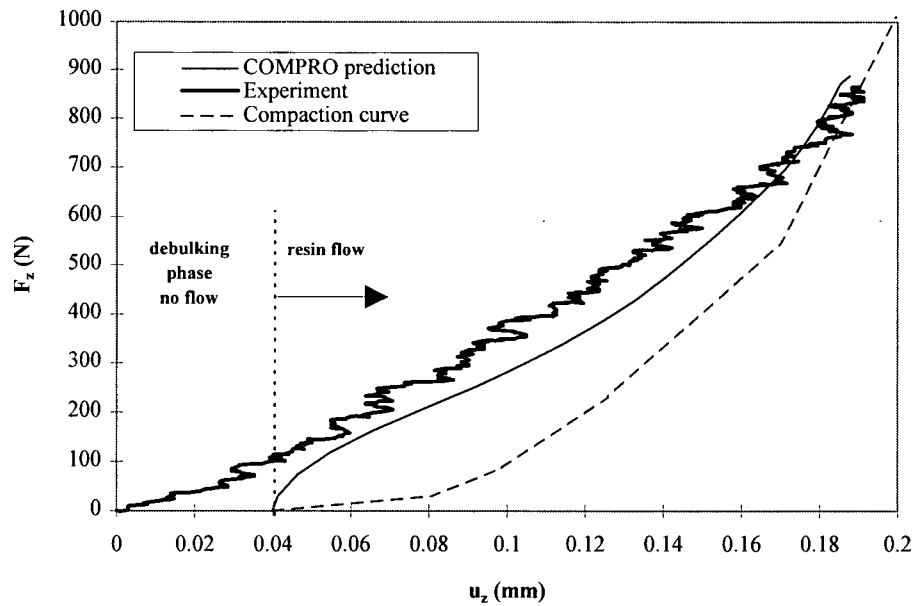


Figure 4.18 Flow-compaction model prediction of the load-displacement behaviour compared with the experimental results of a load controlled compaction test of material B at 140°C (sample 5B02). The fibre bed elastic compaction curve and the onset of resin flow are also shown for reference.

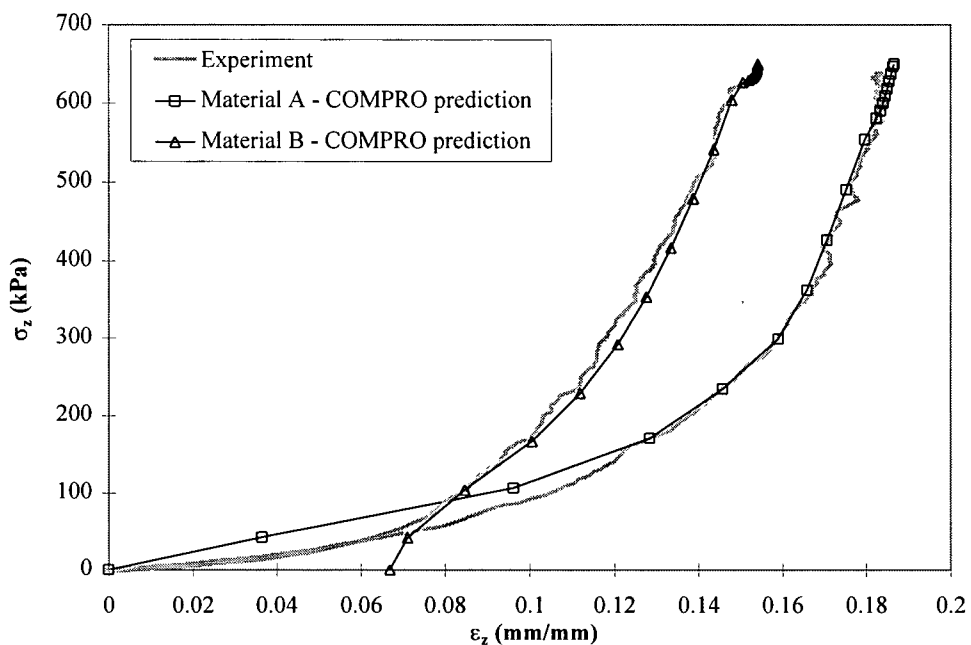


Figure 4.19 Flow-compaction model prediction of the stress-strain behaviour compared with the experimental data of a load controlled compaction test of material A and material B at 170°C (samples 9A01 and 9B01).

Chapter 5 Compaction of Angle Laminates: A Numerical and Experimental Study

This chapter focuses on the study of the compaction behaviour of angle laminates. In the first section, a sensitivity analysis using the flow-compaction model developed in Chapter 3 is presented. The effect of the material properties on the compaction behaviour is studied with this sensitivity analysis. The second section presents results from the experimental study of the compaction of angle laminates having different lay-ups and cured under different processing conditions. The final quality, the resin loss and the thickness profile of the laminates are investigated. Finally, the flow-compaction model is used to simulate the laminates studied, and used to understand the compaction of angle laminates.

5.1 Percolation flow model sensitivity analysis

The variables associated with the flow-compaction model can be classified in three categories: geometry, material properties and boundary conditions. The geometry of the laminate directly affects the resin pressure gradients in the laminate. The material properties consist of the numerous parameters required to characterize the behaviour of the resin and the fibre bed. Finally, the boundary conditions include the bagging methods, the tool interface and the cure cycle used. A sensitivity analysis can have two main goals: investigate the effect of a parameter on the final results given by the model or study the effect of a variation in parameters that are not defined to a satisfactory level of accuracy. Sensitivity analyses on flat panels have been conducted by previous researchers with flow-compaction models (Section 2.3.1), but the study of curved shapes has never been addressed for autoclave processing. Therefore, the present

sensitivity analysis focuses on the effect of material properties on the compaction of an angle laminate. The following properties are investigated:

- resin viscosity
- fibre bed permeability (longitudinal and transverse)
- fibre bed constitutive law (longitudinal, transverse and shear moduli).

The resin viscosity and fibre bed transverse modulus are characterized to a good level of accuracy in Chapter 4. Thus, the effect of small variations of these properties on the compaction of the laminate is studied. For the fibre bed permeability, the range of longitudinal and transverse permeability is obtained from the literature (Appendix B, Section B.3). Finally, the fibre bed longitudinal and shear moduli have never been characterized nor has their effect on the compaction behaviour of angles been addressed in the literature. Thus the sensitivity analysis for these parameters covers a wide range to assess their effect.

5.1.1 Finite element model and runs definition

The laminate geometry for the sensitivity analysis is a 90° angle (L-shaped) laminate with material A (AS4/3501-6) and unidirectional fibres [0°]. The laminate is defined in Figure 5.1. Assuming symmetry and plane strain conditions ($\epsilon_y=0$), the finite element mesh represents one half of the laminate as illustrated in Figure 5.1. The model dimensions and applied boundary conditions are shown in Figure 5.2. The autoclave pressure acts on the top and side surfaces of the laminate. Flow of resin is allowed by imposing a boundary resin pressure equal to the bag pressure. The presence of a rigid tool is simulated by applying a sliding displacement condition at the bottom surface of the laminate. The symmetry boundary condition is satisfied at the right edge of the laminate. For the simulation, the laminate surface temperature is assumed equal to

the air temperature of the autoclave. The cure cycle shown in Figure 5.2 is used for all the simulations. This cure cycle is a standard cure cycle suggested by the manufacturer of material A.

The material properties for the nominal case (SANOM) are given in Figure 5.2 and are taken from the results found in Chapter 4 for material A. The fibre bed longitudinal modulus (E_1) is based on the longitudinal elastic modulus of the fibres¹. The fibre bed shear modulus (G_{13}) is set at 1 MPa for the nominal case. This value is based on the average fibre bed transverse modulus calculated from the compaction curve for material A. In the pressure range of the analysis (i.e. 0-700 kPa), the average transverse modulus is approximately 2 MPa. Thus, the estimated shear modulus is set to one half of the transverse modulus.

Figure 5.3 shows the finite element mesh used for the simulations. A total of 464 elements are used with a constant time step of 1 minute. The flow-compaction module is run when the resin viscosity drops under 1000 Pa.s. Figure 5.3 indicates the location of the nodes where the displacement normal to the surface (u_n) is extracted to obtain the laminate compaction behaviour.

The change of the resin viscosity profile (SAVIS1, SAVIS2 and SAVIS3) was obtained by setting a different resin initial degree of cure (α_0) or by using different values of constants (μ_∞ and κ) for the viscosity relation (Equation B.6). The range of change in the longitudinal fibre bed permeability (SAPER1 and SAPER2) is given in Figure B.8. The range of change in the

¹ The fibre bed longitudinal modulus is estimated at 100 GPa from the rule of mixture (i.e. $E_1=0.5 E$), where $E=200$ GPa (fibre longitudinal modulus), for a fibre volume fraction of approximately 50%.

transverse fibre bed permeability (SAPER3 and SAPER4) is given in Figure B.9. The parameters for the fibre bed constitutive law used are defined in Section 3.2.4 and consist of:

- the fibre bed longitudinal modulus (E_1)
- the fibre bed transverse modulus (E_3) obtained from the fibre bed compaction curve (relation of $\bar{\sigma}_3$ vs ε_3)
- the fibre bed shear modulus (G_{13}).

E_1 and G_{13} are assumed constant but E_3 varies with the transverse strain (ε_3). The fibre bed longitudinal modulus is varied from a high value of 200 GPa (SAE11) to a low value of 1 GPa (SAE12). The fibre bed shear modulus is varied from a high value of 10 MPa (SAG131) to a low value of 10 kPa (SAG132). The change of E_3 is obtained by changing the shape of the compaction curve in the transition region from a low fibre bed modulus to the final very high modulus ($0.1 < \varepsilon_3 < 0.25$). The lower curve (SACUR1) and higher curve (SACUR2) are compared with the nominal case in Figure 5.4.

5.1.2 Results of the sensitivity analysis

Table 5.1 summarizes the results from the sensitivity analysis. The compaction time and the thickness change in the flat section and at the corner of the laminate are shown. As expected, a change of the resin viscosity or the fibre bed permeability affects the full compaction time but not the final thickness of the laminate. On the other hand, the variation of the parameters of the constitutive law influences the final laminate thickness but not the full compaction time. Similar results were obtained by Smith and Poursartip (1993).

Figure 5.5 illustrates this result with the effect of a change in K_2 on the laminate compaction. As reported by Loos and Springer (1983), the processing conditions must be selected such full

compaction of the laminate is achieved before the gel time of the resin. For the case studied (geometry, material and boundary conditions), the laminate compaction time occurs before the gel time of the resin as shown in Figure 5.5. However, under different circumstances, a change of the resin viscosity and the fibre bed permeability could have a significant effect. Some conditions are listed below:

- increase in resin viscosity
- increase in laminate dimensions (thickness for K_2 and length for K_1)
- increase in resin curing rate by changing the cure cycle².

These issues were discussed in detail in previous work (Loos and Springer, 1983; Ciriscioli et al., 1992; Loos and William, 1985; Davé et al., 1987b and Smith and Poursartip, 1993).

The effect of the shape of the compaction curve on the laminate compaction behaviour is presented in Figure 5.6. The laminate final deformation is affected particularly in the flat section of the laminate (points A, B and C). The maximum laminate compaction is reached when the applied load is entirely carried by the fibre bed (i.e. when $\sigma = \bar{\sigma}$, see Figure 2.10). In the present analysis, the maximum applied stress is 700 kPa which corresponds to a fibre bed strain of ≈ 0.19 (Figure 5.4, SANOM). Since full compaction of the laminate is achieved in all cases, for a given applied stress there will be a different compaction strain for a different compaction curve. This is true if the applied stress is in the region of the compaction curve that is varied in the sensitivity analysis (for $0.1 < \varepsilon_3 < 0.25$). The flat section of the laminate is compacted in this range (point A $\varepsilon_3 = 0.19$ and point C, $\varepsilon_3 = 0.16$) but not the corner (point D, $\varepsilon_3 = 0.1$). This explains why the corner

² This would change the gel time of the resin.

deformation is not affected by the change in the compaction curve. These results stress the importance of an accurate measurement of the fibre bed compaction curve. This material property affects directly the accuracy in the prediction of the laminate final thickness.

The effect of the fibre bed longitudinal modulus is presented in Figure 5.7. Increasing E_1 has no effect, while decreasing E_1 increases the thickness change at the corner (Point D). The difference in normal displacement from the corner region (points C and D) compared to the flat section (points A and B) is explained by the presence of the fibres oriented in the $[0^\circ]$ direction. In the curved section of the laminate, normal deformation of the fibre bed gives rise to a tangential deformation component. The presence of very stiff fibres prevents any tangential deformations and consequently any normal or radial deformation. This behaviour is discussed in detail in Section 5.3.6. On the other hand, in the flat section, the geometry allows for normal deformations without any tangential deformation. This explains why the flat section of the laminate can reach the full compaction and why the curved section can not. By reducing E_1 (SAE12), more tangential deformation is possible which increases the ability of the corner to compact.

The effect of the fibre bed shear modulus is presented in Figure 5.8. The variation of G_{13} has a significant effect particularly at the corner (Point D) and in the transition area between the flat and the corner section (Point C). This is best shown in Figure 5.9 where the final deformation of the angle predicted by the various simulations are compared. A low value for G_{13} (SAG132) leads to a laminate with a constant thickness allowing the corner section to reach full compaction. A high value for G_{13} (SAG131) decreases the ability of the corner to compact.

A comparison of the fibre bed shear strain (γ_{13}) distribution for the different simulations is shown in Figure 5.10. For all cases, the shear deformation is uniform and negative in the flat section. There is a high gradient to a maximum positive shear strain at the transition between the flat and curve section for runs SANOM and SAG131. For run SAG132, the shear deformation is in the same direction in the entire laminate. The negative strains in the flat section are caused by the shearing induced by the action of the fibres being pushed away from the corner. The positive shear deformation at the corner (SANOM and SAG131) is caused by the difference in the normal compaction between the flat section and the corner. The maximum strain is at the top surface of the laminate where the thickness difference of the laminate is maximum.

A variation of G_{13} directly influences the magnitude of the shear deformation as shown in Figure 5.10. A decrease of G_{13} (SAG132) increases the ability of the fibre bed to shear as indicated by an increase in the maximum shear deformation compared to the nominal case ($\gamma_{13}=-0.13$ for SAG132 vs $\gamma_{13}=-0.09$ for SANOM), while an increase of G_{13} (SAG131) has the opposite effect ($\gamma_{13}=-0.02$ for SAG131 vs $\gamma_{13}=-0.09$ for SANOM). The actual value of G_{13} is unknown, thus the values for the sensitivity analysis were chosen to highlight the importance of the fibre bed shear behaviour for curved laminates.

5.2 Experimental investigation

This section presents a study of the compaction behaviour of 90° angle laminates under different processing conditions. The results from the experimental tests are compared to the results obtained with the processing model COMPRO in Section 5.3. As discussed in Section 4.1, the parameters studied reflect the major changes in thermoset composite processing methods over

recent years. Therefore, the effect of the following parameters on angle laminate compaction behaviour is investigated:

- materials: A and B
- bagging condition: no-bleed and bleed
- tool geometry: convex tool and concave tool
- lay-up: $[90^\circ]_n$, $[0^\circ]_n$ and $[90^\circ, 0^\circ, +45^\circ, -45^\circ]_n$

where n is the number of layers or group of layers. Table 5.2 presents the test matrix and the sample definition used for the experimental investigation. The sample geometry is the same in all cases. The unidirectional laminates $[90^\circ]_n$ and $[0^\circ]_n$ are designated as $[90]$ and $[0]$ respectively, while the quasi-isotropic laminate $[90^\circ, 0^\circ, +45^\circ, -45^\circ]_n$ is designated as $[Q]$.

The combination of the different parameters were chosen to obtain a wide range of processing conditions and to induce as much variation as possible in the final results. It is important to emphasize that the severity of the problems and defects that are described in subsequent sections do not occur under normal manufacturing conditions.

5.2.1 Testing procedure

The sample dimensions are presented in Figure 5.11 (a). The total number of plies used is adjusted so that the initial thickness of the samples is similar for the two materials³. Thus, the samples with material A and B have respectively 32 and 24 plies. The angles were moulded on two types of tool: a convex and a concave tool. The tool dimensions are shown in

³ Individual plies of material A are thinner than material B.

Figure 5.11 (b). The convex tool is made from a solid block of aluminium and the concave tool is made of an 'L' shape aluminium extrusion. The tools were coated with a release agent that allows for easy removal of the part after processing. Up to six samples were laid-up on one tool. The laminates were prepared by cutting individual ply of prepreg and stacking the prepreg directly on the tool according to the appropriate orientation. The laminates were debulked at room temperature in a vacuum bag after every group of four plies was laid-up.

Once the lay-up was completed, dams were placed around the laminate to prevent any resin flow in the in-plane directions as shown in Figure 5.12. The side dams were made of silicone rubber and the edge dams were made with sealant tape. When bleed conditions were desired, a bleeder cloth was placed on top of the laminate to absorb the squeezed resin. Otherwise, for no-bleed conditions, a teflon impermeable film was placed on top of the laminate to prevent resin flow out of the laminate. Figure 5.12 shows a typical bagging configuration with the different bagging elements mentioned above. A convex and concave tool were enclosed in a single vacuum bag as shown in Figure 5.13. A layer of breather cloth was placed around the tools and the bag was connected to the autoclave vacuum through a single vacuum connector.

The curing was conducted in an experimental autoclave having a chamber diameter of 0.90 m and a length of 2.13 m (Figure 5.14). The autoclave temperature and pressure were controlled by a computer that also acquired the signals from the thermocouples and the pressure sensors connected to the bag or placed inside the autoclave. Figure 5.15 shows the location of the different sensors used to monitor the temperature and the pressure during the cure. A total of

fifteen thermocouples⁴ were used to monitor the temperature. The temperature in the autoclave was controlled based on thermocouples placed at different locations in the bag and the part. The controlling system uses a lead-lag controller algorithm. With this approach, the cure cycle is defined by a series of segments consisting of a ramp or a hold. For the ramp, the heating rate and a target temperature or pressure are specified. When the lagging⁵ thermocouple reaches a certain criteria, the cure cycle continues to the next segment. This method differs from a cure cycle where the target values are given as a function of the cure cycle time. With a lead-lag controller, the timing of the events depend on the temperature history of the part or the actual pressure in the autoclave. Figure 5.16 shows the definition of the segments for the cure cycle chosen in this experiment. This cure cycle is a typical processing cycle for the material used.

At the end of the cure, the specimens were removed from the tool and trimmed as indicated in Figure 5.17. The trimming consisted of removing approximately 12.7 mm of material around all edges of the sample. The trimmed specimens were cut in two to allow observation of the cross-section.

5.2.2 Measurements and data analysis

A series of measurements were taken on the samples before and after cure. The measurements consisted of mass and thickness profiles of the laminate. These parameters are directly compared

⁴ 9 part thermocouples, 4 tool thermocouples and 2 bag thermocouples.

⁵ Defined as the thermocouple having the minimum temperature.

with the results from the numerical simulations in Section 5.3. From these mass measurements, the resin mass loss ratio was computed as follows:

$$M_{\text{rloss}} = -\left(\frac{m_c - m_{c0}}{m_{c0}}\right) \quad (5.1)$$

where m_c is the laminate mass after cure and m_{c0} is the laminate mass before cure. The laminate thickness was measured with calipers at different stations defined in Figure 5.18. From the thickness measurements, the laminate deformation is calculated. The laminate normal strains at the measured stations is defined as follows:

$$\varepsilon_{ni} = \frac{H_i - H_{0i}}{H_{0i}} \quad (5.2)$$

where i is the station number (Figure 5.18) and H_i is the thickness after cure and H_{0i} is the thickness before cure. Assuming that the in-plane deformations (ε_x and ε_y) are small compared to the out of plane deformations (ε_{ni}), the laminate percolation strain is defined as follows:

$$\varepsilon_{\text{percolation}} = \frac{M_{\text{rloss}}}{\rho_R} (V_{f0}\rho_F + (1 - V_{f0})\rho_R) \quad (5.3)$$

where ρ_R is the resin density, ρ_F is the fibre density and V_{f0} the initial fibre volume fraction of the composite. Assuming that the normal deformations are uniform in the flat section of the laminate, the total laminate deformation is defined as:

$$\varepsilon_{\text{total}} = \frac{\sum_i \varepsilon_{ni}}{4} \quad i = 1,2,4,5 \quad (5.4)$$

where ε_{ni} is the deformation measured at the stations corresponding to the flat section of the angle (Figure 5.18). ε_{total} is a measure of the total laminate compaction while $\varepsilon_{percolation}$ is a measure of the compaction caused by resin percolation flow.

5.2.3 Temperature profiles

The temperature profiles in the part and the tool measured during the cure are presented in Figure 5.19. A significant lag between the air temperature in the autoclave and the tool and laminate temperatures is observed particularly during the heating and cooling phases of the cure cycle. This behaviour is attributed to the tool thermal mass. During the hold periods, the temperature is uniform in the tool and the part. No exotherm was observed which is expected given the small thickness of the laminate. The pressure of the autoclave and the bag pressure were constant during the entire cure cycle.

5.2.4 Defects and problems induced by the experimental method

The external defects of the laminate are localized at the corners and are classified in three main categories defined in Figure 5.20. Defect I is a blunt internal wrinkle, defect II is a sharp internal wrinkle, while defect III is an external wrinkle. Table 5.3 lists the defects found in all the specimens tested. From this table, the following statements can be made:

- 1) the laminates moulded with the concave tool contain more defects compared to the convex tool
- 2) the laminates with material A have more defects compared to material B
- 3) the laminates in bleed conditions have more defects compared to no-bleed conditions
- 4) the $[90]$ lay-up have more defects compared to the $[0]$ and $[Q]$ lay-ups.

The defects observed are located on the side of the laminate exposed to the bag. A number of soft material layers are present between the laminate surface and the bag. These layers (i.e. teflon film, bleeder, breather) can form wrinkles due to the curvature of the mould surface. If the layers cannot slip during the application of the pressure, the wrinkle is not eliminated and can affect the surface of the laminate exposed to the bag. The wrinkles were typically more difficult to eliminate with a concave tool. A material having a low resin viscosity such as material A is more susceptible to being affected by a wrinkle in the bag. The presence of the additional layers of the bleeder (i.e. used in the bleed condition) increases the possibility of forming wrinkles and makes the operation of removing the wrinkle more difficult. Finally, the low transverse viscosity of the fibres offers no resistance to the local pressure caused by a wrinkle. Therefore, the [90] lay-up is more susceptible to wrinkle formation and this problem is discussed in Section 5.3.8.

Table 5.4 presents the level of voids found in the laminates. The void level is graded from no voids (0) to many voids (3). The following trends are found from the analysis of Table 5.4:

- 1) more voids are present for the bleed condition compared to the no-bleed condition
- 2) more voids are present for material A compared to material B
- 3) more voids are present at the corner compared to the flat section of the laminate

The void formation in composite materials is attributed to the following factors: entrapped air during the lay-up, moisture in the material and volatiles released during the cure (Loos and Springer, 1983). The resin pressure in the laminate can affect the formation of voids during cure (Loos and Springer, 1983; Davé et al., 1987a). For example, if the local vapor pressure of the void is greater than the resin pressure, a void is created. Thus, the presence of voids indicates a

low resin pressure area in the laminate. In bleed conditions, the resin flows out of the laminate. Thus it is expected from the compaction theory that the resin pressure will drop to zero if the laminate reaches full compaction (Figure 2.10, Full compaction). On the other hand, for a no-bleed condition, the resin is prevented from flowing out of the laminate. Thus, it is expected that the resin pressure is approximately equal to the applied pressure (Figure 2.10, Pressurization). Therefore, this would explain the presence of numerous voids in the bleed conditions compared to the no-bleed conditions. Since material A has a lower resin viscosity, the chances of reaching full compaction are higher compared to material B. This would explain the observed higher void level in material A compared to material B. Finally, the larger number of voids in the corner section compared to the flat section is an indication that the pressure at the corner could be lower and this issue is discussed in Section 5.3.5.

As shown in Figure 5.21, the presence of the dams around the laminates did not prevent the resin from flowing in the in-plane direction. Local resin flow is observed at the corner of some samples particularly with the concave tool. For the concave tool, the silicone rubber did not perfectly seal the tool surface and a small gap where the resin could flow was created. Error in the measured resin loss is expected from these observations and should be considered in the analysis of the results. The results for all parameters calculated from the measured information are presented in Appendix C.

5.2.5 Resin mass loss

At the end of the cure, significant resin flow in the bleeder was noticed in the bag containing the material A laminates as seen in Figure 5.22. The resin flow out of the laminate was so

significant that the resin even bled in the breather. On the other hand, no visible resin flow was observed for the bag containing the material B laminates. After removing the bag, the bleeders for material A were fully saturated with resin. The bleeders for material B were only partially saturated with resin. Table 5.5 presents the resin mass loss ratio calculated using Equation 5.1. The results clearly show the larger amount of resin flow obtained for material A compared to material B. The orientation of the laminate did not affect significantly the amount of resin flow. This is believable since the flow is mainly occurring in the out-of-plane direction. The permeability in this direction is independent of the fibre orientation which affects only the in-plane permeability of the fibre bed. Similar results were obtained by Loos and William (1985) with the compaction of flat laminates.

5.2.6 Thickness profiles

The thicknesses measured at the stations defined in Figure 5.18 before and after cure are presented in Figures 5.23 to 5.26. The thickness of the laminates before cure is indicated by the location of the error bar horizontal marker. The initial thickness profile results from the lay-up and the debulking operations described in Section 5.2.1. The following statements about the initial thickness of the laminate can be made from the results presented:

Convex tool (Figures 5.23 and 5.24)

- 1) for material A (Figure 5.23), the thickness is fairly uniform except for the [90] where the laminate is thinner at the corner
- 2) for material B (Figure 5.24), the laminate is thicker at the corner in most cases.

Concave tool (Figures 5.25 and 5.26)

- 1) for material A (Figure 5.25), the thickness is uniform

- 2) for material B (Figure 5.26), the thickness is uniform except for the [0] where the laminate is thicker at the corner.

In general, the initial thickness of the laminates with material B is less uniform. Material B is more difficult to conform to the corner of the tool. The prepreg for material B is thicker than material A (Table 4.2) which makes it more difficult to bend in the corner. Furthermore, the room temperature resin viscosity for material B is higher than material A, which decreases the ability of the material to deform at the corner. The debulking during the lay-up process was very effective for material A. However, this operation was not capable of compacting the layers of prepreg at the corner for material B. An indication of the better formability at room temperature of material A is the corner thinning observed for the [90] on the convex tool. In this case, the local pressure at the corner is sufficient to deform the material locally. This behaviour was not observed with material B.

The presence of defects at the corner sometime makes the thickness measurements after cure difficult. When a defect is present at the corner, the thickness measurement is taken adjacent to the defect. The presence of a defect at the corner is indicated in Figures 5.23 to 5.26 by a symbol (*) for a minor defect and (***) for a major defect. The following statements for the final thickness of the laminate can be made from the results presented:

Convex tool (Figures 5.23 and 5.24)

- 1) for both materials, the [90] are thinner at the corner
- 2) for both materials, the [0] are thicker at the corner in a bleed condition

Concave tool (Figures 5.25 and 5.26)

- 1) for both materials, the [90] are thicker at the corner

The thickness in the flat section (STN1,2,4 and 5) is in most cases uniform. Thus, the thickness gradient is localized at the corner of the laminate. Figure 5.27 shows the complete thickness profile for representative samples with and without thickness variation. On the left side of Figure 5.27, samples 5AM3 and 5CF3 have a uniform thickness. On the right side of Figure 5.27, samples with corner thinning (5BM7) and corner thickening (5DF7) are presented. This behaviour at the corner of angle laminates was described by Ó Brádaigh (1994) for thermoformed thermoplastic matrix laminates and was attributed to the transverse flow of the material. A driving force is present at the corner that causes the laminate local thickness change. This force acts differently for the convex and the concave tool as corner thinning and thickening are associated with the convex and concave tool respectively (Section 5.3.6).

The ply orientation greatly affects the deformation behaviour at the corner. The composite transverse viscosity (Section 2.3.2.1) is very low. Thus, for the [90] laminates, the material can shear, creating the thickness gradient observed at the corner. For most of the [0] and [Q] laminates, the presence of very stiff fibres prevents the local deformation of the laminate.

The presence of defects also influences the thickness profile of the laminate. Figure 5.28 shows micrographs illustrating the defects found at the corner of the laminates. The presence of a wrinkle in the bag contributes to the higher thickness at the corner measured for the specimens shown in Figure 5.28 (a) and (b). Bag bridging at the corner explains the presence of the resin at the surface exposed to the bag for the sample shown in Figure 5.28 (c). At this point, the bag bridges creating a small gap where resin can be seen to have accumulated by percolation and

increased the local thickness of the laminate. The bridging of the bag occurs typically with concave tools when the plastic film used for the bag cannot conform to the small radius of curvature of the tool. The opposite of bag bridging would be bag indentation shown in Figure 5.33 (d). In this case, the bag wedged into the laminate inducing a bulge of the material on either sides. The presence of $[90^\circ]$ layers in the lay-up for sample 5DF9 (i.e. $[Q]$ lay-up) allowed the local deformation of the laminate. Similar behaviour was reported by Ó Brádaigh (1994) where corner thickening and thinning for thermo-formed thermoplastic matrix cross-ply laminates (i.e. $[0^\circ/90^\circ]_n$) was entirely attributed to the deformation of the $[90^\circ]$ plies.

5.2.7 Strains

The change in the laminate thickness is investigated in this section. In Figures 5.29 to 5.32, the normal strains (ϵ_{ni}) measured at the different stations are presented. On the same graphs, the total strain (ϵ_{total}) and percolation strain ($\epsilon_{percolation}$) are plotted. The total strain can be expressed as follows:

$$\epsilon_{total} = \epsilon_{percolation} + \epsilon_{shear} + \epsilon_{debulking} + \epsilon_{other} \quad (5.5)$$

where ϵ_{shear} is the strain caused by shear flow and $\epsilon_{debulking}$ is the strain caused by the compaction of the voids present in the laminate before cure. Other strains⁶ can also contribute to the thickness change and they are included in ϵ_{other} . From Equation 5.5, a difference between ϵ_{total} and $\epsilon_{percolation}$ is attributed to the other deformation mechanisms. The following statements for the laminate strains can be made from the results presented:

⁶ E.g. strains caused by resin cure shrinkage.

Convex and concave tools (Figures 5.29 to 5.32)

- 1) for material A, $\epsilon_{\text{percolation}} \approx \epsilon_{\text{total}}$
- 2) for material B, $\epsilon_{\text{percolation}} < \epsilon_{\text{total}}$
- 3) bleed conditions increased the magnitude of the strains, particularly with material A

Convex tool (Figures 5.29 and 5.30)

- 1) high thinning strains at the corner occur for material B [90] laminates

Concave tool (Figures 5.31 and 5.32)

- 1) high thickening strains at the corner occur for both materials [90] laminates

The results indicate that for material A, the laminate normal strains are primarily caused by resin flow out of the laminate. This is not the case for material B where the difference between ϵ_{total} and $\epsilon_{\text{percolation}}$ is attributed partially to $\epsilon_{\text{debulking}}$. This result is consistent with the compaction tests on simple laminates presented in Chapter 4, Section 4.4.

The magnitude of the strains in the flat section depends on whether it is a bleed condition. As expected, material A is more sensitive than material B to the change in the bagging condition. This is explained by the low viscosity of the resin in material A. The magnitude of the strains at the corner is more a function of the ply orientation and the presence of defects, while the sign of the strains at the corner depends of the type of tool used.

The high deformation measured at the corner for the [90] laminates is principally caused by the intraply shear flow of the composite. The percolation flow mechanism cannot alone cause the observed strains. The magnitude of the predicted compaction strains at the corner caused by

resin percolation are typically 0.05 (Section 5.3.2). The maximum measured strains at the corner for this material is 0.20. Thus, the difference must be caused by the shear flow of the material⁷.

5.2.8 Discussion

From the result of these experiments, the best combination to obtain a good angle laminate is to use a convex tool with material B and a quasi-isotropic lay-up in a no-bleed condition. This combination is logical considering that the problems encountered (i.e. resin loss, voids, defects and thickness gradients) are related to the resin flow out of the laminate, the ply orientation, the tool used or the effect of the bag on the laminate surface.

A material having a lower resin viscosity is more sensitive to imperfections in the bagging which would cause severe resin mass losses out of the laminate. Even though high viscosity materials are more difficult to conform to a tool having sharp corners, the voids created during the lay-up process are eliminated during cure.

The ply orientation has a significant effect on the compaction behaviour at the corner regardless of the material used. The presence of stiff fibres oriented in the appropriate direction strongly prevents the significant thickness gradient observed at the laminate corner. However, local deformations in some of the laminate plies can still occur under the action of local forces induced by the bagging element imperfections (i.e. wrinkles).

The choice of the tool used can have a significant effect on the final part quality. The lay-up operation is more difficult with the concave tool, where the removal of small wrinkles induced

⁷ Some strain at the corner is probably caused by $\epsilon_{\text{debulking}}$ or ϵ_{other} .

during lay-up is more difficult. The bag can also bridge at the corner and resin rich regions can be created. In the event of introducing an automatic lay-up process machine, the use of a convex tool is therefore recommended .

5.3 Numerical investigation

The objective here is to model the angle laminates considered previously in the experimental studies. With the processing model, it is possible to take into account all the components used during the manufacturing process of the composite laminate. For example, the consideration of the tool in modelling has a significant effect on the predicted temperature profile in the part (Hubert et al., 1995).

A model taking into account the tool and the laminate for a specimen moulded with a convex tool was used to study the viscosity profiles for materials A and B (Figure 5.33). The cure cycle definition used for the experiment (Figure 5.16) was applied to the model. The appropriate heat transfer coefficient for the autoclave (Johnston and Hubert, 1995) was used where convection boundary conditions were applied. The temperature profiles predicted by the model are in very good agreement with the measured temperature profiles as shown in Figure 5.34. The viscosity profiles are also shown in Figure 5.34. The cure cycle chosen gave a long processing window for flow by maintaining the resin viscosity at its minimum for about one hour. As expected, the viscosity of material A is lower than material B. The gel point is reached at 170 minutes and 150 minutes for materials A and B, respectively.

The model incorporating the tool shown in Figure 5.33 is not adequate for the flow-compaction model. The number of elements used to mesh the laminate is not sufficient to ensure accuracy of

the non-linear solution used by the flow-compaction model. Thus, the compaction simulations consider one half of the laminate without the tool. The symmetry condition is adequate since the experiments showed a symmetric compaction for most angles. The temperature profile of the part shown in Figure 5.34 is applied directly to the boundary of the model to make sure that the curing behaviour of the resin is similar to the experiments.

5.3.1 Finite element models definition

The geometry of the finite element models used for the numerical investigation is presented in Figure 5.35. The samples modelled are presented in Table 5.6. Only the specimens in bleed conditions were modelled for this analysis since the formulation currently implemented in the flow-compaction model considers percolation flow only. Two geometries were used, one for the specimens on the convex tool and one for the specimens on the concave tool (Figure 5.35). The dimensions of the models are presented in Table 5.6. The condition at the tool interface was simulated by fixing the displacements at the boundary. This condition is equivalent to the assumption of no-slip at the tool-laminate interface. In reality, slip is probably present at the tool-laminate interface. However, for this analysis, assuming infinite friction was judged acceptable compared to assuming no-friction or sliding conditions at the tool-laminate interface. The latter would result in large in-plane deformations. The experiments showed very little in-plane deformation which is only simulated by no-slip conditions. At the axis of symmetry, a sliding displacement condition was applied. The pressure was applied on the top and left surfaces of the laminate as shown in Figure 5.35. Impermeable conditions were maintained at all surfaces except for the top surface of the laminate where the resin pressure was set to the bag

pressure. This surface represents the bleeder where the resin is allowed to flow freely during cure. The temperature profile of the part was applied to the surfaces except for the symmetry surface where adiabatic conditions were maintained.

The material properties for the different runs are presented in Figure 5.35. For the [0] lay-up, the fibres are in the in-plane longitudinal direction (1 direction). Thus, the fibre bed modulus E_1 is assumed constant at 100 GPa for materials A and B. The out-of-plane response is given by the fibre bed compaction curve shown in Figure 5.35. For the [90] lay-up, the fibres are in the in-plane transverse direction (2 direction). Therefore, the fibre bed elastic behaviour in the 1 and 3 directions corresponds to the out-of-plane response given by the fibre bed compaction curve. Finally, the fibre bed shear modulus is assumed constant for all cases at a value of 0.5 MPa. This value was chosen based on the results of the model compared to the actual experiments.

The mesh size for the finite element models used is presented in Figure 5.36. The convex tool specimen mesh contains 464 elements while the concave tool specimen mesh contains 448 elements. The time step was kept constant during the solution at 1 minute. The flow model was run when the resin viscosity is below 1000 Pa.s. Figure 5.37 shows the location of the nodes used to extract the normal displacements and the resin pressure used in the analysis of the results.

5.3.2 Resin mass losses and laminate thickness predictions

The resin mass losses⁸ predicted by the model are compared with the experimental results in Table 5.7. Very good agreement is obtained for both materials under the different conditions.

⁸ Expressed as the resin mass loss ratio (Equation 5.1).

This confirms that the interaction between the viscosity model, the fibre bed permeability model and the constitutive law chosen is adequate for the materials studied.

The predicted final thicknesses of the laminate are compared to the measured values in Figures 5.38 and 5.39. The thickness of the flat section (Figure 5.37) is compared to the average thickness measured at stations 1,2,4 and 5 (Figure 5.18). The thickness at the corner is directly compared to the measured value (H_3). The initial thickness of the laminate is indicated as reference by the location of the error bar horizontal marker in Figures 5.38 and 5.39. For all simulations, the initial thickness of the laminate was assumed uniform. As discussed in Section 5.2.6, the initial thickness of the laminate was found to be non-uniform. Thus, the comparison between the predictions and the experiments have to be interpreted from this perspective. The general trends observed in the experiments are captured reasonably by the model.

The thickness change predicted by the model (ϵ_n) is compared to the experimental results (ϵ_{total}) in Figures 5.40 and 5.41. The agreement between the simulations and the experiments is better for material A than material B. This is consistent with the results found in Section 5.2.7 ($\epsilon_{total} \approx \epsilon_{percolation}$ for material A). Based on the assumptions of the flow-compaction model, the thickness change from the simulations corresponds mainly to $\epsilon_{percolation}$. The model cannot simulate the exact magnitude of other strains observed in the experiments ($\epsilon_{debulking}$ and ϵ_{shear}). The disagreement with the experiments is particularly noticeable for the [90] lay-up. Typically, these specimens have severe defects at the corner.

5.3.3 Final shape of the laminates

The predicted final shape of the laminates are presented in Figure 5.42. The results shown are for material A only since similar, but smaller magnitude results are obtained for material B. The laminate lay-up has a significant effect on the deformation at the edge of the laminate. The [0] laminates have small lateral deformation and the tool geometry (convex vs concave) influences the sign of the shear deformation in the flat section. This behaviour is not observed for the [90] lay-up where the deformation is more important and always in the direction of the pressure at the edge. The applied pressure caused this deformation and similar deformation profiles were observed on the test specimens as shown in Figure 5.43. The edge of the laminates were cut square before cure. The good agreement between the predicted and observed edge profiles indicates that the value chosen for G_{13} is reasonable.

5.3.4 Compaction of the laminates during cure

The compaction of the laminates is studied by comparing the normal displacement at the flat section and the corner. The results are presented in Figures 5.44 to 5.47. From these figures the following statements can be made:

- 1) Full compaction is reached at the minimum viscosity for material A.
- 2) The compaction of material B is stopped at the resin gel point.
- 3) The compaction of the flat section is similar for all cases.
- 4) The compaction at the corner is faster with the convex tool.

The difference between the two materials comes mainly from the resin type used. The difference in the compaction behaviour between the corner and the flat section indicates that the flow of the resin is affected by the presence of the corner. This issue is discussed in detail in Section 5.3.6.

5.3.5 Resin pressure variation during cure

One way of investigating the flow behaviour of the resin is to look at the resin pressure variation during the compaction of the laminate. The resin pressure gradient in the laminate is the driving force for resin flow. For the simple unidirectional compaction of flat laminates, the resin pressure should drop as the laminate compacts. When full compaction is reached, the resin pressure is equal to zero (Section 2.3.1.3). The predicted variation of the resin pressure during compaction is presented in Figures 5.48 to 5.51. The resin pressure is monitored at two points on the tool surface as indicated in Figure 5.37. The following observations are made from the pressure variation at these points during compaction:

- 1) The resin pressure drops close to zero in all cases for material A.
- 2) The pressure drops by a maximum of 40 kPa for material B.
- 3) The pressure at the corner drops more quickly than in the flat section for the $[0^\circ]$.
- 4) For the convex tool, the pressure at the corner is initially higher compared to the flat section.
- 5) For the concave tool, the pressure at the corner is initially lower compared to the flat section.

The significant pressure drop for material A is consistent with the compaction behaviour observed previously for this material (Section 5.3.4). The resin pressure in material B laminates could explain why the laminates made with material A contained in general more voids (Section 5.2.4). The higher pressure with material B may be enough to prevent the formation of vapor bubbles from the entrapped moisture in the laminate (Loos and Springer, 1983; Davé et al.,

1987a). The faster pressure drop observed at the corner for the [0] lay-up normally implies that the corner reaches full compaction before the flat section of the laminate. However, the final thickness at the corner was higher compared to the flat section which is in contradiction with the theory of consolidation. The pressure gradient observed at the corner (items 3 and 4) is discussed in the next section.

5.3.6 Corner compaction behaviour

The final normal strain distribution in the corner is shown in Figure 5.52. The normal strain is uniform in the flat section of the laminate, while gradients are present at the corner. In most cases as seen in Figure 5.52, the normal strains are lower at the corner except for the [90] lay-up on the convex tool. The resin pressure for all the laminates of material A dropped to zero at the end of the compaction of the laminate (Section 5.3.5). Thus, from the classical theory of compaction for flat laminates, the normal strain should be uniform at any point in the laminate.

However, for curved laminates, the fibres support the load in the corner by a combination of shear and longitudinal loads as shown in Figure 5.53. This behaviour is particular to curvilinear shapes and is significantly different from the simple compaction behaviour of flat panels where shear stresses can be neglected under the loading conditions found during autoclave processing. The presence of very stiff fibres in the longitudinal direction (i.e. [0] lay-up) is blocking the normal deformation of the fibre bed at the corner. For the convex tool, longitudinal compressive stresses are generated by the compaction of the fibre bed. For the concave tool, tensile stresses are induced by the compaction as shown in Figure 5.53. In both cases, the ability of the fibre to shear determines the ease with which the fibres slide to enable compaction at the corner. If the

fibres are constrained from sliding, they can bridge creating a wrinkle, as with the sample shown in Figure 5.54. Thus, in this case, the resin pressure drop is not caused by the transverse load bearing capability of the fibres but by the high compression stresses transmitted along the fibres.

For the [90] lay-up, the fibre bed longitudinal and transverse behaviour is identical, since the material is essentially isotropic in the plane considered. With the convex tool, the corner is thinner, while with the concave tool, the corner is thicker (Figure 5.52). Thus, the stress at the tool interface at the corner is higher for the convex tool while the stress is lower with the concave tool. The applied pressure for the convex tool acts on a larger surface compared to the concave tool as shown in Figure 5.55. Thus to have equilibrium, the reaction stress at the tool surface is higher for the convex tool compared to the concave tool. This pressure gradient constitutes the driving force causing the corner thinning or thickening observed with the [90] laminates. In the flat section, the surface exposed to the pressure is equal to the reaction surface at the tool which leads to a uniform compaction.

5.3.7 Resin flow behaviour during cure

The resin flow behaviour is studied by looking at the resin velocity distribution. The results presented in Figure 5.56 are for material A at 50 minutes. At this time, the compaction accelerates (e.g. Figure 5.44) and large pressure gradients are present. In general, the resin flow is normal in the flat section and longitudinal close to the tool surface (Figure 5.56). For most cases, resin flow out of the laminate is higher at the corner. However, for the [90] with the convex tool, the resin flows away from the corner.

Figures 5.57 and 5.58 present the pressure distribution and the fibre volume fraction distribution corresponding to Figure 5.56. The resin pressure gradient is greater in the direction normal to the tool for most cases. However, a gradient in the longitudinal direction is present except for the [90] with the convex tool. Combined with the lower fibre volume fraction in the corner, the flow direction observed for these cases is explained. For the [90] with the convex tool, the higher fibre volume fraction at the surface of the corner region creates a low permeability zone compared to the surface of the laminate in the flat section. Given that the resin pressure is uniform, the flow is directed towards regions of higher permeability as seen in Figure 5.58.

5.3.8 Discussion

The flow-compaction model developed in this work predicts adequately the deformation of curved laminates caused by percolation flow. The fibre bed constitutive law currently implemented assumes a constant elastic shear modulus (Section 3.2.4). Allowing for G_{13} is a way of evaluating the shear deformation behaviour of the laminate. However, the magnitude of the shear deformation is not predicted which indicates that a better constitutive law is required for the composite. Nevertheless, the current model provides valuable information in understanding the compaction behaviour at the corner. The presence of fibres oriented in the longitudinal direction ([0]) restricts the deformation behaviour of the material. The fibres oriented in the transverse direction ([90]) offer little resistance to deviatoric stresses caused by the moulding geometry (convex vs concave tool) or any pressure intensifier induced by bag imperfections (i.e. wrinkles, gaps, etc.). In some cases, the deformations involved are very large as shown in Figure 5.59, where one can see the sharp wrinkle created by the bagging material.

5.4 Summary

Flow-compaction model sensitivity analysis

- The fibre bed longitudinal and shear modulus significantly affect the compaction behaviour in the corner section of the curved laminates.
- Accurate measurement of the fibre bed compaction curve is critical for accurate prediction of the laminate final thickness.
- As shown previously (e.g. Loos and Springer, 1983; Smith and Poursartip, 1993), the resin viscosity and fibre bed permeability affect the compaction rate of the laminate.

Angle laminate experiments

- The laminate defects (i.e. voids, wrinkles, etc.) are localized at the corner.
- The laminates with material A (low viscosity) exhibit more resin loss compared to material B (high viscosity).
- The final thickness of the laminate is uniform in the flat section.
- In the flat section, the total strain in bleed conditions are principally caused by percolation flow for material A. For material B the total strain is a combination of percolation and debulking strain.
- At the corner, high strains are observed for the [90] lay-up which create corner thinning for the convex tool and corner thickening for the concave tool. These gradients are caused by shear flow of the composite.

Angle laminate simulations

- The percolation flow-compaction model predicts the amount of resin mass loss during the compaction of angle laminates in a bleed condition.
- The final thickness profiles obtained by the model follows the trends observed in the experiments.
- The magnitude of the calculated strains at the corner for the $[90^\circ]$ are lower than the measured strains. The difference is caused by shear flow.
- The flow-compaction model with the current fibre bed constitutive law aids in understanding the effect of the shear deformations at the corner.

5.5 Tables

Table 5.1 Run definition and results for the sensitivity analysis.

Run	Parameter	Result		
		Full compaction time (min.)	Thickness change in flat section (mm)	Thickness change at corner (mm)
Nominal case				
SANOM	see Fig. 5.2	135	-0.95	-0.52
Resin viscosity				
SAVIS1	$\alpha_0=0.1$	140 (+5)	-0.95 (0)	-0.52 (0)
SAVIS2	$\mu_w=3.5 \times 10^{-17}$ Pa.s	135 (0)	-0.95 (0)	-0.52 (0)
SAVIS3	$\kappa=18$	150 (+15)	-0.95 (0)	-0.52 (0)
Fibre bed longitudinal permeability				
SAPER1	L1 (Fig. B.8)	135 (0)	-0.95 (0)	-0.52 (0)
SAPER2	L3 (Fig. B.8)	140 (+5)	-0.95 (0)	-0.52 (0)
Fibre bed transverse permeability				
SAPER3	T1 (Fig. B.9)	125 (-10)	-0.95 (0)	-0.52 (0)
SAPER4	T4 (Fig. B.9)	145 (+10)	-0.95 (0)	-0.52 (0)
Fibre bed compaction curve shape				
SACUR1	see (Fig. 5.4)	135 (0)	-0.99 (-0.04)	-0.52 (0)
SACUR2	see (Fig. 5.4)	135 (0)	-0.91 (+0.04)	-0.52 (0)
Fibre bed longitudinal modulus				
SAE11	$E_1=200$ GPa	135 (0)	-0.95 (0)	-0.52 (0)
SAE12	$E_1=1$ GPa	135 (0)	-0.95 (0)	-0.70 (-0.18)
Fibre bed shear modulus				
SAG131	$G_{13}=10$ MPa	130 (-5)	-0.95 (0)	-0.05 (+0.47)
SAG132	$G_{13}=10$ kPa	135 (0)	-0.95 (0)	-0.95 (-0.43)

* Note: Value in parentheses represents the variation from the nominal case.

Table 5.2 Sample definition for angle processing experiments and test matrix.

Lay-up	Convex tool			
	Material A		Material B	
	No-bleed	Bleed	No-bleed	Bleed
[90]	5BM7	5BM10	5AM1	5AM4
[0]	5BM8	5BM11	5AM2	5AM5
[Q]	5BM9	5BM12	5AM3	5AM6
Lay-up	Concave tool			
	Material A		Material B	
	No-bleed	Bleed	No-bleed	Bleed
[90]	5DF7	5DF10	5CF1	5CF4
[0]	5DF8	5DF11	5CF2	5CF5
[Q]	5DF9	5DF12	5CF3	5CF6

Table 5.3 Type of defects observed after cure of the angles. Typical defects are shown in Fig. 5.20.

		Convex tool			
		Material A		Material B	
Lay-up		No-bleed	Bleed	No-bleed	Bleed
[90]		NONE	III	NONE	NONE
[0]		NONE	III	NONE	NONE
[Q]		NONE	III	NONE	NONE
		Concave tool			
		Material A		Material B	
Lay-up		No-bleed	Bleed	No-bleed	Bleed
[90]		II	II	II	II
[0]		I	I	NONE	I
[Q]		II	I	NONE	II

Table 5.4 Level of voids in the flat section and at the corner of the laminates. Obtained from the visual inspection of the angles after the cure. The void level is ranked on a scale of 0 to 3 corresponding to no voids (0) to large number of voids (3).

		Convex tool							
		Material A				Material B			
		No-bleed		Bleed		No-bleed		Bleed	
Lay-up		Flat	Corner	Flat	Corner	Flat	Corner	Flat	Corner
[90]		0	0	3	2	0	0	0	0
[0]		1	0	0	3	1	0	1	1
[Q]		0	0	2	3	0	0	0	1
		Concave tool							
		Material A				Material B			
		No-bleed		Bleed		No-bleed		Bleed	
Lay-up		Flat	Corner	Flat	Corner	Flat	Corner	Flat	Corner
[90]		1	0	3	2	0	0	0	0
[0]		1	0	3	3	0	1	1	2
[Q]		0	0	3	3	0	1	2	3

Table 5.5 Resin mass loss ratio calculated from the mass of the laminates before and after cure (Equation 5.1).

		Convex tool			
		Material A		Material B	
Lay-up		No-bleed	Bleed	No-bleed	Bleed
[90]		2%	17%	0%	4%
[0]		1%	16%	0%	3%
[Q]		3%	15%	0%	3%
		Concave tool			
		Material A		Material B	
Lay-up		No-bleed	Bleed	No-bleed	Bleed
[90]		6%	16%	1%	4%
[0]		7%	16%	0%	3%
[Q]		9%	13%	0%	2%

Table 5.6 Finite element model dimensions and material input used for the simulations of the angle laminates. The models and the material input are defined in Figure 5.35.

Sample	Mesh	L (mm)	H (mm)	R (mm)	Material Lay-up
5BM10	Convex	63	4.96	4.57	A [90]
5BM11	Convex	63	4.96	4.57	A [0]
5AM4	Convex	63	4.8	4.57	B [90]
5AM5	Convex	63	4.8	4.57	B [0]
5DF10	Concave	63	4.96	6.35	A [90]
5DF11	Concave	63	4.96	6.35	A [0]
5CF4	Concave	63	4.8	6.35	B [90]
5CF5	Concave	63	4.8	6.35	B [0]

Table 5.7 Comparison of the resin mass loss ratio obtained from the experiments and the predictions with the finite element program (COMPRO).

Lay-up	Convex tool			
	Material A		Material B	
	Experiments	COMPRO	Experiments	COMPRO
[90]	17%	17%	4%	4%
[0]	16%	14%	3%	4%
Lay-up	Concave tool			
	Material A		Material B	
	Experiments	COMPRO	Experiments	COMPRO
[90]	16%	16%	4%	3%
[0]	16%	15%	3%	3%

5.6 Figures

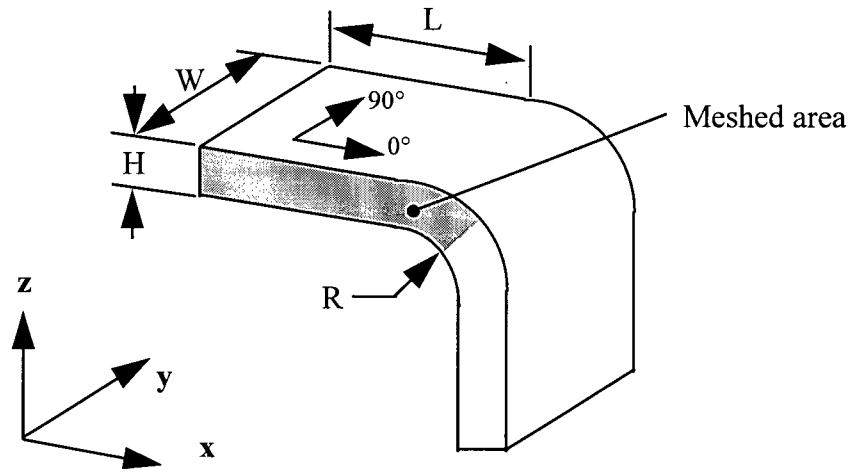


Figure 5.1 Angle laminate geometric definition for modelling.

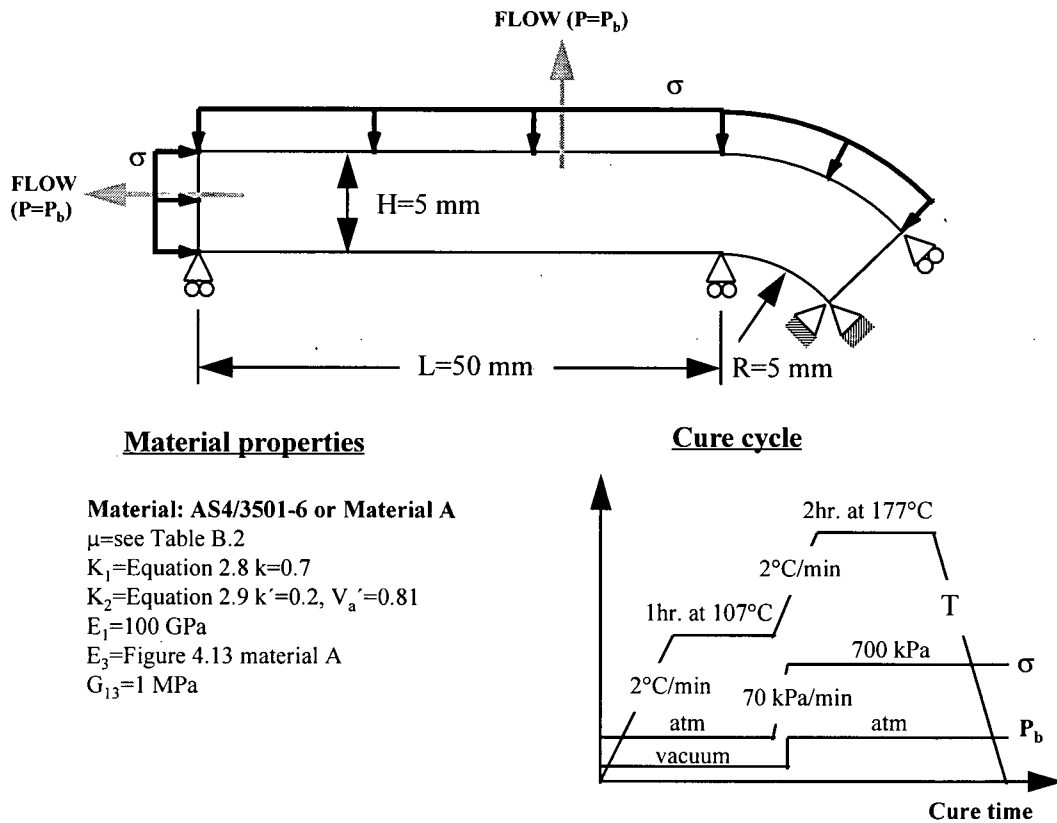


Figure 5.2 Finite element model dimensions, boundary conditions and material properties input for the nominal case of the sensitivity analysis (SANOM).

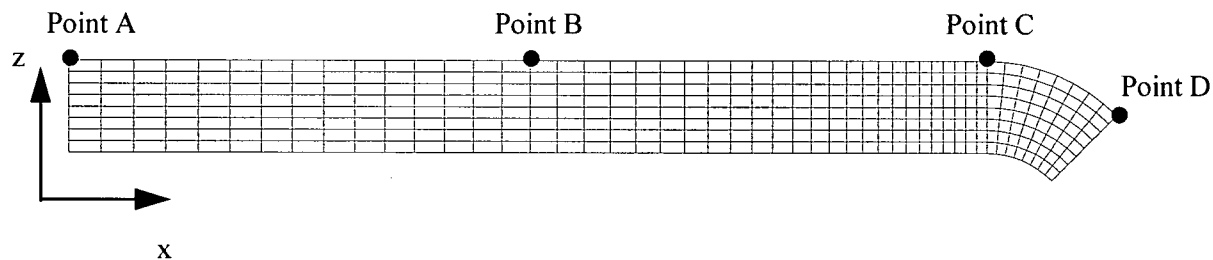


Figure 5.3 Finite element mesh used for the sensitivity analysis. The location for the normal displacement (u_n) outputs is shown.

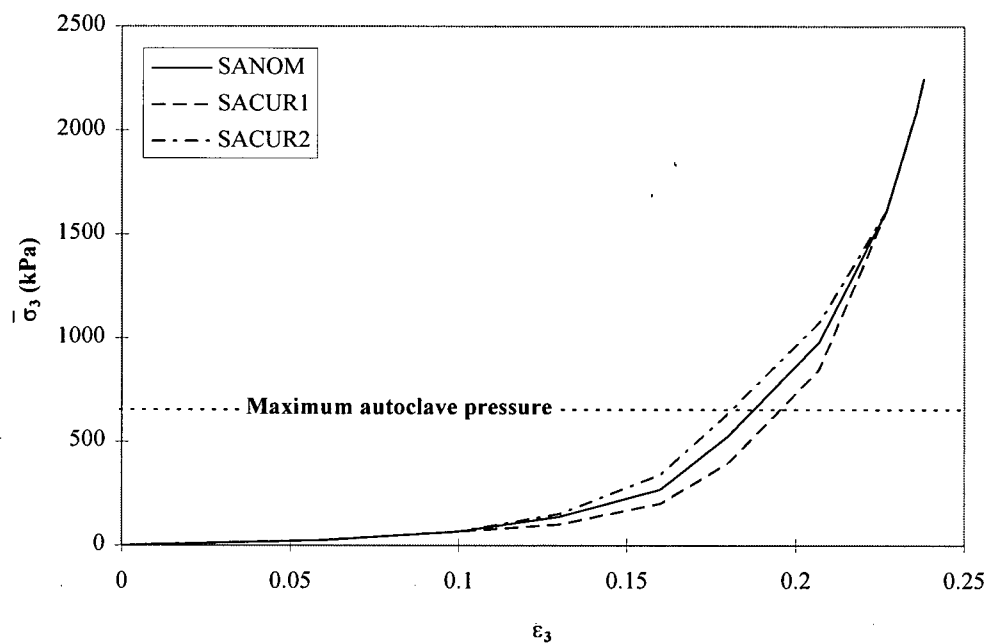


Figure 5.4 Compaction curves used for the sensitivity analysis to investigate the effect of shifting the fibre bed effective stress in the stiffening region ($0.1 < \epsilon_3 < 0.25$).

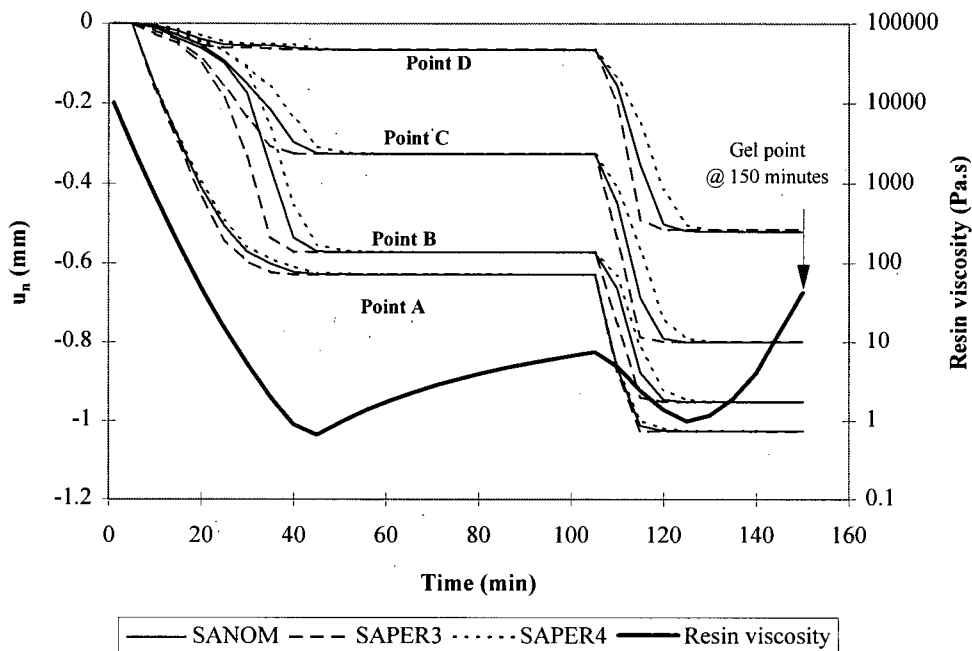


Figure 5.5 Effect of the variation of the transverse permeability on the angle compaction behaviour. The viscosity profile is also shown indicating the gel time of the resin.

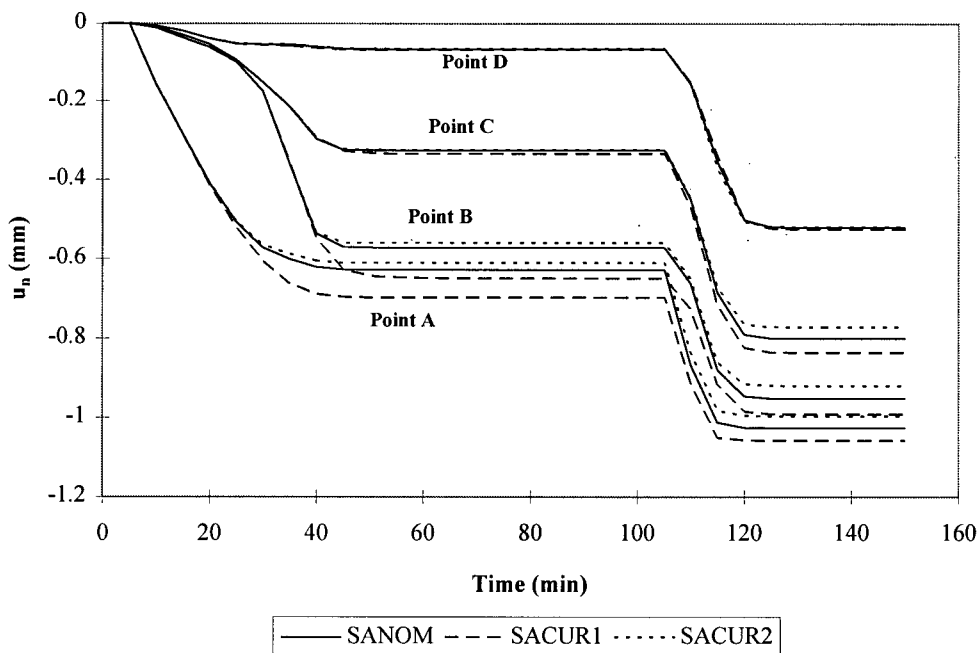


Figure 5.6 Effect of the compaction curve shape on the angle compaction behaviour.

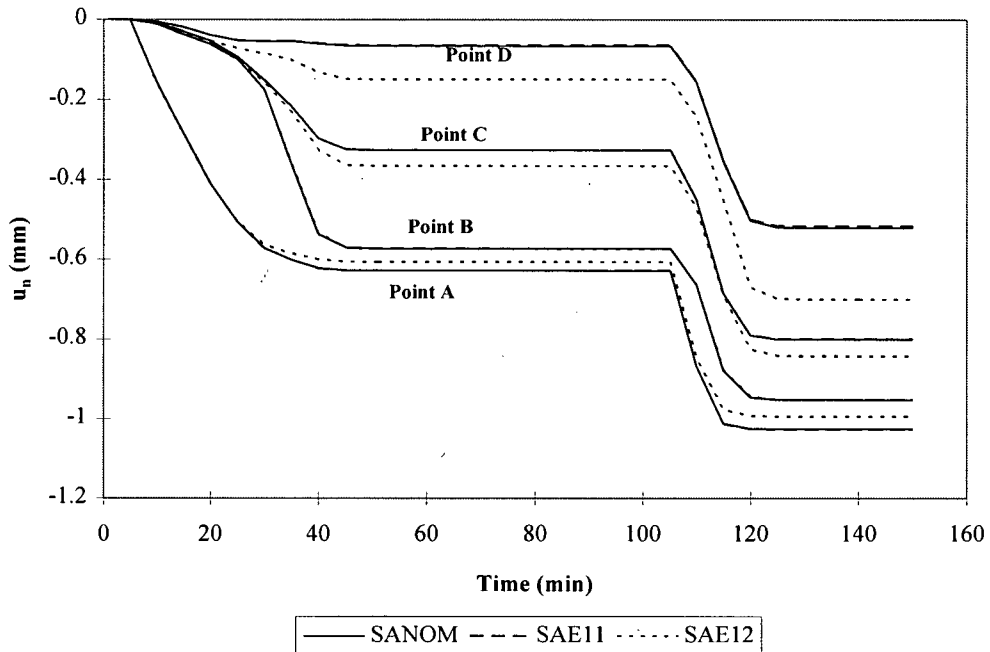


Figure 5.7 Effect of the fibre bed longitudinal modulus (E_1) on the angle compaction behaviour.

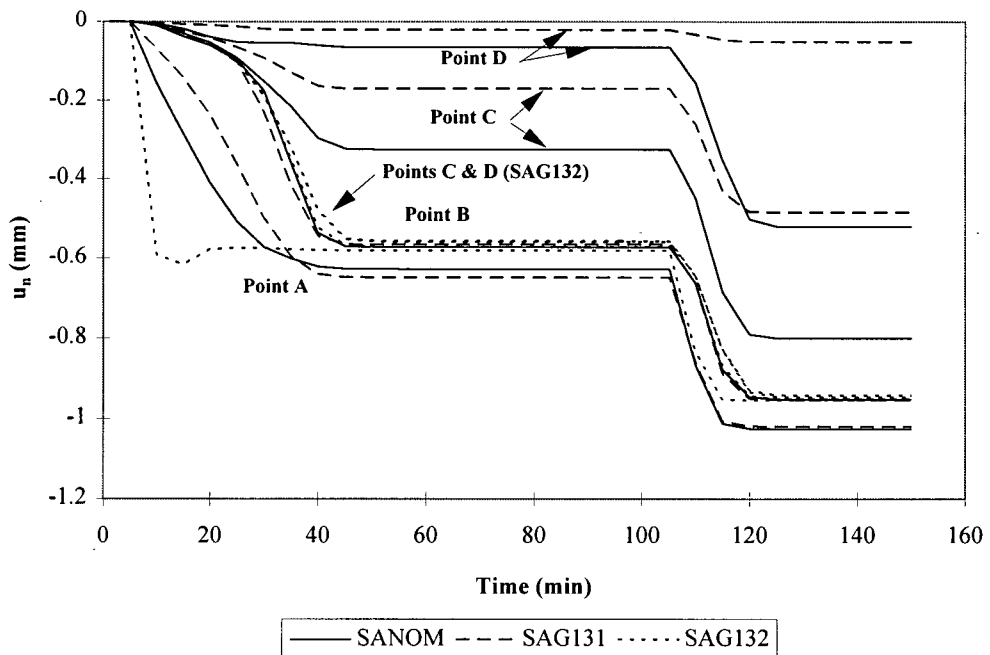


Figure 5.8 Effect of the fibre bed shear modulus (G_{13}) variation on the angle compaction behaviour.

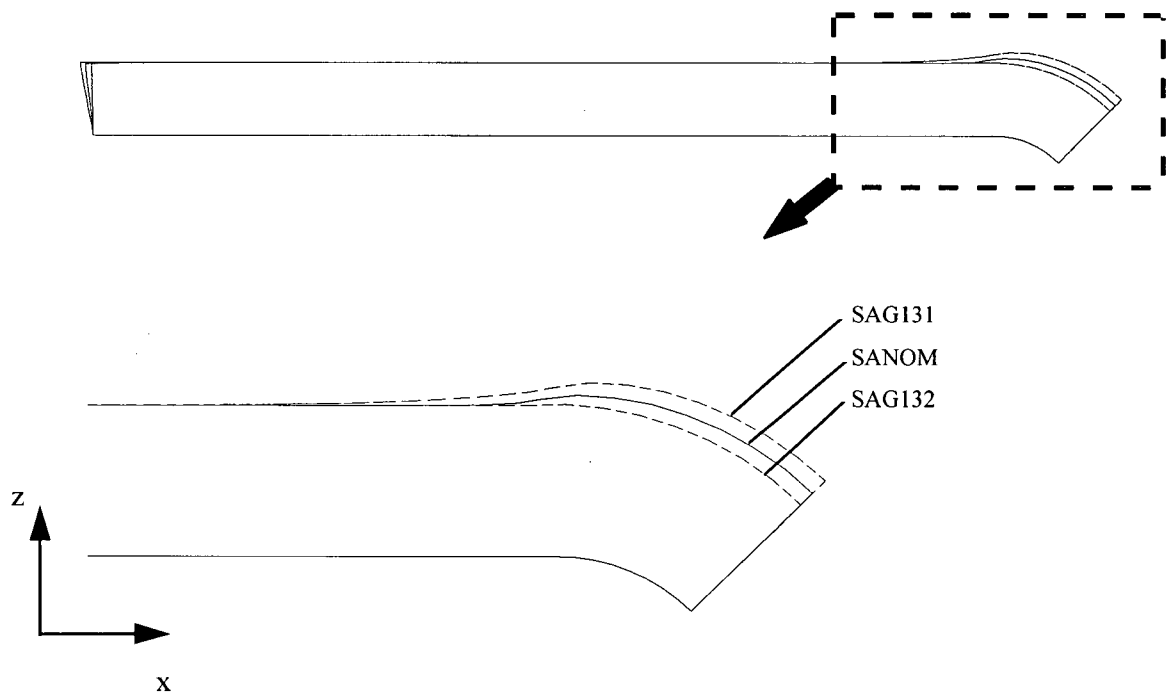
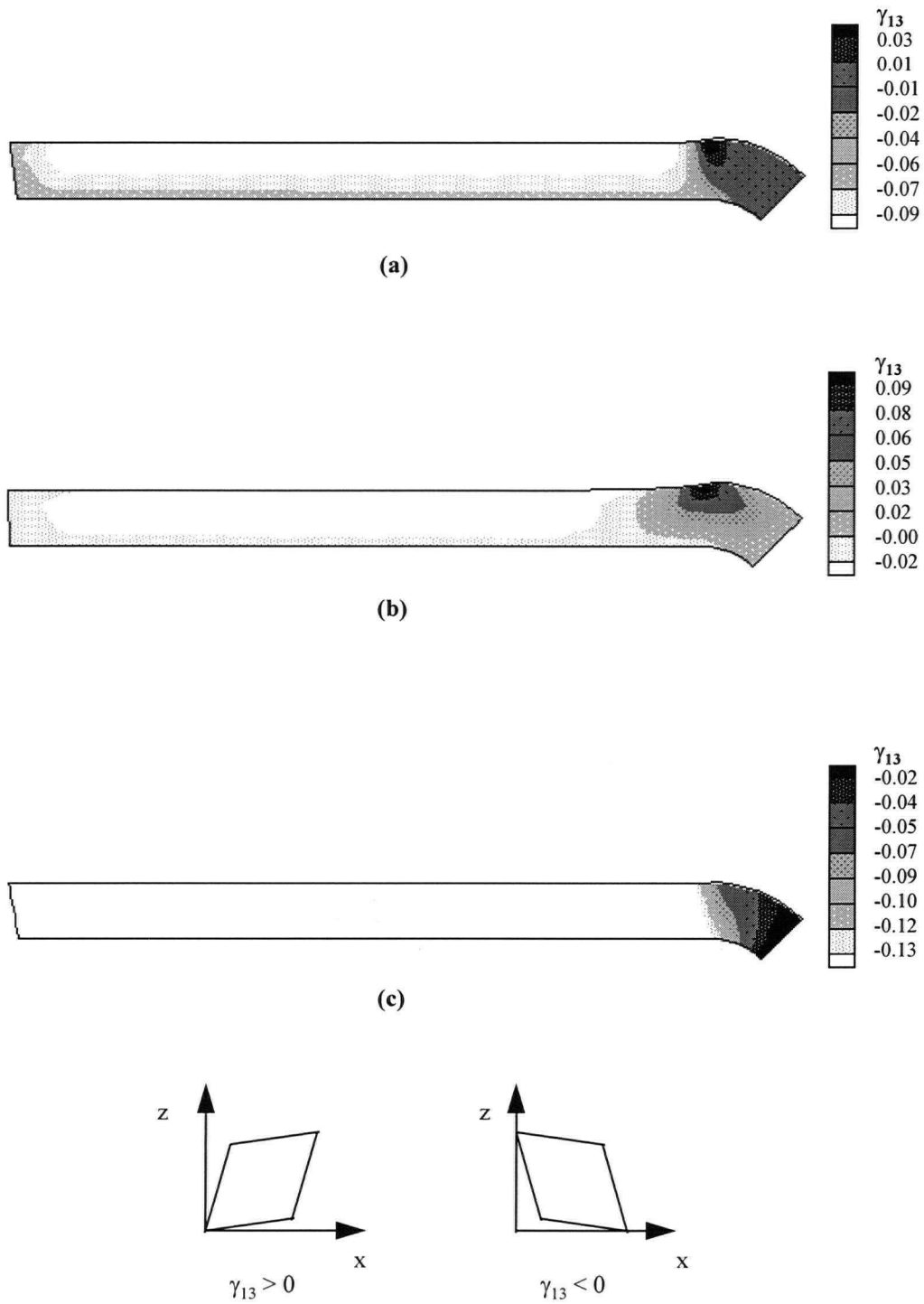


Figure 5.9 Effect of the fibre bed shear modulus (G_{13}) on the final shape of the angle. The deformation behaviour at the corner is enlarged.



Shear deformation definition

Figure 5.10 Effect of the fibre bed shear modulus (G_{13}) on the final shear deformation (γ_{13}) distribution in the laminate, (a) SANOM, (b) SAG131 and (c) SAG132.

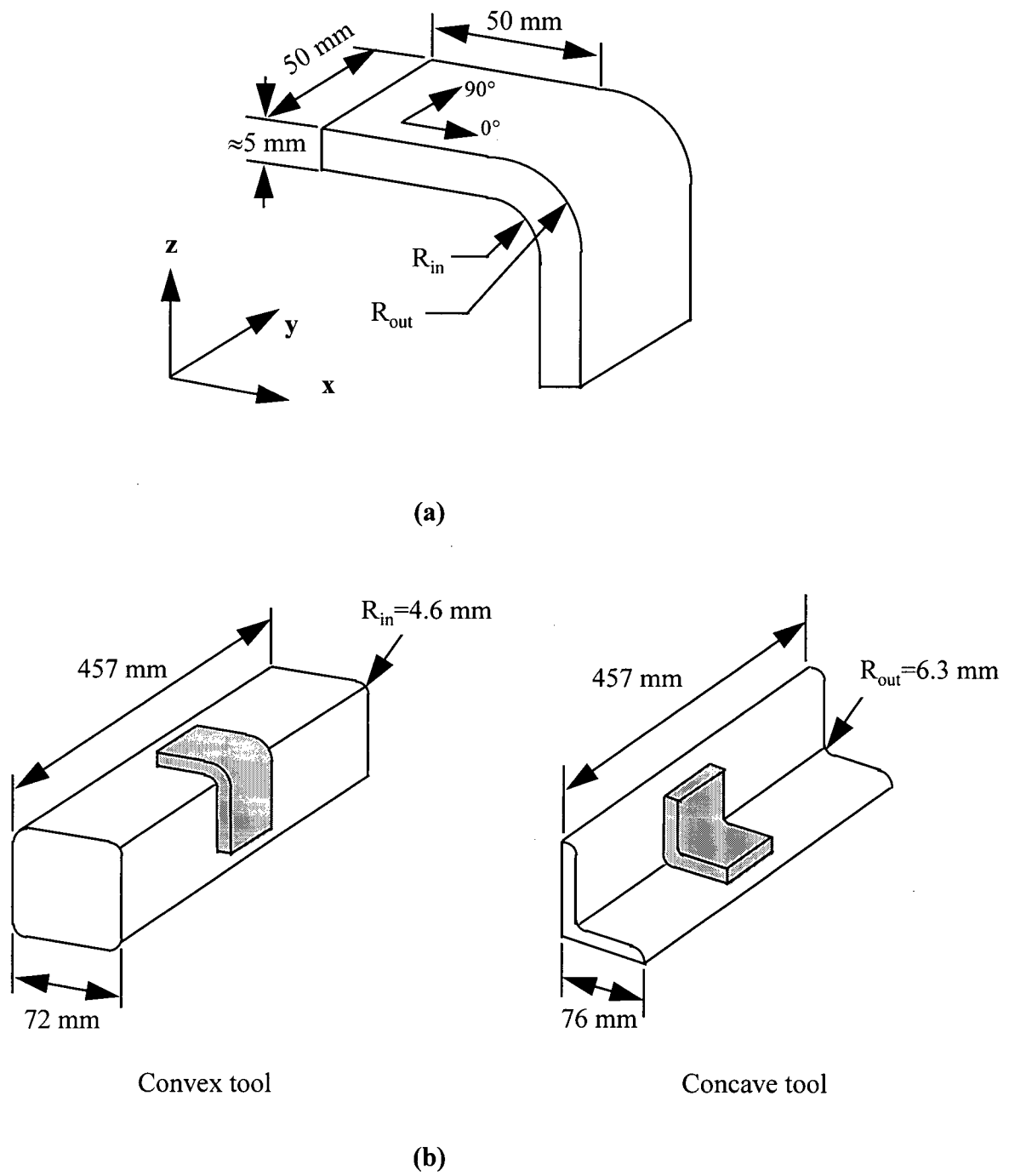
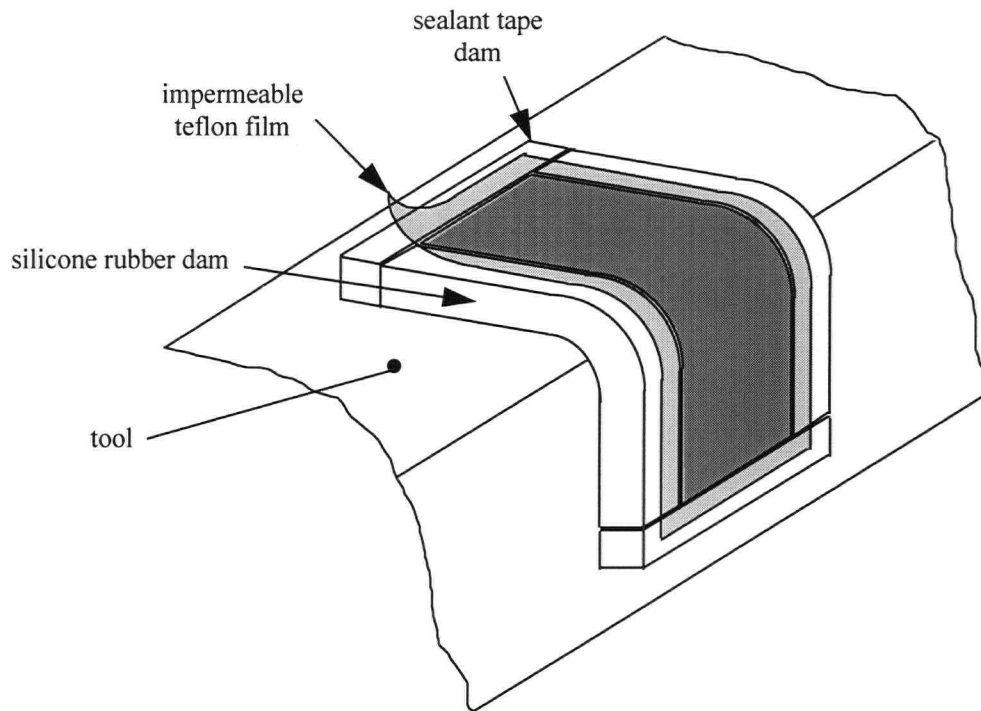
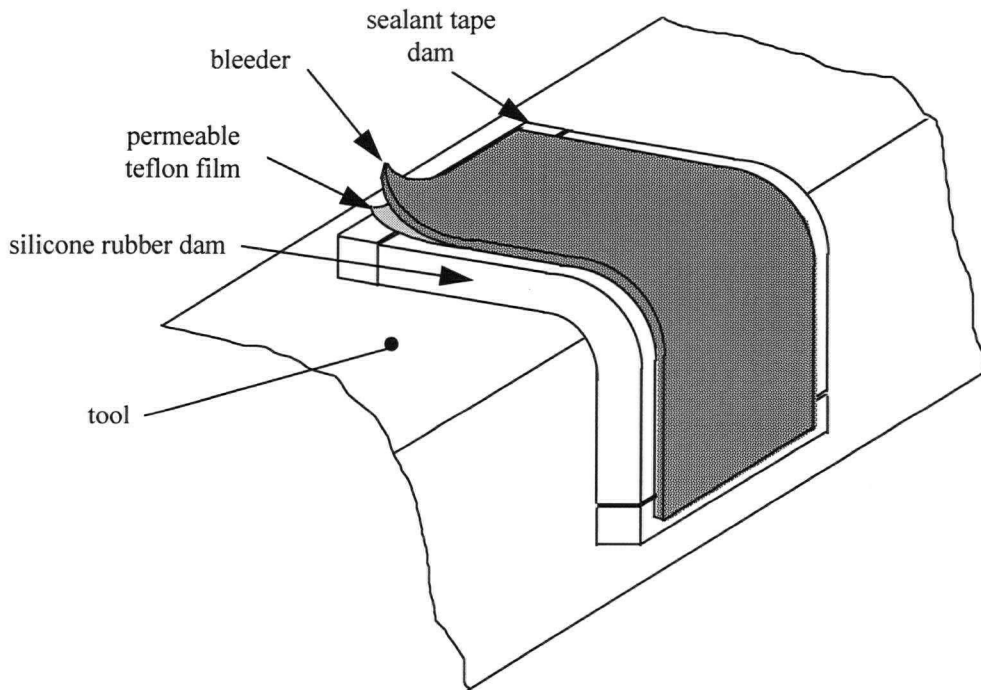


Figure 5.11 Angle laminate compaction experiments, (a) laminate dimensions and fibre orientation definition, (b) tool dimensions.



No-bleed bagging



Bleed bagging

Figure 5.12 Typical bagging configurations for no-bleed and bleed conditions. Configuration for the convex tool is shown in this figure.

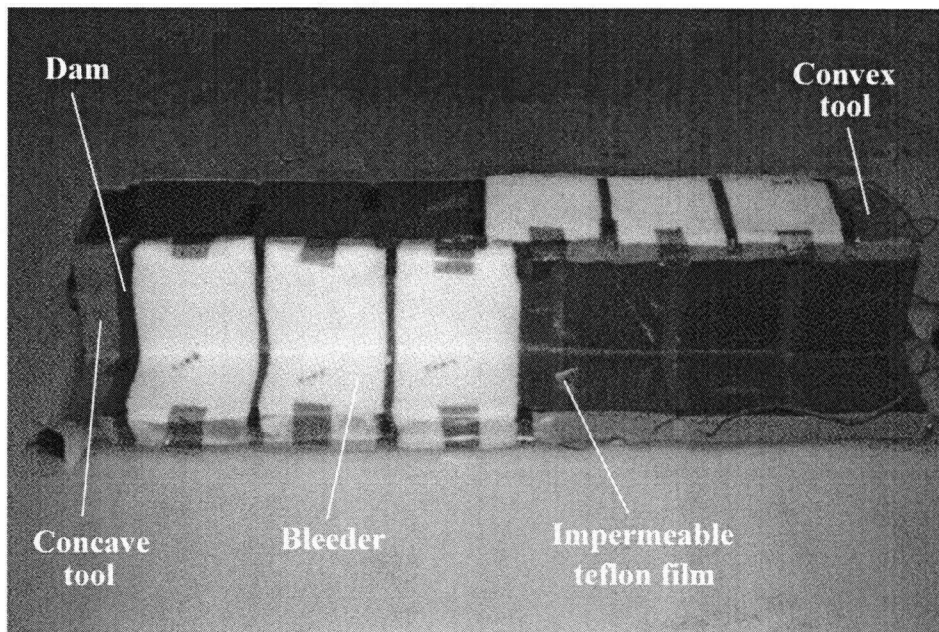


Figure 5.13 Photograph of the tools with the bagging elements before the installation of the breather and the vacuum bag.

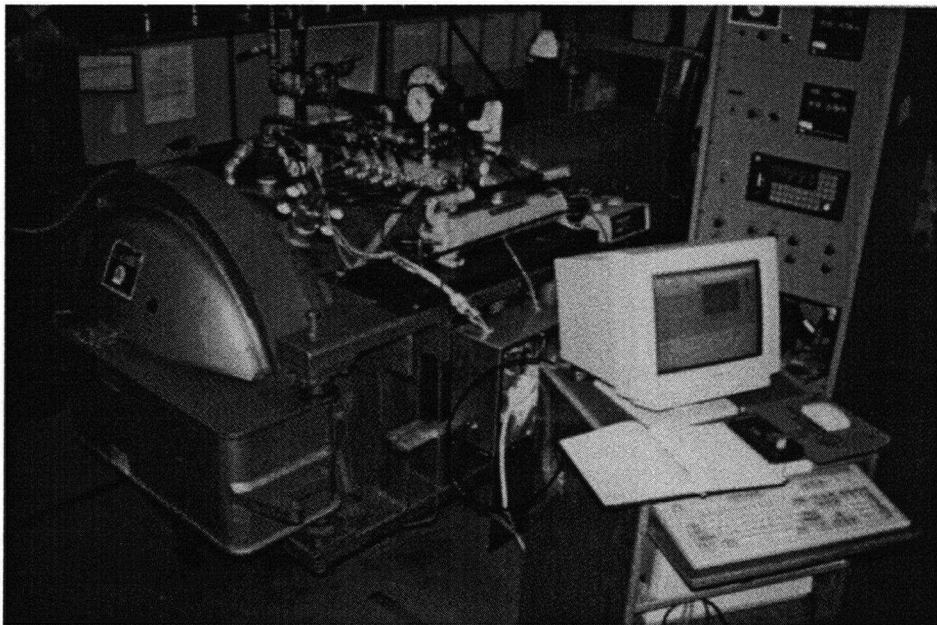
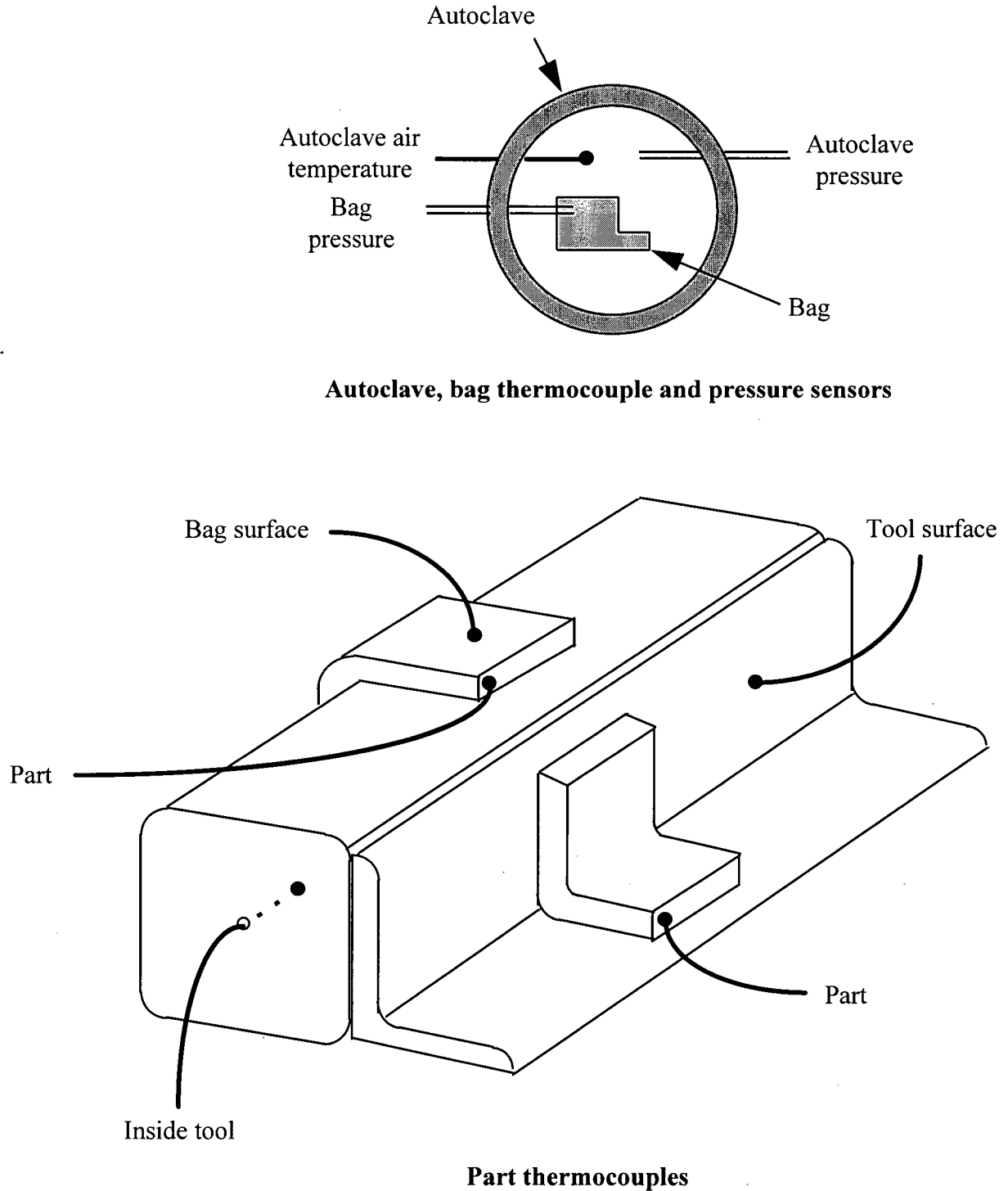


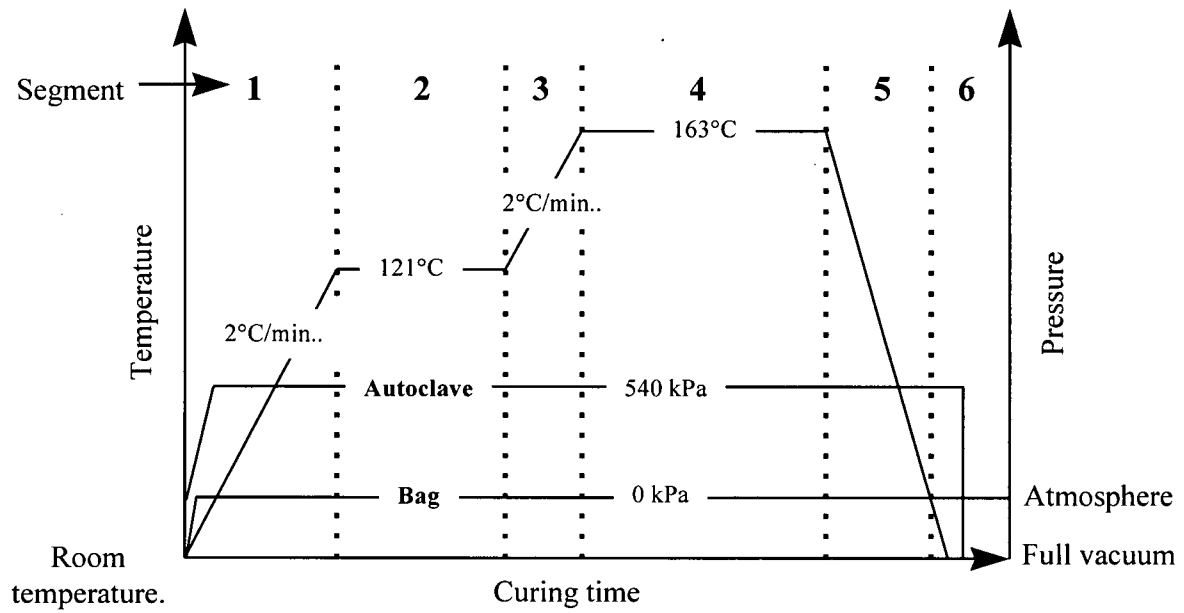
Figure 5.14 Photograph of the autoclave and the computer controlling the cure cycle.



Autoclave, bag thermocouple and pressure sensors

Part thermocouples

Figure 5.15 Definition of the processing parameters measured for the autoclave and the bag (top) and typical location of the thermocouples on the tool and in the part (bottom). The part thermocouples are embedded about 5 mm inside the part.



Segments definition

Segment	Hold (min)	Temperature (°C)	Rate (°C/min)	Pressure (kPa) gauge	Vacuum (kPa)	Criteria* (°C)
1		121	2	540	101**	115
2	30					
3		163	2			157
4	120					
5		25				50
6				0		

* The criteria is based on the lagging thermocouple (the coolest during heating and the hottest during cooling).

** The bag is initially under full vacuum. The bag is vented to the atmosphere when the autoclave pressure reaches 200 kPa

Figure 5.16 Cure cycle used and segment definition for the autoclave control system for the angle compaction experiment.

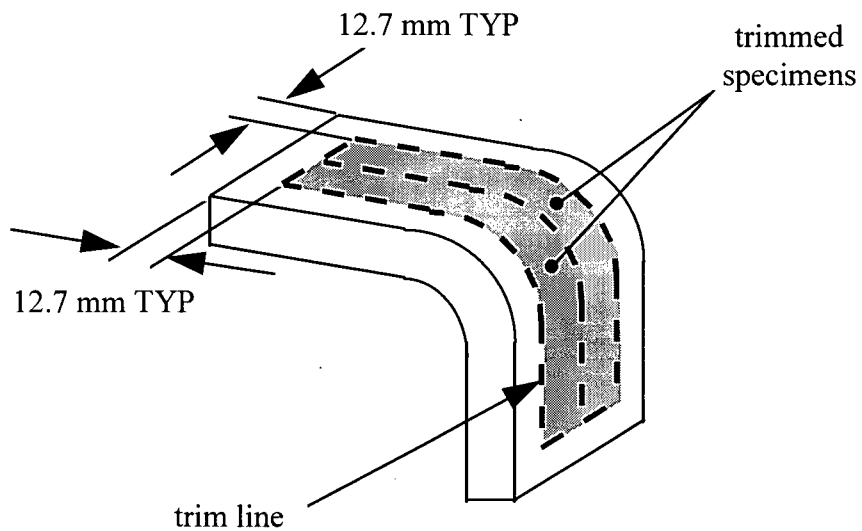


Figure 5.17 Laminate trimming after the cure.

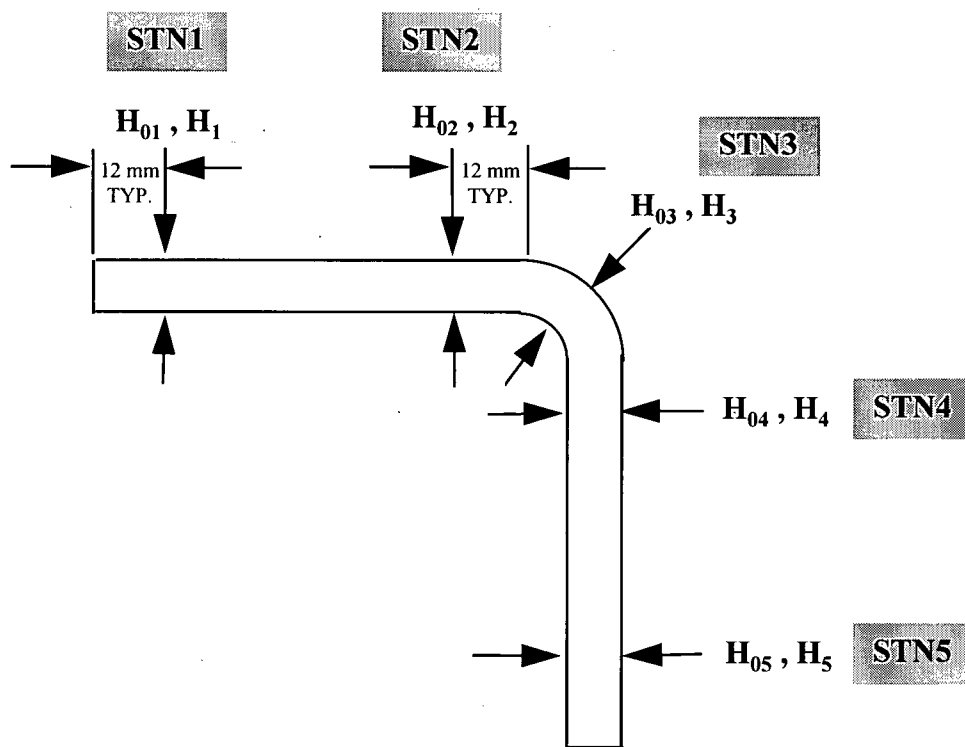


Figure 5.18 Angle thickness measurement stations.

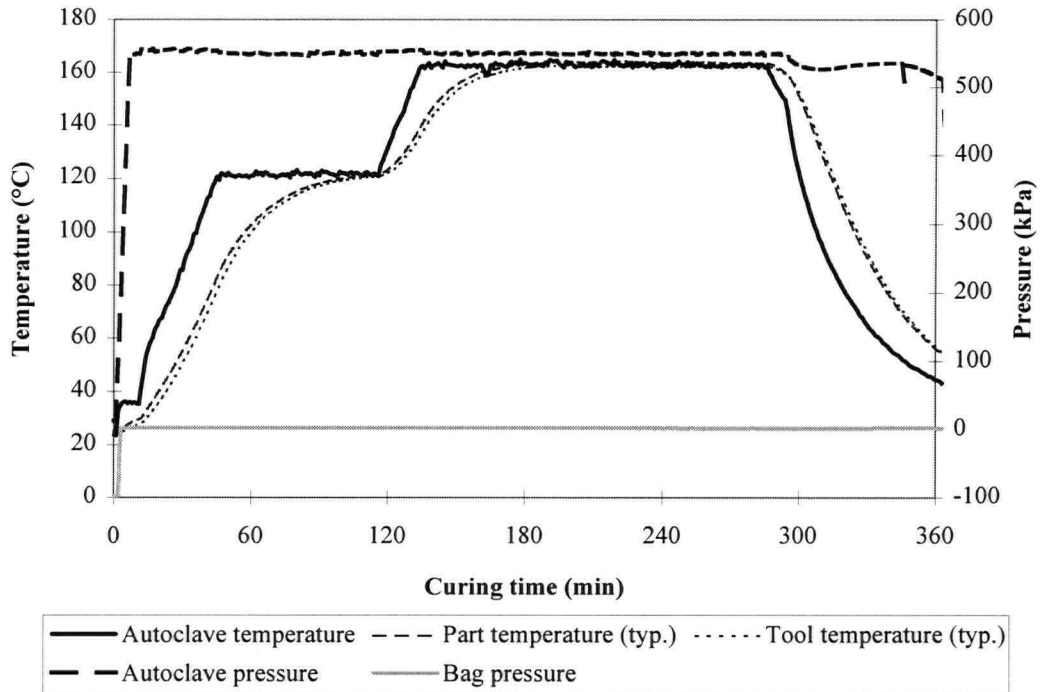


Figure 5.19 Temperature and pressure variation recorded during the cure showing the temperature gradients between the autoclave, tool and part temperatures. The tool and part temperatures shown are representative of the results for all thermocouples located in similar areas.

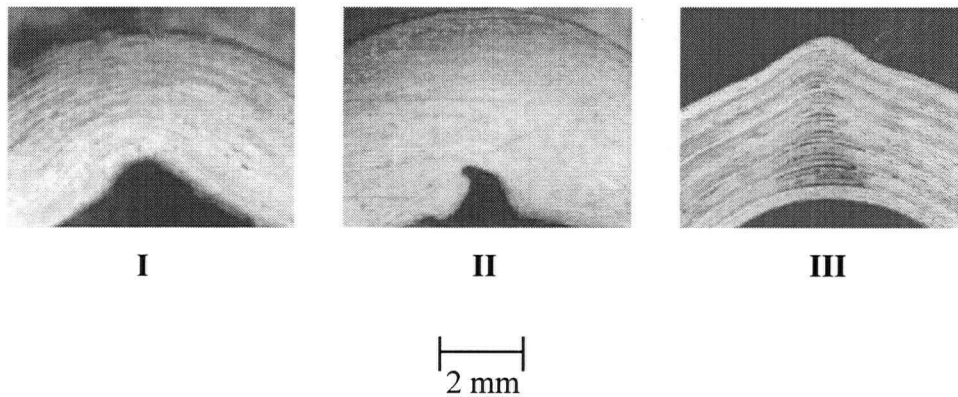


Figure 5.20 Photographs of the cross-section of samples showing the aspect of the defects found. The defects distribution is presented in Table 5.3.

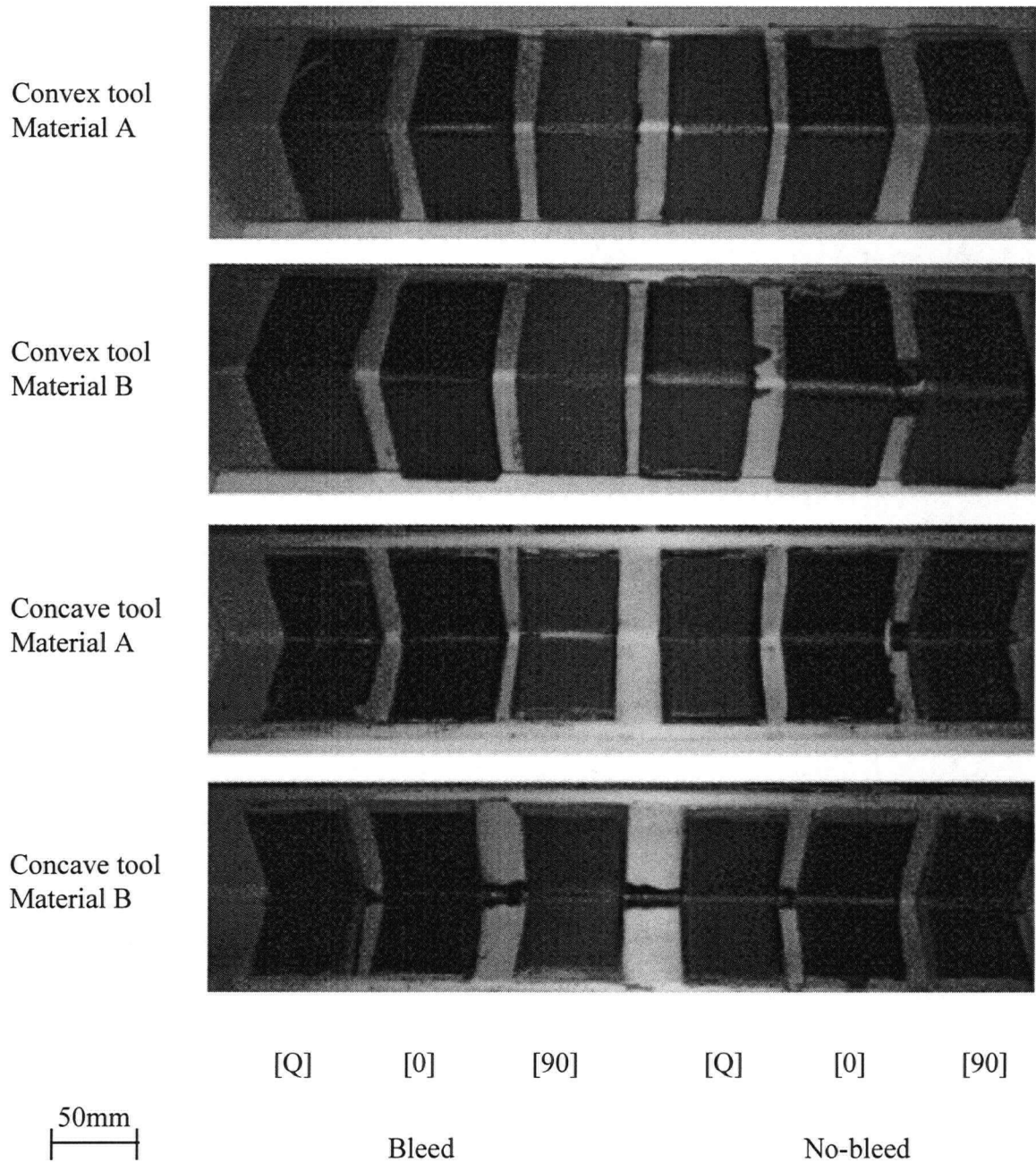


Figure 5.21 Photographs of the samples after removal of the bagging elements. Resin can be seen at the edges of the samples.

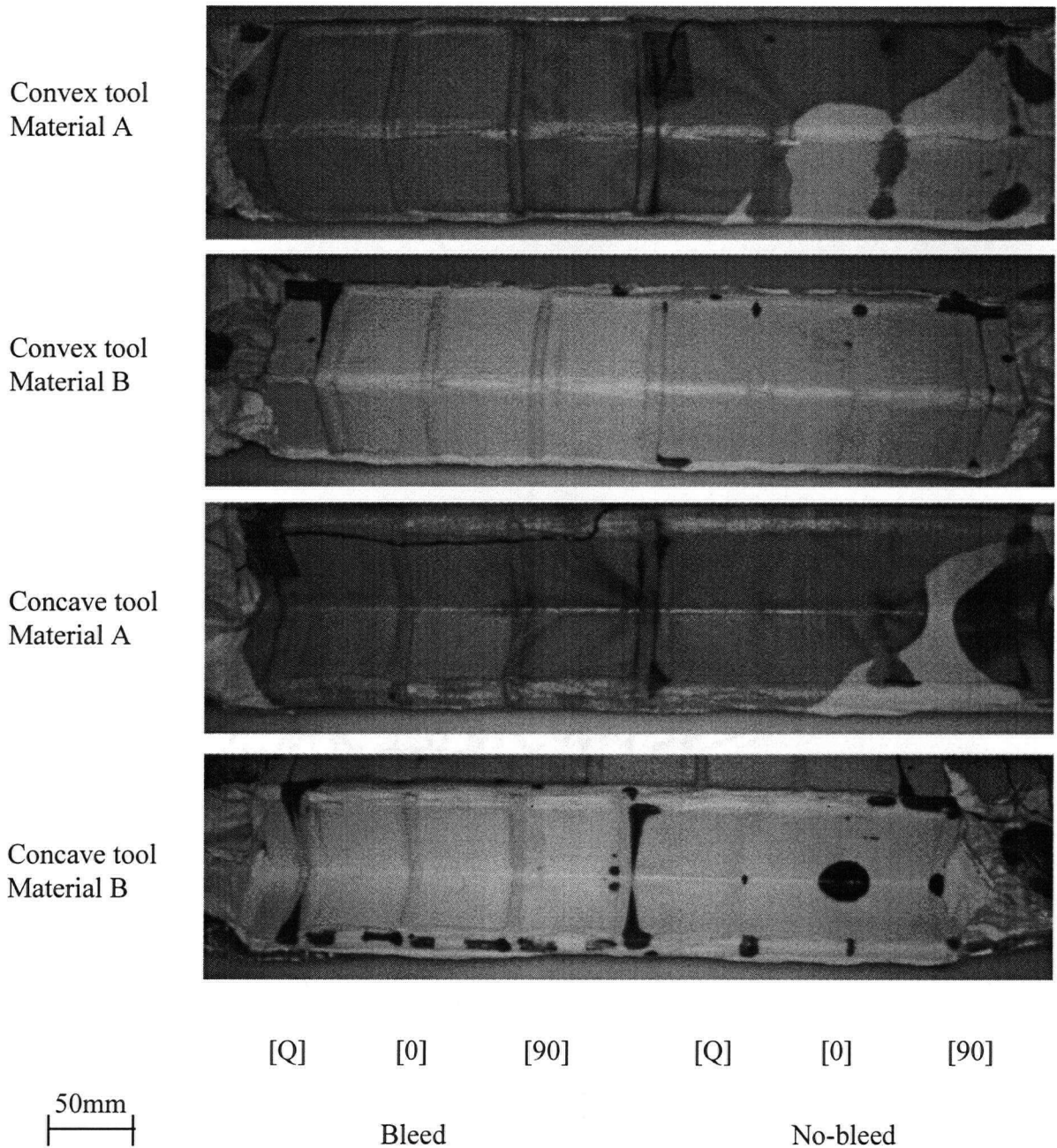


Figure 5.22 Photographs showing the exterior aspect of the bags after cure. Resin is seen mainly with material A.

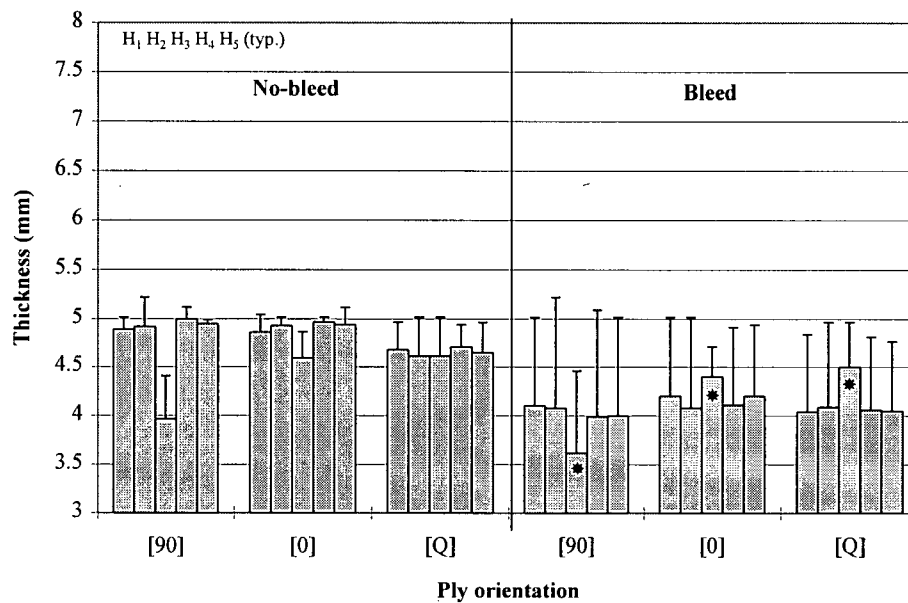


Figure 5.23 Thickness measurements after cure for material A with convex tool. The top of the error bar corresponds to the initial thickness of the laminate. The symbol * indicates the presence of minor defect at the corner.

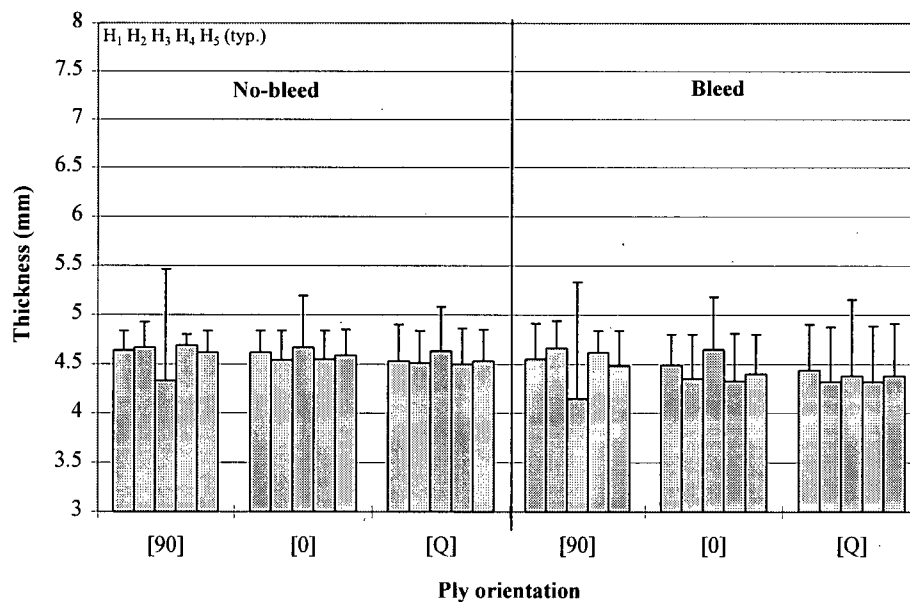


Figure 5.24 Thickness measurements after cure for material B with convex tool. The top of the error bar corresponds to the initial thickness of the laminate.

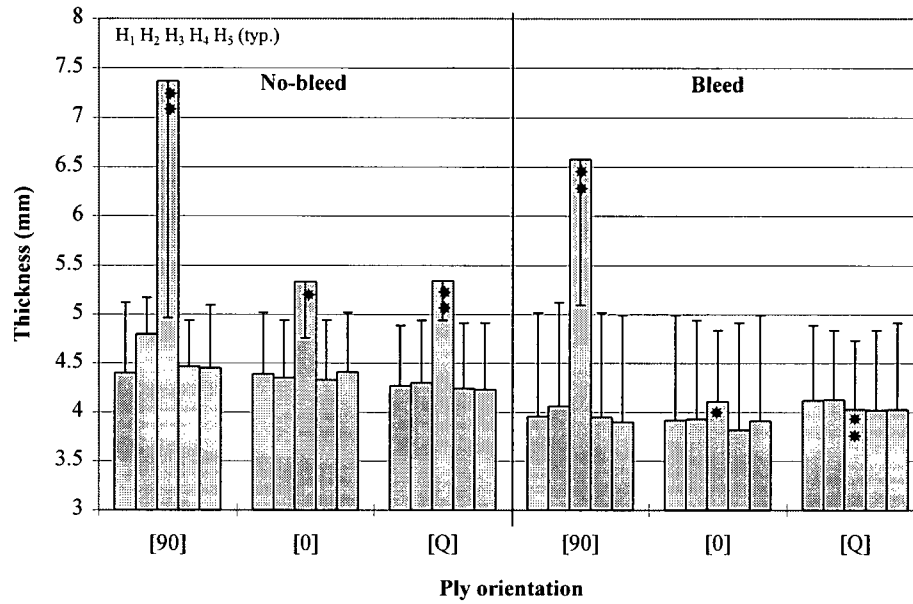


Figure 5.25 Thickness measurements after cure for material A with concave tool. The top of the error bar corresponds to the initial thickness of the laminate. The symbols * and ** indicate the presence of minor and major defects at the corner respectively.

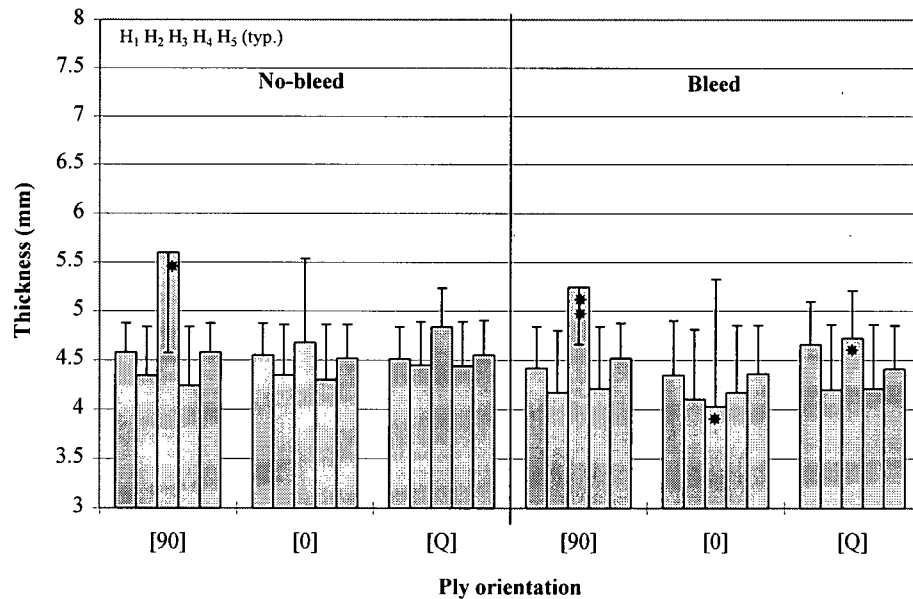


Figure 5.26 Thickness measurements after cure for material B with concave tool. The top of the error bar corresponds to the initial thickness of the laminate. The symbols * and ** indicate the presence of minor and major defects at the corner respectively.

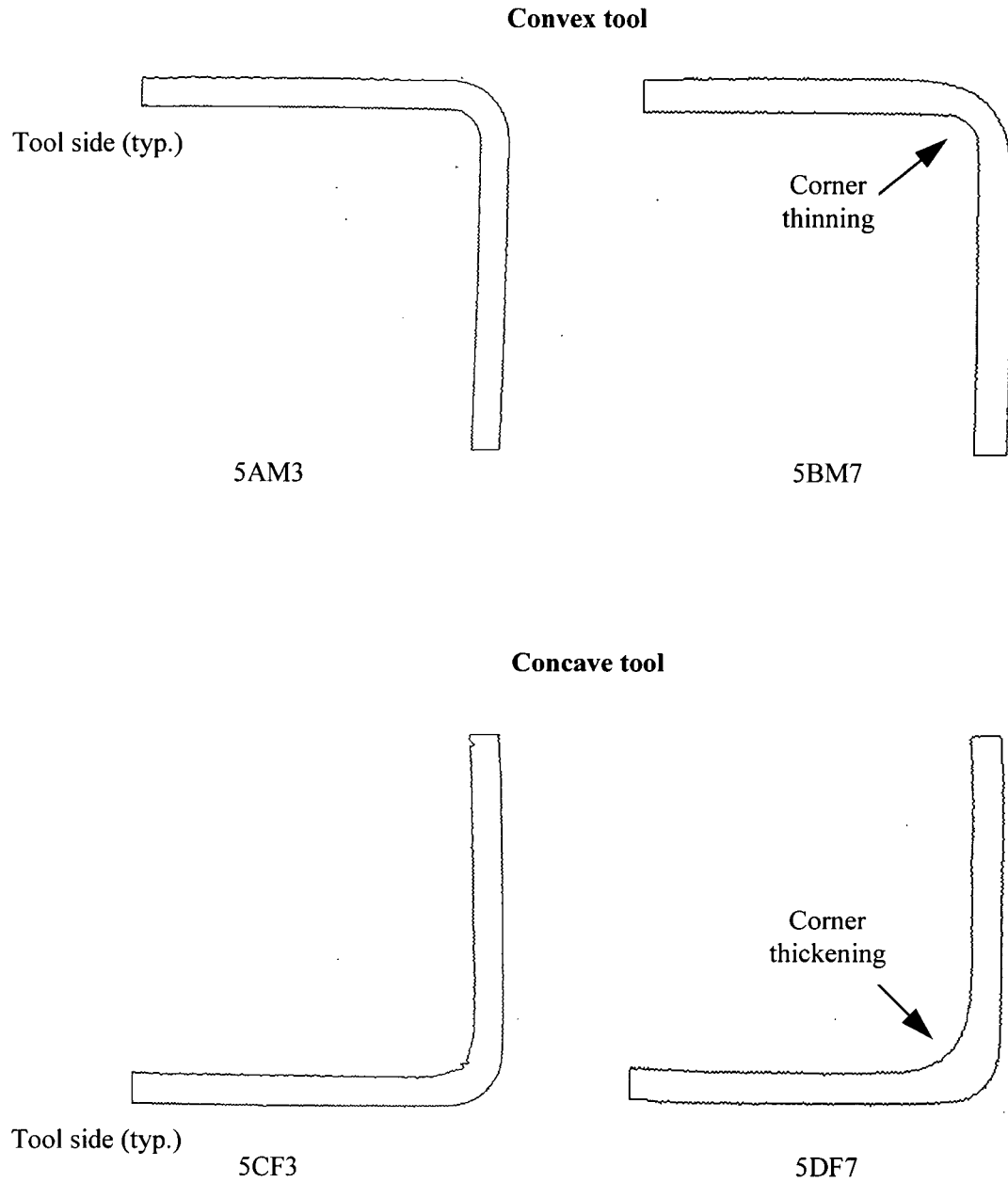


Figure 5.27 Angle profiles obtained from image analysis of photographs of the specimen cross-sections. Good quality samples are shown on the left (5AM3 and 5CF3). On the right, thickness gradients at the corner for [90] samples (5BM7 and 5DF7) are exemplified by corner thinning and thickening.

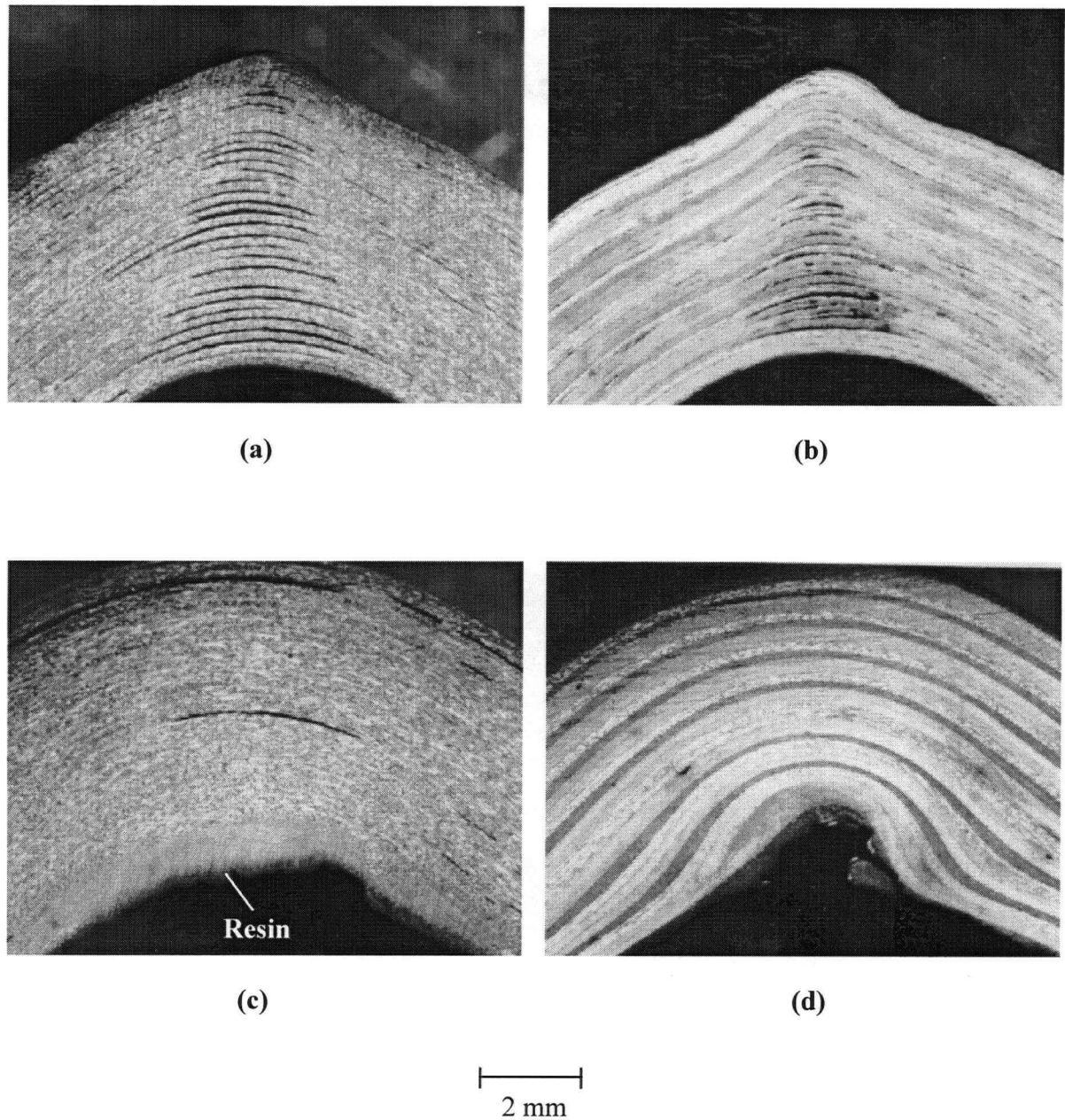


Figure 5.28 Microphotographs of the cross-section of samples with defect at the corner for convex tool ((a) and (b)) and concave tool ((c) and (d)), (a) [0] sample (5BM11), (b) [Q] sample (5BM12), (c) [0] sample (5DF8) and (d) [Q] sample (5DF9).

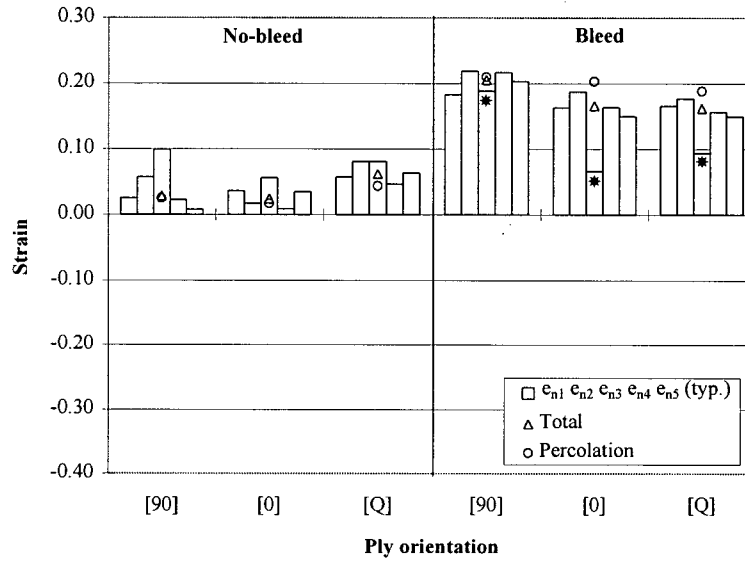


Figure 5.29 Laminate strains for material A with convex tool. The strains at the measuring points are shown by the white bars. The total strain (ϵ_{total}) and the percolation strain ($\epsilon_{percolation}$) are also shown. The symbol * indicates the presence of minor defect at the corner. The strain sign is inverted so that positive indicates compression.

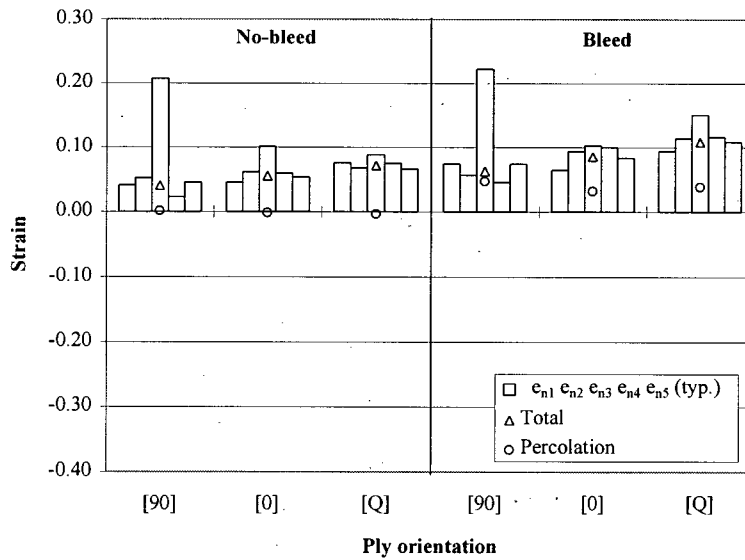


Figure 5.30 Laminate strains for material B with convex tool. The strains at the measuring points are shown by the white bars. The total strain (ϵ_{total}) and the percolation strain ($\epsilon_{percolation}$) are also shown. The strain sign is inverted so that positive indicates compression.

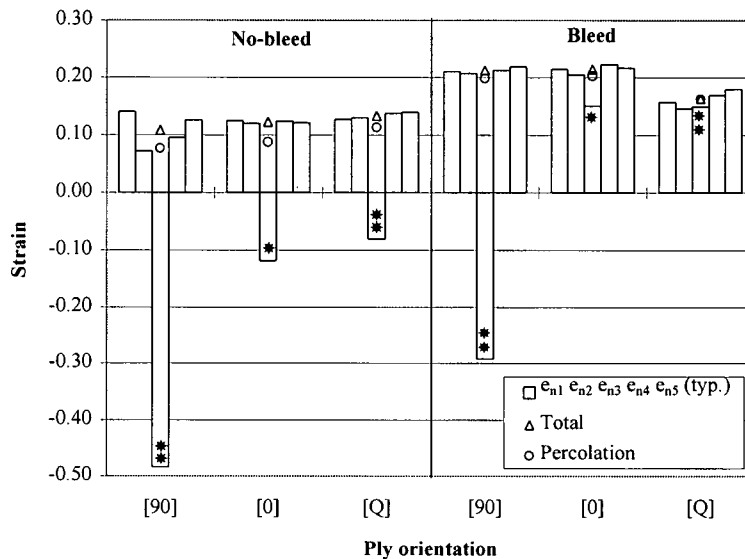


Figure 5.31 Laminate strains for material A with concave tool. The strains at the measuring points are shown by the white bars. The total strain (ϵ_{total}) and the percolation strain ($\epsilon_{percolation}$) are also shown. The symbols * and ** indicate the presence of minor and major defects at the corner respectively. The strain sign is inverted so that positive indicates compression.

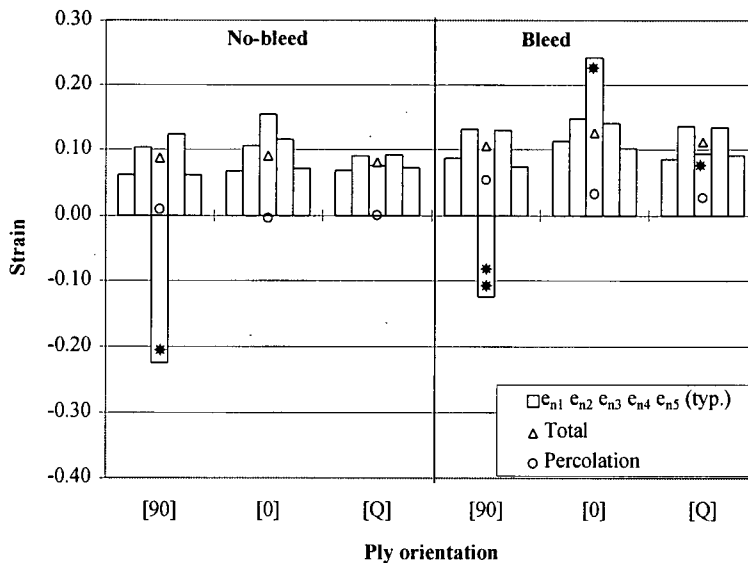


Figure 5.32 Laminate strains for material B with concave tool. The strains at the measuring points are shown by the white bars. The total strain (ϵ_{total}) and the percolation strain ($\epsilon_{percolation}$) are also shown. The symbols * and ** indicate the presence of minor and major defects at the corner respectively. The strain sign is inverted so that positive indicates compression.

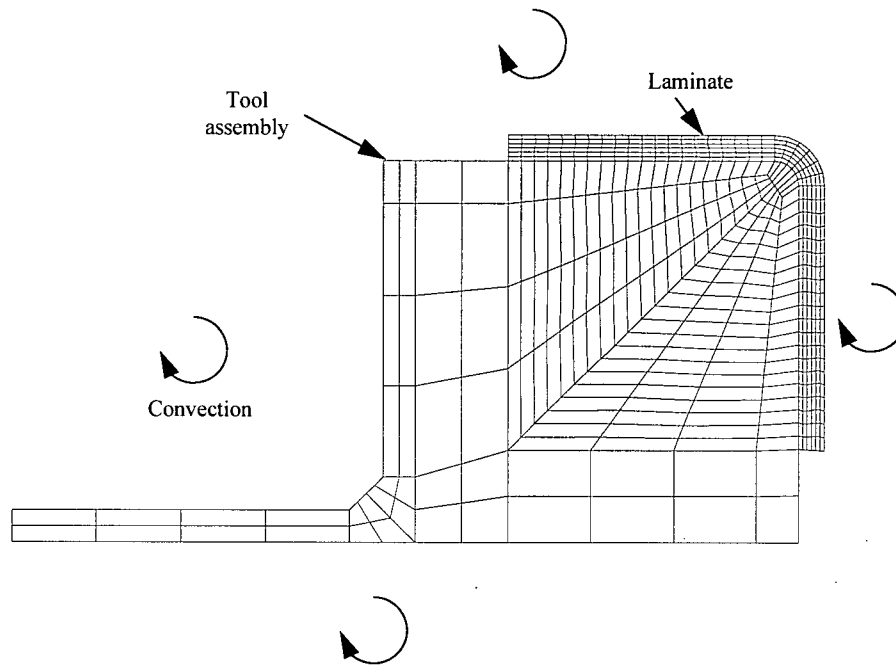


Figure 5.33 Finite element mesh including the tool and the laminate used for temperature predictions.

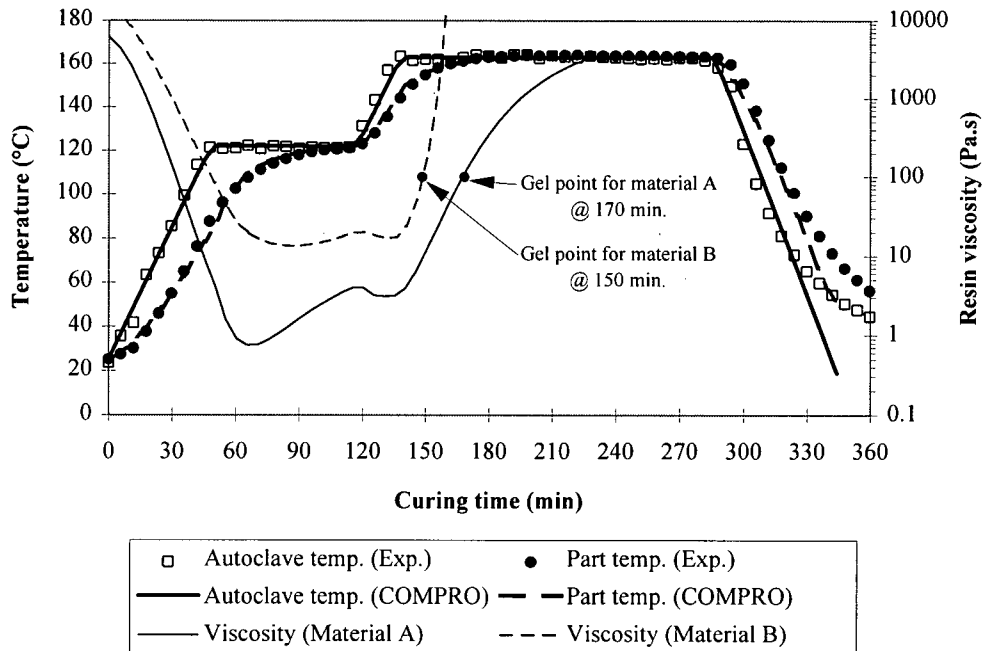
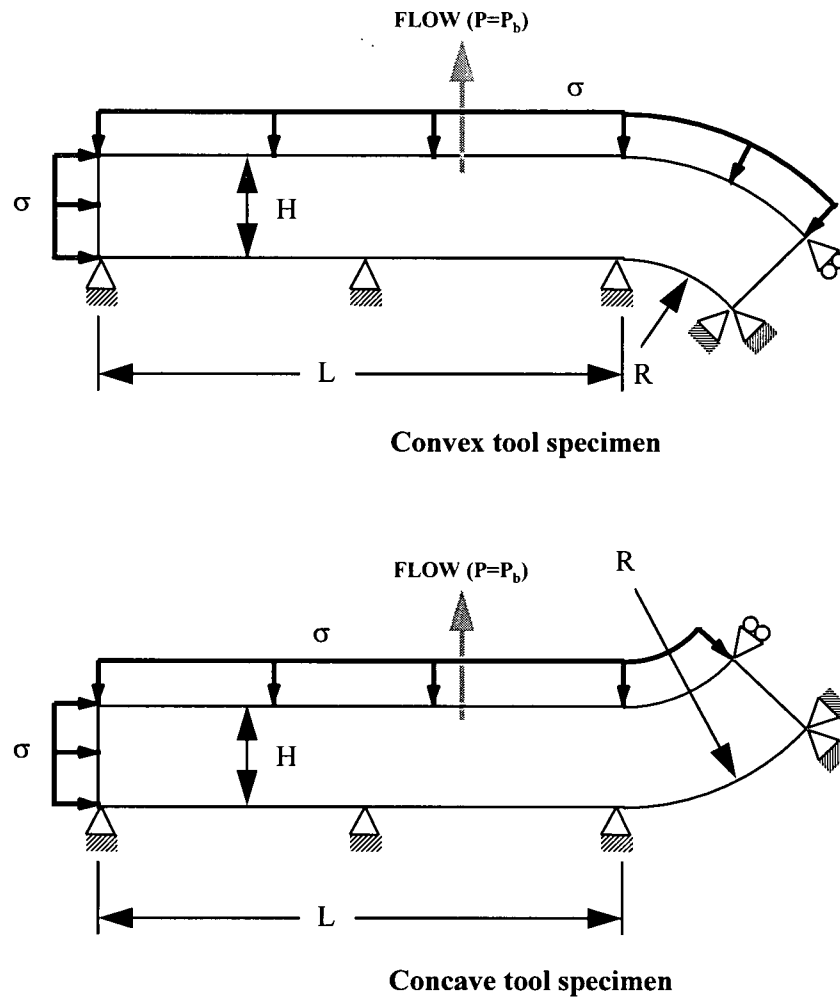


Figure 5.34 Temperature profiles predicted by COMPRO compared to the experiments. The viscosity profiles predicted for the two materials are also shown indicating the gel time of the resin.



Material properties

Material: A

μ =see Table B.2
 K_1 =Eqn. 2.8 $k=0.7$
 K_2 =Eqn. 2.9 $k'=0.2, V_a'=0.81$
 [0°]
 $E_1=100$ GPa
 E_3 =see compaction curve
 $G_{13}=0.5$ MPa
 [90°]
 $E_1=E_3$ =see compaction curve
 $G_{13}=0.5$ MPa

Material: B

μ =see Table B.2
 K_1 =Eqn. 2.8 $k=0.7$
 K_2 =Eqn. 2.9 $k'=0.2, V_a'=0.68$
 [0°]
 $E_1=100$ GPa
 E_3 =see compaction curve
 $G_{13}=0.5$ MPa
 [90°]
 $E_1=E_3$ =see compaction curve
 $G_{13}=0.5$ MPa

Compaction curves

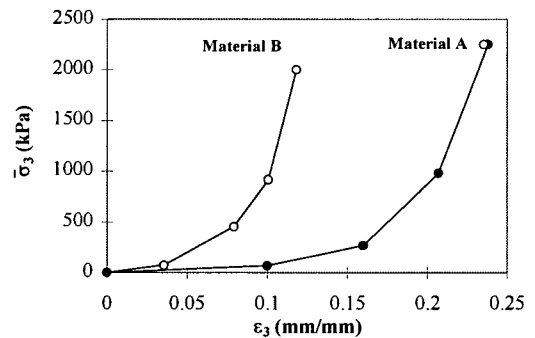
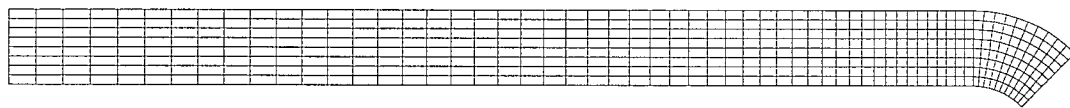
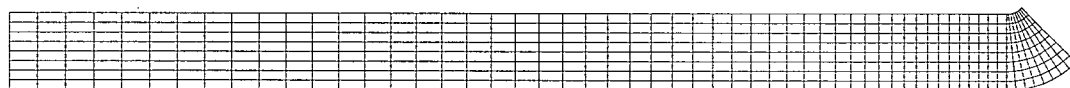


Figure 5.35 Finite element models definition and material properties for angle laminate simulations.

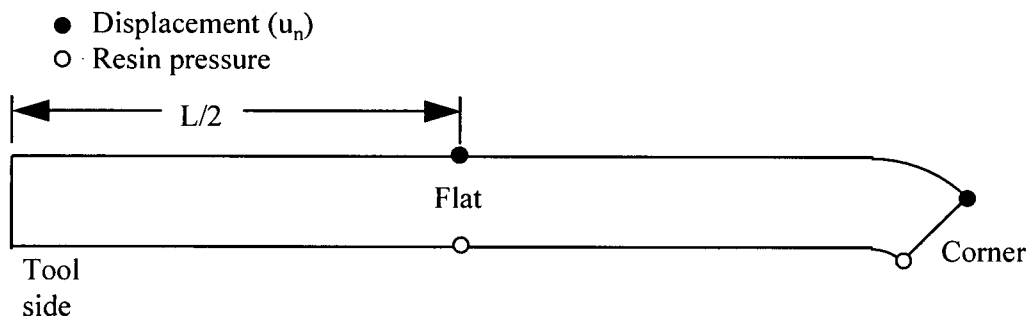


Convex tool specimen

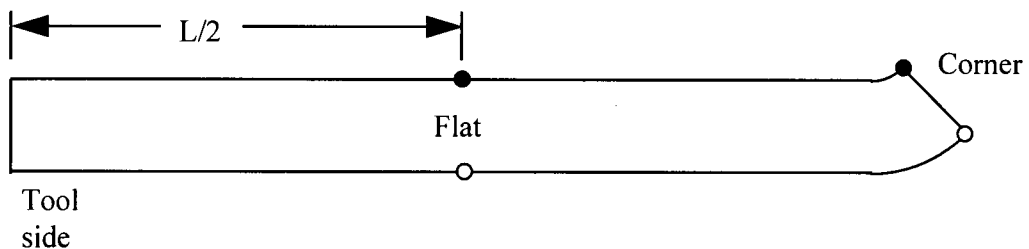


Concave tool specimen

Figure 5.36 Finite element meshes for convex tool specimens (464 elements) and concave tool specimens (448 elements).



Convex tool specimen



Concave tool specimen

Figure 5.37 Location of node outputs of COMPRO simulations for the normal displacement and the resin pressure.

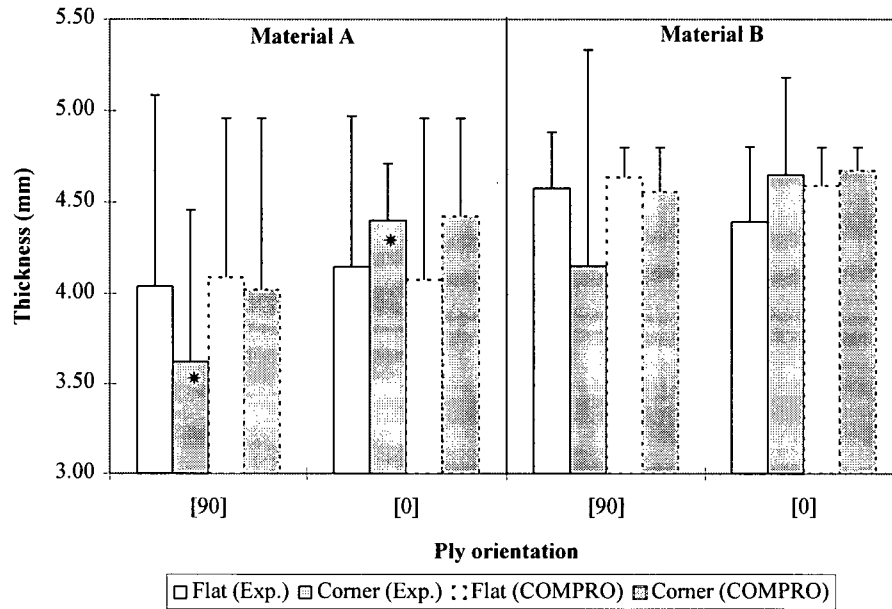


Figure 5.38 Comparison between the predicted and measured final thickness for the convex tool laminates. The top of the error bar corresponds to the initial thickness of the laminate. The symbol * indicates the presence of a minor defect at the corner.

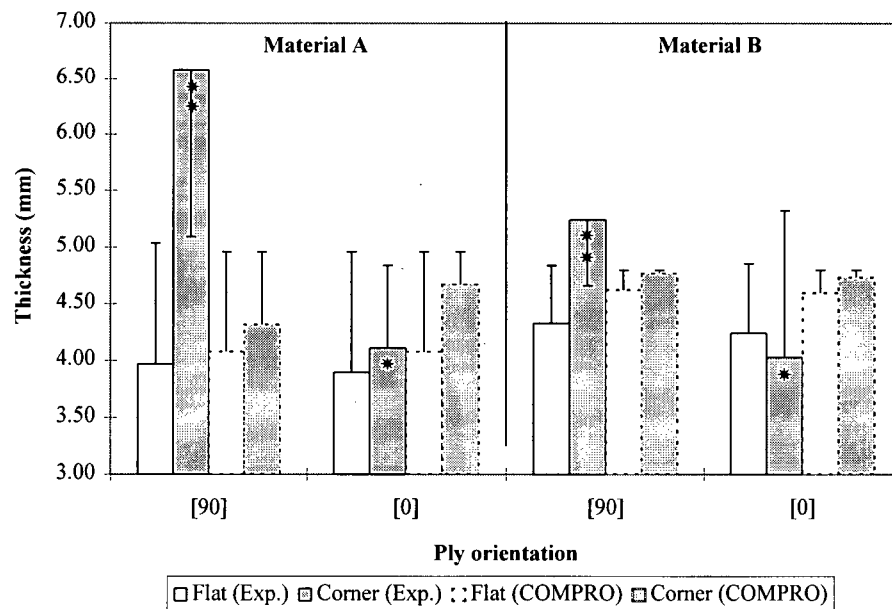


Figure 5.39 Comparison between the predicted and measured final thickness for the concave tool laminates. The top of the error bar corresponds to the initial thickness of the laminate. The symbols * and ** indicate the presence of minor and major defects at the corner respectively.

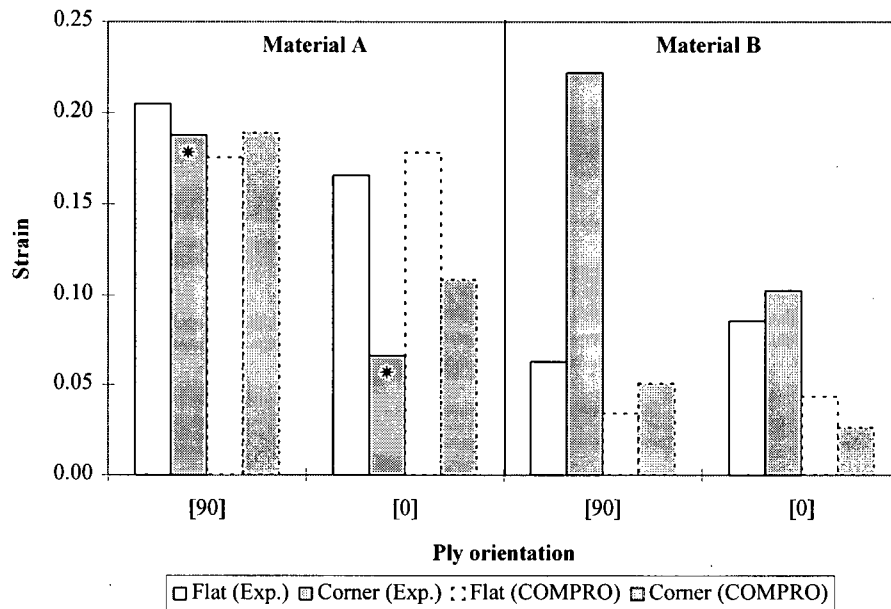


Figure 5.40 Comparison between the experimental (ϵ_{total}) and predicted (ϵ_n) normal strain for convex tool laminates. The symbol * indicates the presence of a minor defect at the corner. The strain sign is inverted so that positive indicates compression.

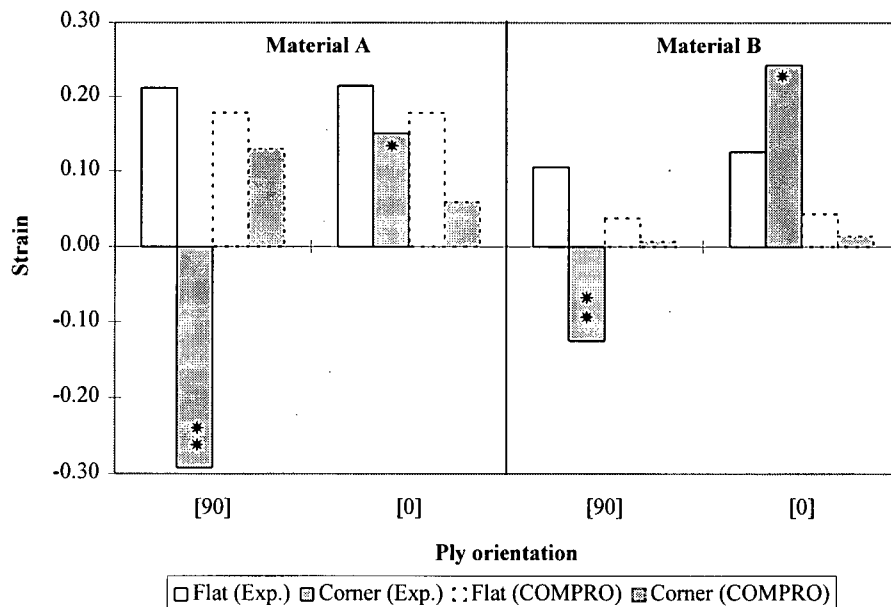


Figure 5.41 Comparison between the experimental (ϵ_{total}) and predicted (ϵ_n) normal strain for concave tool laminates. The symbols * and ** indicate the presence of minor and major defects at the corner respectively. The strain sign is inverted so that positive indicates compression.

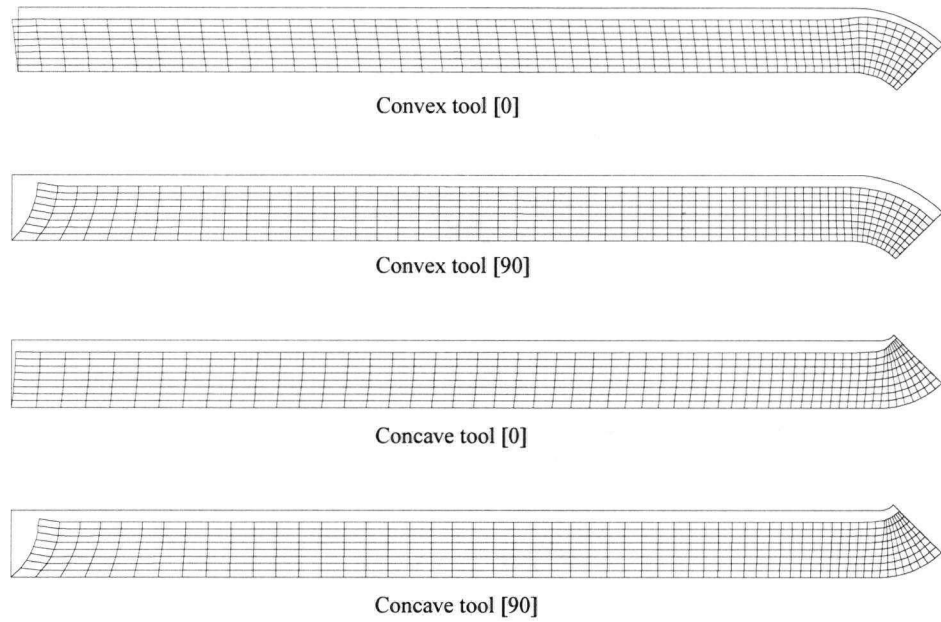
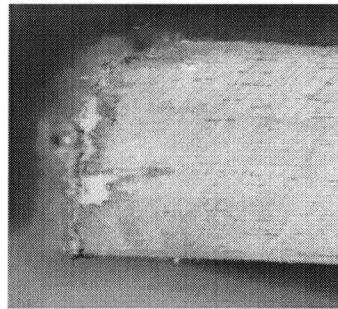


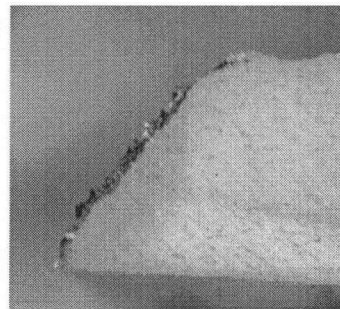
Figure 5.42 Predicted deformed shape at the end of the compaction for material A laminates. The original shape of the laminate is shown by the solid line.

Bag side



Tool side

[0]



[90]

2 mm

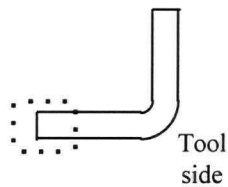


Figure 5.43 Photograph of the edge profile of the laminates after cure for sample moulded with concave tool. The cross-sections shown are in the x-z plane (Figure 5.11 (a)).

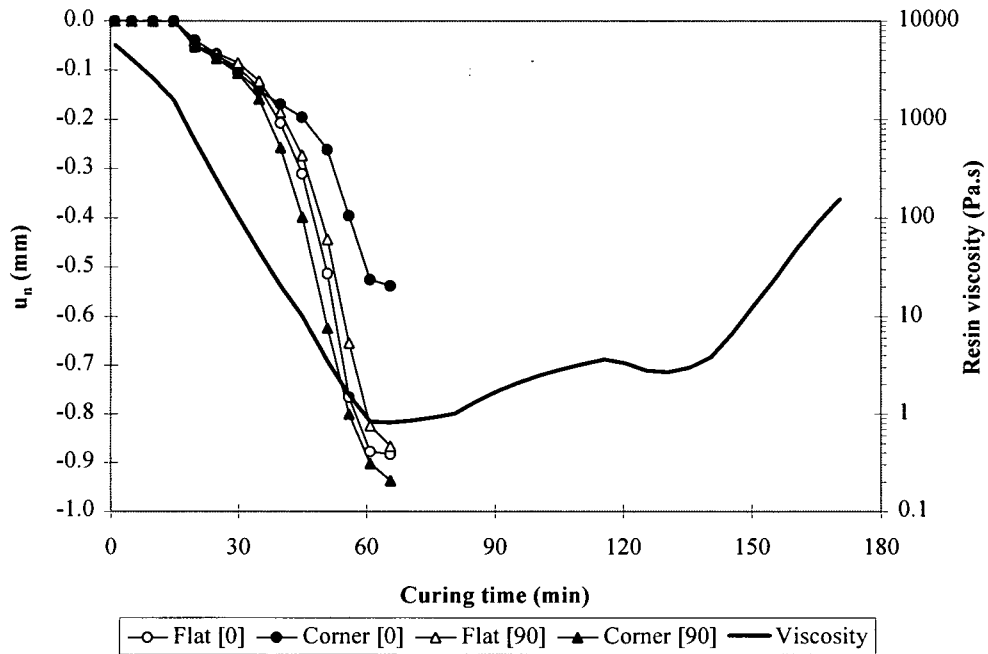


Figure 5.44 Angle laminate compaction behaviour predicted by COMPRO for material A, convex tool. The viscosity profile for the resin is also shown.

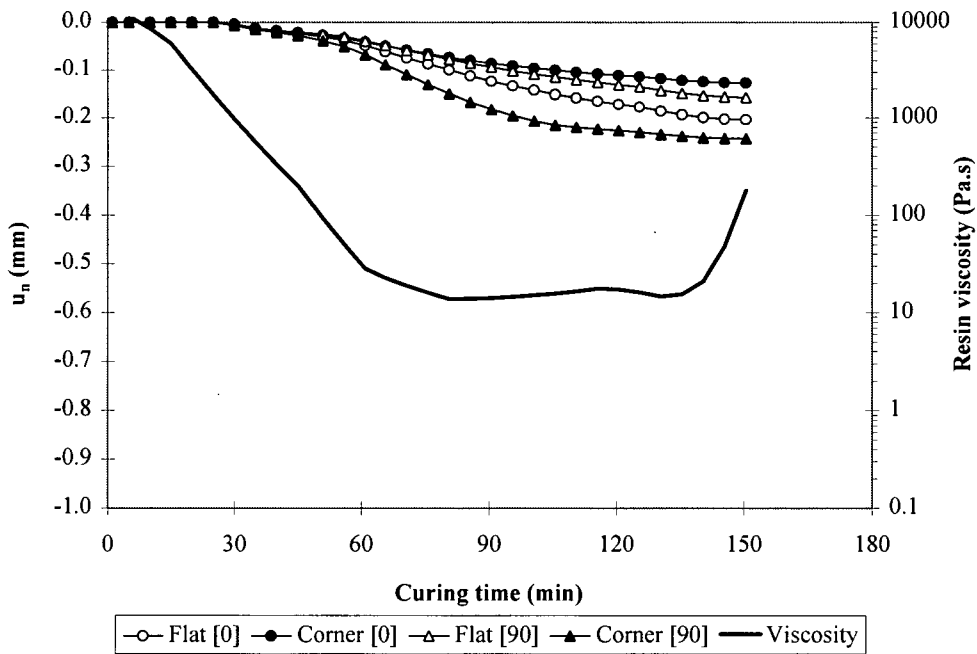


Figure 5.45 Angle laminate compaction behaviour predicted by COMPRO for material B, convex tool. The viscosity profile for the resin is also shown.

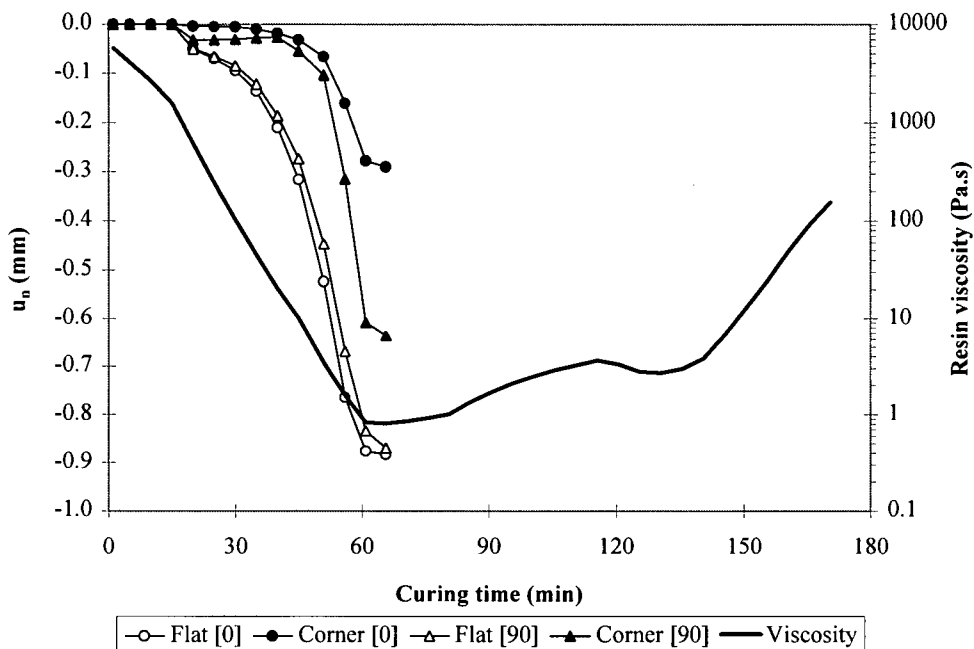


Figure 5.46 Angle laminate compaction behaviour predicted by COMPRO for material A, concave tool. The viscosity profile for the resin is also shown.

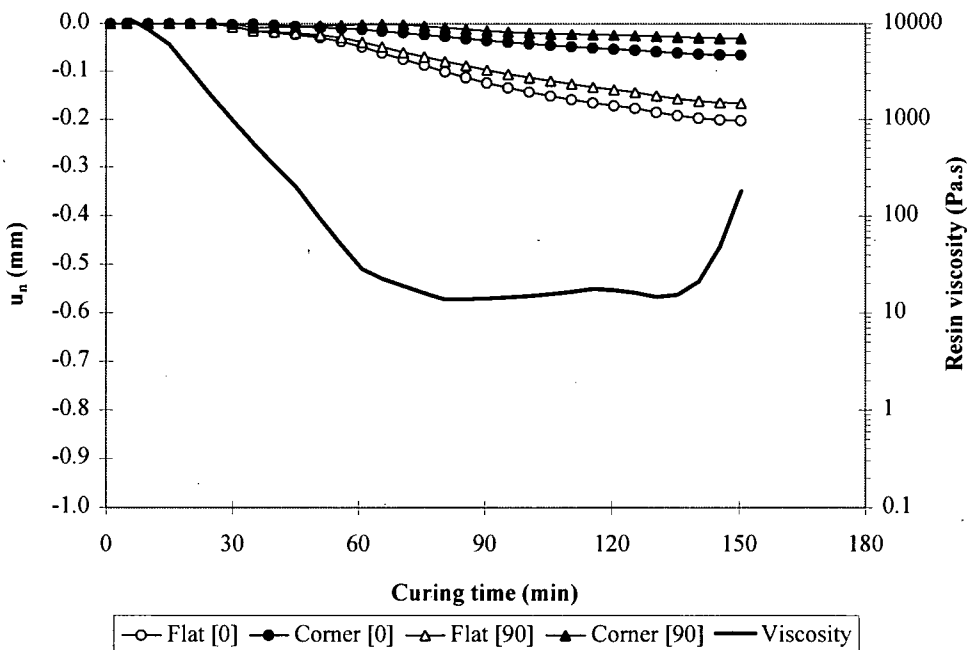


Figure 5.47 Angle laminate compaction behaviour predicted by COMPRO for material B, concave tool. The viscosity profile for the resin is also shown.

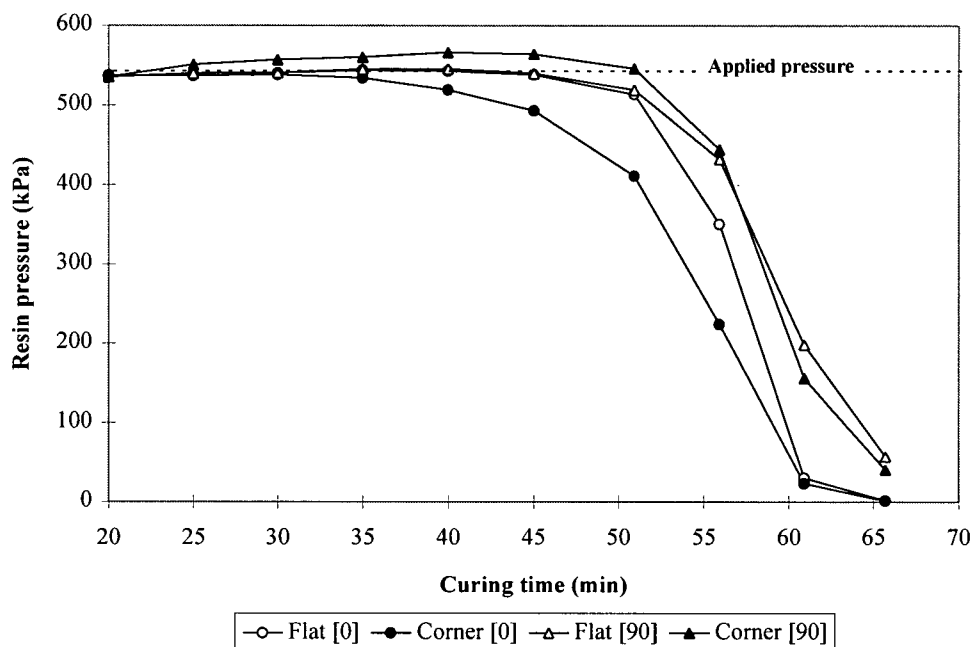


Figure 5.48 Resin pressure variation at the tool surface (Figure 5.37) predicted by COMPRO for material A, convex tool.

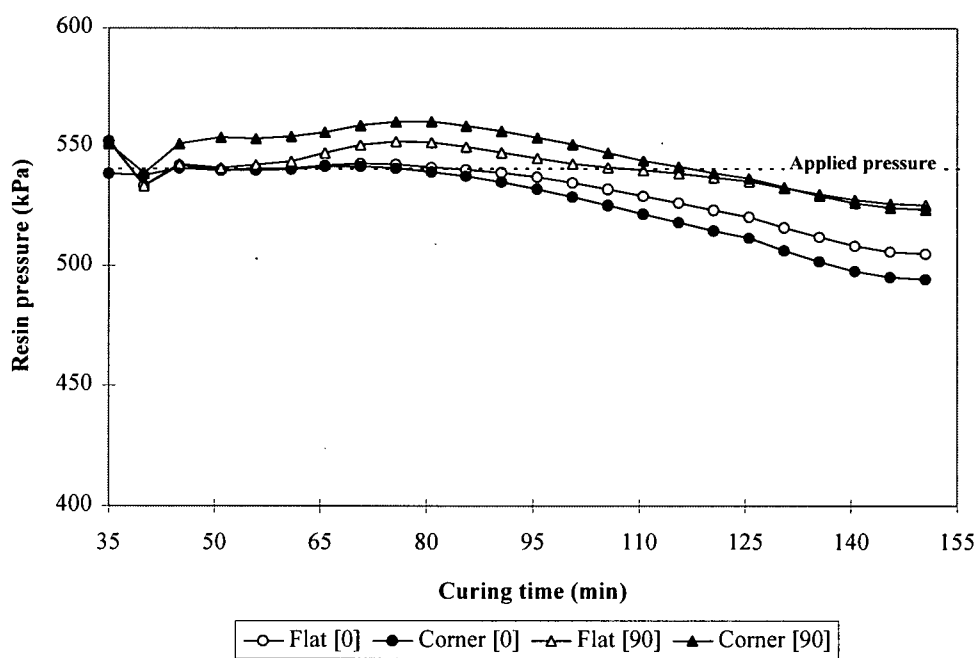


Figure 5.49 Resin pressure variation at the tool surface (Figure 5.37) predicted by COMPRO for material B, convex tool.

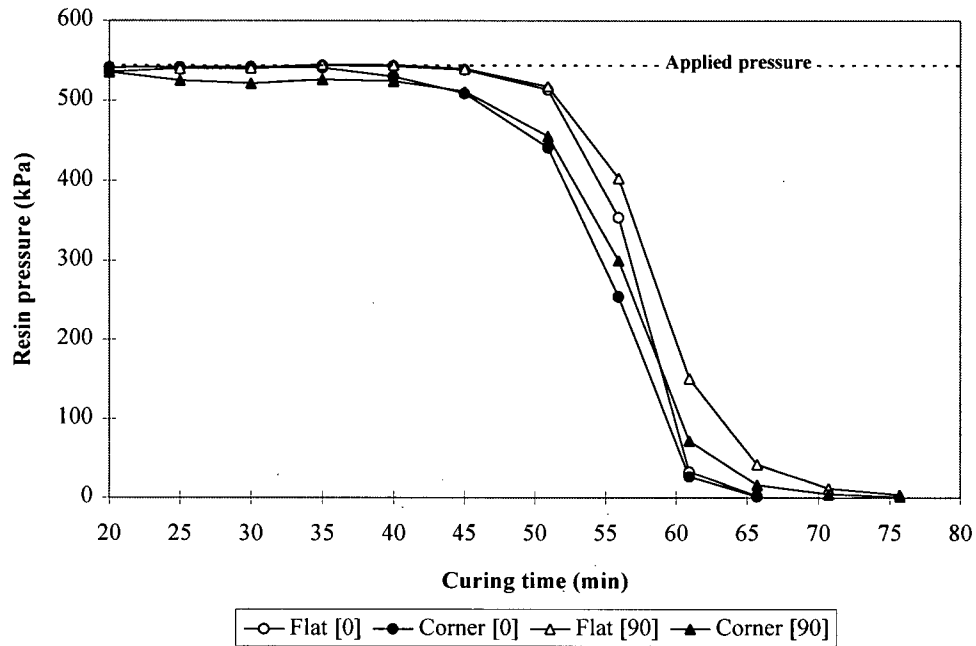


Figure 5.50 Resin pressure variation at the tool surface (Figure 5.37) predicted by COMPRO for material A, concave tool.

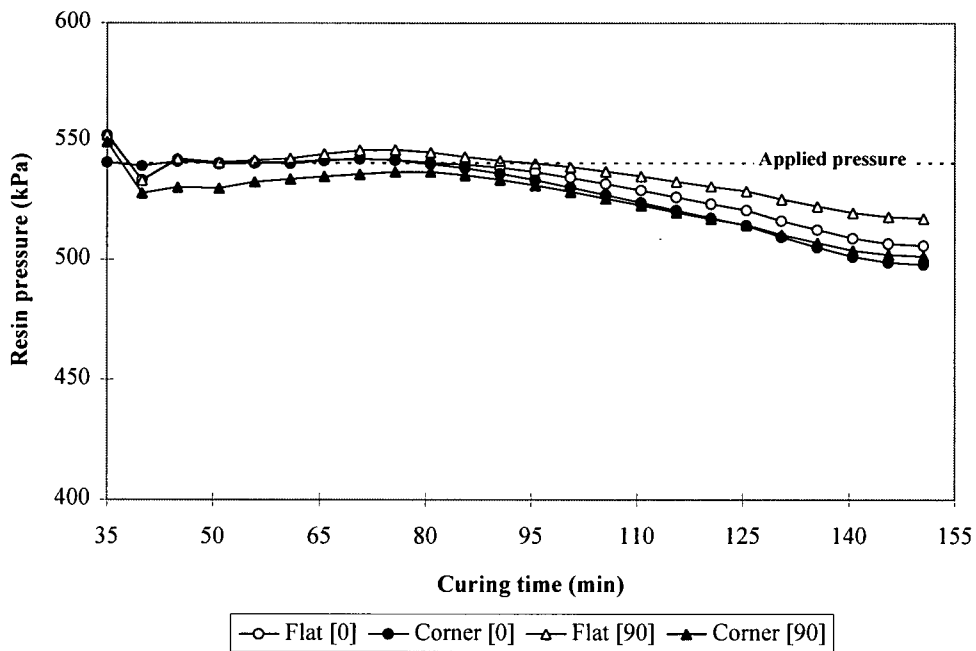


Figure 5.51 Resin pressure variation at the tool surface (Figure 5.37) predicted by COMPRO for material B, concave tool.

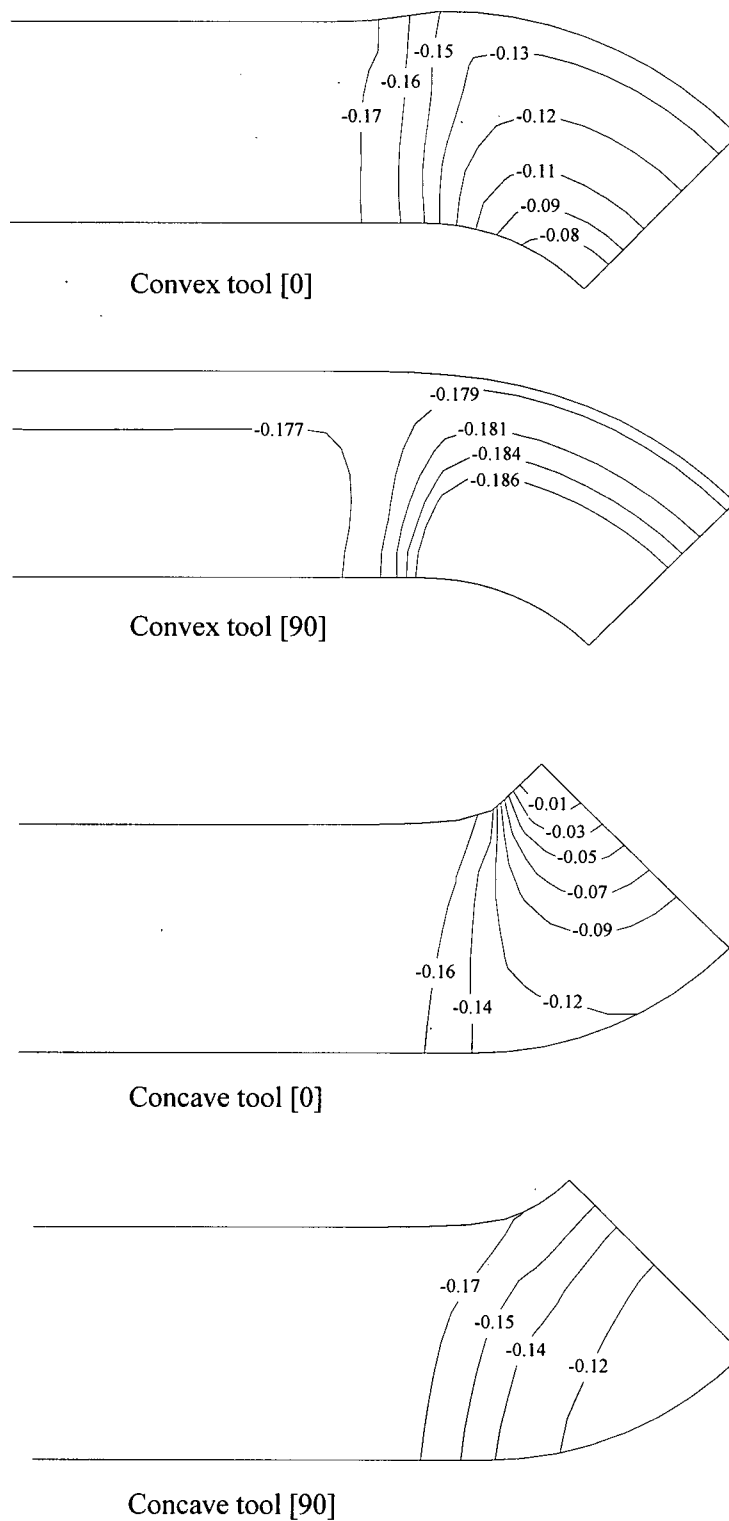


Figure 5.52 Contours for the normal strain ϵ_3 at the end of compaction predicted by COMPRO for laminates with material A.

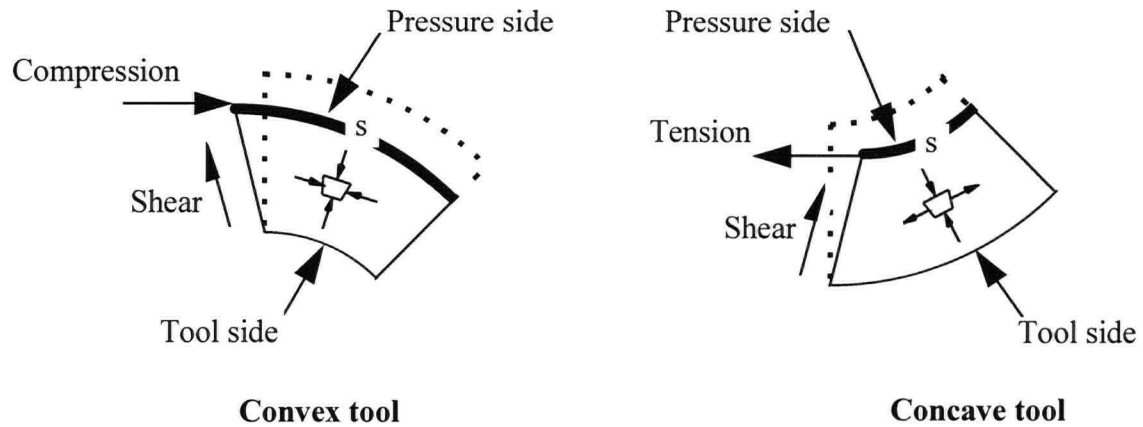


Figure 5.53 Longitudinal and shear stresses generated by the compaction of a curvilinear fibre bed for convex and concave tool configurations. The original shape is shown by the dotted lines. The fibres are oriented along s and are assumed to be very stiff in that direction.

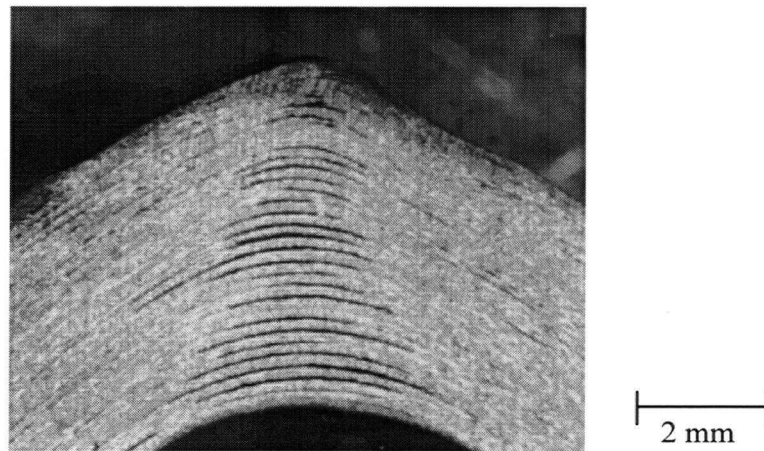
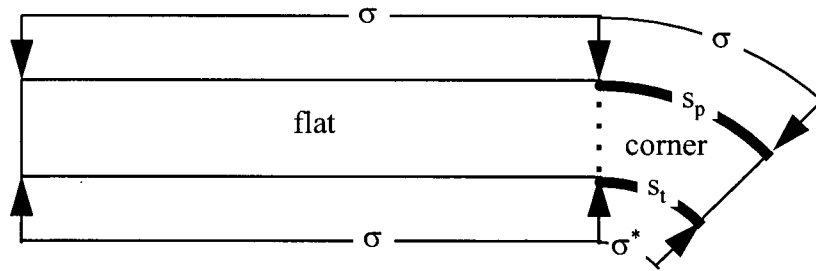
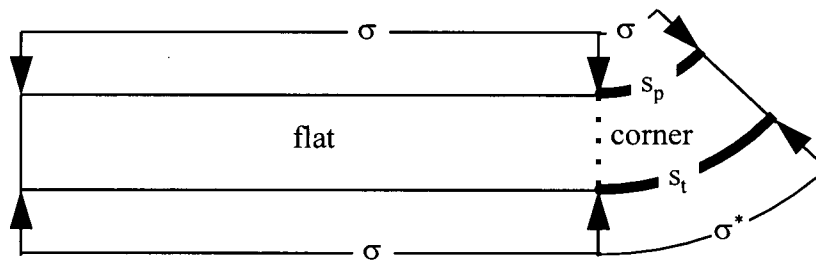


Figure 5.54 Photograph of a wrinkle at the corner of a $[0]$ lay-up with material A on a convex tool. The fibres are bridging at the corner creating voids (dark lines).



$$s_p > s_t \rightarrow \sigma^* > \sigma$$

Convex tool



$$s_p < s_t \rightarrow \sigma^* < \sigma$$

Concave tool

Figure 5.55 Reaction stress at the corner (σ^*) for the different tool configuration, convex and concave. σ is the applied pressure, s_p is the surface exposed to the pressure and s_t is the surface exposed to the tool.

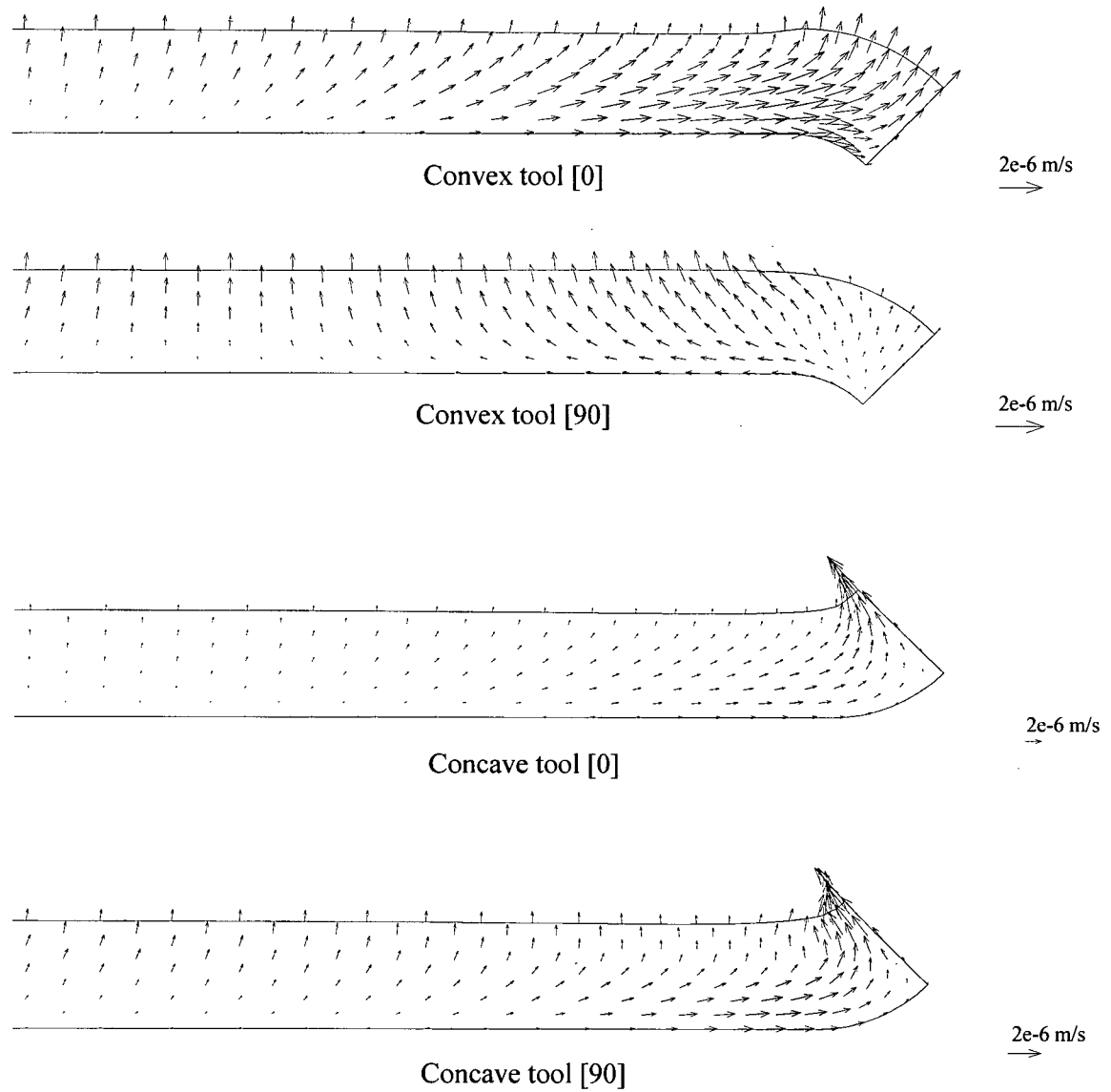


Figure 5.56 Resin velocity vector plot predicted by COMPRO during the compaction of the laminates at $t=50$ minutes for material A.

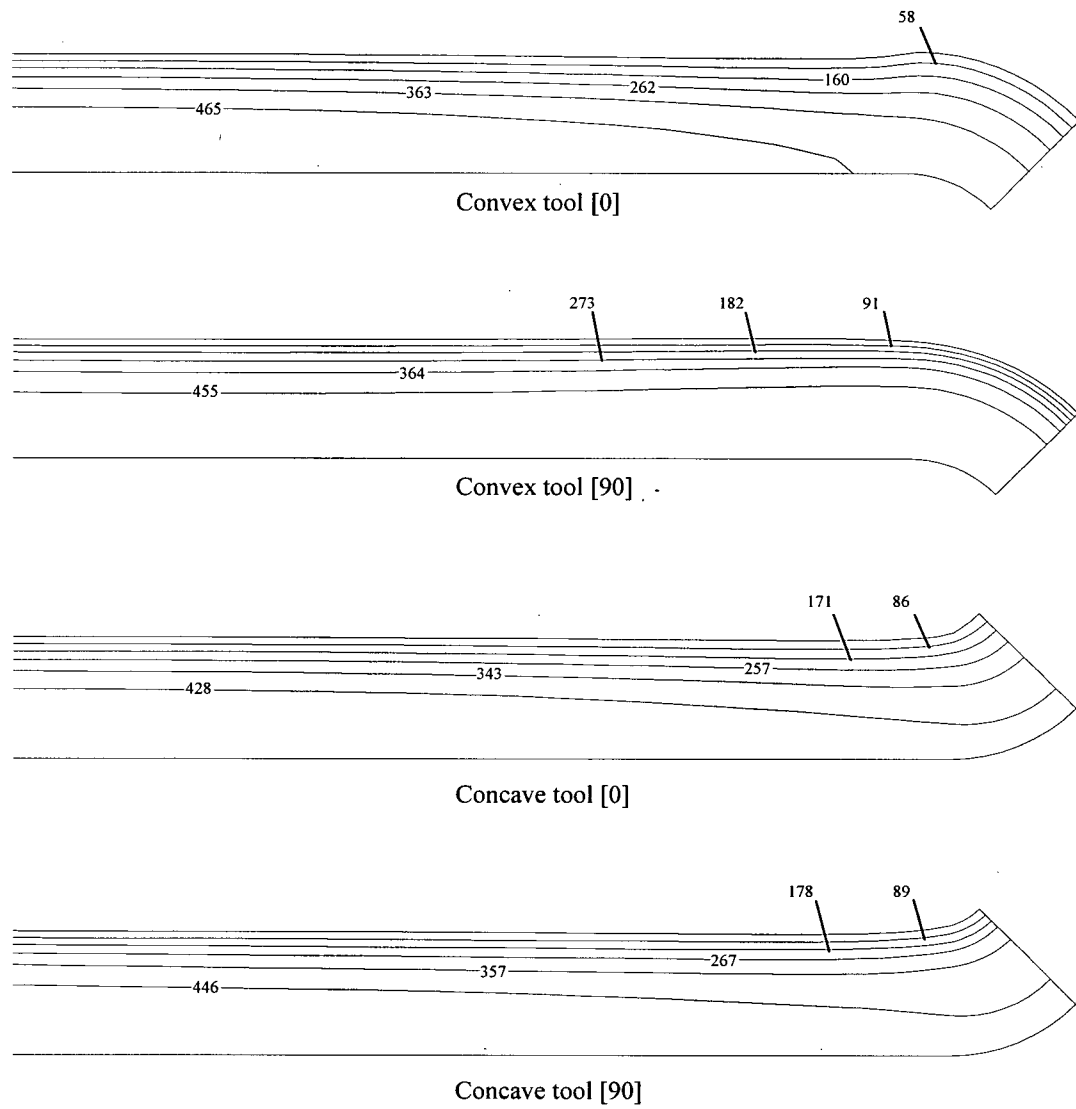


Figure 5.57 Resin pressure (kPa) contours predicted by COMPRO during the compaction of the laminates at $t=50$ minutes for material A.

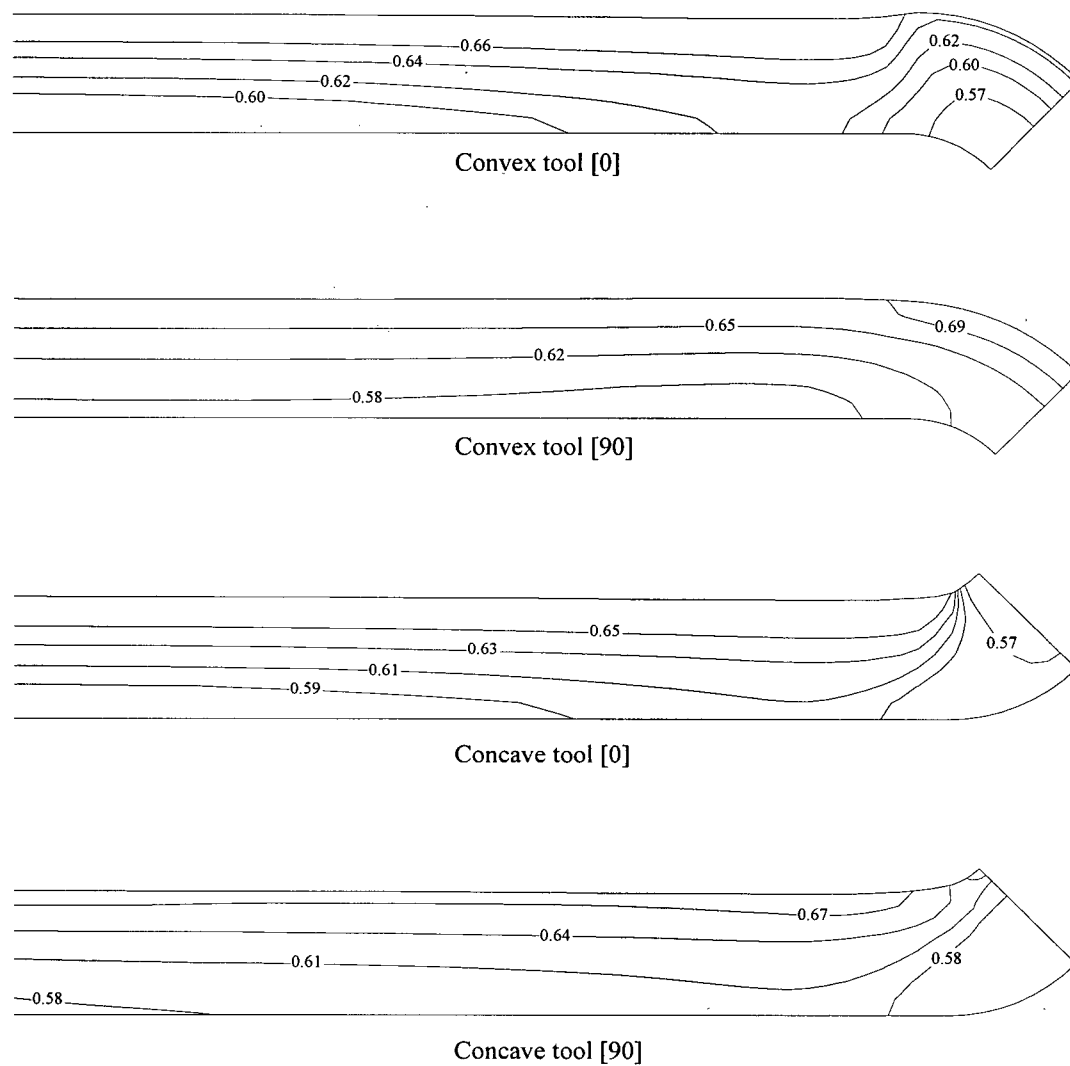


Figure 5.58 Fibre volume fraction contours predicted by COMPRO during the compaction of the laminates at $t=50$ minutes for material A.

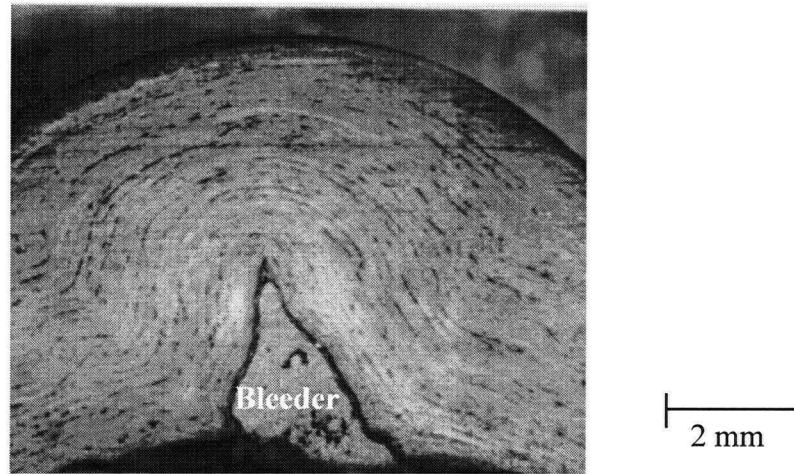


Figure 5.59 Photograph of a wrinkle at the corner of a [90] lay-up with material A on concave tool. The bag wedged the laminate at the corner. The bleeder stayed included in the laminate as shown.

Chapter 6 Aspects of Shear Flow and the Interaction with Percolation

Flow

The study of the compaction of angle laminates presented in Chapter 5 shows that part of the local deformation of the laminate at the corner is caused by shear flow. This behaviour is mainly observed when the fibres are oriented in the direction perpendicular to the flow direction (i.e. [90] lay-up). In this chapter, shear flow behaviour and its interaction with percolation flow of the resin is investigated for a simple laminate geometry. In the first section, results from the direct observation of the deformation behaviour of a laminate during compaction are presented. In the following section, the analysis of results of shear flow and percolation flow for different compaction conditions is presented.

6.1 Shear flow experimental investigation

The shear flow modelling is based on assumptions regarding the behaviour of the material during the flow process. The analytical approach for shear modelling was presented in Section 2.3.2.1.

The composite is assumed to behave as a highly anisotropic viscous fluid with:

- incompressibility and inextensibility in the fibre direction
- straight fibres that remain perfectly aligned during flow.

From these assumptions, the velocity components for planar flow (i.e. flow in the x-z plane) of the laminate shown in Figure 6.1 can be expressed as follows (Rogers, 1989):

$$v_x = -x \frac{\partial v_z}{\partial z}, \quad v_y = 0 \quad \text{and} \quad v_z = f(z, t) \quad (6.1)$$

where $f(z,t)$ is a function defining the velocity variation in the laminate. For the case studied in the shear flow experiments, the fibres are all oriented in the y direction, perpendicular to the flow direction (Figure 6.1). Thus the velocity in the y direction is zero because the fibre are assumed inextensible in this direction. The function for the velocity distribution $f(z,t)$ has the form (Rogers, 1989):

$$f(z, t) = Az^3 + Bz \quad (6.2)$$

where A and B are a function of time. The functions A and B are determined from the following boundary conditions:

- $v_x=0$ at $x=0$
- $v_z=0$ at $z=0$ and $v_z=\pm dH/dt$ at $z=\pm H$
- $\tau_{xz}=\pm\alpha_x v_x$ at $z=\pm H$

where τ_{xz} is the shear stress and α_x is a slip constant. The condition of the shear stress (τ_{xz}) at the boundary is to simulate the possible effect of friction at the tool-laminate interface. The slip constant (α_x) is expressed as a function of the composite transverse viscosity (η_T):

$$\alpha_x = \lambda_x \eta_T \quad (6.3)$$

where λ_x is a slip coefficient. For the no-slip condition, $\lambda_x \rightarrow \infty$, for the zero friction condition, $\lambda_x=0$ and for an intermediate friction condition, $0 < \lambda_x < \infty$. Balasubramanyam et al. (1989) gave the expression for A and B for the velocity profile function:

$$A = \frac{-dH/dt}{2H^2(H + 3/\lambda_x)} \quad \text{and} \quad B = -3AH(2/\lambda_x + H) \quad (6.4)$$

where dH/dt is the loading rate and H is defined in Figure 6.1. Using Equations 6.1-4, the longitudinal velocity (v_x) profile is plotted for different boundary conditions in Figure 6.2. As seen in Figure 6.2, the boundary condition at the laminate-interface affects the velocity profile through the thickness of the laminate. A no-slip condition leads to a parabolic profile with $v_x=0$ at the tool surface ($z/H=1$). A zero friction condition gives a uniform velocity distribution and in this case, the material deforms as a plug. The friction condition still results in a parabolic velocity profile but with a slip velocity at the tool-laminate interface. Therefore, the choice of proper assumptions becomes critical in any attempt to model the shear flow of composites.

The present experiment is designed to observe the material deformation during the flow process. The displacement of markers embedded in the laminate are monitored during the application of a normal deformation to the specimen. From the displacement profile observed at different location in the laminate, it is possible to deduce the velocity profile. This is done by using functions having the same form as the velocity functions (Equations. 6.1 and 6.2) to fit the measured displacement. Thus, the displacements profile would have the following form:

$$u_x = -x(A^*z^2 + B^*), \quad u_z = A^*z^3 + B^*z \quad (6.5)$$

where A^* and B^* are constants used for the fit. The magnitude of the displacements at the boundary will indicate the presence of slippage at the tool-laminate interface.

6.1.1 Experimental procedure

The test configuration for the shear flow experiment is shown in Figure 6.3. The compression load was applied by two parallel plates. A sample with the fibres oriented in the y direction is placed between two aluminium shims coated with a release agent. A teflon film is placed as

shown to retain any resin drops that could flow out of the laminate and cause potential damage to the testing jig. The specimen is loaded by applying a deformation in the z direction causing the material to flow in the x direction.

The deformation of the material is observed from the edge of the specimen as illustrated in Figure 6.3. This is done by placing the specimen assembly in a loading jig adapted to the chamber of an environmental scanning electron microscope (ESEM). A photograph of the loading jig is shown in Figure 6.4. The specimen is compacted by two aluminium parallel plates driven by two stepper motors at a constant loading rate of about 0.4 mm/min.. The specimen is heated¹ in order to trigger resin flow. This is done by a small heater placed beneath the plates. As the composite is heated, volatiles are released by the curing reaction. Therefore, a perfect vacuum would be very difficult to obtain and the observation of the specimen could not be possible in a conventional electron microscope². However, the ESEM can work when the chamber is maintained at a weak vacuum (30 torrs). The experiments were conducted at the Electron Microscopy Center of Texas A&M University with an ElectroScan ESEM E-3 environmental scanning electron microscope. The magnification used during the test was 50X.

The samples were prepared using material B. This material, in the present testing configuration, flows mainly by shear without any significant amount of percolation flow in the direction of the fibres. This is very important because the flow of resin in the y direction can cover the markers. A test temperature of 50°C was chosen to minimize percolation flow.

¹ At room temperature, the composite transverse viscosity is too high.

² A conventional electron microscope requires a high vacuum (10^{-5} torr).

Tungsten wires having a diameter of 25 μm were used for the markers. Tungsten has a much higher atomic mass than the average mass of the elements composing the composite (mainly carbon). Thus, the contrast between the markers and the composite is enhanced, particularly with the use of the backscatter electron detector. The marker diameter was chosen to avoid any major disturbance to the flow and to be easily seen in the ESEM. The markers were embedded between the prepreg plies during the lay-up. Figure 6.5 shows the location of the markers.

Four samples were prepared for the experiments: two samples of 10 plies (10_1 and 10_2) and two of 20 plies (20_1 and 20_2). The samples were compacted before the test in a vacuum bag at 50°C for 15 minutes. This procedure removed any entrapped air bubbles in the sample and ensured that the markers were surrounded with material. Finally, the sample were trimmed to have straight edges and the viewing surface was polished³ to obtain a good image quality. The samples dimensions are presented in Table D.1 of Appendix D.

The test procedure consisted of loading the specimen in increments of plates displacement (u_{plate}). The deformation of the specimen during the compaction was recorded on a video tape. Still images of the markers were taken before and after the load increments⁴. The procedure to obtain the position of the markers from the video recording and the still images is presented in detail in Appendix D. From the original position of the markers, the displacements (u_x and u_z) of the markers after each load increment were computed.

³ Using 600 grit polishing paper.

⁴ The images were taken when the compaction load stabilized to a constant value.

6.1.2 Resin percolation

The success of the experimental procedure relied mainly on whether the markers remained visible during the test. On average, half of the markers were covered with resin by the end of the test. However, most of the markers were still visible after the first load increment. Therefore, the specimen displacement analysis was conducted principally at this load increment (Load 1).

Figure 6.6 illustrates the percolation of the resin observed at the sample surface at different load increments. The amount of resin flow at the surface increased as the specimen was loaded. During the loading of the specimen, the compaction load increased to reach a maximum (i.e. the peak load) when the loading was stopped. Then, the load relaxed and eventually stabilized to a constant value (i.e. the relaxed load). The relaxation time was about 3-4 minutes. The magnitude of the peak and relaxed load for the different loading increments is presented in Table 6.1.

For an ideal fluid (as assumed by the shear flow theory), the load should relax to zero. However, for all the specimens, the relaxed load increased with the applied displacement (u_{plate}). The relaxed load corresponds to the elastic load carried by the fibre bed induced by the resin percolation. In general, more resin percolation is observed for thin specimens compared to thick specimens. As seen in Table 6.1, the thin specimens have higher relaxed loads compared to the thick specimens. The increase of the relaxed load with the amount of percolation clearly supports the importance of the elastic response of the fibre bed.

6.1.3 Displacement profiles

The deformation at the edge surface of the sample is shown in Figure 6.7. For the thin specimen, the surface was irregular and non-symmetric as seen in Figure 6.7 (a). Different conditions at the plate-tool interface for the top and bottom plates could explain this behaviour. For the thick specimen, the edge surface had a symmetric parabolic shape (Figure 6.7 (b)).

The displacement profiles obtained for a thick specimen are presented in Figures 6.8-6.10. The following statements can be made for the displacement profiles:

- 1) The longitudinal displacement profile is parabolic as seen in Figure 6.8.
- 2) The longitudinal displacement increases linearly from the laminate middle ($x=0$) to the edge ($x=L$) as shown in Figure 6.9.
- 3) The vertical displacements are uniform along the length of the laminate as shown in Figure 6.10.

In all cases, good agreement with the fit functions for u_x and u_z of Equation 6.5 was obtained. This confirms that the kinematic expressions developed (Equations 6.1-6.4) represent adequately the deformation of the material.

6.1.4 Condition at the plate-laminate interface

The observation of the deformation of the sample at the plate interface is presented in Figure 6.11. In this figure, images from the video recording were taken at different times during the loading of the sample. The deformation of the material at the interface with the plate can be seen by following the deformation of a small patch of resin outlined on Figure 6.11. Initially, the patch had almost a regular round shape. As the specimen was loaded, the shape of the patch stretched in the flow direction. This indicates that a velocity (v_x) gradient exists through the

sample thickness. This will cause the shearing action which is precisely the assumed deformation mode of the material. Furthermore, the point in contact with the plate translated in the direction of the flow (Figure 6.11). Thus, the material is slipping at the interface between the plate and the laminate. The velocity gradient combined with the slippage at the plate interface is only obtained with a friction condition ($0 < \lambda_x < \infty$).

The variation of displacement of the markers close to the surface of the laminate was studied during the specimen loading. The position of a surface defect of the sample at the plate-laminate interface ($z/H=1$) was also measured. The results for the variation of u_x and u_z with time are presented in Figure 6.12. The following observation can be made from this figure:

During the loading:

- ***variation of u_z***

The marker close to the surface ($z/H=0.8$) and the surface defect ($z/H=1$) responded instantaneously with the application of the load. However, the marker located at $z/H=0.5$ started to move in the z direction at about 20 seconds after the application of the load. Initial compaction of the specimen explains the lag observed for this marker.

- ***variation of u_x***

A lag is observed for the marker at the center ($z/H=0.5$) which corresponds to the initial compaction of the laminate (i.e. debulking). The longitudinal displacement observed at the surface clearly indicates the presence of slippage at the plate-laminate interface. However, the lag for the surface defect indicates that in the early stage of the loading, a no-slip condition is present at the interface.

When the load is stopped:

The normal displacement (u_z) of the markers stopped instantaneously. However, the markers continued to move in the x direction before they eventually stop. This behaviour is attributed to the viscoelastic nature of the material.

The variation of the longitudinal displacement (u_x) profile during the loading of thin and thick specimens is presented in Figures 6.13 and 6.14. The development of a parabolic displacement profile is seen by looking at the transient position of the markers. The movement of the surface defect confirms the slippage at the plate-laminate interface. In the early stages of the loading, no-slip conditions are present⁵. Therefore, a critical shear stress at the boundary is clearly present at the plate-laminate interface.

From the assumptions stated in Section 6.1, the following condition is present at the boundary:

$$\tau_{xz} = \alpha_x v_{xwall} \quad (6.6)$$

where v_{xwall} is the longitudinal velocity at the plate-laminate interface. Replacing the slip constant α_x in Equation 6.6 by the expression given in Equation 6.3, yields:

$$\tau_{xz} = \lambda_x \eta_T v_{xwall} \quad (6.7)$$

From the constitutive relations (Equation 2.23), the shear stress is related to the strain rate as follows⁶:

⁵ u_x at the surface is zero at $t=17$ seconds (Figure 6.13) and at $t=35$ seconds (Figure 6.14).

⁶ For the fibres oriented in the y direction, $\mathbf{a}=(0,1,0)$ and plane-strain is assumed.

$$\tau_{xz} = \eta_T(\partial v_x/\partial z + \partial v_z/\partial x) \quad (6.8)$$

From the loading conditions, $\partial v_z/\partial x = 0$, since the vertical velocity profile is uniform along the specimen (Figure 6.10). Combining Equation 6.7 and 6.8 gives a relation between $\partial v_z/\partial z$ and v_{xwall} :

$$\partial v_x/\partial z = \lambda_x v_{xwall} \quad (6.9)$$

Values for $\partial v_z/\partial z$ and v_{xwall} were calculated from the transient displacement of the markers shown in Figures 6.13 and 6.14. Figure 6.15 shows the variation of v_{xwall} and $\partial v_z/\partial z$ with time for a thin specimen. The curves have similar shapes which indicates that a linear relationship exists between the two variables. In Figure 6.16, $\partial v_z/\partial z$ is plotted against v_{xwall} for the thin and the thick specimens. A linear regression in the data leads to a value for λ_x of 4000 which corresponds to a friction condition at the plate-laminate interface ($0 < \lambda_x < \infty$). Furthermore, the results presented in Figure 6.16 show that a critical value of strain rate, $(\partial v_z/\partial z)_o$, must be exceeded before flow occurs. In fact, this value corresponds to a critical shear stress, $(\tau_{xz})_o$, at the plate-laminate interface (Equation 6.8). Thus below this value of $(\tau_{xz})_o$, no-slip conditions are essentially present at the plate-laminate interface.

6.2 Experimental investigation of flow mechanisms

The objective of the flow mechanisms tests is to investigate the conditions that favor percolation or shear flow during the laminate compaction. A schematic of the setup is presented in Figure 6.17. The test configuration is identical to the compaction curve experiments presented in Section 4.2. A normal compaction load was applied to a rectangular specimen by a solid piston

(Figure 4.1). The in-plane transverse deformation was blocked ($\epsilon_y=0$). In this configuration, the vertical deformation of the material (ϵ_z) imposed by the piston caused the material to flow in the longitudinal direction as illustrated in Figure 6.17. Therefore, the possible flow mechanisms corresponding to a given vertical deformation of the specimen are:

- 1) the resin flows in the x direction relative to the fibre bed by percolation (Figure 6.18 (a))
- 2) the resin and the fibre shear together in the x direction by shear (Figure 6.18 (b))
- 3) a combination of 1) and 2).

In light of the above, percolation flow can be measured by the volumetric strain calculated from the resin mass loss during the test. Furthermore, shear flow can be measured by the magnitude of the longitudinal strain obtained from the change in the specimen length. The effect of a given parameter on the different flow mechanisms can be studied by comparing the magnitude of these two primary variables (i.e. volumetric strain and longitudinal strain). In the following section, details of the experimental technique and the data analysis are given. Then the results for the different testing conditions selected are presented and discussed.

6.2.1 Experimental procedure

The test matrix for the experiments was determined from the parameters affecting the flow behaviour of the laminate. Among them, the fibre orientation and the resin viscosity play a significant role. The effect of fibre orientation was studied by comparing the compaction behaviour between a $[0^\circ]$ and a $[90^\circ]$ lay-up. The effect of the resin viscosity was given by comparing material A and B. The test was also conducted at two different temperatures to

investigate the viscosity change for one material. Table 6.2 presents the test matrix and the sample definition used.

The temperatures chosen for the test were based on the flow number variation with temperature for the material studied. The flow number (FN) is proportional to the amount of resin flow possible at a given temperature and is defined as follows:

$$FN = \int_0^{t_{gel}} 1/\mu(t)dt \quad (6.10)$$

where t_{gel} is the time at gelation and $\mu(t)$ is the resin viscosity change with time at a given curing temperature. Figure 6.19 compares the variation of FN with the curing temperature between material A and B. Those curves were computed from experimental viscosity variation for isothermal cures. According to Figure 6.19, the temperature of 100°C corresponds to a maximum flow number for material A and a low flow number for material B. A temperature of 140°C corresponds to the maximum flow number for material B while the flow number of material A is still very high. Thus, the test were conducted at a temperatures of 100°C and 140°C.

The experimental setup used for the flow mechanism tests is shown in Figure 4.a. The specimen geometry and measurements are defined in Figure 4.6. The specimen dimensions were $W_0=25$ mm x $L_0=50$ mm and 8 ply thick. The samples were prepared following the same procedure used for the compaction tests (Section 4.2.2). For each condition, a minimum of three samples were tested. The specimen loading condition corresponded to a typical autoclave pressure cycle. The specimen was loaded under load control to a pressure of 700 kPa at a rate of 70 kPa/min. At the maximum load, the specimen was rapidly unloaded to stop the flow process.

6.2.2 Extraction of the results

The specimens were measured and weighed before and after the test. From these measurements, the specimen deformation was computed. Since the magnitude of the strains measured were important, finite strain relations were used to calculate the strains from the measured displacements. For a deformed body, the Green strain tensor e_{ij} is defined as (e.g. Karasudhi, 1991):

$$e_{ij} = \frac{1}{2} [u_{i,j} + u_{i,i} + u_{k,i}u_{k,j}] \quad (6.11)$$

where i,j and $k=1-3$ and u is the displacements vector of the body. Using this notation, the finite strains of the specimen in the different directions can be expressed as function of the specimen dimensions:

$$e_x = \frac{1}{2} \left[\left(1 + \frac{L' - L_0}{L_0} \right)^2 - 1 \right] \quad (6.12)$$

$$e_y = \frac{1}{2} \left[\left(1 + \frac{W' - W_0}{W_0} \right)^2 - 1 \right] \quad (6.13)$$

$$e_z = \frac{1}{2} \left[\left(1 + \frac{H' - H_0}{H_0} \right)^2 - 1 \right] \quad (6.14)$$

where L' , L_0 , W' , W_0 , H' and H_0 are the specimen dimensions defined in Figure 4.5. For the volumetric strain (ε_v) calculation, Equation 4.1 was used. As discussed in Section. 6.2, ε_v is associated with percolation flow and e_x with shear flow. Therefore, these variables can be used to investigate the presence of either flow mechanisms with a good level of accuracy.

The contribution of each flow mechanism to the vertical deformation of the sample is more difficult to evaluate. Consider the specimen shown in Figure 6.17. The specimen volumetric strain can be expressed in term of the deformations:

$$\frac{\Delta V}{V_0} = \varepsilon_v = (e_x + e_y + e_z) + (e_x e_y + e_x e_z + e_y e_z) + e_x e_y e_z \quad (6.15)$$

Depending of the flow mechanism, the following assumptions can be made:

Percolation flow

- 1) resin movement relative to the fibre bed
- 2) resin mass loss ($\varepsilon_v \neq 0$)
- 3) no deformation of the fibre bed in the x-y plane ($e_x \approx 0$ and $e_y \approx 0$)

Shear flow

- 1) resin and fibre bed move together
- 2) no resin mass loss (the material is assumed incompressible and $\varepsilon_v = 0$)
- 3) deformation of the fibre bed in the x-y plane ($e_x \neq 0$ and $e_y \neq 0$).

From these assumptions and Equation 6.15, the vertical deformation caused by a particular flow mechanism can be expressed as follows:

- for vertical strains caused by percolation flow only:

$$e_z^P = \frac{\varepsilon_v - e_y}{1 + e_y} \quad (6.16)$$

- for vertical strains caused by shear flow only:

$$e_z^S = \frac{-(e_x + e_y + e_x e_y)}{(1 + e_x + e_y + e_x e_y)} \quad (6.17)$$

Equations 6.16 and 6.17 would represent the contribution of percolation and shear flow to the vertical deformation of the specimen. For a general case, the principle of superposition cannot be applied and therefore:

$$e_z^P + e_z^S \neq e_z \quad (6.18)$$

where e_z is the total measured vertical strain. Therefore, the deformation from the different flow mechanisms cannot be isolated. However, even if the samples were not perfectly blocked in the y direction ($e_y \neq 0$), the transverse in-plane deformation (e_y) was very small compared to the strains in the other directions. Thus, Equations 6.16 and 6.17 can be simplified and new expressions for e_z^P and e_z^S are:

$$e_z^P = \epsilon_v \quad \text{and} \quad e_z^S = \frac{-e_x}{1+e_x} \quad \text{for} \quad e_y \approx 0 \quad (6.19)$$

With Equation 6.19, the contribution of the different flow mechanisms to the specimen vertical strain can be approximately determined. This approach is adequate here, since the objective of the present test was to conduct a qualitative investigation of the parameters controlling the flow mechanisms. The results from the measurements on all the specimens tested are presented in Appendix E.

6.2.3 General observations

Typical samples after testing are shown in Figure 6.20. The elongation in the x direction for the [90°] specimens is clearly seen in Figure 6.20. In most cases, the fibers remain straight after the deformation of the sample. The resin flow front at the edge of the sample was non-uniform particularly for the samples having a ply orientation of [90°]. The resin flows preferentially

along the interface between the specimen and wall of the mould. The dimension of the sample is smaller in the y direction compared to the x direction. Therefore, if a gap exists between the sample and the mould wall, percolation flow in that gap would be preferred instead of the expected flow in the entire section. Before the test, the samples did not match exactly the width of the mould providing a small gap between the sample boundary and the mould wall. This experimental deficiency was more critical for [90°] samples, because the sample could not deform to fill the gap. Nevertheless, the experiment helped understanding the major effects influencing the flow mechanisms.

6.2.4 Percolation and shear strain analysis

The average values for the strains (ϵ_v , e_x , e_y , e_z^P and e_x^S) and the standard deviation are given in Table E.5 of Appendix E. The average variation of e_x (shear) and ϵ_v (percolation) is presented in Figure 6.21 and the following observations can be made:

- ϵ_v (*percolation*)
 - 1) $\epsilon_v \neq 0$ for all testing conditions.
 - 2) ϵ_v for material A is larger compared to material B.
 - 3) An increase of temperature increases ϵ_v particularly for material B.

- e_x (*shear*)
 - 1) $e_x \approx 0$ for a ply orientation of [0°].
 - 2) $e_x > 0$ for a ply orientation of [90°].
 - 3) An increase of temperature increases e_x particularly for material A

The ply orientation has a small effect on the magnitude of the percolation strain. However, the effect of the ply orientation on the shear strain is very important. For a [0°] orientation, the

presence of very stiff fibres prevent any deformation in the x direction. This result confirms the assumption of the fibres inextensibility discussed in Section 2.3.2. For a $[90^\circ]$ orientation, the deformation of the sample in the x direction is not prevented by the presence of the fibres. This deformation mode is known as transverse flow or squeeze flow and has been investigated mainly on thermoplastics (Section 2.3.2.1).

The difference in ε_v observed between materials A and B can be caused by two factors. The first factor is the resin viscosity difference between material A and B. The second factor is the difference in the fibre bed compaction curve between the two materials. As seen in Figure 4.13, for a given applied pressure, the corresponding compaction strain is larger for material A.

6.2.5 Flow mechanisms contribution

The contribution of percolation and shear flow on the total laminate deformation is presented in Figure 6.22. Percolation flow is the dominant mechanism with the $[0^\circ]$ ply orientation, while the $[90^\circ]$ ply orientation is characterized by the presence of percolation and shear flow. The fibre orientation in the direction of flow totally prevents the material from shearing.

As expected, the magnitude of e_z^P for the $[0^\circ]$ ply orientation is a function of the fibre bed compaction curve and the resin viscosity. The difference in the fibre bed compaction curve for materials A and B (Figure 4.13) explains the difference in e_z^P between the two materials. Furthermore, the effect of resin viscosity is shown by increase of e_z^P for both materials from 100°C to 140°C (e_z^P increases by 13% for material A and by 87% for material B).

For the $[90^\circ]$ lay-ups, the interaction between the two mechanisms clearly influences the magnitude of e_z^P and e_z^S . Shear flow is the dominant deformation mechanism for material B

which exhibit little percolation flow. However, percolation is equally or more dominant compared to shear flow for material A.

The effect of temperature on shear flow is different for material A and B. For material A, an increase in temperature significantly increases the shear flow contribution as the percolation flow remains constant. However, for material B, an increase in temperature decreases the shear flow contribution while the percolation flow increases. This behaviour shows again the complex interaction between the two flow mechanisms.

6.2.6 Discussion

By looking at the material properties characterizing the two flow mechanisms, it is possible to understand the interaction between them. The key material properties influencing percolation and shear flow are:

- *Percolation flow*
 - resin viscosity
 - fibre bed permeability
 - fibre bed compaction curve
- *Shear flow*
 - composite viscosity

The resin viscosity has a more significant effect on percolation flow compared to shear flow.

The resin viscosity coupled with the fibre bed permeability are the key material properties controlling the percolation flow of the composite.

The fibre bed elastic behaviour is important for the interaction between the two flow mechanisms. As seen in Equation 2.24, the total stress applied to the sample is divided into

reaction stresses and stresses related to the material deformation and the composite viscosity. Percolation flow introduces an elastic component to the stress tensor, which must be included in the stress equilibrium equation.

As discussed in Section 4.4.2.1, viscous effects are dominant in the initial stage of laminate compaction. Thus, it is at this stage that the shear flow mechanism would more likely occur since the elastic stresses transferred to the fibres are very small. For a material with a low viscosity resin (material A), the load is rapidly carried by the fibre bed giving little time for the shear flow to occur. However, for a material with a high resin viscosity (material B), percolation is very slow allowing more time for the material to shear.

The composite viscosity is a function of the resin viscosity and the fibre volume fraction (Equation 2.26). If the fibre volume fraction of the composite increases (i.e. due to percolation flow), the composite viscosity increases accordingly. This effect explains the decrease in the shear flow magnitude when the percolation flow increases.

It is clear that there is a continuous competition between the two flow mechanisms at all times during the compaction of the laminate.

6.2.7 Flow mechanism map

The concept of processing maps is presented in Ashby (1992). These maps are a very useful method of presenting information, identifying the different mechanisms and their interaction for a given problem. For the testing geometry considered in these experiments, a schematic flow mechanism map is presented in Figure 6.23. For this map, the parameters are the resin viscosity

and the laminate elastic modulus⁷ in the direction of flow. The zones indicate the dominant flow mechanisms observed during the experiment. The map presented is a qualitative representation of the observed flow behaviour. At low resin viscosity, percolation is dominant, while at high viscosity, shear flow more likely occurs when the fibres are oriented in the transverse direction. It is important to note that this map was constructed based on tests at [0°] and [90°] orientations. Thus, point I assumes that at a certain intermediate fibre orientation, shear flow become significant compared to no-flow and percolation flow conditions.

6.3 Summary

Shear flow experiments

- The displacement profiles obtained from the position of the markers are in good agreement with the kinematic relations assumed by a shear flow modelling approach.
- The analysis of the transient displacement profiles indicates that friction is present at the plate-laminate interface after a critical shear stress at the interface is exceeded. Prior to that critical shear stress, no-slip condition is present.
- Observations of the sample surfaces during loading indicates the presence of resin percolation at a local level. The non-zero residual load measured after each loading increments is attributed to the elastic response of the fibre bed.

⁷ This parameter is influenced by the laminate lay-up (i.e. the fibre orientation).

Flow mechanisms experiments

- An interaction exists between percolation and shear flow which depends on the state of the material (i.e. resin viscosity, fibre orientation and fibre bed elastic stresses).
- For the test configuration chosen, the resin viscosity is the major parameter influencing percolation flow.
- For the test configuration chosen, the fibre orientation is the principal factor influencing shear flow.

6.4 Tables

Table 6.1 Shear flow experiments loading increments (u_{plate}) with corresponding peak and relaxed load. The peak load corresponds to the load measured as the loading is stopped. The relaxed load corresponds to the stable load measured after the load is stopped.

Load step	u_{plate} (mm)	Peak load (N)	Relaxed load (N)
Thin sample (10_2)			
1	0.17	89	23
2	0.36	178	66
3	0.43	298	169
Thick sample (20_2)			
1	0.27	32	18
2	0.48	67	39
3	0.66	94	63

Table 6.2 Flow mechanisms test matrix and sample definition. The variable n corresponds to the specimen number tested in the condition specified.

Fibre orientation	100°C		140°C	
	Material		Material	
	A	B	A	B
[0°]	4A0n	4B0n	5A0n	5B0n
[90°]	4A90n	4B90n	5A90n	5b90n

6.5 Figures

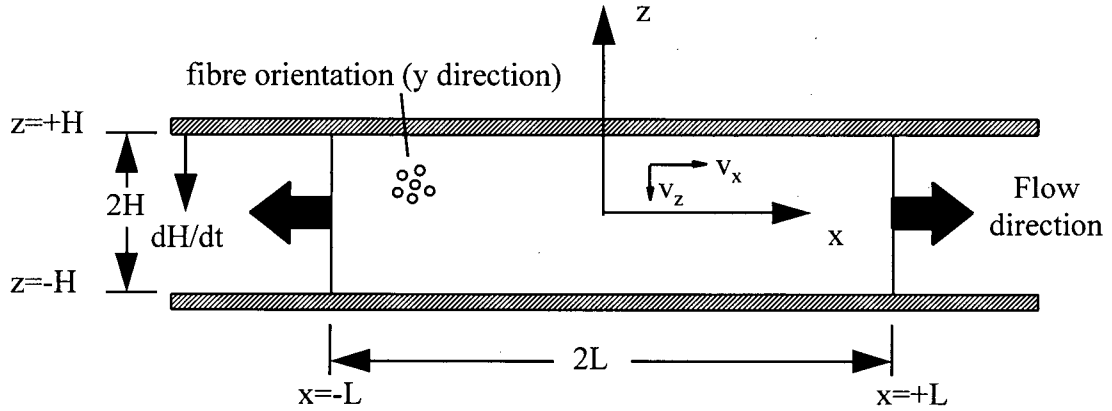


Figure 6.1 Dimensions and variables definition for the shear flow model.

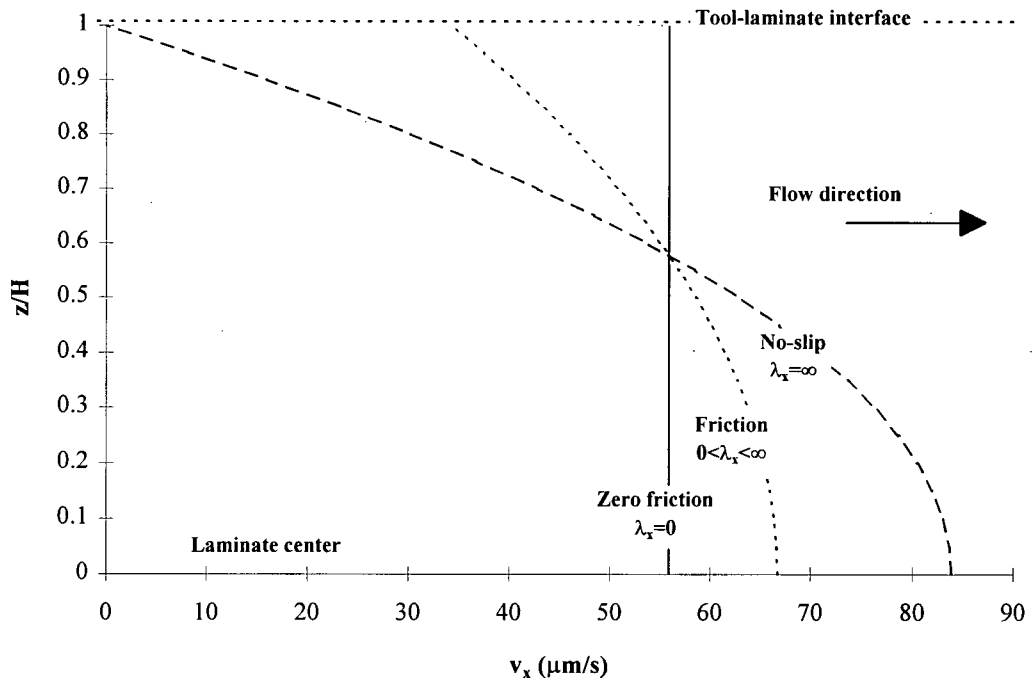


Figure 6.2 Effect of the tool-laminate interface boundary conditions on the predicted longitudinal velocity (v_x) profile shape with Equation 6.1.

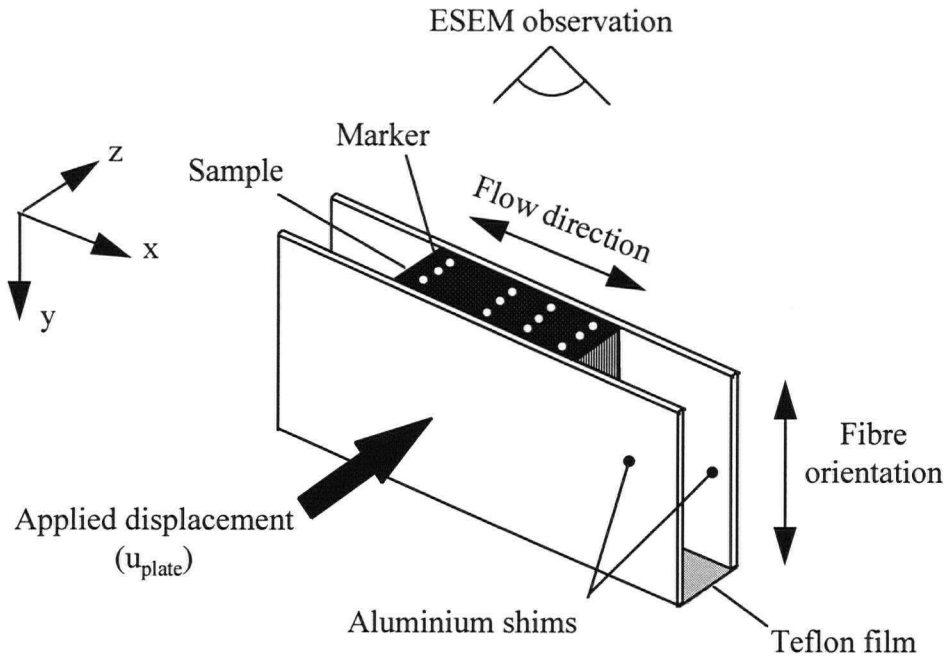


Figure 6.3 Shear flow test configuration.

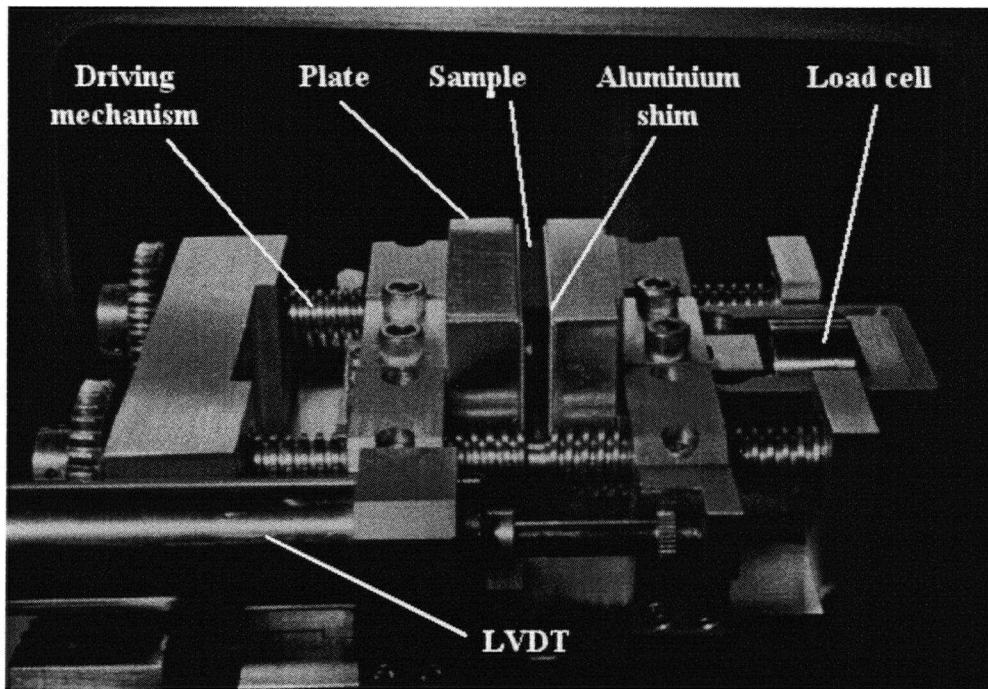
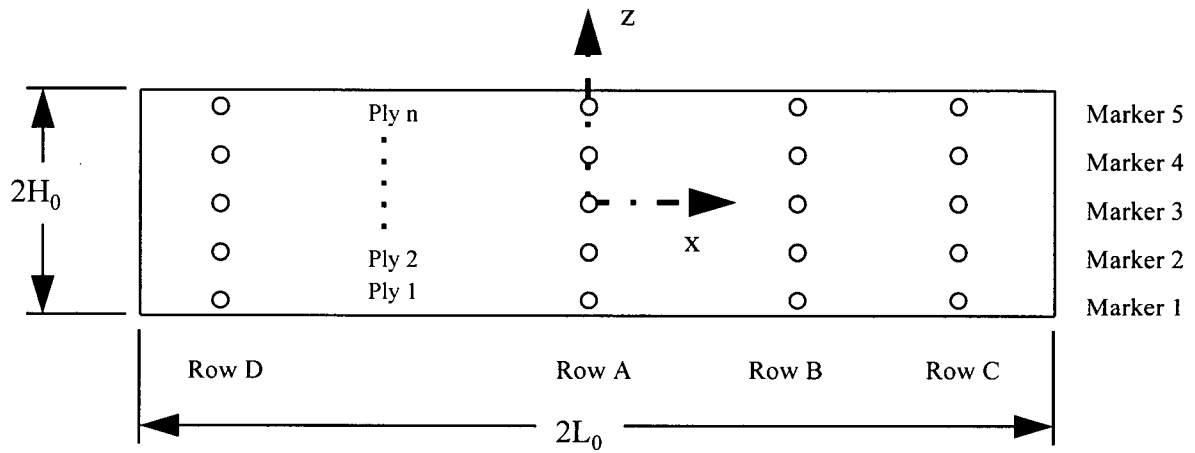


Figure 6.4 Photograph of the loading jig for the shear flow experiments showing the principal components.



n is the total number of ply

Row	x (mm)	
A	0.0	
B	6.0	
C	11.0	
D	-11.0	
Marker	Interface ply*	
1	1-2	<i>2-3</i>
2	3-4	<i>6-7</i>
3	5-6	<i>10-11</i>
4	7-8	<i>14-15</i>
5	9-10	<i>18-19</i>

* values in italic are for 20 ply samples.

Figure 6.5 Definition of the marker positions before the test.

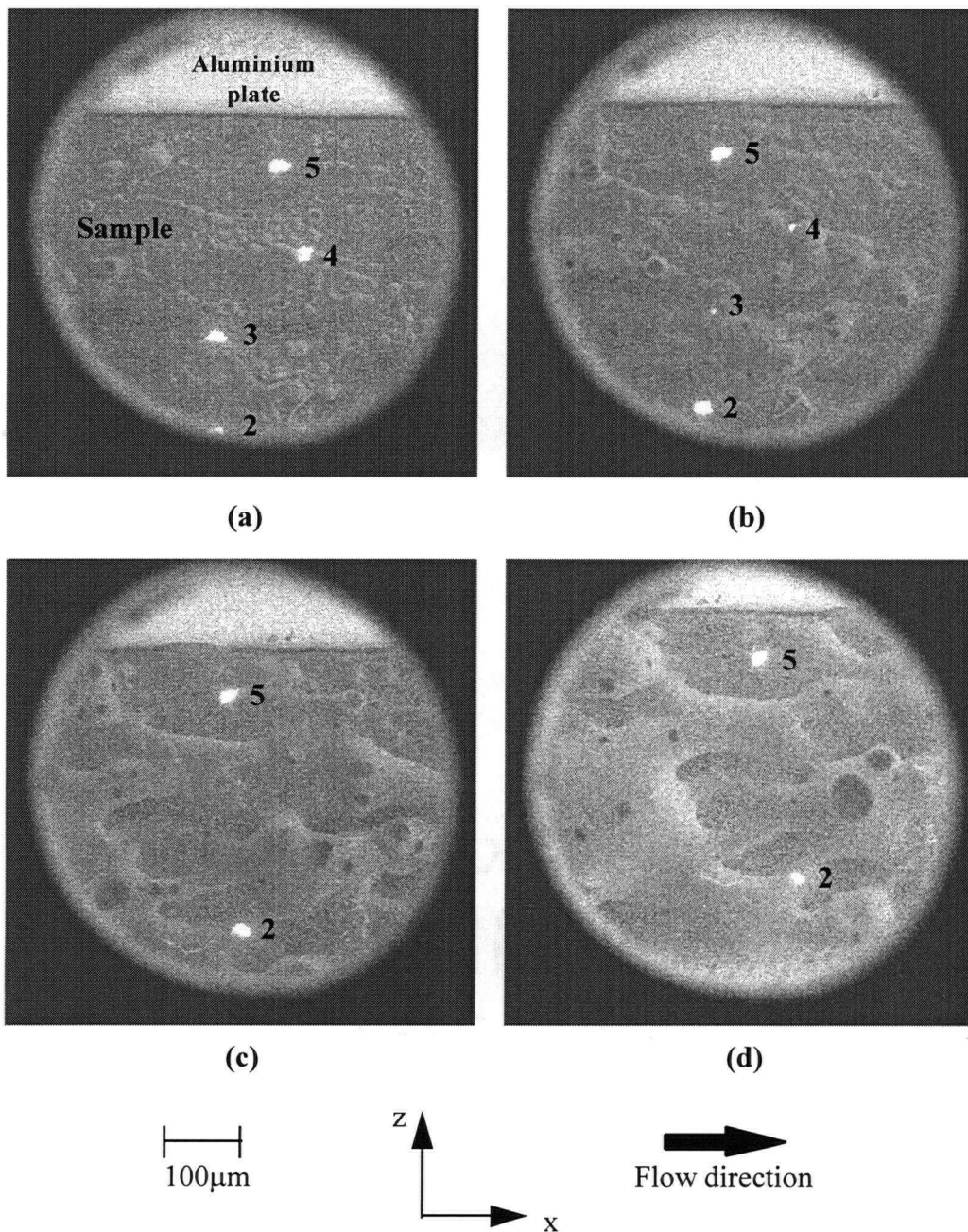


Figure 6.6 Micrographs (50X) of sample 10_2 (markers 2, 3, 4, 5 - Row C) at different load increments, (a) no load, (b) Load 1, (c) Load 2 and (d) Load 3. The percolation of the resin becomes visible as the load applied increases.

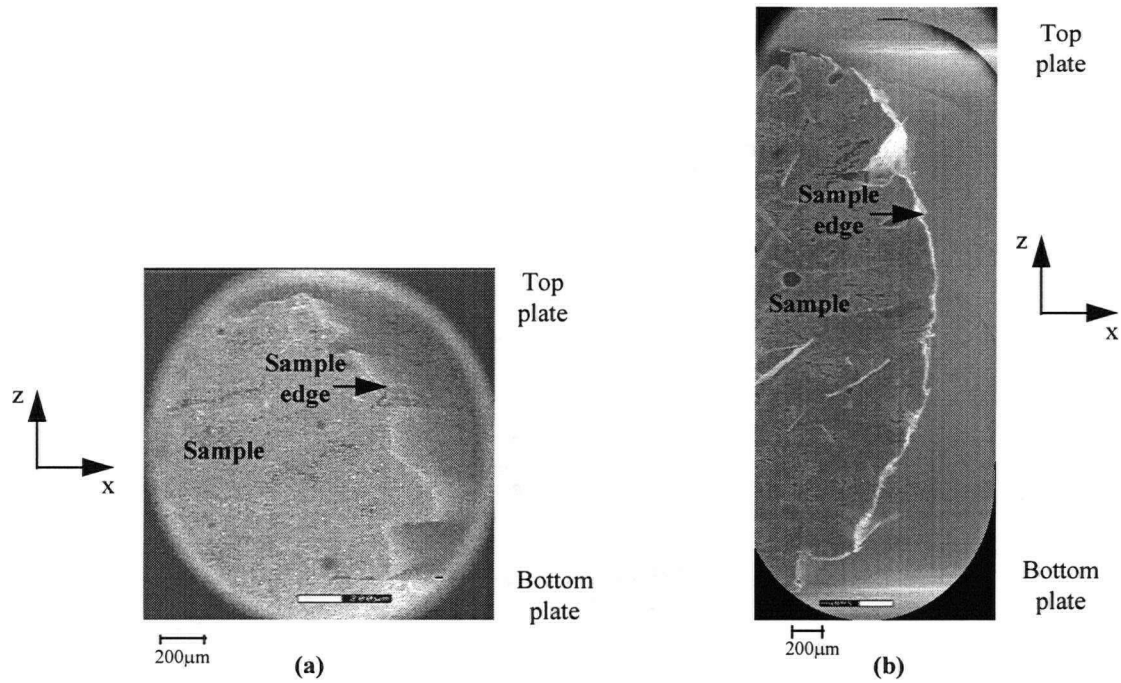


Figure 6.7 Micrographs (50X) comparing the specimen edge surface profile after Load 1 for (a) thin sample 10_2, (b) thick sample 20_2.

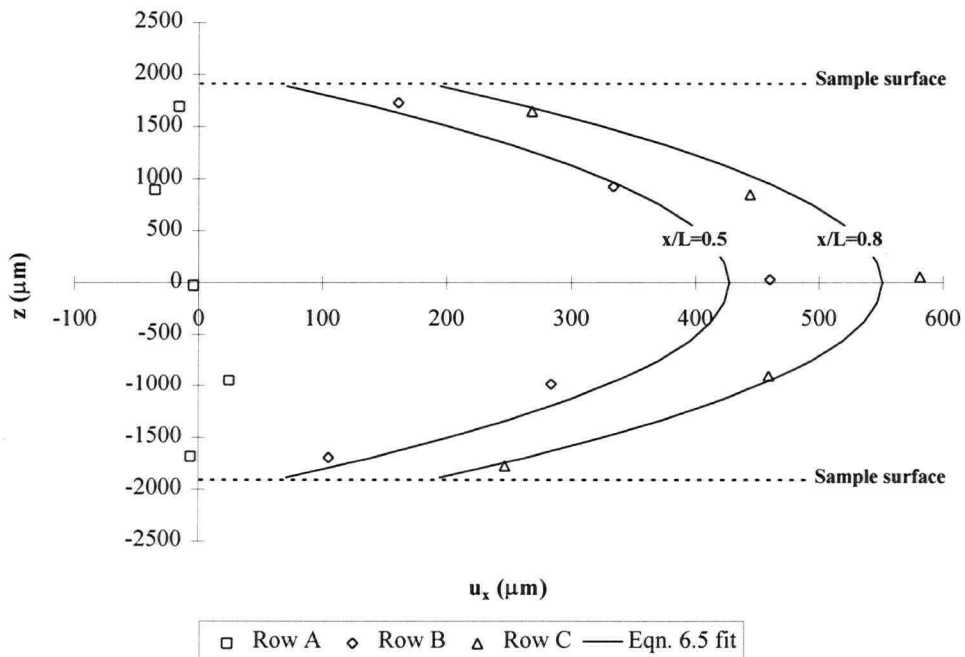


Figure 6.8 Markers displacement (u_x) profiles of a thick sample 20_1, Load 1 (Rows A, B and C) compared with the displacement profile using the function for u_x in Equation 6.5 to fit the experimental points.

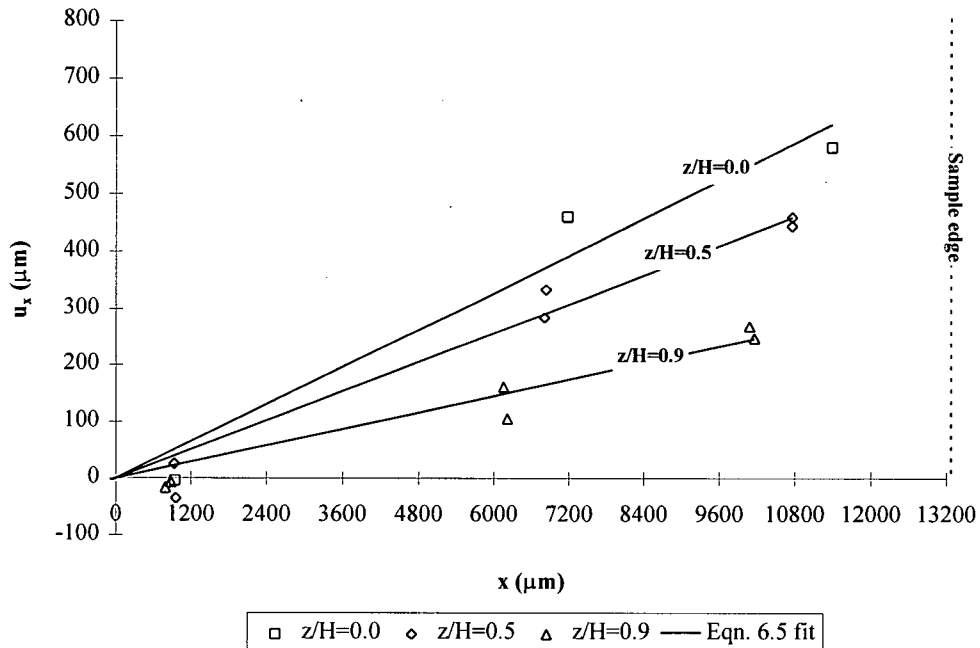


Figure 6.9 Markers displacement (u_x) profiles along the length of a thick sample 20_1, Load 1 (Rows A, B and C) compared with the displacement profile using the function for u_x in Equation 6.5 to fit the experimental points.

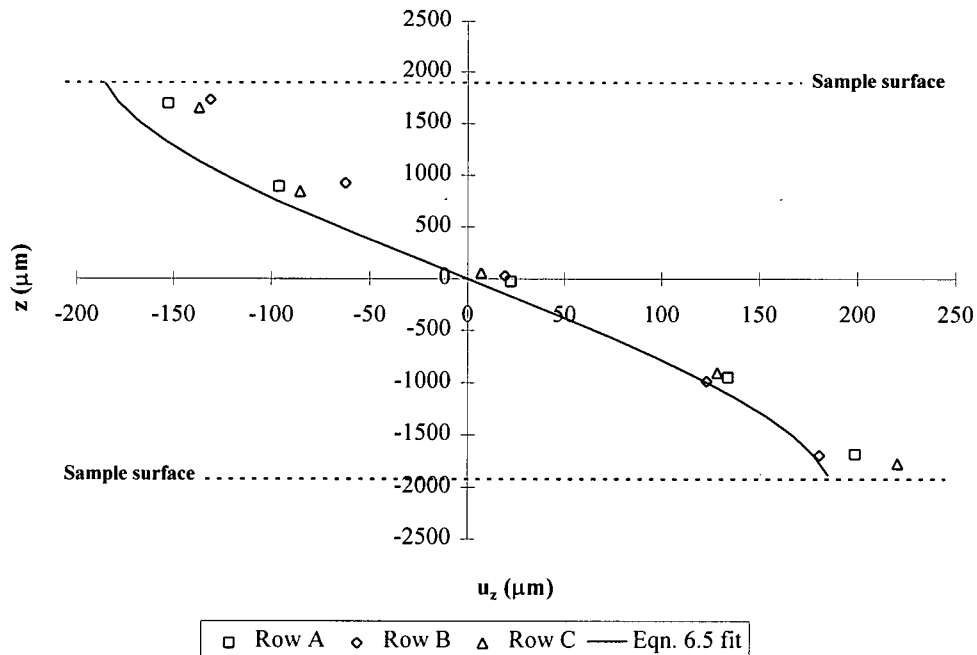


Figure 6.10 Markers displacement (u_z) profiles of a thick sample 20_1, Load 1 (Rows A, B and C) compared with the displacement profile using the function for u_z in Equation 6.5 to fit the experimental points.

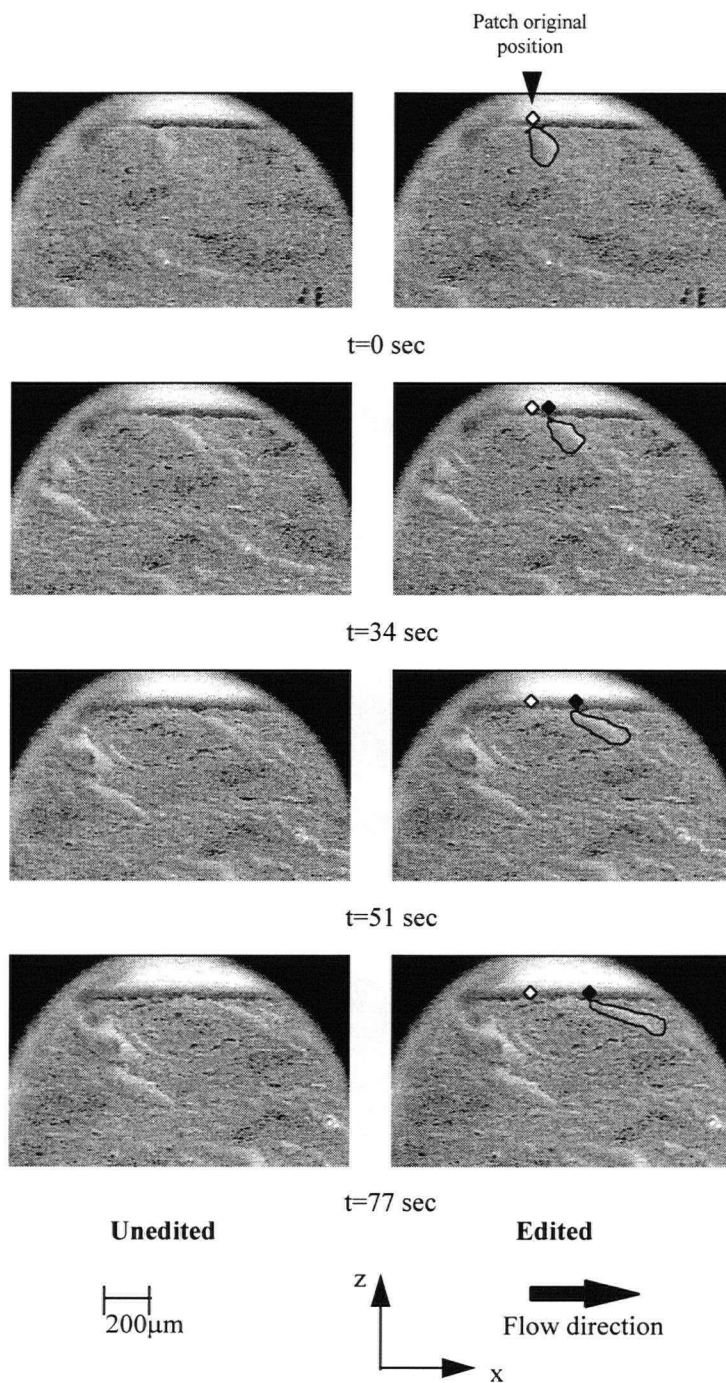


Figure 6.11 Micrographs (50X) taken from a video recording showing the plate-laminate interface at different time intervals during Load 2 increment of sample 10_2 (Row C). Images on the left are untouched, images on the right are overlaid to illustrate the deformation of a surface patch of resin as the specimen is loaded.

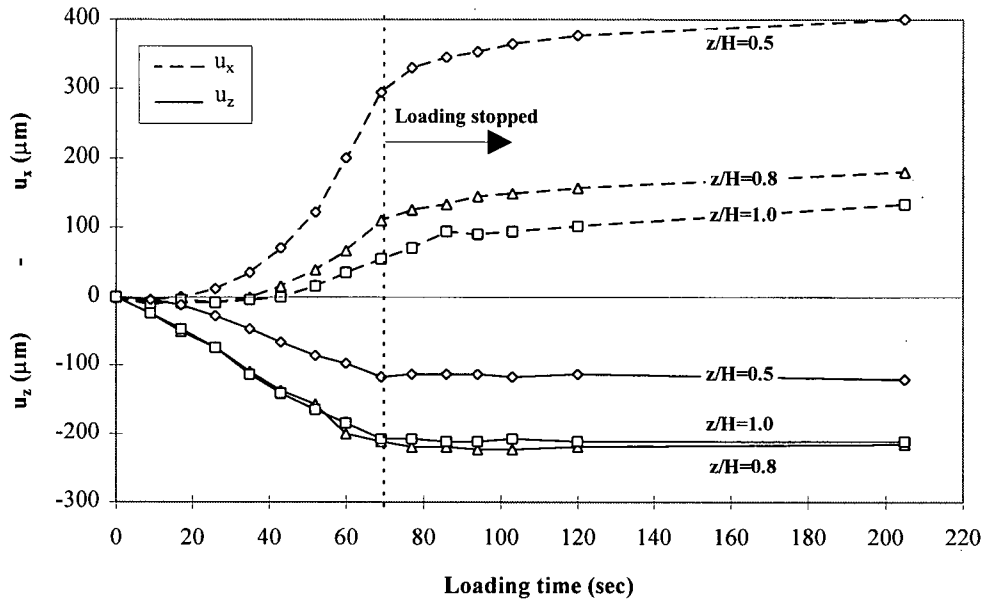


Figure 6.12 Variation of the marker displacements (u_x and u_z) with time during and after loading for sample 20_1, Load 1 (markers 1,2 and surface - Row C).

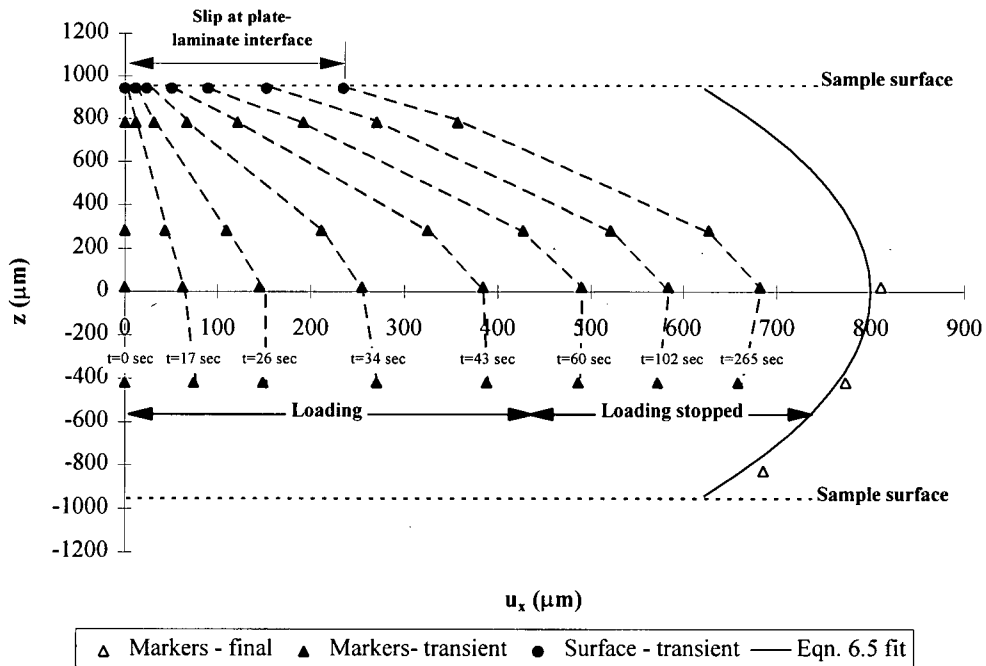


Figure 6.13 Markers displacement (u_x) profiles of thin sample 10_2, Load 1 (Row C). The final displacement profile is compared with the displacement profile using the function for u_x in Equation 6.5 to fit the experimental points. The transient markers displacement are obtained from a video tape recording taken during compaction.

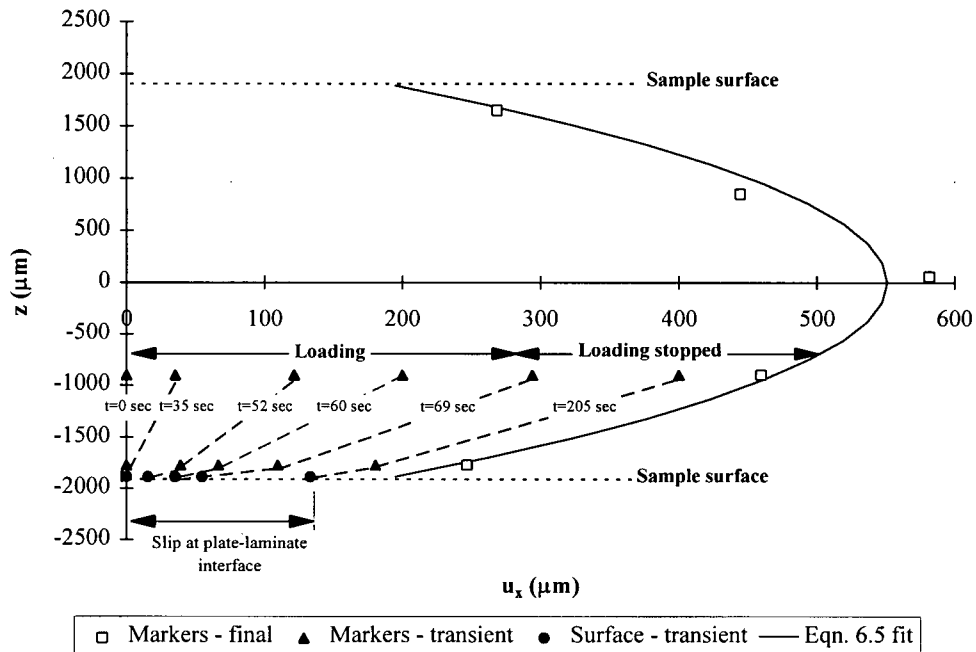


Figure 6.14 Markers displacement (u_x) profiles of a thick sample 20_1, Load 1 (Row C). The final displacement profile is compared with the displacement profile using the function for u_x in Equation 6.5 to fit the experimental points. The transient markers displacement are obtained from a video tape recording taken during compaction.

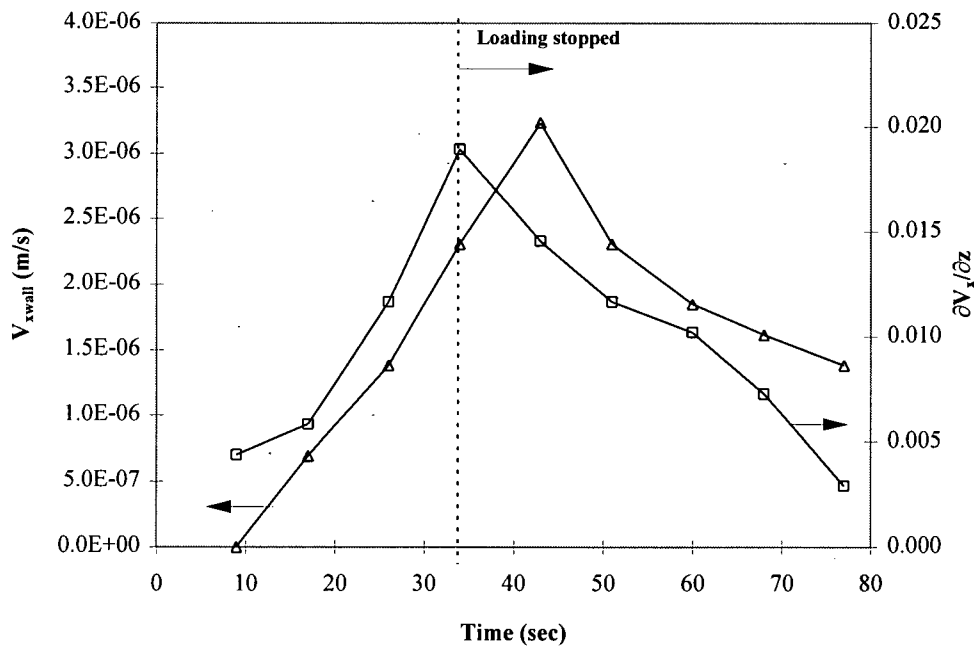


Figure 6.15 Variation of the slip velocity at the plate-laminate interface (V_{xwall}) and the shear strain rate close to the surface ($\partial v_x / \partial z$) with time for a thin specimen (10_2).

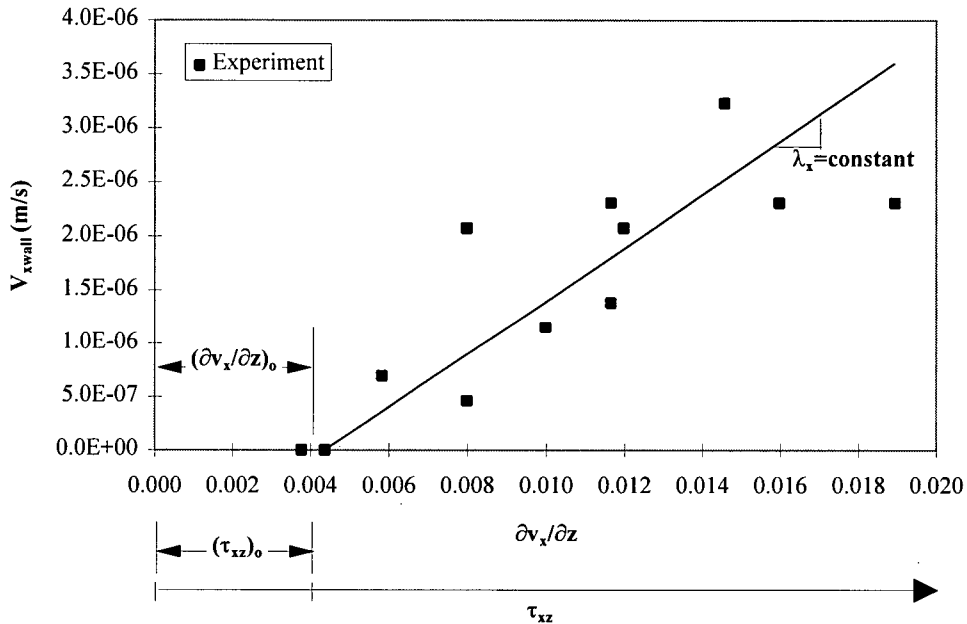


Figure 6.16 Variation of the slip velocity at the plate-laminate interface (V_{xwall}) with the shear strain rate close to the sample surface ($\partial v_x/\partial z$) for a thin and thick sample. The critical shear strain rate $(\partial v_x/\partial z)_0$ is shown which correspond to a critical shear stress $(\tau_{xz})_0$ after which the sample starts to slip.

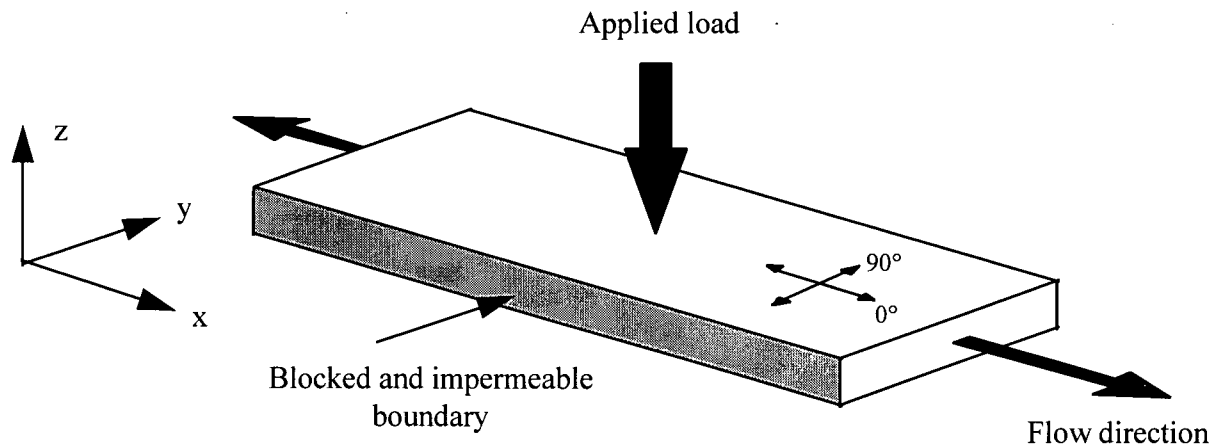


Figure 6.17 Specimen configuration for the flow mechanisms experiments.

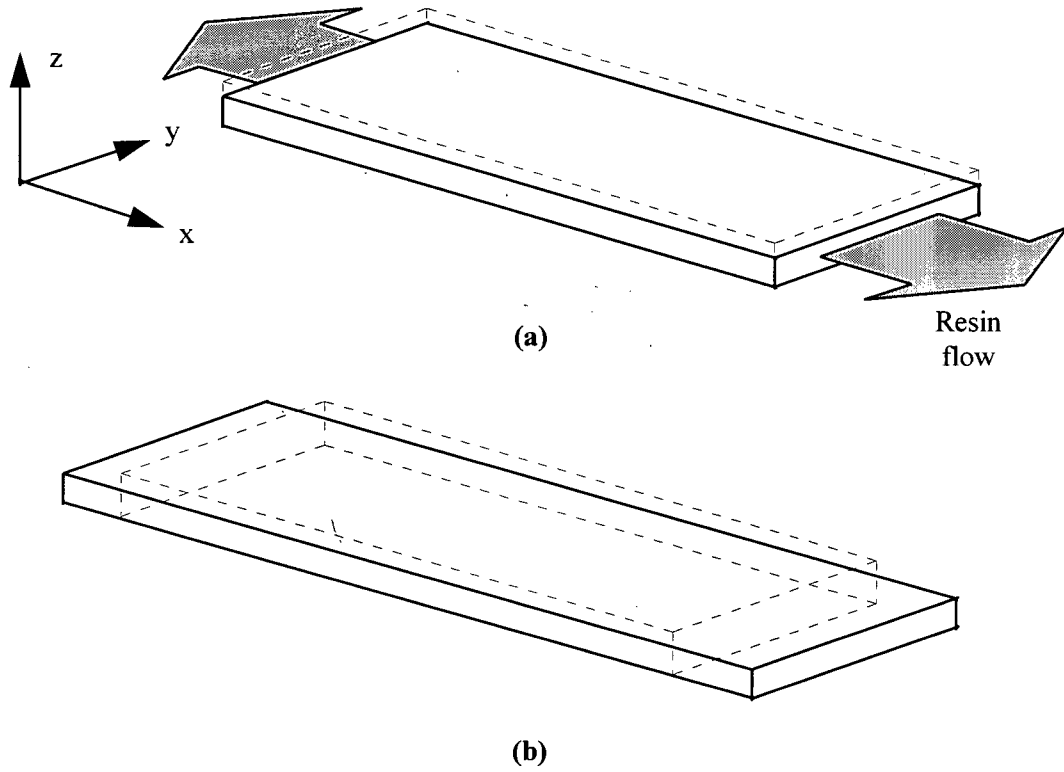


Figure 6.18 Possible flow mechanisms, (a) percolation and (b) shear. The initial sample dimension is indicated by the dashed line.

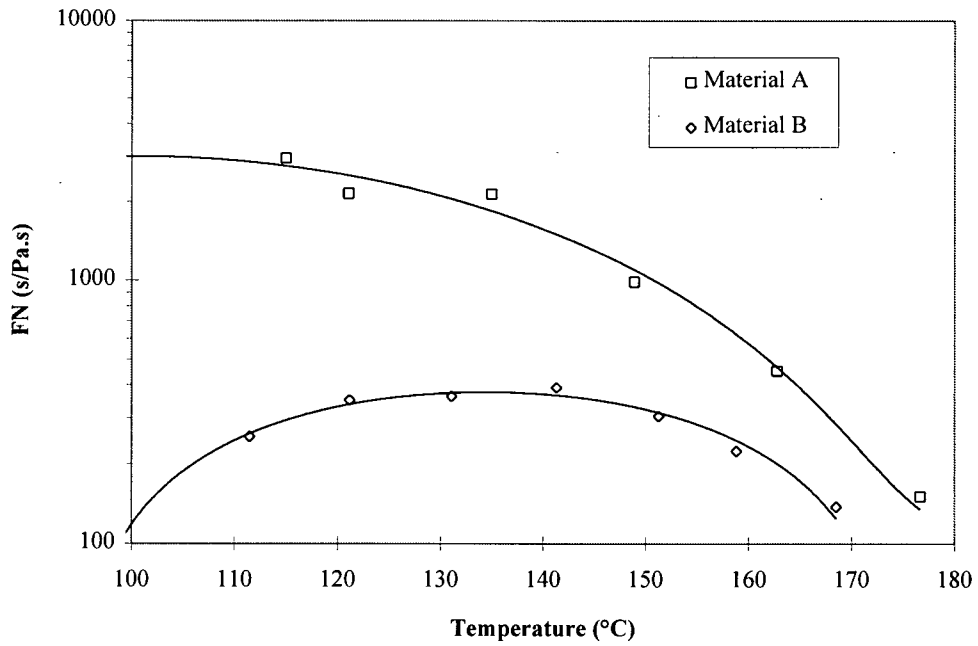


Figure 6.19 Flow number variation with curing temperature for material A and B.

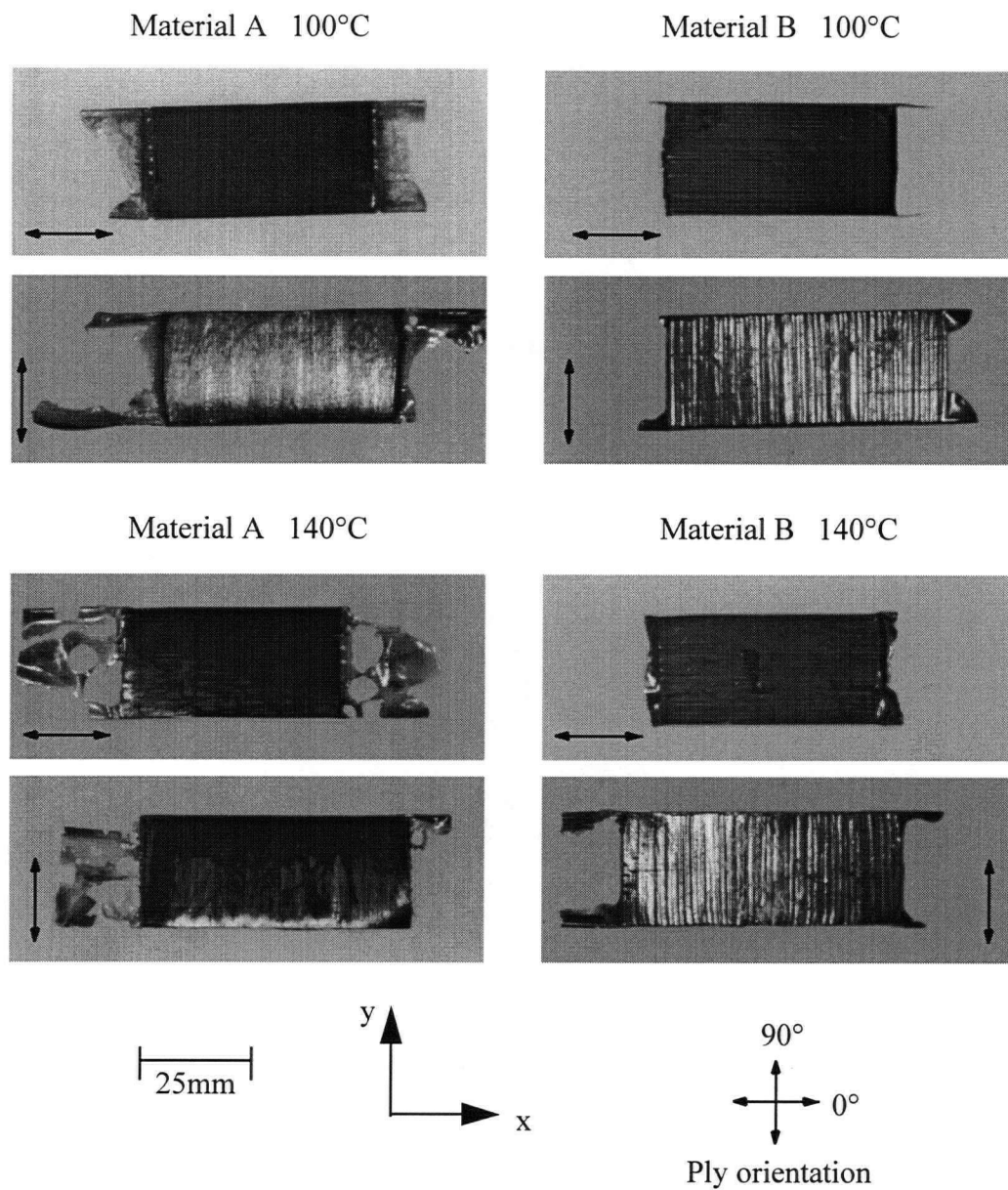


Figure 6.20 Plane view photograph of typical specimens after testing.

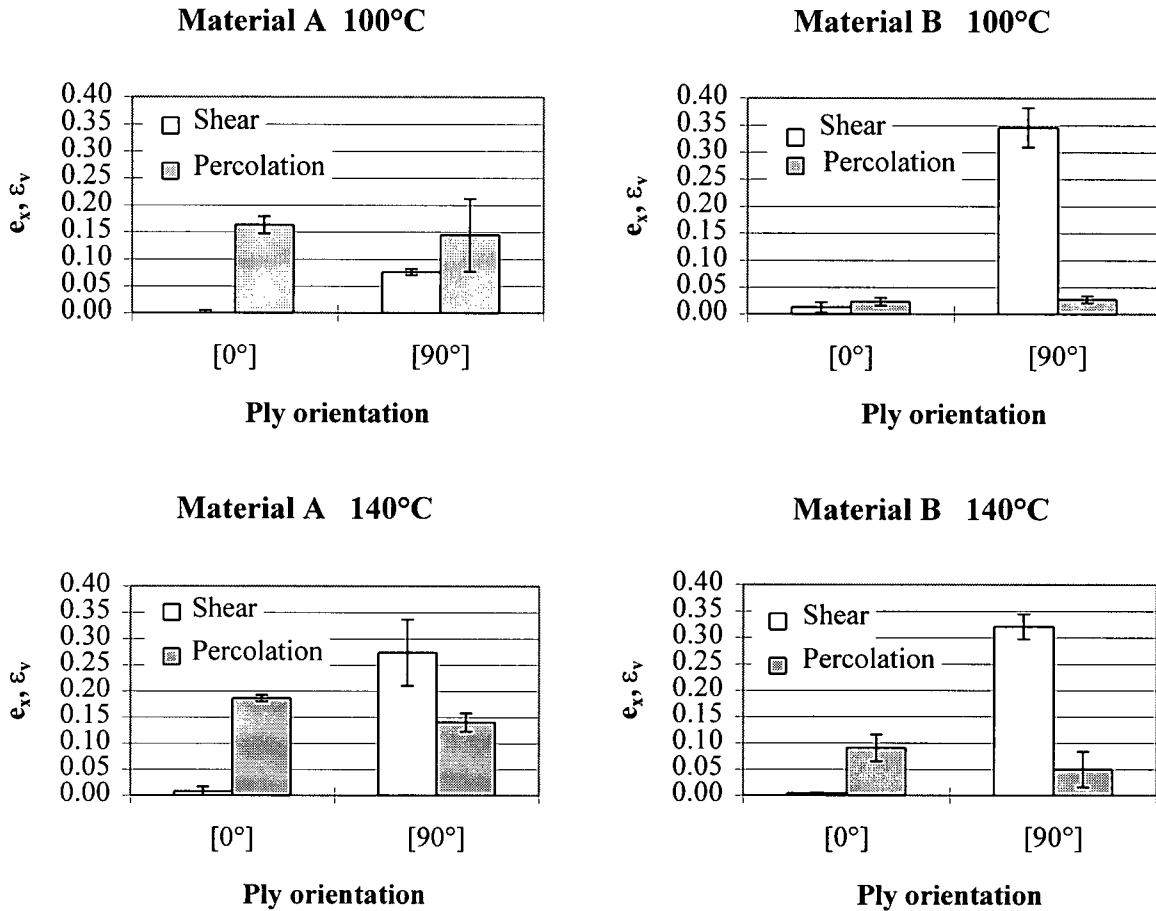


Figure 6.21 Effect of ply orientation on ϵ_x (shear) and ϵ_v (percolation). The results shown are the average for three samples and the error bars represent the standard variation. The strain sign is inverted so that positive indicates compression.

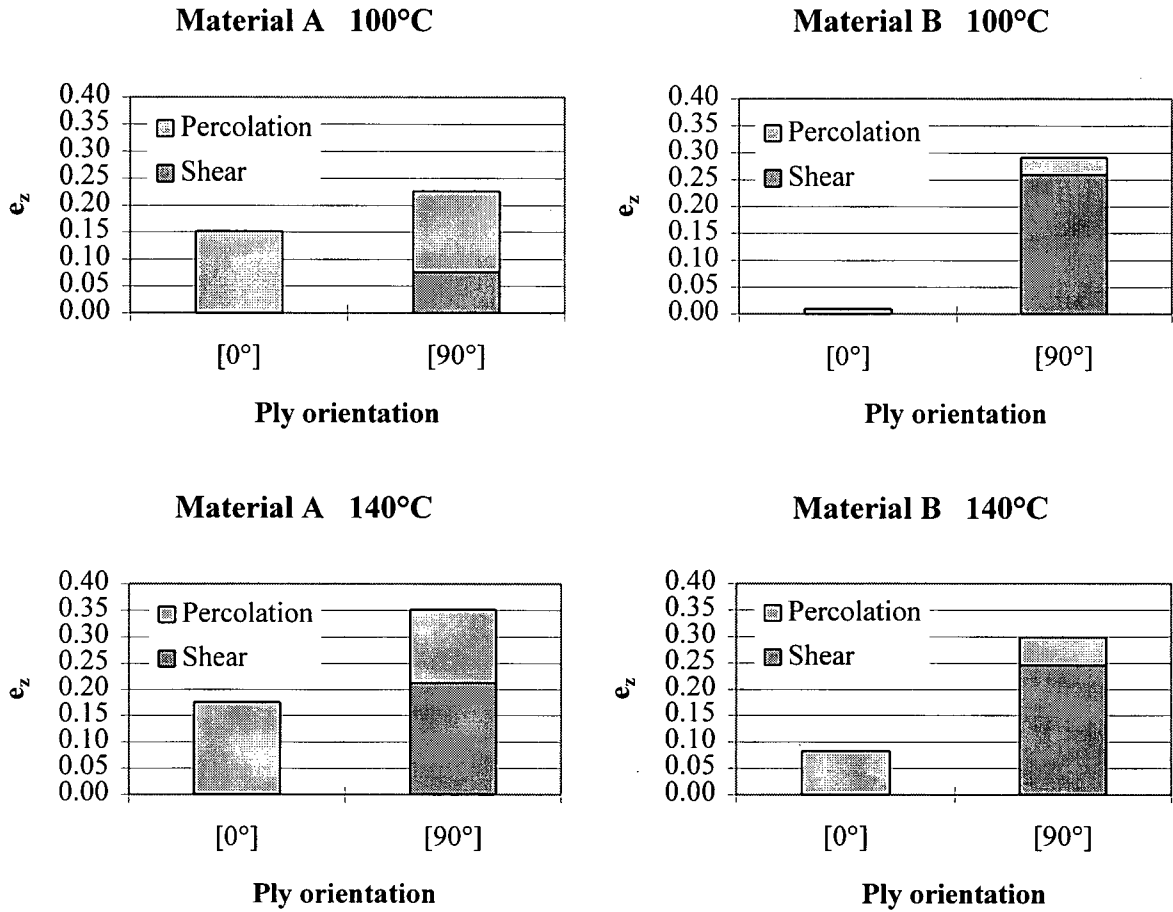


Figure 6.22 Effect of ply orientation on e_z^P (percolation) and e_z^S (shear). The results shown are the average of three samples. The strain sign is inverted so that positive indicates compression. The strains are added to obtain the total strain of the sample e_z .

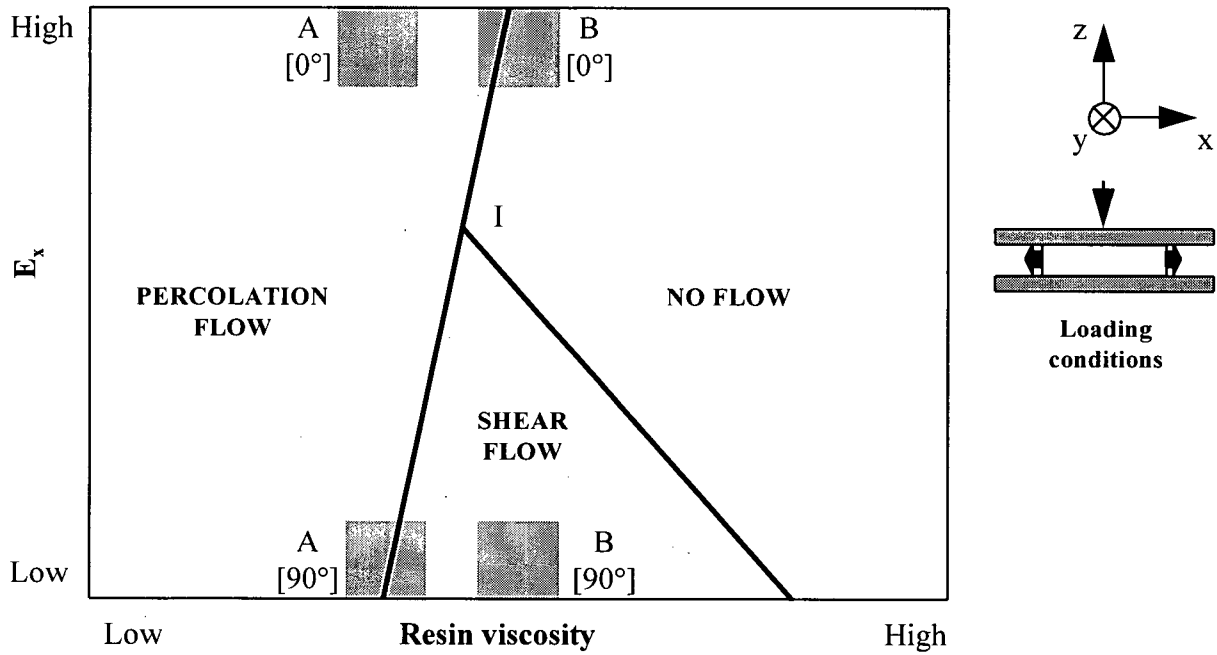


Figure 6.23 Flow mechanisms map for a uniaxial loading condition. The range of viscosity and laminate elastic modulus (E_x) in the flow direction for material A and B is shown as a reference. For $[0^\circ]$ and $[90^\circ]$, the fibres are oriented in the x and y direction respectively.

Chapter 7 Conclusions and Further Work

The main objective of this work was to investigate the flow and compaction of complex shape laminates. To achieve this objective, the work was subdivided into numerical and experimental investigations. Two second generation composite prepregs with significant rheological differences were studied. The following conclusions can be drawn from this work:

1) A 2-D flow-compaction finite element model has been developed

A flow-compaction model was developed based on the effective stress formulation coupled with a percolation flow approach. The flow-compaction model was integrated in a general process model where other physical issues involved during composites processing such as heat transfer and cure kinetics were implemented. The current formulation successfully describes the compaction behaviour of complex shape laminates caused by resin percolation.

2) A new method to measure the fibre bed compaction curve has been developed

Accurate measurements of the fibre bed compaction curve are essential for any attempt to predict the final thickness of the laminate. A direct, accurate and quick method has been developed to obtain the fibre bed compaction curve without disturbing the fibre arrangement.

3) The fibre bed shear response controls the compaction of curved laminates

The fibre bed shear response has a significant effect on the compaction of curved laminates. This parameter of the constitutive law controls the ability of the fibres to slide in order to conform to a curved shape.

4) The compaction of curved laminates involves percolation and shear flow

The curved laminate deformation is a combination of percolation and shear flow. The large deformations observed at the corner of the $[90^\circ]$ lay-up are caused by shear flow. The presence of fibres oriented in other directions such as $[0^\circ]$ or $[\pm 45^\circ]$ prevents local deformation at the corner. The interaction between percolation and shear flow depends on the relationship between the material properties and the stress distribution in the laminate. Furthermore, the resin viscosity is the major parameter controlling percolation flow. For shear flow, the fibre orientation is the dominant parameter controlling the laminate deformation.

5) Direct observations of shear flow have been conducted

The observations of the displacement of markers embedded in a laminate are consistent with the functions used in the shear flow theory. Thus the assumed kinematic relations correctly describe the deformation of the material. Moreover, friction exists at the plate-laminate interface above a critical stress at the interface. The interaction between the part and the tool is a major source of the development of residual stresses during cure.

7.1 Further work

A significant advance would be to upgrade the flow-compaction model with a better description of shear flow. In the current constitutive law, the shear deformation behaviour is purely elastic. A solution would be to consider shear deformation as plastic flow which involves plastic deformation of the material. Thus the work would consist of developing a constitutive law that incorporates the plastic behaviour of the material. Furthermore, using an incremental solution method, one would update the mesh after each time step to take into account the permanent

deformation of the material. This would solve one of the problems with the current method of solution where the small strain approach is used.

The use of embedded markers to monitor the laminate deformation was very useful and provided valuable information. It would be very useful to apply this technique to study the compaction of curved laminates. Thus a special compaction fixture could be designed to load the specimen while the movement of the markers are observed at the corner. Furthermore, the analysis of the local fibre volume fraction distribution in the laminate would also provide very important information on the flow behaviour in this area of the laminate.

Finally, the expansion of the concept of flow mechanisms maps would provide valuable guidance for the process modeller and the composite parts manufacturer. In this work, the flow mechanism map was constructed for a particular loading condition and sample geometry. The analysis of the governing equations for the flow mechanisms combined with more experiments would help to build a family of maps. Therefore, based on the manufacturing arrangement chosen, the composite designer would have a quick idea of the problems related to flow that could be encountered during processing.

References

- Adams, K.L. and Rebenfeld, L., "Permeability Characteristics of Multilayer Fiber Reinforcements. Part I: Experimental Observations", *Polymer Composites*, Vol. 12, No. 3, 1991, pp. 179-185.
- Ahn, K.J., Seferis, J.C., Price, J.O. and Berg, A.J., "Permeation Measurements Through Prepreg Laminates", *Sampe Journal*, Vol. 27, No. 6, 1991, pp. 19-25.
- Ashby, M. F., "Materials Selection in Mechanical Design", Pergamon Press, Oxford, 1992.
- ASTM D3171-76. "Standard Test Method for Fiber Content of Resin-Matrix Composites by Matrix Digestion", *Annual Book of ASTM Standards*, Vol 15.03, American Society for Testing and Materials, Philadelphia, 1994.
- Åström, B.T., Pipes, R.B. and Advani, S.G., "On Flow through Aligned Fiber Beds and Its Application to Composites Processing", *Journal of Composite Materials*, Vol. 26, No. 9, 1992, pp. 1351-1373.
- Balasubramanyam, R., Jones, R.S. and Wheeler, A.B., "Modelling Transverse Flows of Reinforced Thermoplastic Materials", *Composites*, Vol. 20, No. 1, 1989, pp. 33-37.
- Barnes, J.A. and Cogswell, F.N., "Transverse Flow Processes in Continuous Fibre-Reinforced Thermoplastic Composites", *Composites*, Vol. 20, No. 1, 1989, pp. 38-42.
- Bartlett, C.J., "Use of the Parallel Plate Plastometer to Characterize Glass-Reinforced Resins: 1. Flow Model", *Journal of Elastomers and Plastics*, Vol. 10, 1978, pp. 369-376.
- Berglund, L.A. and Kenny, J.M., "Processing Science for High Performance Thermoset Composites", *SAMPE Journal*, Vol. 27, No. 2, 1991, pp. 27-37.
- Biot, M.A., "General Theory of Three-dimensional Consolidation", *Journal of Applied Physics*, Vol. 12, 1941, pp. 155-164.
- Bogetti, T.A. and Gillespie, Jr., J.W., "Two-Dimensional Cure Simulation of Thick Thermosetting Composites", *Journal of Composite Materials*, Vol. 25, No. 3, 1991, pp. 239-273.
- Bruschke, M.V. and Advani, S.G., "A Finite Element/Control Volume Approach to Mold Filling in Anisotropic Porous Media", *Polymer Composites*, Vol. 11, No. 6, 1990, pp. 398-405.
- Bruschke, M.V. and Advani, S.G., "Flow of generalized Newtonian fluids across a periodic array of cylinders", *Journal of Rheology*, Vol. 37, No. 3, 1993, pp. 479-498.
- Cai, Z. and Berdichevsky, A.L., "Estimation of the Resin Flow Permeability of Fiber Tow Preforms Using the Self-Consistent Method", *Polymer Composites*, Vol. 15, No. 3, 1994, pp. 240-246.
- Cai, Z. and Gutowski, T.G., "The 3-D Deformation Behavior of Lubricated Fiber Bundles", *Journal of Composite Materials*, Vol. 26, No. 8, 1992a, pp. 1207-1237.
- Cai, Z. and Gutowski, T., "Winding and Consolidation Analysis for Cylindrical Composite Structures", *Journal of Composite Materials*, Vol. 26, No. 9, 1992b, pp. 1374-1399.

References

- Chan, C.Y., Beris, A.N. and Advani, S.G., "3-D Simulation of Fiber-Fluid Interactions During Composite Manufacturing Using The Galerkin Boundary Element Method", in: "Computer Aided Design in Composite Material Technology Volume III", Computational Mechanics Publications, Oxford, 1992, pp.385-403.
- Chan, A.W., Larive, D.E. and Morgan, R.J., "Anisotropic Permeability of Fiber Preforms: Constant Flow Rate Measurement", *Journal of Composite Materials*, Vol. 27, No. 10, 1993, pp. 996-1008.
- Christensen, R.M., "Effective Viscous Flow Properties for Fiber Suspensions under Concentrated Conditions", *Journal of Rheology*, Vol. 37, No. 1, 1993, pp. 103-121.
- Ciriscioli, P.R., Wang, Q. and Springer, G.S., "Autoclave Curing-Comparisons of Model and Test Results", *Journal of Composite Materials*, Vol. 26, No. 1, 1992, pp. 90-102.
- Coffin, D.W., Pipes, R.B. and Simacek, P., "First-Order Approximations for the Effective Shearing Viscosities of Continuous-Fiber Suspensions", *Journal of Composite Materials*, Vol. 29, No. 9, 1995, pp. 1169-1179.
- Cogswell, F.N., "The experience of thermoplastic structural composites during preprocessing", *Composites Manufacturing*, 2, 3/4, 1991, pp. 208-216.
- Collyer, A.A. and Clegg, D.W., "Rheology Measurement", Elsevier Applied Science, New York, 1988.
- Cook, R.D., Malkus, D.S. and Plesha, M.E., "Concepts and Applications of Finite Element Analysis", Third Edition, John Wiley & Sons, New York, 1989.
- Darcy, H., "Les Fontaines Publiques de la Ville de Dijon", Dalmont, Paris, 1856.
- Davé, R., Kardos, J.L. and Dudukovic, M.P., "A Model for Resin Flow During Composite Processing: Part 1 - General Mathematical Development," *Polymer Composites*, Vol. 8, No. 1, 1987a, pp. 29-38.
- Davé, R., Kardos, J.L. and Dudukovic, M.P., "A Model for Resin Flow During Composite Processing: Part 2 - Numerical Analysis for Unidirectional Graphite/Epoxy Laminates," *Polymer Composites*, Vol. 8, No. 2, 1987b, pp. 123-132.
- Davé, R., "A Unified Approach to Modeling Resin Flow During Composite Processing," *Journal of Composite Materials*, Vol. 24, No. 1, 1990, pp. 22-41.
- Dealy, J.M. and Wissbrun, K.F., "Melt Rheology and its Role in Plastics Processing", Van Nostrand Reinhold, New York, 1990.
- Dhatt, G. and Touzot, G., "The Finite Element Method Displayed", John Wiley & Sons, New York, 1984.
- Dudukovic, M.P., Kardos, J.L., Yoon, I.S. and Yang, Y.B., "Autoclave Processing of Long Fiber Thermoplastic Composites", *Chemical Engineering and Science*, Vol. 45, No. 8, 1990, pp. 2519-2526.
- Dusi, M.R., Lee, W.I., Ciriscioli, P.R. and Springer, G.S., "Cure Kinetics and Viscosity of Fiberite 976 Resin," *Journal of Composite Materials*, Vol. 21, No. 3, 1987, pp. 243-261.

References

- Frank-Susich, D., Laananen, D. and Ruffner, D., "Computer-Aided Cure Optimization", Proceedings of the 37th International SAMPE Symposium, Vol. 37, Anaheim, California, March 1992, pp. 1075-1088.
- Gebart, B.R., "Permeability of Unidirectional Reinforcements for RTM", Journal of Composite Materials, Vol. 26, No. 8, 1992, pp. 1100-1133.
- Groves, D.J. and Stocks, D.M., "Rheology of thermoplastic-carbon fibre composite in the elastic and viscoelastic states", Composites Manufacturing, Vol. 2, No. 3/4, 1991, pp. 179-184.
- Groves, D.J., "A characterization of shear flow in continuous fibre thermoplastic laminates", Composites, Vol. 20, No. 1, 1989, pp. 28-32.
- Gutowski, T.G., "A Resin Flow/Fiber Deformation Model for Composites," SAMPE Quarterly, Vol. 16, No. 4, 1985, pp. 58-64.
- Gutowski, T.G., Kingery, J. and Boucher, D., "Experiments in Composites Consolidation: Fiber Deformation," Society of Plastic Engineers, Annual Technical Conference, 1986a, pp. 1316-1320.
- Gutowski, T.G., Cai, Z., D., Kingery, J. and Wineman, S.J., "Resin Flow/Fiber Deformation Experiments," SAMPE Quarterly, Vol. 17, No. 4, 1986b, pp. 54-58.
- Gutowski, T.G., Morigaki, T. and Cai, Z., "The Consolidation of Laminate Composites," Journal of Composite Materials, Vol. 21, No. 2, 1987a, pp. 172-188 .
- Gutowski, T.G., Cai, Z., Bauer, S., Boucher, D., Kingery, J. and Wineman, S.J., "Consolidation Experiments for Laminate Composites," Journal of Composite Materials, Vol. 21, No. 7, 1987b, pp. 650-669.
- Gutowski, T.G., and Dillon, G., "The Elastic Deformation of Lubricated Carbon Fiber Bundles: Comparison of Theory and Experiments", Journal of Composite Materials, Vol. 26, No. 16, 1992, pp. 2330-2347 .
- Holl, M.W. and Rehfield, L.W., "An Evaluation of the Current Status of Automated Process Control for Thermosetting Composites", Composites Materials Testing and Design, ASTM STP 1120, Philadelphia, 1992, pp. 308-319.
- Hubert, P., Johnston, A., Poursartip, A. and Vaziri, R., "A Two-Dimensional Finite Element Processing Model for FRP Composite Components", Proceedings of The 10th International Conference on Composite Materials (ICCM-10), Whistler, B.C., August 1995, pp. 149-156.
- Hubert, P., "Preliminary Study of Hercules 8552 Epoxy Resin Viscosity Modeling", Internal Project Report, Vancouver, BC, February 1995.
- Johnston, A. and Hubert, P., "Residual Deformation in Composites of Large Complex Forms, Final Contract Report", The Boeing Company, Contract Reference 9-4454-94MJH-301, May 1995.
- Jones, R.S. and Oakley, D., "An Interpretation of Rheological Data in Terms of Model Systems", Composites, Vol. 21, No. 5, 1990, pp. 415-418.

References

- Jones, R.S. and Roberts, R.W., "Anisotropic shear flow in continuous fibre composites", *Composites*, Vol. 25, No. 3, 1994, pp. 171-176.
- Kaprielian, P.V. and O'Neill, J.M., "Shearing Flow of Highly Anisotropic Laminated Composites", *Composites*, Vol. 20, No. 1, 1989, pp. 43-47.
- Karasudhi, P., "Fundations of Solid Mechanics", Kluwer Academic Publication, Boston, 1991.
- Kenny, J.M., Apicella, A. and Nicolais, L., "A Model for the Thermal and Chemorheological Behavior of Thermoset. I: Processing of Epoxy Based Composites," *Polymer Engineering and Science*, Vol. 29, No. 15, 1989, pp. 973-983.
- Kenny, J.M., Maffezzoli, A. and Nicolais, L., "A Model for the Thermal and Chemorheological Behavior of Thermoset Processing: (II) Unsaturated Polyester Based Composites," *Composites Science and Technology*, Vol. 38, No. 4, 1990, pp. 339-358.
- Kenny, J.M., "Integration of Precess Models with Control and Optimization of Polymer Composites Fabrication", *Proceedings of the Third Conference on Computer Aided Design in Composites Materials Technology*, 1992, pp. 530-544.
- Kim, Y.R., McCarthy, S.P. and Fanucci, J.P., "Compressibility and Relaxation of Fiber Reinforcements During Composite Processing", *Polymer Composites*, Vol. 12, No. 1, 1991, pp. 13-19.
- Lam, R.C. and Kardos, J.L., "The Permeability and Compressibility of Aligned and Cross-Plied Fiber Beds During Processing of Composites," *ANTEC 89*, 1989, pp. 1408-1412.
- Lee, W.I., Loos, A.C. and Springer, G.S., "Heat of Reaction, Degree of Cure, and Viscosity of Hercules 3501-6 Resin", *Journal of Composite Materials*, Vol. 16, 1982, pp. 510-520.
- Lewis, R.W. and Schrefler, B.A., "The Finite Element Method in the Deformation and Consolidation of Porous Media", John Wiley and Sons, Chichester, 1987.
- Loos, A.C. & Springer, G.S., "Curing of Epoxy Matrix Composites," *Journal of Composite Materials*, Vol. 17, No. 2, 1983, pp. 135-169.
- Loos, A.C. and William, T.F. Jr., "Resin Flow During Autoclave Cure of Graphite-Epoxy Composites", in: "High Modulus Fiber Composites in Ground Transportation and High Volume Applications", ASTM STP 873, D.W. Wilson Ed., American Society for Testing and Materials, Philadelphia, 1985, pp. 119-130.
- Lundstrom, T.S. and Gebart, B.R., "Effect of Perturbation on Fibre Architecture on Permeability Inside Fibre Tows", *Journal of Composite Materials*, Vol. 29, No. 4, 1995, pp. 424-443.
- Mackenzie, K.A., 1993, "Measurement of Resin Pressure in Composite Laminates During Cure", M. A. Sc. thesis, The University of British Columbia, Vancouver, BC, Canada.
- Mijovic, J. and Lee, C.H., "A Comparison of Chemorheological Models for Thermoset Cure," *Journal of Applied Polymer Science*, Vol. 38, No. 2, 1989, pp. 2155-2170.
- Ó Brádaigh, C.M., McGuinness, G.B. and Pipes, R.B., "Numerical analysis of stresses and deformations in composite materials sheet forming: central indentation of a circular sheet", *Composites Manufacturing*, Vol. 4, No. 2, 1993, pp. 67-83.

References

- Ó Brádaigh, C.M., "Sheet forming of composite materials", in: "Flow and Rheology in Polymer Composites Manufacturing", ed. S.G. Advani, Elsevier, Oxford, 1994.
- Owen, D.R.J. and Hinton, E., "Finite Elements in Plasticity", Pineridge Press Ltd., Swansea, 1980.
- Pipes, R.B., "Anisotropic Viscosities of an Oriented Fiber Composite with a Power-Law Matrix", *Journal of Composites Materials*, 26, 10, 1992, pp. 1536-1552.
- Poursartip, A., Riahi, G., Frederick, L. and Lin, X., "A Method to Determine Resin Flow During Curing of the Composites Laminates", *Polymer Composites*, Vol. 13, No. 1, 1992, pp. 58-65.
- Purslow, D. and Childs, R., "Autoclave Moulding of Carbon Fibre-Reinforced Epoxies", *Composites*, Vol. 17, No. 2, 1986, pp. 127-136.
- Rogers, T.G., "Squeezing flow of fibre-reinforced viscous fluids", *Journal of Engineering Mathematics*, Vol. 23, 1989, pp. 81-89.
- Rogers, T.G. and O'Neill, J.M., "Theoretical analysis of forming flows of fibre-reinforced composites", *Composites Manufacturing*, Vol. 2, No. 3/4, 1991, pp. 153-160.
- Saliba, T.E., Hofmann, D. and Smolinski, P., "Development of an In Situ Hall-Effect Sensor for On-Line Monitoring of Thickness and Compaction during Composite Curing", *Composites Sciences and Technology*, Vol. 51, 1994, pp. 1-9.
- Scherer, R. and Friedrich, K., "Inter- and intraply-slip flow processes during thermoforming of CF/PP-laminates", *Composites Manufacturing*, Vol. 2, No. 2, 1991, pp. 92-96.
- Skartsis, L., Bamin, Khomami, B. and Kardos, J.L., "Polymeric Flow through Fibrous Media", *Journal of Rheology*, Vol. 36, No. 4, 1992a, pp. 589-620
- Skartsis, B.K. and Kardos, J.L., "Resin Flow Through Fiber Beds During Composite Manufacturing Processes. Part I: Review of Newtonien Flow Through Fiber Beds", *Polymer Engineering and Science*, Vol. 32, No. 4, 1992b, pp. 221-230
- Skartsis, B.K. and Kardos, J.L., "Resin Flow Through Fiber Beds During Composite Manufacturing Processes. Part II: Numerical and Experimental Studies of Newtonien Flow Through Ideal and Actual Fiber Beds", *Polymer Engineering and Science*, Vol. 32, No. 4, 1992c, pp. 231-239
- Smith, G.D. and Poursartip, A., "A Comparison of Two Resin Flow Models for Laminate Processing", *Journal of Composite Materials*, Vol. 27, No. 17, 1993, pp. 1695-1711.
- Springer, G.S., "Resin Flow During the Cure of Fiber Reinforced Composites," *Journal of Composite Materials*, Vol. 16, No. 5, 1982, pp. 400-410.
- Tam, A.S. and Gutowski, T.G., "Ply-Slip During the Forming of Thermoplastic Composite Parts", *Journal of Composites Materials*, Vol. 23, 1989, pp. 587-605.
- Tang, J., Lee, W.I. and Springer, G.S., "Effects of Cure Pressure on Resin Flow, Voids, and Mechanical Properties," *Journal of Composite Materials*, Vol. 21, No. 5, 1987, pp. 421-440.
- Terzaghi, K., "Theoretical Soil Mechanics", John Wiley and Sons, New York, 1943.

References

Trochu, F., Gauvin, R. and Zhang, Z., "Simulation of Mold Filling in Resin Transfer Molding by Non-Conforming Finite Elements", in: "Computer Aided Design in Composite Material Technology Volume III", Computational Mechanics Publications, Oxford, 1992, pp.109-120.

Vermeer, P.A. and Verruijt, A., "An Accuracy Condition for Consolidation by Finite Element", International Journal for Numerical and Analytical Methods in Geomechanics, Vol. 5, 1981, pp. 1-14.

Wheeler, A.B. and Jones, R.S., "A characterization of anisotropic shear flow in continuous fibre composite materials", Composites Manufacturing, Vol. 2, No. 3/4, 1991, pp. 192-196.

Williams, J.G., Morris, C.E.M., and Ennis, B.C., "Liquid Flow Through Aligned Fiber Beds," Polymer Engineering and Science, Vol. 14, No. 6, 1974, pp. 413-419.

Young, W.-B., "Resin Flow Analysis in the Consolidation of Multi-Directional Laminated Composites", Polymer Composites, Vol. 16, No. 3, 1995, pp. 250-257.

Appendix A Flow-Compaction Model Details

This appendix contains details of the finite element formulation for the flow-compaction model presented in Chapter 3. The derivation of the composite continuity equation is first presented in Section A.1 followed by the development of the Galerkin residual equations in Section A.2. Then, the shape functions used and their derivatives are presented in Section A.3. The numerical integration method used and the computation of the element load vector is presented in Section A.4. The element fibre bed properties (i.e. permeability and elastic modulus) calculations are discussed in Section A.5. Finally, details on the computation of the state variables are presented in Section A.6.

A.1 Composite continuity equation

For a given representative element containing fibres and resin, the conservation of mass has to be satisfied. The mass conservation relations for each of the composite constituents can be written:

- The mass conservation for the fibres is:

$$(\rho_F(1-\phi)\dot{u}_i)_i + \frac{\partial((1-\phi)\rho_F)}{\partial t} = 0 \quad (\text{A.1})$$

where ρ_F is the fibre density, ϕ is the fibre bed porosity and \dot{u}_i is the fibre bed velocity.

Performing the time and spatial derivatives, Equation A.1 is reduced to:

$$\dot{u}_{i,i}(1-\phi) + (\rho_F(1-\phi))_i \frac{\dot{u}_i}{\rho_F} - \dot{\phi} + \frac{(1-\phi)}{\rho_F} \dot{\rho}_F = 0 \quad (\text{A.2})$$

- The mass conservation for the resin is:

$$(\rho_R \phi \dot{u}_{Ri})_{,i} + \frac{\partial(\phi \rho_R)}{\partial t} = 0 \quad (\text{A.3})$$

where \dot{u}_{Ri} is the resin velocity. Equation A.3 can be reduced to:

$$\dot{u}_{Ri,i} \phi + (\rho_R \phi)_{,i} \frac{\dot{u}_{Ri}}{\rho_R} + \dot{\phi} + \frac{\phi}{\rho_R} \dot{\rho}_R = 0 \quad (\text{A.4})$$

To obtain the mass conservation for an element of the composite, Equations A.2 and A.4 are combined:

$$\dot{u}_{i,i} (1 - \phi) + (\rho_F (1 - \phi))_{,i} \frac{\dot{u}_i}{\rho_F} - \dot{\phi} + \frac{(1 - \phi)}{\rho_F} \dot{\rho}_F + \dot{u}_{Ri,i} \phi + (\rho_R \phi)_{,i} \frac{\dot{u}_{Ri}}{\rho_R} + \dot{\phi} + \frac{\phi}{\rho_R} \dot{\rho}_R = 0 \quad (\text{A.5})$$

The resin velocity can be expressed in terms of the Darcy's velocity (the resin velocity relative to the fibre bed) using the following relation:

$$\dot{u}_{Ri} = \frac{v_i}{\phi} + \dot{u}_i \quad (\text{A.6})$$

where v_i is the relative velocity between the fibres and the resin. Substituting Equation A.6 in Equation A.5 the continuity equation becomes:

$$\dot{u}_{i,i} + \frac{1}{\rho_F} (\rho_F (1 - \phi))_{,i} \dot{u}_i + \frac{(1 - \phi)}{\rho_F} \dot{\rho}_F + \left(\frac{v_i}{\phi} \right)_{,i} \phi + \frac{1}{\rho_R} (\rho_F \phi)_{,i} \left(\frac{v_i}{\phi} \right) + \frac{1}{\rho_R} (\rho_F \phi)_{,i} (\dot{u}_i) + \frac{\phi}{\rho_R} \dot{\rho}_R = 0 \quad (\text{A.7})$$

Equation A.7 can be simplified by assuming that the fibres and the resin are incompressible:

$$\begin{aligned} (\rho_R)_{,i} &= 0 \quad \text{and} \quad \dot{\rho}_R = 0 \\ (\rho_F)_{,i} &= 0 \quad \text{and} \quad \dot{\rho}_F = 0 \end{aligned} \quad (\text{A.8})$$

With the assumptions of Equation A.8, Equation A.7 simplifies to:

$$(\dot{u}_i)_{,i} + \left(\frac{v_i}{\phi} \right)_{,i} \phi = 0 \quad (\text{A.9})$$

Assuming spatial variation of the porosity to be negligible ($\phi_{,i} \approx 0$), the continuity equation becomes:

$$(\dot{u}_i)_{,i} + (v_i)_{,i} = 0 \quad (\text{A.10})$$

A.2 Residual equations development

This section presents the details of the integration of the residual equations.

- **Stress equilibrium**

The Galerkin residual equation for the stress equilibrium relation (Equations 3.13 and 3.14) is:

$$\int_{\Omega} \left((\bar{\sigma}_{ij} - \delta_{ij}P)_{,j} + F_i \right) W_k d\Omega = 0 \quad (\text{A.11})$$

Equation A.11 is rearranged as follows:

$$\int_{\Omega} \bar{\sigma}_{ij,j} W_k d\Omega - \int_{\Omega} (\delta_{ij}P)_{,j} W_k d\Omega = - \int_{\Omega} F_i W_k d\Omega \quad (\text{A.12})$$

The first term of the LHS¹ of Equation A.12 can be rewritten as:

$$\int_{\Omega} \bar{\sigma}_{ij,j} W_k d\Omega = \int_{\Omega} (\bar{\sigma}_{ij} W_k)_{,j} d\Omega - \int_{\Omega} \bar{\sigma}_{ij} W_{k,j} d\Omega \quad (\text{A.13})$$

¹ Left Hand Side

Applying Green's theorem, the first integral of the RHS² of Equation A.13 becomes:

$$\int_{\Omega} (\bar{\sigma}_{ij} W_k)_{,j} d\Omega = \int_{\Gamma} (\bar{\sigma}_{ij} n_j) W_k d\Gamma \quad (\text{A.14})$$

where n_j is the unit normal vector to the boundary of the domain Γ .

The second term of the LHS of Equation A.12 can be rewritten as:

$$\int_{\Omega} (\delta_{ij} P)_{,j} W_k d\Omega = \int_{\Omega} (\delta_{ij} P W_k)_{,j} d\Omega - \int_{\Omega} \delta_{ij} P W_{k,j} d\Omega \quad (\text{A.15})$$

After applying Green's theorem, the first integral of the RHS of Equation A.15 becomes:

$$\int_{\Omega} (\delta_{ij} P W_k)_{,j} d\Omega = \int_{\Gamma} \delta_{ij} P n_j W_k d\Gamma \quad (\text{A.16})$$

Replacing the LHS terms of Equation A.12 with Equations A.13-16, the stress equilibrium residual equation becomes:

$$\int_{\Omega} \bar{\sigma}_{ij} W_{k,j} d\Omega - \int_{\Omega} \delta_{ij} P W_{k,j} d\Omega = \int_{\Omega} F_i W_k d\Omega + \int_{\Gamma} (\bar{\sigma}_{ij} n_j) W_k d\Gamma - \int_{\Gamma} \delta_{ij} P n_j W_k d\Gamma \quad (\text{A.17})$$

The two boundary integrals of Equation A.17 are combined together:

$$\int_{\Gamma} \sigma_i^n W_k d\Gamma = \int_{\Gamma} (\bar{\sigma}_{ij} n_j) W_k d\Gamma - \int_{\Gamma} \delta_{ij} P n_j W_k d\Gamma \quad (\text{A.18})$$

where σ_i^n is the applied traction normal to the boundary of the domain defined as:

$$\sigma_i^n = \bar{\sigma}_{ij} n_j - \delta_{ij} P n_j \quad (\text{A.19})$$

² Right Hand Side

Substituting Equation A.18 in Equation A.17, the residual equation for the stress equilibrium simplifies to:

$$\int_{\Omega} \bar{\sigma}_{ij} W_{k,j} d\Omega - \int_{\Omega} \delta_{ij} P W_{k,j} d\Omega = \int_{\Omega} F_i W_k d\Omega + \int_{\Gamma} \sigma_i^n W_k d\Gamma \quad (\text{A.20})$$

• *Continuity*

The Galerkin residual equation for the continuity (Equations 3.13 and 3.15) is:

$$\int_{\Omega} \left(-(\dot{u}_i)_{,i} + \left(\frac{K_{ij}}{\mu} (P + \rho_R gh)_{,j} \right)_{,i} \right) W_k d\Omega = 0 \quad (\text{A.21})$$

Equation A.21 can be rearranged as follows:

$$-\int_{\Omega} (\dot{u}_i)_{,i} W_k d\Omega + \int_{\Omega} \left(\frac{K_{ij}}{\mu} (P + \rho_R gh)_{,j} \right)_{,i} W_k d\Omega = 0 \quad (\text{A.22})$$

The second term of the LHS of Equation A.22 can be written as:

$$\int_{\Omega} \left(\frac{K_{ij}}{\mu} (P + \rho_R gh)_{,j} \right)_{,i} W_k d\Omega = \int_{\Omega} \left(\frac{K_{ij}}{\mu} (P + \rho_R gh)_{,j} W_k \right)_{,i} d\Omega - \int_{\Omega} \frac{K_{ij}}{\mu} (P + \rho_R gh)_{,j} W_{k,i} d\Omega \quad (\text{A.23})$$

After applying Green's theorem, the first integral of the RHS of Equation A.23 becomes:

$$\int_{\Omega} \left(\frac{K_{ij}}{\mu} (P + \rho_R gh)_{,j} W_k \right)_{,i} d\Omega = \int_{\Gamma} \frac{K_{ij}}{\mu} (P + \rho_R gh)_{,j} n_i W_k d\Gamma \quad (\text{A.24})$$

Replacing the LHS terms of Equation A.21 with Equations A.23-24, the continuity residual equation becomes:

$$-\int_{\Omega} (\dot{u}_i)_{,i} W_k d\Omega - \int_{\Omega} \frac{K_{ij}}{\mu} (P + \rho_R gh)_{,j} W_{k,i} d\Omega = -\int_{\Gamma} \frac{K_{ij}}{\mu} (P + \rho_R gh)_{,j} n_i W_k d\Gamma \quad (\text{A.25})$$

The pressure head component in the second term of the LHS of Equation A.25 can be extracted, thus:

$$-\int_{\Omega} (\dot{u}_i)_{,i} W_k d\Omega - \int_{\Omega} \frac{K_{ij}}{\mu} P_{,j} W_{k,i} d\Omega = \int_{\Omega} \frac{K_{ij}}{\mu} (\rho_R gh)_{,j} W_{k,i} d\Omega - \int_{\Gamma} \frac{K_{ij}}{\mu} (P + \rho_R gh)_{,j} n_i W_k d\Gamma \quad (\text{A.26})$$

Furthermore, the boundary integral of Equation A.26 can be written as follows:

$$\int_{\Gamma} \frac{K_{ij}}{\mu} (P + \rho_R gh)_{,j} n_i W_k d\Gamma = \int_{\Gamma} q^n W_k d\Gamma \quad (\text{A.27})$$

where q^n is the applied flux normal to the boundary of the domain. Substituting Equation A.27 in Equation A.26, the residual equation for the continuity simplifies to:

$$-\int_{\Omega} (\dot{u}_i)_{,i} W_k d\Omega - \int_{\Omega} \frac{K_{ij}}{\mu} P_{,j} W_{k,i} d\Omega = \int_{\Omega} \frac{K_{ij}}{\mu} (\rho_R gh)_{,j} W_{k,i} d\Omega - \int_{\Gamma} q^n W_k d\Gamma \quad (\text{A.28})$$

A.3 Element shape functions and their derivatives

The element used is a plane bilinear isoparametric element shown in Figure A.1. For this type of element, the shape functions are (Cook et al, 1989):

$$\mathbf{N} = \begin{bmatrix} \frac{1}{4}(1-\xi)(1-\eta) \\ \frac{1}{4}(1+\xi)(1-\eta) \\ \frac{1}{4}(1+\xi)(1+\eta) \\ \frac{1}{4}(1-\xi)(1+\eta) \end{bmatrix} \quad (\text{A.29})$$

where ξ and η are the natural coordinates defined in Figure A.1. The derivatives of the shape functions in the ξ, η coordinate system are:

$$\mathbf{N}_{,\xi} = \begin{bmatrix} -\frac{1}{4}(1-\eta) \\ \frac{1}{4}(1-\eta) \\ \frac{1}{4}(1+\eta) \\ -\frac{1}{4}(1+\eta) \end{bmatrix} \quad \text{and} \quad \mathbf{N}_{,\eta} = \begin{bmatrix} -\frac{1}{4}(1-\xi) \\ -\frac{1}{4}(1+\xi) \\ \frac{1}{4}(1+\xi) \\ \frac{1}{4}(1-\xi) \end{bmatrix} \quad (\text{A.30})$$

To obtain the shape function derivatives in the real coordinate system (x-z) the following relation is used:

$$\begin{Bmatrix} \mathbf{N}_{,x} \\ \mathbf{N}_{,z} \end{Bmatrix} = \mathbf{J}^{-1} \begin{Bmatrix} \mathbf{N}_{,\xi} \\ \mathbf{N}_{,\eta} \end{Bmatrix} \quad (\text{A.31})$$

where \mathbf{J} is the Jacobian matrix defines as:

$$\mathbf{J} = \begin{bmatrix} \sum_{i=1,4} \mathbf{N}_{,\xi} x_i & \sum_{i=1,4} \mathbf{N}_{,\xi} z_i \\ \sum_{i=1,4} \mathbf{N}_{,\eta} x_i & \sum_{i=1,4} \mathbf{N}_{,\eta} z_i \end{bmatrix} \quad (\text{A.32})$$

with x_i and z_i representing the nodal coordinates of the element.

The matrices \mathbf{B} and \mathbf{G} containing the shape functions derivatives in the system of residual equations (Equations 3.24-3.29) are defined as follows:

$$\mathbf{B} = \begin{bmatrix} N_{1,x} & 0 & N_{2,x} & 0 & N_{3,x} & 0 & N_{4,x} & 0 \\ 0 & N_{1,z} & 0 & N_{2,z} & 0 & N_{3,z} & 0 & N_{4,z} \\ N_{1,z} & N_{1,x} & N_{2,z} & N_{2,x} & N_{3,z} & N_{3,x} & N_{4,z} & N_{4,x} \end{bmatrix} \quad (\text{A.33})$$

and

$$\mathbf{G} = \begin{bmatrix} N_{1,x} & N_{2,x} & N_{3,x} & N_{4,x} \\ N_{1,z} & N_{2,z} & N_{3,z} & N_{4,z} \end{bmatrix} \quad (\text{A.34})$$

The Kronecker vector δ is defined as follows:

$$\delta = \begin{Bmatrix} 1 \\ 1 \\ 0 \end{Bmatrix} \quad (\text{A.35})$$

A.4 Element spatial integration and load vector calculation

The element spatial integration is applied to the domain and the boundary integrals. Both are solved numerically using the Gaussian quadrature technique. The integrals in Equations 3.24-3.29 are expressed in a general form. The present problem is solved in the x-z plane and the integrals can be rewritten as:

$$\int_{\Omega} f(\Omega) d\Omega = \int_{-1}^1 \int_{-1}^1 f(\xi, \eta) |\mathbf{J}| d\xi d\eta \quad (\text{A.36})$$

where $|\mathbf{J}|$ is the determinant of the Jacobian matrix. For each element, the matrices \mathbf{S} , \mathbf{L} , \mathbf{L}^T and \mathbf{H} are evaluated using Gaussian quadrature. The integrals are solved as follows:

$$\int_{-1}^1 \int_{-1}^1 f(\xi, \eta) |\mathbf{J}| d\xi d\eta = \sum_{k=1}^n \sum_{l=1}^n f(\xi_k, \eta_l) |\mathbf{J}| w_k w_l \quad (\text{A.37})$$

where k and l are integrating Gauss points, w_k and w_l are Gauss point weights and ξ_k and η_l are the coordinates of the Gauss points. The number of Gauss points used depends on the type of element. For a bilinear element, four Gauss points are required and they are located as shown in Figure A.1. The Gauss point locations are at $\xi = \pm 1/\sqrt{3}$ and $\eta = \pm 1/\sqrt{3}$ and the weights are $w=1.0$ (Cook et al., 1989).

The relation presented in Equation A.37 is also used to evaluate the body load integrals in F^S and F^P (Equations 3.28 and 3.29). The composite body load integral in Equation 3.28 is given by:

$$\int_{\Omega} \mathbf{N}^T \mathbf{F}^g d\Omega \quad (\text{A.38})$$

where \mathbf{F}^g is a vector representing the gravity forces acting over a unit volume of the composite element. Since gravity acts in the z direction only, the term \mathbf{F}^g is given by:

$$\mathbf{F}^g = \begin{bmatrix} 0 \\ \rho_c g_z \end{bmatrix} \quad (\text{A.39})$$

where g_z is the gravitational acceleration and ρ_c is the density of the composite. The integration of Equation A.38 over an element is equivalent to distributing the body load of the element to its nodes. The matrix containing the pressure head in Equation 3.29 can be expressed by:

$$\mathbf{H}^d = \int_{\Omega} \frac{\mathbf{K}}{\mu} (\rho_R g) \mathbf{G} h d\Omega \quad (\text{A.40})$$

where h is the z coordinate at the element nodes above a reference line or datum (Figure A.2).

The boundary integrals in Equations 3.28 and 3.29 contain non-essential boundary conditions: external traction σ_i^n and external mass flux or resin flux q^n . The applied consistent force is simply divided equally between the two nodes defining the boundary (Figure A.2). This force is calculated by multiplying the element face stress by the length of the element edge on which the stress acts. The mass flux at a boundary is naturally set to zero (i.e. for the cases studied, no prescribed resin fluxes are applied at the boundary of the domain and $q^n=0$). The only situation when resin is flowing through a boundary is when a set resin pressure is applied at the boundary (i.e. free flow boundary condition).

A.5 Element fibre bed properties calculation

The fibre bed properties are calculated in the element coordinate system (x', z') defined in Figure A.3. Then, the properties are transformed to the global coordinate system (x, z) . First, the fibre bed permeability matrix (\mathbf{K}) computation is presented followed by the fibre bed tangent modulus matrix calculation (\mathbf{D}_T).

A.5.1 Fibre bed permeability matrix

The permeability matrix is obtained from the fibre volume fraction calculated at a Gauss point. The permeability in the z' direction is directly obtained from the ply transverse permeability K_2 . The permeability in the x' direction is obtained by a weighted average technique from the ply permeabilities K_1 and K_2 , and the ply orientation θ . The following procedure is used:

- *At a given Gauss point*

1. Calculate fibre volume fraction (V_f) (Section A.6.2).
2. Calculate K_1 and K_2 for each ply of the element using a given permeability model.
3. Calculate $K_{x'}^i$ for each ply using the relation:

$$\frac{1}{K_{x'}^i} = \frac{\cos^2 \theta_i}{K_1} + \frac{\sin^2 \theta_i}{K_2} \quad (\text{A.41})$$

4. Calculate the element longitudinal permeability $K_{x'}^e$ with:

$$K_{x'}^e = \frac{1}{A_e} \sum_{i=1}^n A_i K_{x'}^i \quad (\text{A.42})$$

where A_e is the element area and A_i is the ply area within the element.

5. Calculate the element transverse permeability K_z^e as follows:

$$K_z^e = K_2 \quad (\text{A.43})$$

6. Build the element permeability matrix in the local element coordinate system (x',z') as follows:

$$\mathbf{K}^e = \begin{bmatrix} K_{x'}^e & 0 \\ 0 & K_{z'}^e \end{bmatrix} \quad (\text{A.44})$$

7. Transform the element permeability matrix to the global coordinate system with:

$$\mathbf{K} = \mathbf{T}^T \mathbf{K}^e \mathbf{T} \quad (\text{A.45})$$

where

$$\mathbf{T} = \begin{bmatrix} \cos\beta & \sin\beta \\ -\sin\beta & \cos\beta \end{bmatrix} \quad (\text{A.46})$$

and β is the angle between the local and global coordinate system (Figure A.3).

A.5.2 Fibre bed tangent modulus matrix

The tangent modulus matrix is obtained from the strains calculated at a Gauss point. The constitutive law used to compute the tangent modulus matrix was introduced in Section 3.2.4.

The tangent modulus matrix is written as follows:

$$\mathbf{D}_T = \begin{bmatrix} E_1 & 0 & 0 \\ 0 & E_3 & 0 \\ 0 & 0 & G_{13} \end{bmatrix} \quad (\text{A.47})$$

where the input properties are the fibre bed:

- longitudinal elastic modulus, E_1

- transverse elastic modulus E_3^c in compression calculated from the fibre bed compaction curve
- transverse elastic modulus E_3^t in tension
- shear modulus G_{13}

The variation of $\bar{\sigma}_3$ versus ϵ_3 is non-linear (Figure A.4). Therefore, \mathbf{D}_T has to be updated during the solution based on the actual fibre strain because E_3 is not constant. The non-linear relationship between $\bar{\sigma}_3$ and ϵ_3 is present when the fibre bed is in compression, thus $E_3=f(\epsilon_3)$ if $\epsilon_3 < 0$. If the fibre bed is in tension, the fibre bed transverse modulus is assumed constant, thus $E_3=cte$ if $\epsilon_3 > 0$. The procedure to calculate the tangent modulus matrix is the following:

- *At a given Gauss point*

1. Calculate strain vector ϵ from the element nodal displacements using Equation 3.20.
2. Transform ϵ to the local coordinate system of the element to get ϵ^e (Equation A.58).
3. Extract the transverse strain ϵ_3^i .
4. If ϵ_3^i is in tension then $E_3=E_3^t$
5. If ϵ_3^i is in compression then calculate the slope of the compaction curve as illustrated in Figure A.4 to obtain E_3 .
6. Build the element tangent modulus matrix in the local element coordinate system (x',z') as follows:

$$\mathbf{D}_T^e = \begin{bmatrix} E_1 & 0 & 0 \\ 0 & E_3 & 0 \\ 0 & 0 & G_{13} \end{bmatrix} \quad (\text{A.48})$$

7. Transform \mathbf{D}_T^e to the global coordinate system with:

$$\mathbf{D}_T = \mathbf{T}_e^T \mathbf{D}_T^e \mathbf{T}_e \quad (\text{A.49})$$

where

$$\mathbf{T}_e = \begin{bmatrix} \cos^2 \beta & \sin^2 \beta & \cos \beta \sin \beta \\ \sin^2 \beta & \cos^2 \beta & -\cos \beta \sin \beta \\ -2 \cos \beta \sin \beta & 2 \cos \beta \sin \beta & \cos^2 \beta - \sin^2 \beta \end{bmatrix} \quad (\text{A.50})$$

and β is the angle between the local and global coordinate system (Figure A.3).

A.6 Element state variables computation

The element state variables are calculated during the iterative solution loop or at the end of the solution when the problem has converged. During the iterative solution, the element effective stresses are computed at the integration Gauss points for the calculation of the element internal load vector (Equation 3.39). When the problem has converged, the fibre bed effective stresses, the element strains, the element fibre volume fraction and the resin velocity are calculated at the centroid of the element. Finally, the total laminate mass loss is calculated.

A.6.1 Fibre bed effective stresses and element strains

The element strains are calculated from the nodal displacements of the element at a given time during the solution. From the strains calculated, the effective stresses are computed based on the fibre bed constitutive law. The element strains and effective stresses are computed according the following procedure:

• *At a given Gauss point*

1. Calculate strain vector $\boldsymbol{\varepsilon}$ from the element nodal displacements using Equation 3.20.
2. Transform $\boldsymbol{\varepsilon}$ to the local coordinate system of the element to get $\boldsymbol{\varepsilon}^e$ (Equation A.58).
3. Calculate element effective stresses based on the fibre bed constitutive law:
 - a) Calculate $\bar{\sigma}_1^i$ using $\bar{\sigma}_1^i = E_1 \varepsilon_1^i$
 - b) Calculate $\bar{\sigma}_{13}^i$ using $\bar{\sigma}_{13}^i = G_{13} \gamma_{13}^i$
 - c) If ε_3^i is in tension then $\bar{\sigma}_3^i = E_3 \varepsilon_3^i$
 - d) If ε_3^i is in compression $\bar{\sigma}_3^i$ is obtained from the compaction curve as illustrated in Figure A.4.
4. Transform $\bar{\sigma}^e$ to global coordinate to obtain $\bar{\sigma}$ (Equation A.59).

A.6.2 Fibre volume fraction

The element fibre volume fraction is computed from the element strains. The fibre volume fraction is defined as:

$$V_f = \frac{v_f}{v_c} \quad (\text{A.51})$$

where v_f and v_c are respectively the volume of fibre and the volume of the composite. The fibre volume is assumed to remain constant in the element. Therefore the volume of fibres for a given element is expressed as:

$$v_f = V_{f0} v_{c0} = \text{cte} \quad (\text{A.52})$$

where V_{f0} is the initial fibre volume fraction and v_{c0} is the initial volume of the element. At a given time during the solution, the element volumetric strain is defined as:

$$\varepsilon_v = \frac{\Delta v_c}{v_{c0}} = \frac{v_c - v_{c0}}{v_{c0}} \quad (\text{A.53})$$

Replacing v_c (Equation A.53) and v_f (Equation A.52) in Equation A.51, the relation for the fibre volume fraction is obtained as function of the element volumetric strain as:

$$V_f = \frac{V_{f0}}{\varepsilon_v + 1} \quad (\text{A.54})$$

The element fibre volume fraction is computed as followed:

- *At a given Gauss point*

1. Calculate strain vector ε from the element nodal displacements using Equation 3.20.
2. Calculate the volumetric strain using:

$$\varepsilon_v = \varepsilon_x + \varepsilon_z \quad (\text{A.55})$$

3. Calculate the fibre volume fraction using Equation A.54.

A.6.3 Resin velocity

The resin velocity \mathbf{v} is computed at the centroid of the element using the following relation:

$$\mathbf{v} = \frac{\mathbf{K}}{\mu} \mathbf{G} \mathbf{a}^p \quad (\text{A.56})$$

where \mathbf{a}^P is the pressure at nodes of the element and \mathbf{G} is defined from Equation A.34. The resin velocity is a vector having a component in the x and z directions. The following procedure is used to calculate the resin velocity:

- *At the centroid of the element*

1. Get element pressure at node \mathbf{a}^P .
2. Calculate element permeability (Section A.5.1).
3. Get the element resin viscosity.
4. Compute \mathbf{v} using Equation A.56.

A.6.4 Laminate mass loss

The laminate mass loss is computed from the element volumetric strains. This assumption is valid for a fully saturated porous medium. Any volumetric strains are caused by a resin volume loss. The total mass loss of the laminate is calculated by doing the summation of the mass loss for all the element forming the laminate:

$$m_{\text{rloss}} = \sum_{e=1}^n \rho_R^e \varepsilon_v^e A^e \quad (\text{A.57})$$

where ε_v^e is the element volumetric strain calculated at the element centroid (Equation A.55), ρ_R^e is the resin density at the element and A^e is the element area.

A.6.5 Stresses and strains coordinate transformation

The element effective stresses and strains are transformed from the local (x',z') to global (x,z) coordinate system and vice versa (see Figure A.3). The following transformation are used:

- *from global to local*

$$\varepsilon^e = \mathbf{T}_e \varepsilon \quad \text{and} \quad \bar{\sigma}^e = \mathbf{T}_e^{-T} \bar{\sigma} \quad \text{with setting } \beta = +\beta \text{ to define } \mathbf{T}_e \text{ (Equation A.50)} \quad (\text{A.58})$$

- *from local to global*

$$\varepsilon = \mathbf{T}_e \varepsilon^e \quad \text{and} \quad \bar{\sigma} = \mathbf{T}_e^{-T} \bar{\sigma}^e \quad \text{with setting } \beta = -\beta \text{ to define } \mathbf{T}_e \text{ (Equation A.50)} \quad (\text{A.59})$$

A.7 Figures

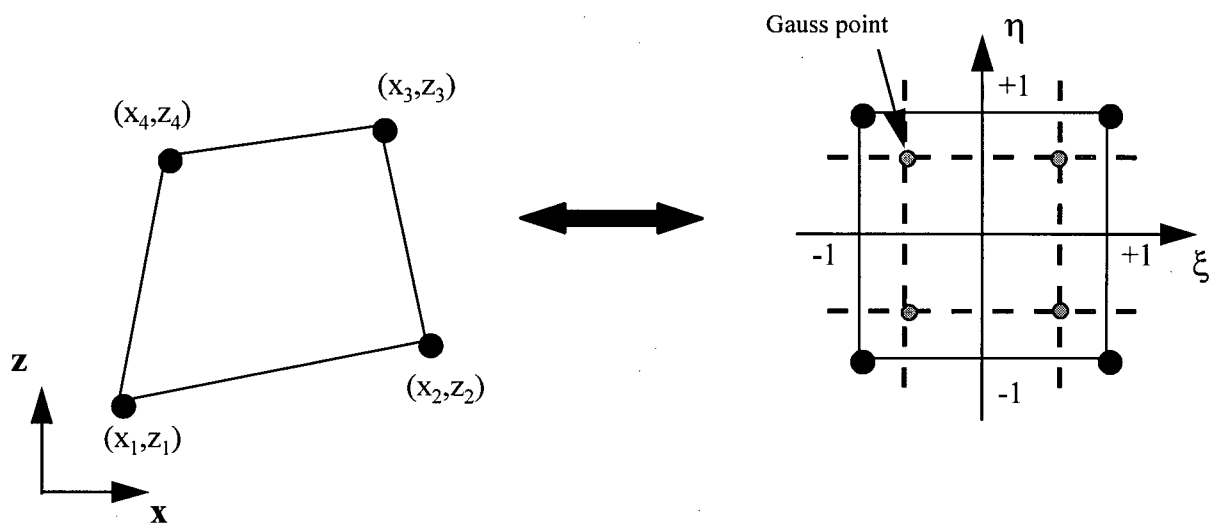


Figure A.1 Bilinear quadrilateral element: isoparametric transformation and Gauss points location.

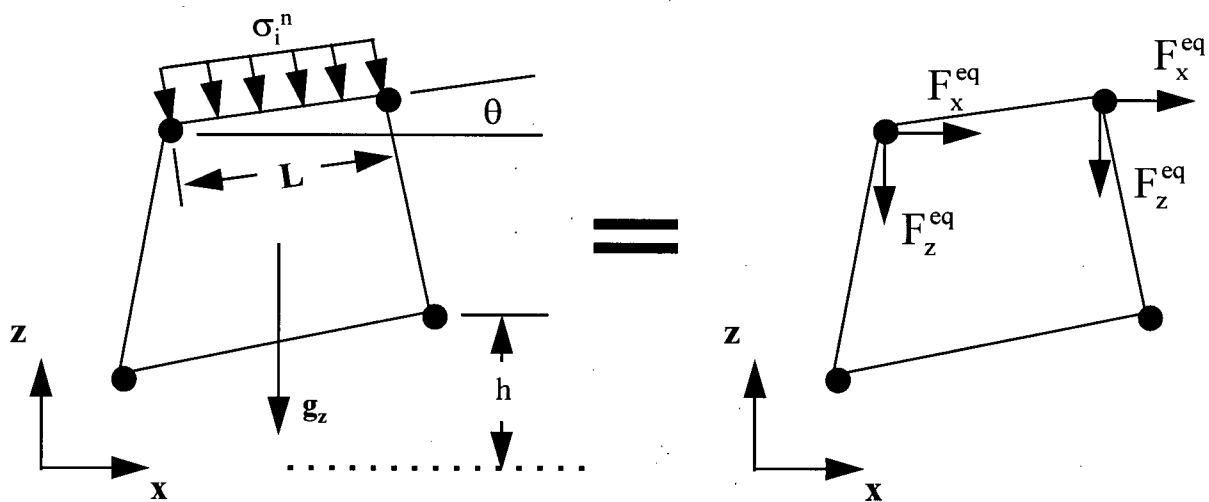
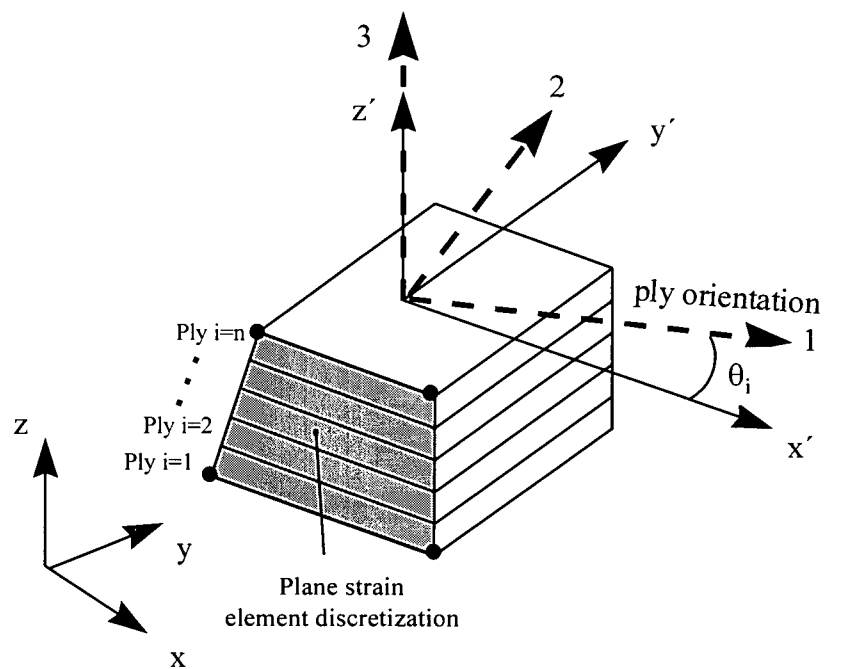
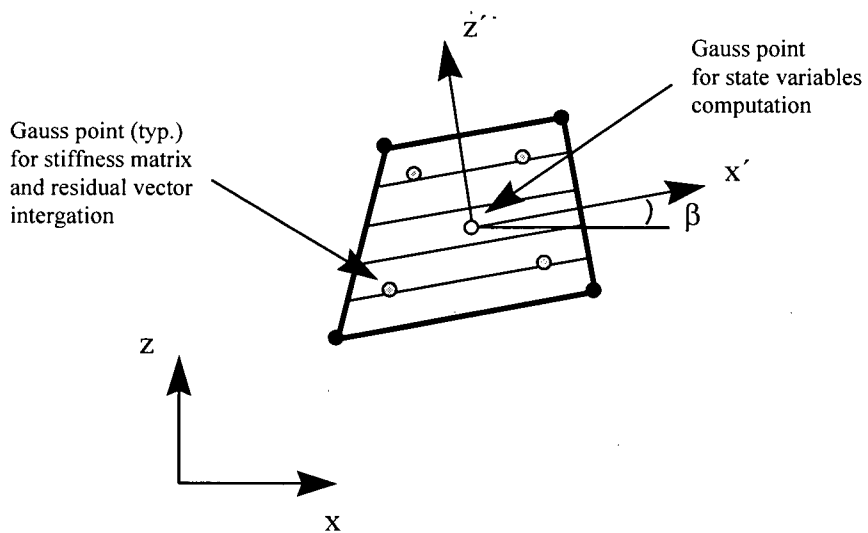


Figure A.2 Computation of equivalent nodal load vectors due to the applied external pressure.



General view



Plane view

Figure A.3 Element coordinate system.

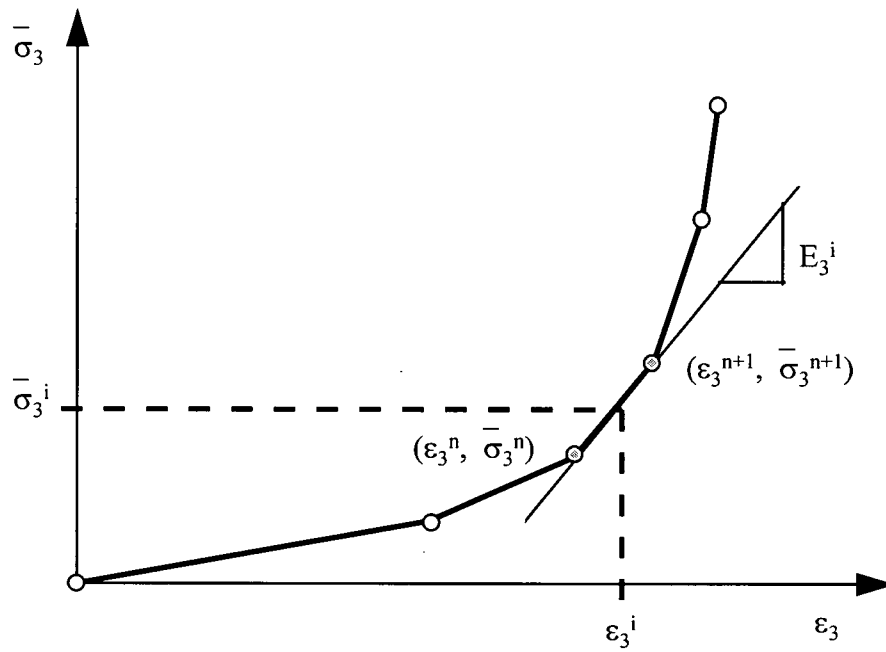


Figure A.4 Tangent modulus and effective stress calculation from the fibre bed compaction curve.

Appendix B Material Properties and Characterization

This appendix presents the cure kinetics models (Section B.1), the viscosity models (Section B.2) and the fibre bed permeability models (Section B.3) used for the materials studied. The results from the load-unload method used to measure the fibre bed compaction curve are presented in Section B.4.

B.1 Resin cure kinetics

The resin degree of cure and the temperature are the two state variables that fully describe the resin state at any time during the curing process. The cure kinetics model predicts the rate of cure of the resin as a function of time and temperature. The determination of the cure kinetics constants for the model requires a series of DSC (Dynamic Scanning Calorimetry) runs at constant or variable temperature (i.e. isothermal or dynamic runs). From the measured variation of the heat generated during curing, the rate of cure is calculated as follows:

$$\frac{d\alpha}{dt} = \frac{dq/dt}{H_r} \quad (\text{B.1})$$

where dq/dt is the rate of heat generation and H_r is the total heat of reaction for a complete cure. The resin degree of cure is then calculated by integrating Equation B.1 with respect to time. The choice for a particular cure kinetics equation depends on the type of the curing reaction of the resin studied. The accuracy of the prediction of resin dependent properties such as viscosity is strongly related to the accuracy of the cure kinetics model.

The cure kinetics equation for 3501-6 (i.e. resin in material A) was obtained from Lee et al. (1982). This resin has two different reactions occurring during the cure. Therefore, two different equations are used to describe the curing behaviour of this resin:

$$\begin{aligned} \frac{d\alpha}{dt} &= (C_1 + C_2\alpha)(1-\alpha)(B-\alpha) \quad \alpha \leq 0.3 \\ \frac{d\alpha}{dt} &= C_3(1-\alpha) \quad \alpha > 0.3 \end{aligned} \tag{B.2}$$

where

$$\begin{aligned} C_1 &= A_1 e^{-\Delta E_1/RT} \\ C_2 &= A_2 e^{-\Delta E_2/RT} \\ C_3 &= A_3 e^{-\Delta E_3/RT} \end{aligned} \tag{B.3}$$

A_1, A_2, A_3 are coefficients, $\Delta E_1, \Delta E_2, \Delta E_3$ are the reaction activation energies, R is the universal gas constant, T is the temperature and B is a constant. The values of the model constants for 3501-6 are presented in Table B.1 and were obtained by a non-linear least-squares curve fit to the $d\alpha/dt$ versus α relation obtained from Equation B.1.

The cure kinetics equation for 8552 resin was obtained from Johnston and Hubert (1995). The curing process of this resin can be described by a single modified autocatalytic equation:

$$\frac{d\alpha}{dt} = \frac{Ae^{-E_a/RT}\alpha^m(1-\alpha)^n}{\left(1 + e^{C(\alpha - (\alpha_{C0} + \alpha_{CT}))}\right)} \tag{B.4}$$

where E_a is the activation energy, T the temperature and m, n, A, C, α_{C0} and α_{CT} are experimentally determined constants. The standard autocatalytic equation was modified to take into account the decrease in the curing rate at high degrees of cure. This phenomenon is attributed to the change of the rate controlling mechanism from kinetics to diffusion, and occurs

as the resin glass transition temperature approaches the cure temperature. The value of the model constants for 8552 are presented in Table B.1 and were obtained using a weighted least-squares curve fit to the $d\alpha/dt$ versus α relation obtained from Equation B.4. The model is in good agreement with the experimental data within the temperature range found in typical processing conditions (Johnston and Hubert, 1995).

The determination of the resin degree of cure (α) consists of integrating Equation B.2 or B.4 with respect to time. In the present model, this task is performed by the thermochemical module as described in Section 3.1. The initial degree of cure, α_0 , has to be provided for the determination of α at a given time and temperature. For material A, a value of $\alpha_0=0.01$ was arbitrarily chosen. Since material B was slightly more advanced in cure (Section 4.1), a value of $\alpha_0=0.06$ was selected.

B.2 Resin viscosity

The resin viscosity is an essential material property for the flow model. As seen in Section 2.1, the resin viscosity can be determined by empirical equations assuming that the resin temperature and degree of cure are known at any time during the curing process. To determine the constants for the viscosity models, the viscosity of the resin is measured at different curing stages. This is commonly done with an oscillatory rotational rheometer. With this apparatus, the resin sample is sheared in torsion between two parallel discs (Figure B.1). The torque $T(t)$ applied to the specimen and the resulting angular displacement $\theta(t)$ are monitored. The resin viscosity is approximated as the complex viscosity $\eta^*(\omega)$ defined by (Collyer and Clegg, 1988):

$$\eta^*(\omega) = \frac{\sigma^*}{\dot{\gamma}^*(\omega)} \quad (\text{B.5})$$

where σ^* is the complex stress, $\dot{\gamma}^*(\omega)$ is the complex strain rate and ω is the oscillations frequency. The complex stress is calculated from the applied torque and the sample geometry. The complex strain rate is obtained from the angular displacement, the oscillations frequency and the sample geometry. The use of complex functions for η , σ and $\dot{\gamma}$ is more convenient when dealing with harmonic functions. The real and imaginary parts of the complex functions are associated to the elastic and viscous behaviour of the material respectively. In its fluid phase, the resin response is dominated by viscous behaviour. Thus, the resin viscosity correspond mainly to the imaginary part of the complex viscosity (i.e. $\mu \approx \eta''$, for $\eta'' \gg \eta'$ where η' and η'' are respectively the real and imaginary part of η^*). For low shear rates, the viscosity obtained from a oscillatory test can be approximated as the Newtonian fluid viscosity or steady state viscosity (Dealy and Wissbrun, 1990).

B.2.1 Viscosity model for 3501-6 resin

A viscosity model for 3501-6 resin was proposed by Lee et al. (1982):

$$\mu = \mu_{\infty} \exp(U / RT) \exp(\kappa\alpha) \quad (\text{B.6})$$

where μ_{∞} , U and κ are experimentally determined constants and T , α and R are respectively the temperature, the degree of cure and the universal gas constant. Equation B.6 is an Arrhenius type relation activated by temperature and degree of cure. The viscosity predictions from this model were compared with dynamic cure data provided by Hercules Advanced Materials & Systems Co. (Figure B.2). The model fails to predict the viscosity behaviour at temperatures below

100°C. This suggests that the constants used by Lee do not describe adequately the temperature-viscosity relationship. Using the experimental data from Figure B.2, a new set of constants for Equation B.6 were computed. Equation B.6 can be rewritten as follows:

$$\ln \mu = \ln \mu_{\infty} + U/RT + \kappa\alpha \quad (\text{B.7})$$

For small values of α , in the early stages of the curing, the relation between $\ln \mu$ and $1/T$ is linear and the constant U can be determined. This constant represent the temperature effect on the viscosity change and is referred to as the activation energy for the temperature. A plot of $\ln \mu$ versus $1/T$ is presented in Figure B.3 for the experimental results of Figure B.2 for a range of temperatures from 50°C to 90°C. At this stage, the resin degree of cure is still relatively low ($\alpha < 0.03$). From a linear regression analysis of the data in Figure B.3, a value of the activation energy, $U=114477$ J/mol, is extracted. Since the value of U is changed from $U=90800$ J/mol (Lee et al., 1982) to $U=114477$ J/mol, new values for the other constants have to be determined. From a best fit to the results of Figure B.2, a new set of constants for Equation B.6 was determined and are listed in Table B.2. As shown in Figure B.2, the viscosity model with the new set of constant is in better agreement with the experimental data over the entire temperature range. However, the present model constants predicts a lower minimum viscosity for the run at 5°C/min. In a typical autoclave cure, the heating rates rarely exceed 4°C/min. Therefore, it is expected that the viscosity model predictions will be acceptable for most real processing conditions.

B.2.2 Viscosity model for 8552 resin

No viscosity model data was available from the literature for Hercules 8552 resin. Therefore, tests were performed to measure the viscosity for this resin and an empirical model was used to fit the data.

B.2.2.1 Testing procedure

The neat resin was supplied to The Boeing Company. by Hercules Advanced Materials & Systems Company. All the experiments were conducted at the Boeing Material Technology Laboratory in Seattle, WA. A Rheometric RMS-800 parallel plate rheometer was used to measure the neat resin viscosity. The viscosity model constants were determined by a series of isothermal cure runs. A series of dynamic cures and a typical cure cycle run were conducted to validate the viscosity model. Table B.3 lists the different runs for this set of experiments.

The samples were sheared between two 50 mm parallel discs. A dynamic or sinusoidal wave torque signal was applied to the sample. The frequency of the signal was 10 rad/s at a maximum shear strain of 25%. The gap between the plates was about 0.6 mm and was measured precisely for each sample before the test. The following experimental procedure was typically followed:

1. New disks were installed on the apparatus
2. The disks were heated to the initial target temperature
3. The resin sample was poured between the disks
4. The disks were then brought together until a small compression load was measured
5. The sample was heated to the initial target temperature (this step took about five minutes)
6. The test was started
7. The test was stopped when the resin reached its gel point or if the test lasted more than two hours.

B.2.2.2 Experimental results

Figure B.4 shows the measured resin viscosity variation with time for the isothermal cure runs. For most of the runs, the expected trends were followed: as the cure temperature increases, the gel point¹ time and the initial minimum viscosity decrease. For the runs at high cure temperatures ($> 150^{\circ}\text{C}$), the initial sample heating can increase the degree of cure of the sample and hence the initial viscosity. This might explain the higher minimum viscosity measured for the run at 170°C . The results from the runs at temperatures over 150°C should be used with caution since one cannot guarantee that the initial degree of cure of the resin is near zero when the target temperature is reached.

Figure B.5 shows the resin viscosity variation with temperature for the dynamic cure runs. As the cure temperature ramp rate increases, the minimum viscosity decreases since the resin cures at a higher temperature. Also, in the initial stages of the dynamic run, ($< 130^{\circ}\text{C}$) viscosity is a function of temperature only as the resin degree of cure is still very low.

Figure B.6 shows the resin viscosity variation with time for a typical cure cycle. The viscosity curve has two minima: one after the first temperature ramp and one during the second temperature ramp just before gelation. During the hold time, the viscosity increases with time because of an increase in the degree of cure. Compared with the dynamic runs, the typical cure cycle gives a higher minimum viscosity and a lower gel point temperature.

¹ Taken when the viscosity reaches 100 Pa.s.

B.2.2.3 Viscosity model

The viscosity model used by Lee et al. (Equation B.6) was unsuccessful in predicting the viscosity profile of 8552 resin (Hubert, 1995). Lee's model can predict the viscosity variation due to temperature and degree of cure up to a degree of cure of 0.35, but cannot predict the high viscosity change near the gel point. A more complex empirical model by Kenny (1992) gave better results for 8552 resin. The model is as follows:

$$\mu = A_{\mu} \exp(E_{\mu} / RT) \left[\alpha_g / (\alpha_g - \alpha) \right]^{(A+B\alpha)} \quad (\text{B.8})$$

where A_{μ} , E_{μ} , A and B are experimentally determined parameters, R is the universal gas constant and α_g is the degree of cure at gelation. Again, Equation B.8 is an Arrhenius type relation where temperature and degree of cure effects are uncoupled. The model for 3501-6 resin (Equation B.6) assumes only a constant relationship between the degree of cure and the logarithm of the viscosity. On the other hand, Equation B.8 attempts to represent more comprehensively the effect of the degree of cure on the resin viscosity by incorporating the degree of cure at gelation in the relation. One can see that as α approaches α_g , the resin viscosity increases dramatically as the polymer becomes a three dimensional network.

Equation B.8 can be rewritten as follows:

$$\ln \mu = \ln A_{\mu} + E_{\mu} / RT + (A + B\alpha) \ln \left(\frac{\alpha_g}{\alpha_g - \alpha} \right) \quad (\text{B.9})$$

When the degree of cure is very small ($\alpha \approx 0$), Equation B.9 can be simplified to:

$$\ln \mu = \ln A_{\mu} + E_{\mu} / RT \quad (\text{B.10})$$

The slope of a linear regression through the data of $\ln\mu$ versus $1/T$ yields the value of E_μ . To cover a more complete range of variation of viscosity due to the temperature, the data from the dynamic runs at $1^\circ\text{C}/\text{min}$, $2^\circ\text{C}/\text{min}$ and $5^\circ\text{C}/\text{min}$ results are used. The degree of cure remains very low in the initial stages of the cure ($0.06 < \alpha < 0.07$). Figure B.7 shows the variation of $\ln\mu$ versus $1/T$ over a temperature range of 60 - 145°C . From a linear regression in the results of Figure B.7, the slope of the curve gives $E_\mu = 76536 \text{ J/mol}$. The gel point degree of cure is evaluated to be 0.47 from the viscosity tests. To evaluate the other constants, a best fit was done by changing the constants A_μ , A and B to fit the experimental data from the isothermal and dynamic runs. The best fit constants are given in Table B.2.

Figure B.4 shows the comparison of the viscosity model with the isothermal runs. Although there is an offset between the predicted and the measured viscosity, the model captures the increasing viscosity as the gel point is approached. The comparison with the dynamic runs (Figure B.5) confirms that the model describes the dramatic increase of viscosity as the resin reaches the gel point. The initial stage of the dynamic run is simulated well by the model. As with the 3501-6 viscosity model, the model for 8552 tends to predict a lower minimum viscosity particularly for the runs at $5^\circ\text{C}/\text{min}$ and $10^\circ\text{C}/\text{min}$. Again, this is not too critical because in practice heating rates found in typical autoclave rarely exceed $4^\circ\text{C}/\text{min}$. Finally, the viscosity model predictions are compared with experiments for a typical cure cycle in Figure B.6. Excellent agreement is found between the viscosity model and the experimental results.

B.3 Fibre bed permeability

The fibre bed permeability is a very difficult property to measure and was the subject of numerous detailed investigations as outlined in Section 2.2.2. Rather than trying to measure the permeability of the materials used, models published in the literature are used. The permeability for the fibre bed is given by the longitudinal and the transverse direction (i.e. K_1 and K_2) of an unidirectional fibre bed.

To get bounds on the range of permeability values found in the literature (Table B.4), the longitudinal and transverse permeabilities were calculated for a fibre bed having a fibre volume fraction ranging from 55 to 80%. The fibres are assumed to have a constant diameter of 8.0 μm . Figure B.8 shows the prediction of the different models for the longitudinal permeability. The three sources for the longitudinal permeability follow the same trend and they define a zone of variation for K_1 bounded by L1 and L3. Figure B.9 shows the predictions for the transverse permeability. The type of variation can be separated in two groups: T1 and T2 are the Kozeny equation type and T3, T4 and T5 are the modified Kozeny type where K_2 dramatically decreases as the fibre bed is compacted. A sensitivity analysis with the flow-compaction model is conducted in Section 5.1 to evaluate the effect of the permeability variation on the compaction of a typical laminate.

The permeability variations used as nominal values for the materials studied were chosen from the literature.

- ***longitudinal permeability, K_1***

The Kozeny equation is used (Equation 2.8):

$$K_1 = \frac{r_f^2 (1 - V_f)^3}{4k_1 V_f} \quad (\text{B.11})$$

with $r_f=4 \times 10^{-6}$ m and $k_1=0.7$ for material A and B.

- *transverse permeability*

The modified Kozeny equation from Gutwoski et al. (1987b), (Equation 2.9) is used:

$$K_2 = \frac{r_f^2 \left(\sqrt{\frac{V_a'}{V_f}} - 1 \right)^3}{4k' \left(\frac{V_a'}{V_f} + 1 \right)} \quad (\text{B.12})$$

with $r_f=4 \times 10^{-6}$ m, $k'=0.2$ for both materials, and $V_a'=0.81$ for material A and $V_a'=0.68$ for material B. The values used for V_a' corresponds to the value for V_a used to fit Gutowski's model to the results obtained from the compaction tests (Figure 4.10 for material A and Figure 4.12 for material B).

B.4 Compaction curve characterization with the load-unload method

With this method, the specimen was successively loaded and unloaded, and the maximum applied displacement was gradually increased for each loading-unloading step. During the loading phase, the applied load corresponds to a combination of the fibre bed elastic response and the resin viscous behaviour (Figure 4.2 (a)). The determination of the fibre bed elastic response requires the knowledge of the resin pressure at any time during the test. This is done by measuring the resin pressure or by calculating the resin pressure from a simple analytical viscoelastic model of the actual test (Figure 4.2 (b)). Accurate measurements of the resin

pressure are very difficult to obtain (Makenzie, 1993). Therefore, for the present analysis, the resin pressure load was calculated from a simple viscoelastic solution (Gutwoski et al., 1987a):

$$F_p = \frac{\mu L dh/dt}{3K_x hW} \quad (B.13)$$

where F_p is the resin pressure load, μ is the resin viscosity, K_x is the longitudinal permeability of the laminate, dh/dt is the loading rate and L , h and W are the specimen dimensions.

During the unloading phase, the fibre bed should deform elastically back to its original shape. In theory, the load measured during the unloading phase corresponds to the fibre bed effective stress. This is true only if the unloading is performed at a very slow rate so that the specimen remains in contact with the piston. In practice, nothing guarantees that this condition exists and therefore makes the interpretation of the data from the unloading phase difficult.

Figure B.10 presents the procedure used in calculating the load-displacement curve for the fibre bed from the load-unload test. From the load-displacement curves for the different steps, a master loading curve is built. This process consists of shifting the loading curves from each load-unload increment until they form a master curve (Figure B.10 (a)). Then, the resin pressure load is computed using Equation B.13 (Figure B.10 (b)). Finally, the fibre bed load is extracted (Figure B.10 (c)) by subtracting the resin pressure load from the total applied load using the effective stress principle (Equation 2.19). This method was used only for material A and two specimens were tested (6A01 and 6A02). The test conditions and the sample measurements are summarized in Table B.5.

B.4.1 Results

A typical load-displacement curve obtained by the load-unload test method is presented in Figure B.11. The test consisted of five load-unload cycles from which the following observations can be made:

- 1) As expected, the loading and unloading curves for any one cycle cannot be superposed. This behaviour confirms that the material is not purely elastic and the measured load is a combination of the resin pressure load and the fibre bed load.
- 2) The loading and unloading curves from different cycles cannot be superposed. Resin lost during one cycle does not flow back in the laminate. Therefore, a permanent deformation is created after each load-unload cycle.

As illustrated in Figure B.10 (a), the analysis of the test data consists of building a master loading curve. By taking the loading segments for each cycle, it is possible to shift the curves from cycles 2 to 5 in order to form a continuous loading curve from the curve of cycle 1 (Total load curve of Figure B.12). The testing parameters were used as input in Equation B.13 to calculate the resin pressure load. Finally, the fibre bed load was evaluated by simply subtracting the resin pressure load curve from the total load curve (Figure B.12). This procedure was repeated for sample 6A02 and the compaction curves obtained are compared with Gutowski's model (Equation 2.3) in Figure B.13. The compaction curves for the two specimens are similar: the effective stress is low ($\bar{\sigma}_3 < 200$ kPa) for strains lower than 0.2. After that point, $\bar{\sigma}_3$ increases dramatically as the maximum fibre bed compaction is reached. The parameters used in Gutowski's model (β , V_a and E_f , Equation 2.3) were chosen such that the maximum compaction

strain matches the experimental curves (Figure B.13). The shape of the compaction curves and the model are different, particularly between strains of 0.16 and 0.22.

B.4.2 Comparison with load-hold method

The fibre bed compaction curves obtained for materials A with the load-unload method and load-hold method (Section 4.3) are presented in Figure B.14. The predicted load-displacement curves using the compaction curves obtained from the two testing methods are compared with the experimental data from the validation tests (Section 4.4) in Figure B.15. The compaction curve obtained by the load-hold method is in good agreement with the experimental data. However, the load-unload curve failed to predict the load-displacement behaviour after a displacement of 0.3 mm.

The load-unload testing method, consisting of several loadings and unloadings of the specimen, could affect the fibre arrangement. A similar phenomenon was observed by Kim et al. (1991). They found that the shape of the compaction curve was affected by the number of loading-unloading cycles. The repetitive loading and unloading of the specimen could change the fibre arrangement or cause fibre breakage. This would imply that at each cycle, the fibre bed architecture is different. Therefore, the final compaction curve obtained by the load-unload method is in fact the compaction curve of a 'changing' fibre bed. On the other hand, with the load-hold method, the compaction curve is loaded to its maximum compaction strain in a single step. In this case, the fibre bed is compacted in a continuous monotonic manner.

Next, the load-unload method required the calculation of the resin pressure in order to compute the fibre bed compaction curve. The introduction of a calculated parameter can lead to some

errors in the determination of the actual fibre bed compaction curve. This problem is eliminated in the load-hold method where the fibre bed compaction curve is directly obtained from the experimental load-displacement curve.

B.5 Tables

Table B.1 Constants for the cure kinetics models of the resins.

Material A resin 3501-6 (Equation B.2)	Material B resin 8552 (Equation B.4)
$A_1=3.5017 \times 10^7 \text{ sec}^{-1}$ $A_2=3.3567 \times 10^7 \text{ sec}^{-1}$ $A_3=3.2667 \times 10^3 \text{ sec}^{-1}$ $\Delta E_1=80700 \text{ J/mol}$ $\Delta E_2=77800 \text{ J/mol}$ $\Delta E_3=56600 \text{ J/mol}$ $B=0.47$	$E_a=66500 \text{ J/mol}$ $A=1.53 \times 10^5 \text{ sec}^{-1}$ $m=0.813$ $n=2.74$ $C=43.1$ $\alpha_{C0}=5.48 \times 10^{-3}$ $\alpha_{CT}=-0.190/^\circ\text{C}$

Table B.2 Constants for the viscosity models of the resins.

Material A resin 3501-6 (Equation B.6)	Material B resin 8552 (Equation B.8)
$\mu_\infty=4.6 \times 10^{-17} \text{ Pa.s}$ $U=114477 \text{ J/mol}$ $\kappa=14.8$	$A_\mu=3.45 \times 10^{-10} \text{ Pa.s}$ $E_\mu=76536 \text{ J/mol}$ $A=3.8$ $B=2.5$ $\alpha_g=0.47$

Table B.3 Test matrix for material B resin 8552 viscosity characterization.

Sample	Run type
VH1101	Isothermal at 110°C
VH1201	Isothermal at 120°C
VH1301	Isothermal at 130°C
VH1401	Isothermal at 140°C
VH1501	Isothermal at 150°C
VH1601	Isothermal at 160°C
VH1701	Isothermal at 170°C
VR2C1	Dynamic at 2°C /min
VR5C1	Dynamic at 5°C /min
VR10C1	Dynamic at 10°C /min
VRKC1	Typical cure cycle *

* The cure cycle is a ramp of 1°C/min to 124°C, a hold of 60 min. and a ramp of 1°C/min to 177°C.

Table B.4 Summary of the fibre bed permeability variations for unidirectional fibre beds available from the literature.

Variation	Equation and constants
Longitudinal	
L1	Equation 2.8 $k=0.35$ (Dave et al. (1987b))
L2	Equation 2.8 $K=0.7$ (Gutwoski et al. (1987a))
L3	Equation 2.11 $c=57$ (Gebart (1992))
Transverse	
T1	Equation 2.8 $k=6$ (Dave et al. (1987b))
T2	Equation 2.8 $k=17.9$ (Gutwoski et al. (1987a))
T3	Equation 2.9 $k'=0.2, V_a'=0.82$ (Gutwoski et al. (1987a))
T4	Equation 2.9 $k'=0.2, V_a'=0.76$ (Gutwoski et al. (1987a))
T5	Equation 2.10 $C=0.4, V_{fmax}=0.785$ (Gebart (1992))

Table B.5 Test definition and measurement results for the determination of the fibre bed compaction curve tests.

Test definition				Measurements before test				Measurements after test			
Sample	Material	Test method	Temp. (°C)	M ₀ (g)	L ₀ (mm)	W ₀ (mm)	H ₀ (mm)	M' (g)	L' (mm)	W' (mm)	H' (mm)
6A01	A	Load-unload	142	4.30	47.75	24.96	2.51	3.61	48.58	24.84	2.19
6A02	A	Load-unload	142	4.46	48.37	25.56	2.53	4.01	48.00	24.80	2.23
7A01	A	Load-hold	105	4.79	52.01	24.96	2.56	4.05	52.43	25.03	2.30
7A02	A	Load-hold	106	4.74	52.42	24.68	2.60	4.00	52.49	24.99	2.28
7B01	B	Load-hold	143	5.98	52.30	25.41	3.27	5.98	52.78	25.22	2.97
7B02	B	Load-hold	148	5.60	50.66	25.41	3.15	5.37	50.82	25.20	2.74

* All tests are performed at a constant temperature and at a loading rate of 0.1 mm/min.

Table B.6 Test definition and measurement results for the fibre bed compaction curve validation tests.

Test definition				Measurements before test				Measurements after test			
Sample	Material, lay-up	Pressure	Temp. (°C)	M ₀ (g)	L ₀ (mm)	W ₀ (mm)	H ₀ (mm)	M' (g)	L' (mm)	W' (mm)	H' (mm)
4A01	A, 8 ply	*	100	2.28	49.01	25.25	1.29	1.94	49.25	24.64	1.08
4B02	B, 8 ply	*	100	2.86	48.93	25.21	1.63	2.80	49.17	24.77	1.49
5A01	A, 8 ply	*	140	2.26	48.22	25.18	1.26	1.91	48.29	24.75	1.14
5B02	B, 8 ply	*	140	2.77	47.80	25.03	1.64	2.49	49.62	24.77	1.32
9A01	A, 16 ply	**	170	4.73	52.42	25.11	2.55	3.92	52.33	25.15	1.97
9B01	B, 16 ply	**	170	5.55	51.98	25.41	3.14	5.27	52.62	25.22	2.62

* Load to 700 kPa at 70 kPa/min and unload to 0 kPa at 1000 kPa/min.

** Load to 700 kPa at 140 kPa/min, hold for 5 min and unload to 0 kPa at 140 kPa/min.

*** All tests are performed at a constant temperature and under load controlled conditions.

B.6 Figures

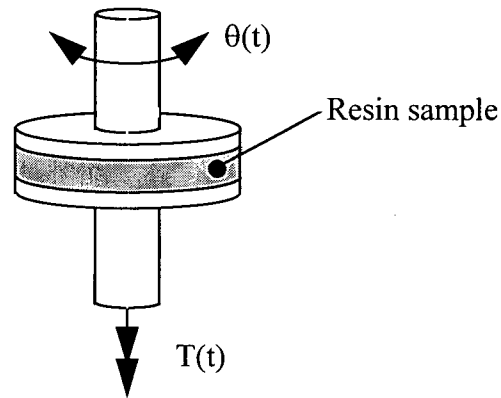


Figure B.1 Parallel plate viscosity test setup, torsional oscillation ($\theta(t)$) is applied to the specimen and the torque $T(t)$ is measured by a load cell.

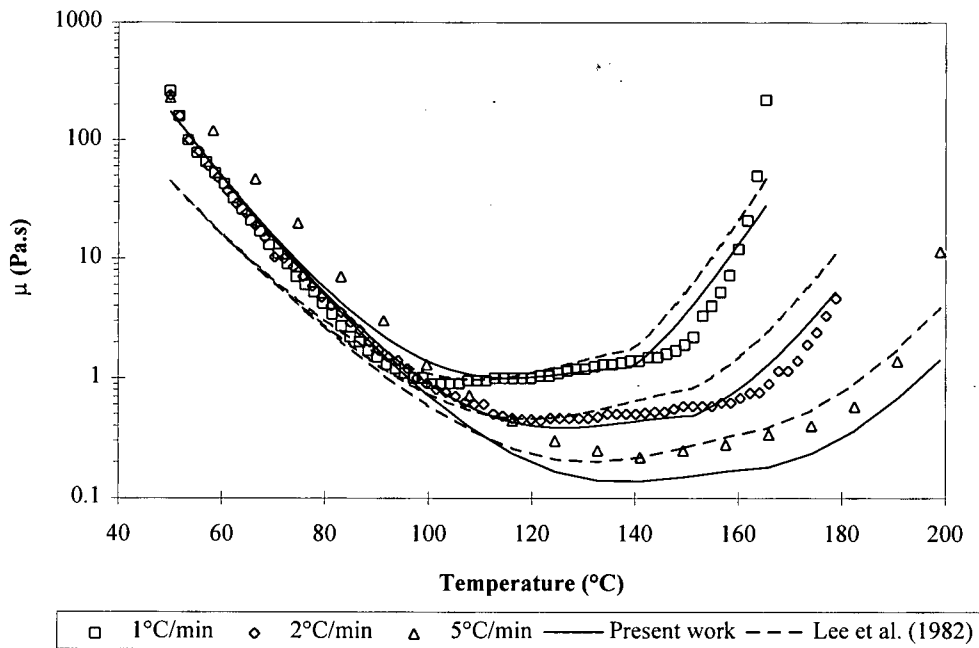


Figure B.2 Dynamic cure viscosity results (start temperature: 50°C) for material A resin (3501-6) and comparison with model predictions (Equation B.6) using constants from Table B.2 and constants in Lee et al. (1982).

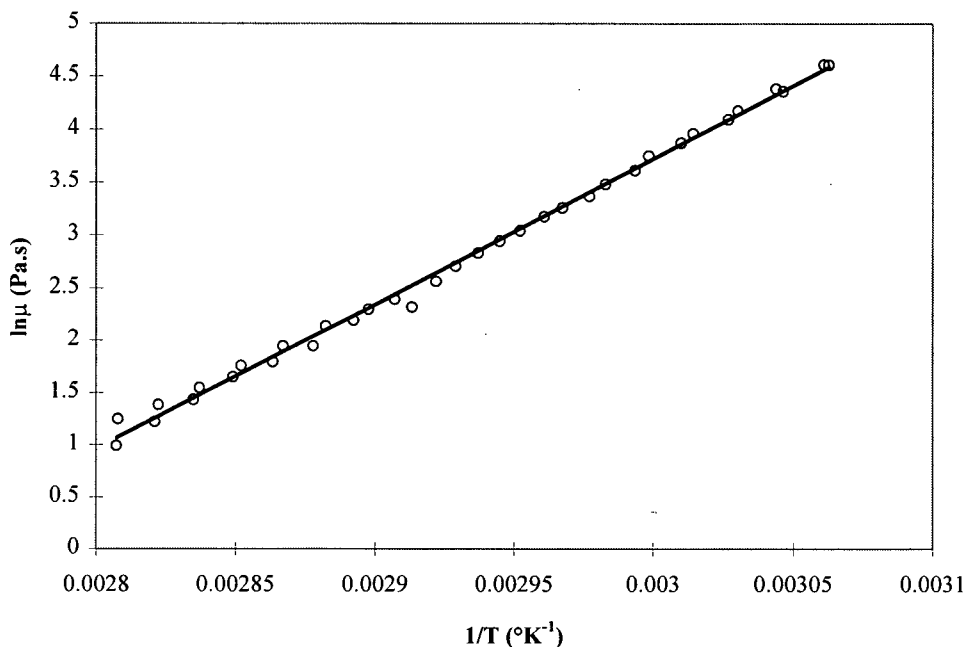


Figure B.3 Variation of $\ln \mu$ versus $1/T$ (Equation B.7 with $\alpha \approx 0$) for material A resin (3501-6) over a range of 50°C to 90°C. A linear regression leads to a value of 114477 J/mol for the activation energy U .

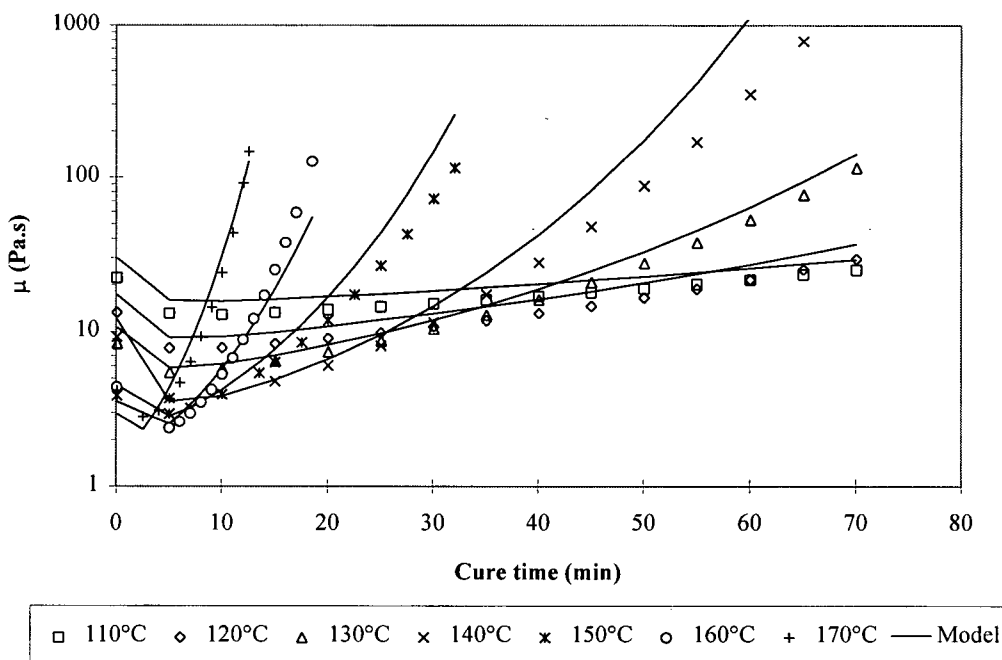


Figure B.4 Isothermal viscosity results for material B resin (8552) and comparison with model predictions (Equation B.8) using constants from Table B.2.

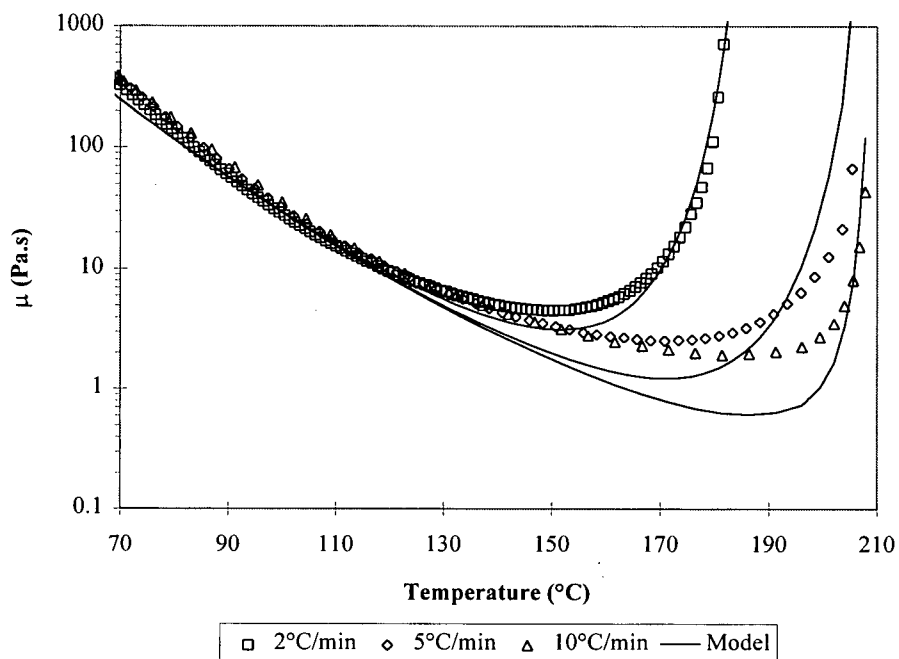


Figure B.5 Dynamic viscosity results (start temperature: 60°C) for material B resin (8552) and comparison with model predictions (Equation B.8) using constants from Table B.2.

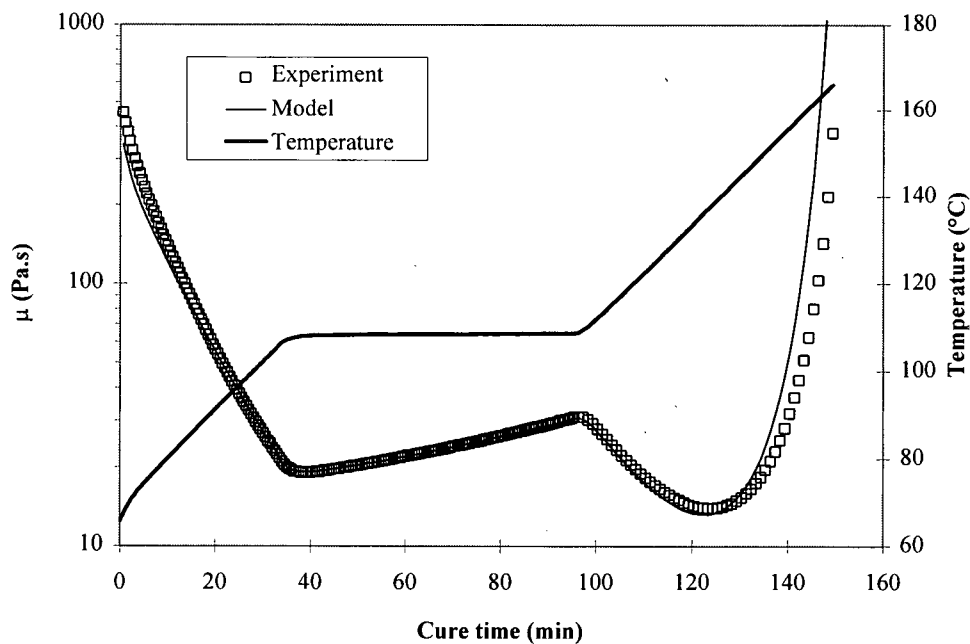


Figure B.6 Typical cure cycle viscosity results (start temperature: 60°C) for material B resin (8552) and comparison with model predictions (Equation B.8) using constants from Table B.2.

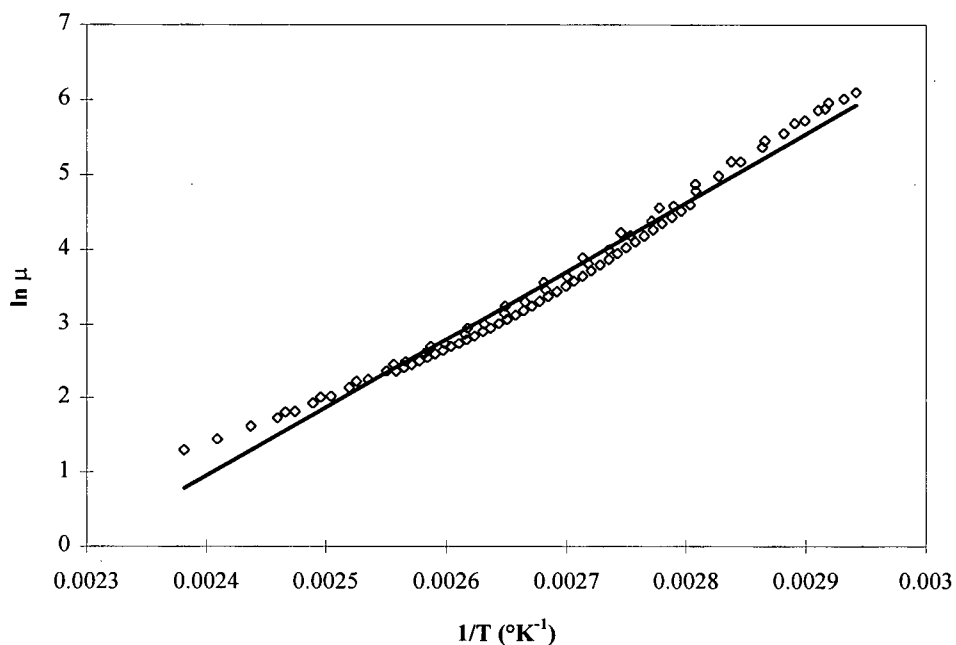


Figure B.7 Variation of $\ln \mu$ versus $1/T$ (Equation B.10) for material B resin (8552) over a range of 60°C to 145°C . A linear regression leads to a value of 76536 J/mol for the activation energy E_μ .

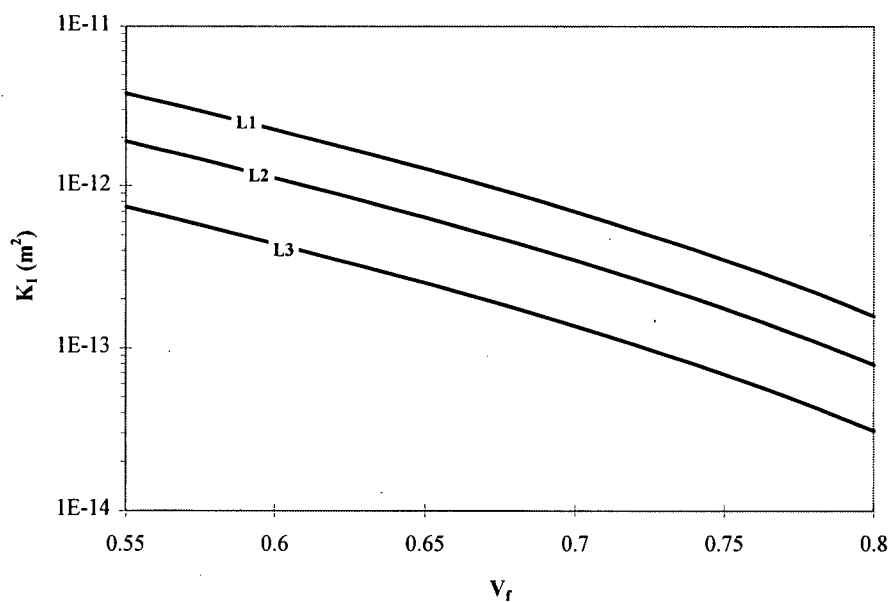


Figure B.8 Longitudinal permeability prediction for a unidirectional fibre bed from different sources (Table B.4) as a function of the fibre volume fraction.

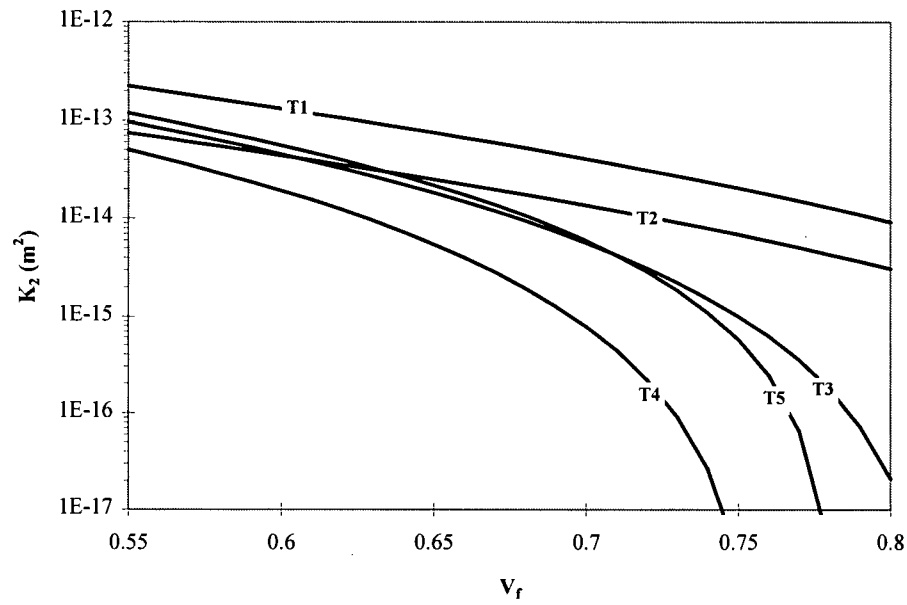


Figure B.9 Transverse permeability prediction for a unidirectional fibre bed from different sources (Table B.4) as a function of the fibre volume fraction.

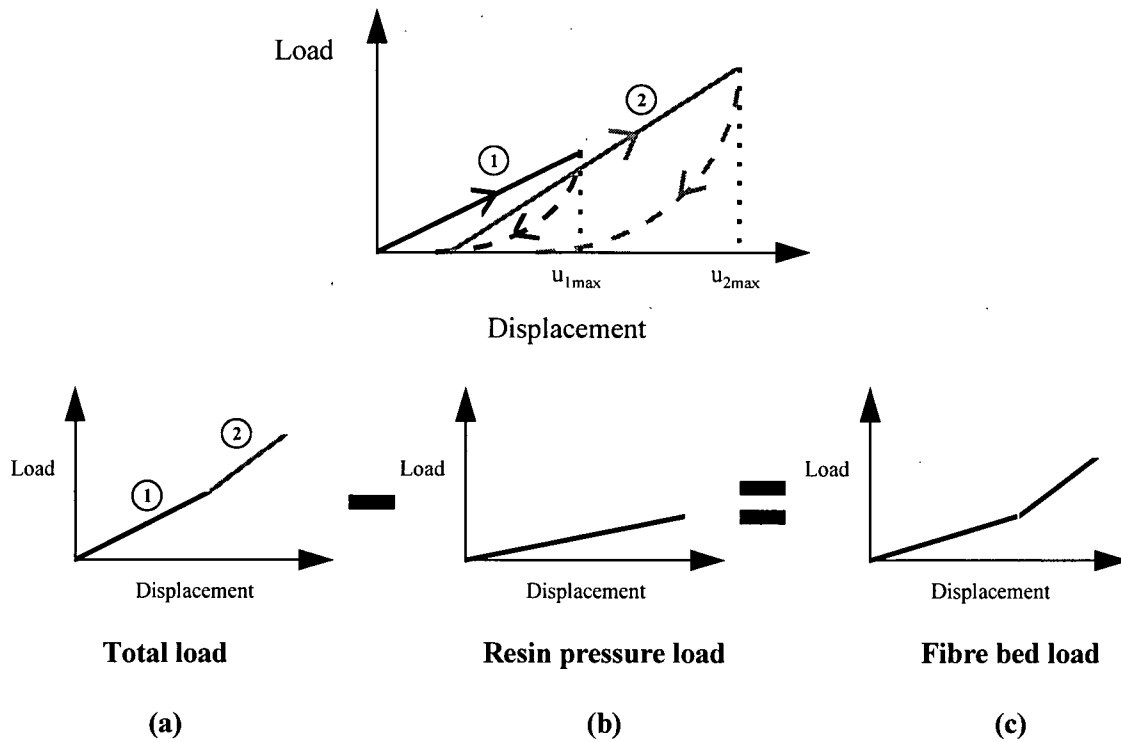


Figure B.10 Compaction curve computation for the load-unload test method, (a) master loading curve built from load-unload cycles, (b) resin pressure is computed, (c) the fibre bed load is calculated by subtracting (b) from (a).

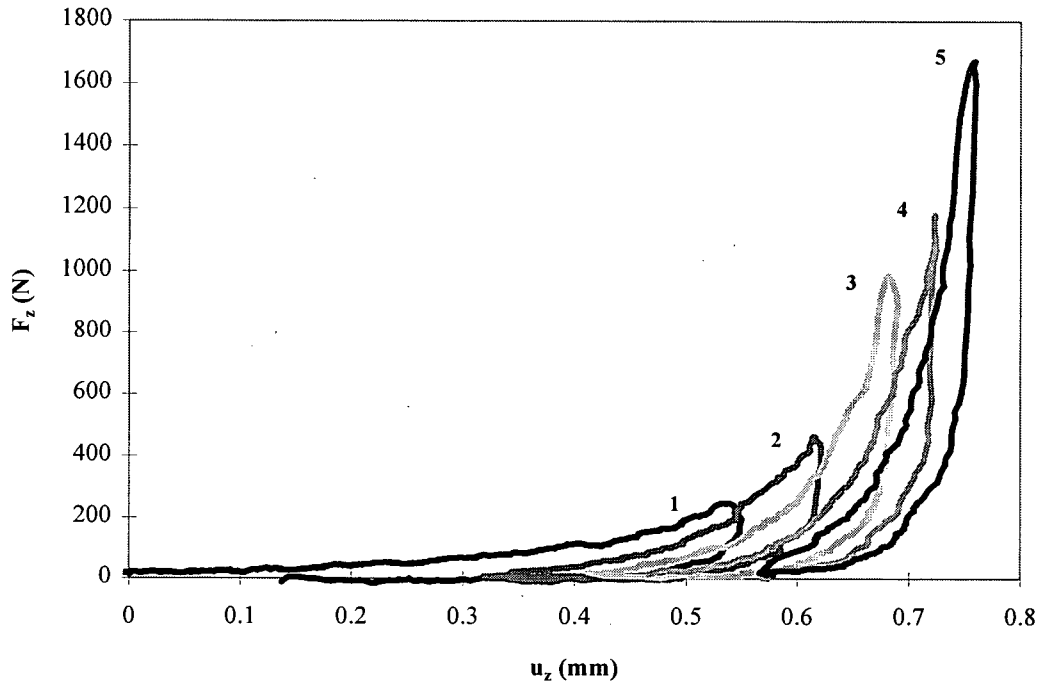


Figure B.11 Load-displacement curves for different load-unload cycles (1 to 5) for load-unload compaction test (material A, 6A01).

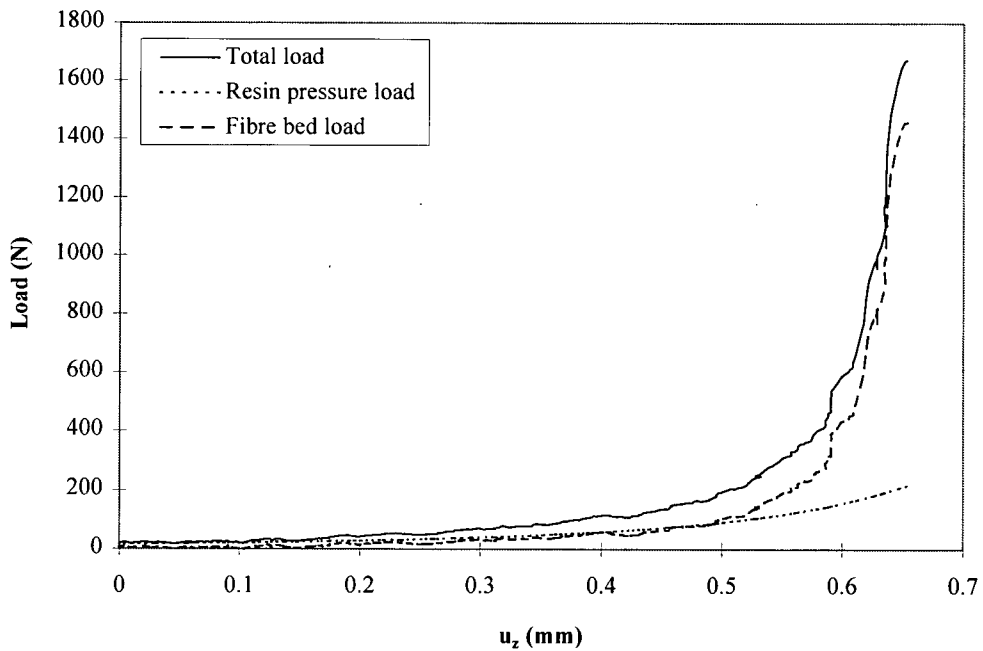


Figure B.12 Load-displacement curves for load-unload compaction test (material A, 6A01) showing the different components of the total load: the resin pressure load calculated from Equation B.13 and the fibre bed elastic load.

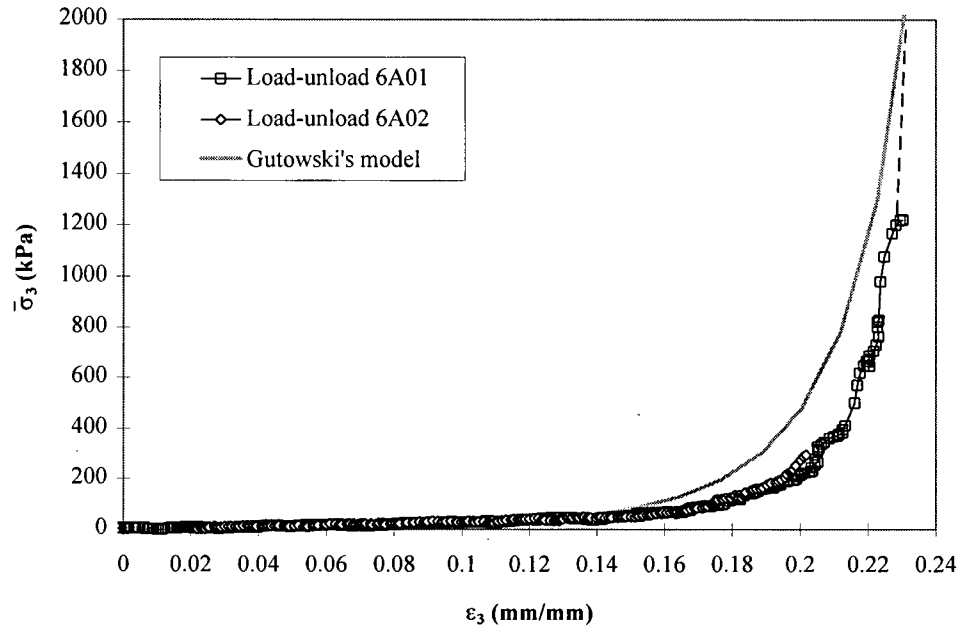


Figure B.13 Compaction curve for material A obtained with the load-unload method for samples 6A01 and 6A02. A comparison with Gutowski's model (Equation 2.3) is presented with $\beta=350$, $V_a=0.81$, $V_{f0}=0.558$ and $E_f=230$ GPa.

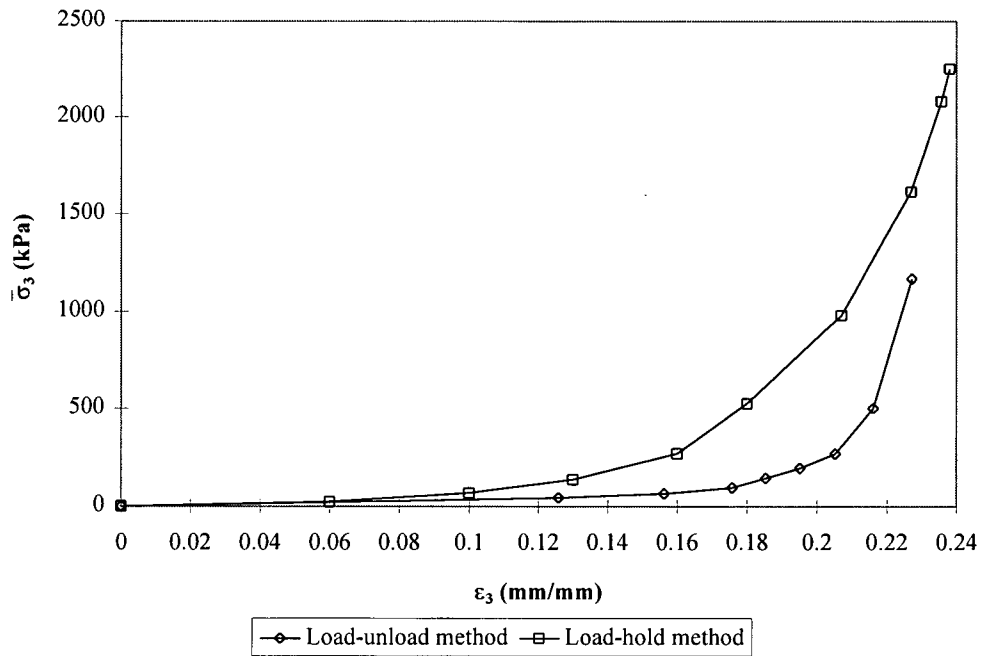


Figure B.14 Comparison of the compaction curves for the materials studied. For the material A, the curve obtained by both testing methods are shown.

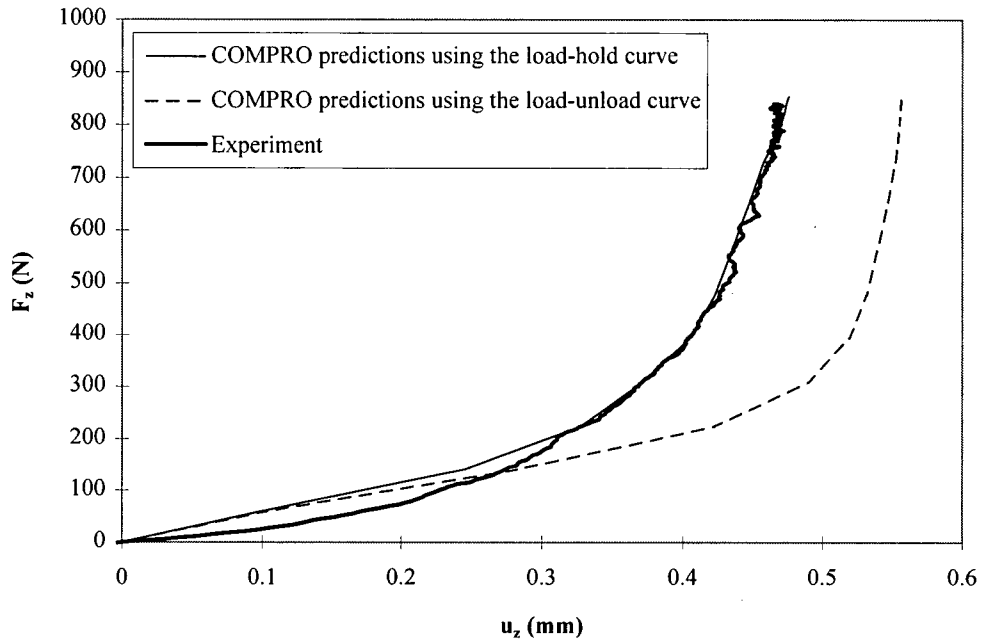


Figure B.15 Comparison of the load-displacement behaviour predictions using the compaction curves obtained by the load-unload and load-hold method respectively. The results are compared with specimen 9A01 (material A) experimental results.

Appendix C Results of Angle Laminate Compaction Experiments

The thickness and laminate mass measured before and after cure are presented in Table C.1. The thicknesses are measured at the location shown in Figure C.1. From the measurements presented in Table C.1, the laminate strains are calculated using the following relations:

- *laminate normal strain*

$$\varepsilon_{ni} = \frac{H_i - H_{0i}}{H_{0i}} \quad (C.1)$$

- *laminate total strain*

$$\varepsilon_{total} = \frac{\sum_i \varepsilon_{ni}}{4} \quad i = 1,2,4,5 \quad (C.2)$$

- *laminate percolation strain*

$$\varepsilon_{percolation} = \frac{(m_c - m_{c0})}{\rho_R} (V_{f0}\rho_F + (1 - V_{f0})\rho_R) \quad (C.3)$$

where m_{c0} is the laminate mass before cure, m_c is the laminate mass after cure, V_{f0} is the initial fibre volume fraction, ρ_R is the resin density and ρ_F is the fibre density. Details on the assumptions for the Equations C.1-C.3 are discussed in Section 5.2.2. Table C.2 presents the laminate strains calculated for all the sample tested.

C.1 Tables

Table C.1 Thickness and laminate mass measurements on the angle laminates before and after the cure.

Sample	m _{c0} (g)	H ₀₁ (mm)	H ₀₂ (mm)	H ₀₃ (mm)	H ₀₄ (mm)	H ₀₅ (mm)	m _c (g)	H ₁ (mm)	H ₂ (mm)	H ₃ (mm)	H ₄ (mm)	H ₅ (mm)
5AM1	49.85	4.84	4.93	5.46	4.80	4.84	49.78	4.64	4.67	4.33	4.69	4.62
5AM2	49.54	4.84	4.84	5.19	4.84	4.85	49.59	4.62	4.54	4.67	4.55	4.59
5AM3	49.83	4.90	4.84	5.08	4.86	4.85	49.96	4.53	4.51	4.63	4.50	4.53
5AM4	50.05	4.91	4.94	5.33	4.84	4.84	48.11	4.55	4.66	4.15	4.62	4.48
5AM5	48.94	4.80	4.80	5.18	4.81	4.80	47.65	4.49	4.35	4.65	4.33	4.40
5AM6	49.90	4.90	4.88	5.16	4.89	4.91	48.32	4.44	4.32	4.38	4.32	4.38
5BM7	52.73	5.02	5.22	4.41	5.12	4.99	51.72	4.89	4.92	3.97	5.00	4.95
5BM8	52.87	5.04	5.02	4.86	5.02	5.12	52.20	4.86	4.93	4.59	4.97	4.94
5BM9	52.82	4.97	5.02	5.02	4.94	4.97	51.01	4.68	4.61	4.61	4.71	4.65
5BM10	52.81	5.02	5.22	4.46	5.09	5.02	43.86	4.10	4.08	3.62	3.99	4.00
5BM11	52.51	5.02	5.02	4.71	4.91	4.94	43.90	4.20	4.08	4.40	4.11	4.20
5BM12	52.67	4.84	4.97	4.97	4.81	4.76	44.68	4.04	4.09	4.50	4.06	4.05
5CF1	42.71	4.88	4.84	4.57	4.84	4.88	42.37	4.58	4.34	5.60	4.24	4.58
5CF2	43.01	4.88	4.86	5.54	4.86	4.86	43.13	4.55	4.35	4.68	4.30	4.52
5CF3	42.97	4.84	4.89	5.23	4.89	4.90	42.93	4.51	4.45	4.84	4.44	4.55
5CF4	43.20	4.84	4.80	4.66	4.84	4.88	41.28	4.42	4.17	5.24	4.21	4.52
5CF5	42.72	4.90	4.81	5.32	4.85	4.85	41.56	4.35	4.10	4.03	4.17	4.36
5CF6	42.91	5.09	4.86	5.21	4.86	4.85	41.94	4.66	4.20	4.72	4.21	4.41
5DF7	45.22	5.12	5.17	4.97	4.94	5.09	42.45	4.40	4.80	7.37	4.47	4.45
5DF8	45.63	5.02	4.94	4.76	4.94	5.02	42.43	4.39	4.35	5.33	4.33	4.41
5DF9	45.43	4.89	4.94	4.94	4.91	4.91	41.30	4.27	4.30	5.34	4.24	4.23
5DF10	44.61	5.02	5.12	5.09	5.02	4.99	37.47	3.96	4.06	6.58	3.95	3.90
5DF11	45.66	4.99	4.94	4.84	4.91	4.99	38.18	3.92	3.93	4.11	3.82	3.91
5DF12	44.56	4.89	4.84	4.74	4.84	4.91	38.70	4.12	4.13	4.03	4.02	4.03

Table C.2 Laminate normal strains, total strain and percolation strain.

Sample	ϵ_{n1}	ϵ_{n2}	ϵ_{n3}	ϵ_{n4}	ϵ_{n5}	ϵ_{total}	$\epsilon_{percolation}$
5AM1	-0.04	-0.05	-0.21	-0.02	-0.05	-0.04	0.00
5AM2	-0.05	-0.06	-0.10	-0.06	-0.05	-0.06	0.00
5AM3	-0.08	-0.07	-0.09	-0.07	-0.07	-0.07	0.00
5AM4	-0.07	-0.06	-0.22	-0.05	-0.07	-0.06	-0.05
5AM5	-0.06	-0.09	-0.10	-0.10	-0.08	-0.09	-0.03
5AM6	-0.09	-0.11	-0.15	-0.12	-0.11	-0.11	-0.04
5BM7	-0.03	-0.06	-0.10	-0.02	-0.01	-0.03	-0.02
5BM8	-0.04	-0.02	-0.06	-0.01	-0.03	-0.02	-0.02
5BM9	-0.06	-0.08	-0.08	-0.05	-0.06	-0.06	-0.04
5BM10	-0.18	-0.22	-0.19	-0.22	-0.20	-0.21	-0.21
5BM11	-0.16	-0.19	-0.07	-0.16	-0.15	-0.17	-0.20
5BM12	-0.17	-0.18	-0.09	-0.16	-0.15	-0.16	-0.19
5CF1	-0.06	-0.10	0.22	-0.12	-0.06	-0.09	-0.01
5CF2	-0.07	-0.11	-0.15	-0.12	-0.07	-0.09	0.00
5CF3	-0.07	-0.09	-0.07	-0.09	-0.07	-0.08	0.00
5CF4	-0.09	-0.13	0.12	-0.13	-0.07	-0.11	-0.05
5CF5	-0.11	-0.15	-0.24	-0.14	-0.10	-0.13	-0.03
5CF6	-0.08	-0.14	-0.09	-0.13	-0.09	-0.11	-0.03
5DF7	-0.14	-0.07	0.48	-0.10	-0.13	-0.11	-0.08
5DF8	-0.12	-0.12	0.12	-0.12	-0.12	-0.12	-0.09
5DF9	-0.13	-0.13	0.08	-0.14	-0.14	-0.13	-0.11
5DF10	-0.21	-0.21	0.29	-0.21	-0.22	-0.21	-0.20
5DF11	-0.21	-0.20	-0.15	-0.22	-0.22	-0.21	-0.20
5DF12	-0.16	-0.15	-0.15	-0.17	-0.18	-0.16	-0.16

C.2 Figures

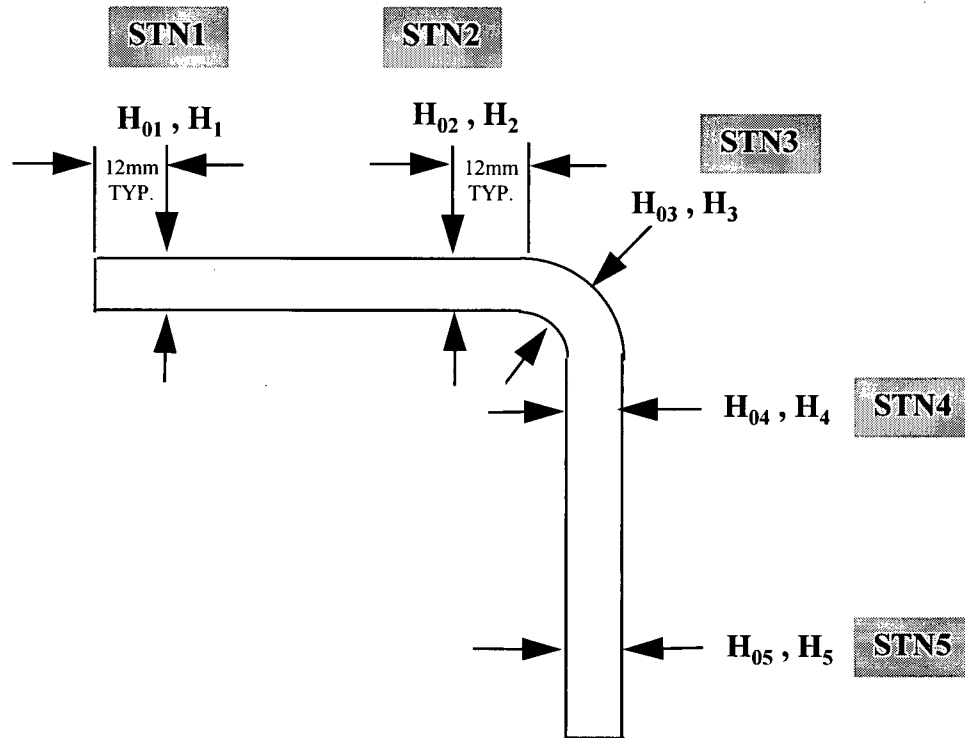


Figure C.1 Angle thickness measurement stations.

Appendix D Results of Shear Flow Experiments

This appendix presents the methodology used to calculate the position of the markers from the image analysis and the parameters measured during the test. Figure D.1(a) shows the parameters measured during the test from the image analysis and the actual stage position given by the ESEM. The position of the stage (x_{stage} and z_{stage}) was given in a coordinate system called the ESEM Coordinate System (Figure D.1 (a)). For each image, the position of the stage was recorded. The marker position was measured by taking the position of the marker in pixel and is converted in microns to obtain the position of the marker in the local coordinate system of the image (x_{frame} and z_{frame}). Thus, the position of the marker is known in the coordinate system of the ESEM by a simple coordinate transformation illustrated in Figure D.1 (a).

The results presented in Chapter 6 are given in a local coordinate system with the origin located at the center of the sample as shown in Figure D.1 (b). The position of the marker in this local coordinate system is obtained from the following measurements (Figure D.1 (a)):

- the marker position (x_{ESEM} , z_{ESEM})
- the plates position z_{TOP} and z_{BOT}
- the sample edge surfaces position x_{LEFT} and x_{RIGHT}

From the above, the following variables are extracted:

- *sample dimensions, length (2L) and thickness (2H)*

$$2H = |z_{\text{TOP}} - z_{\text{BOT}}| \quad \text{and} \quad 2L = |x_{\text{RIGHT}} - x_{\text{LEFT}}| \quad (\text{D.1})$$

- *marker position, (x_i, z_i)*

$$x_i = x_{\text{ESEM}} - (x_{\text{RIGHT}} - L) \quad \text{and} \quad z_i = z_{\text{ESEM}} - (z_{\text{TOP}} - H) \quad (\text{D.2})$$

where i is for a given marker.

The sample dimensions before the test are presented in Table D.1. The raw data obtained for the test is presented in Tables D.2-D.5. The plate position and the edge surface position in Table D.6.

D.1 Tables

Table D.1 Sample dimensions before the test.

Sample	2L (mm)	2H (mm)	W (mm)
10_1	24.34	1.93	14.62
10_2	24.09	1.90	15.68
20_1	24.70	3.76	16.53
20_2	24.96	3.74	14.77

Table D.2 Marker positions for sample 10_1.

Marker	Row A		Row B		Row C		Row D	
	x_{ESEM} (μm)	z_{ESEM} (μm)						
	Initial position							
1	2300	-901	7163	-925	11348	-867	-	-
2	2165	-534	7288	-556	11398	-557	-	-
3	2167	-71	7348	-128	11493	-87	-	-
4	1970	318	7310	294	-	-	-	-
5	-	-	7183	713	-	-	-	-
	Load 1							
1	2245	-782	7529	-772	-	-	-	-
2	2225	-450	7821	-468	12425	-485	-	-
3	-	-	8091	-170	12708	-82	-	-
4	-	-	8114	232	-	-	-	-
5	-	-	-	-	-	-	-	-
	Load 2							
1	2215	-738	-	-	13780	-814	-	-
2	2230	-403	8401	-412	14060	-454	-	-
3	-	-	8851	-252	-	-	-	-
4	-	-	8891	138	-	-	-	-
5	-	-	-	-	-	-	-	-
	Load 3							
1	-	-	-	-	-	-	-	-
2	2423	-322	9387	-337	15015	-542	-	-
3	-	-	9962	-282	15420	-427	-	-
4	-	-	9957	118	-	-	-	-
5	-	-	-	-	-	-	-	-

Table D.3 Marker positions for sample 10_2.

Marker	Row A		Row B		Row C		Row D	
	x_{ESEM} (μm)	z_{ESEM} (μm)						
	Initial position							
1					10758	-961	-	-
2	1355	-436	6695	-478	10950	-553	-9773	-532
3	1183	-186	6715	-88	11028	-113	-9990	-230
4	1753	244	7065	247	11478	150	-9363	235
5	1548	609	6960	602	11003	650	-9258	581
	Load 1							
1	-	-	-	-	11444	-888	-	-
2	1268	-147	7122	-522	11724	-536	-10867	-519
3	-	-	7165	-130	11839	-136	-	-
4	1608	218	7480	217	-	-	-10329	257
5	1388	503	7195	529	-	-	-9887	593
	Load 2							
1	-	-	-	-	12416	-770	-	-
2	1516	-412	7946	-532	12830	-497	-12432	-470
3	-	-	-	-	-	-	-	-
4	1501	199	-	-	-	-	-11757	225
5	1256	451	7891	433	-	-	-	-
	Load 3							
1	-	-	-	-	13404	-758	-	-
2	-	-	8142	-523	13899	-508	-13797	-478
3	-	-	-	-	-	-	-	-
4	1395	157	-	-	-	-	-13079	212
5	-	-	7987	382	-	-	-	-

Table D.4 Marker positions for sample 20_1.

Marker	Row A		Row B		Row C		Row D	
	x_{ESEM} (μm)	z_{ESEM} (μm)						
Initial position								
1	1442	-1829	6777	-1841	10722	-1918	-	-
2	1498	-1094	7371	-1132	11321	-1049	-9939	-1096
3	1505	-170	7741	-117	11954	-88	-10355	-124
4	1522	746	7397	777	11316	700	-8924	1731
5	1355	1546	6713	1582	10645	1504	-9630	1552
Load 1								
1	1436	-1630	6882	-1659	10969	-1698	-	-
2	1523	-960	7655	-1009	11781	-920	-10878	-918
3	1501	-147	8202	-98	12536	-81	-	-
4	1487	650	7731	715	11761	615	-9321	842
5	1339	1394	6874	1451	10913	1367	-9954	1393
Load 2								
1	1453	-1481	-	-	11359	-1540	-	-
2	-	-	-	-	-	-	-11600	-925
3	-	-	-	-	13400	-94	-	-
4	1473	535	8132	673	12468	544	-9882	775
5	1342	1246	-	-	11299	1207	-10438	1258

Table D.5 Marker positions for sample 20_2.

Marker	Row A		Row B		Row C		Row D	
	X _{ESEM} (μm)	Z _{ESEM} (μm)	X _{ESEM} (μm)	Z _{ESEM} (μm)	X _{ESEM} (μm)	Z _{ESEM} (μm)	X _{ESEM} (μm)	Z _{ESEM} (μm)
	Initial position							
1	1825	-1807	6795	-1849	10815	-1800	-	-
2	2340	-1006	7118	-1073	11443	-1157	-	-
3	2487	-113	7350	-251	11274	-231	-	-
4	1579	845	7007	840	10451	732	-	-
5	-	-	6717	1575	-	-	-	-
	Load 1							
1	1859	-1636	6953	-1682	11089	-1630	-	-
2	2385	-870	7424	-954	11983	-1050	-	-
3	2564	-56	7725	-206	11864	-179	-	-
4	1598	811	7281	836	10913	698	-	-
5	-	-	6817	1526	-	-	-	-
	Load 2							
1	-	-	7150	-1581	11507	-1538	-	-
2	-	-	7789	-909	12640	-983	-	-
3	2411	-42	8139	-240	12510	-185	-	-
4	1580	745	7589	786	11401	628	-	-
5	-	-	6911	1401	-	-	-	-
	Load 3							
1	-	-	7325	-1501	-	-	-	-
2	-	-	8133	-867	13239	-955	-	-
3	2744	-73	8518	-265	13174	-226	-	-
4	1532	623	7838	730	11855	552	-	-
5	-	-	6967	1280	-	-	-	-

Table D.6 Position of the plates and the sample edges for the sample tested and all load increments.

Load	Plate		Sample	
	Z _{TOP} (μm)	Z _{BOT} (μm)	X _{LEFT} (μm)	X _{RIGHT} (μm)
	10_1			
0	855	-1105	-	-
1	727	-966	-	-
2	632	-905	-	-
3	544	-788	-	-
	10_2			
0	808	-1076	-	-
1	722	-992	-12987	14335
2	567	-901	-14560	15589
3	575	-881	-16088	16088
	20_1			
0	1743	-2034	-12651	13766
1	1577	-1834	-13362	14460
2	1441	-1682	-14477	15375
	20_2			
0	1747	-2025	-11836	14208
1	1664	-1836	-12685	14983
2	1560	-1733	-13372	15558
3	1436	-1673	-14060	16311

D.2 Figures

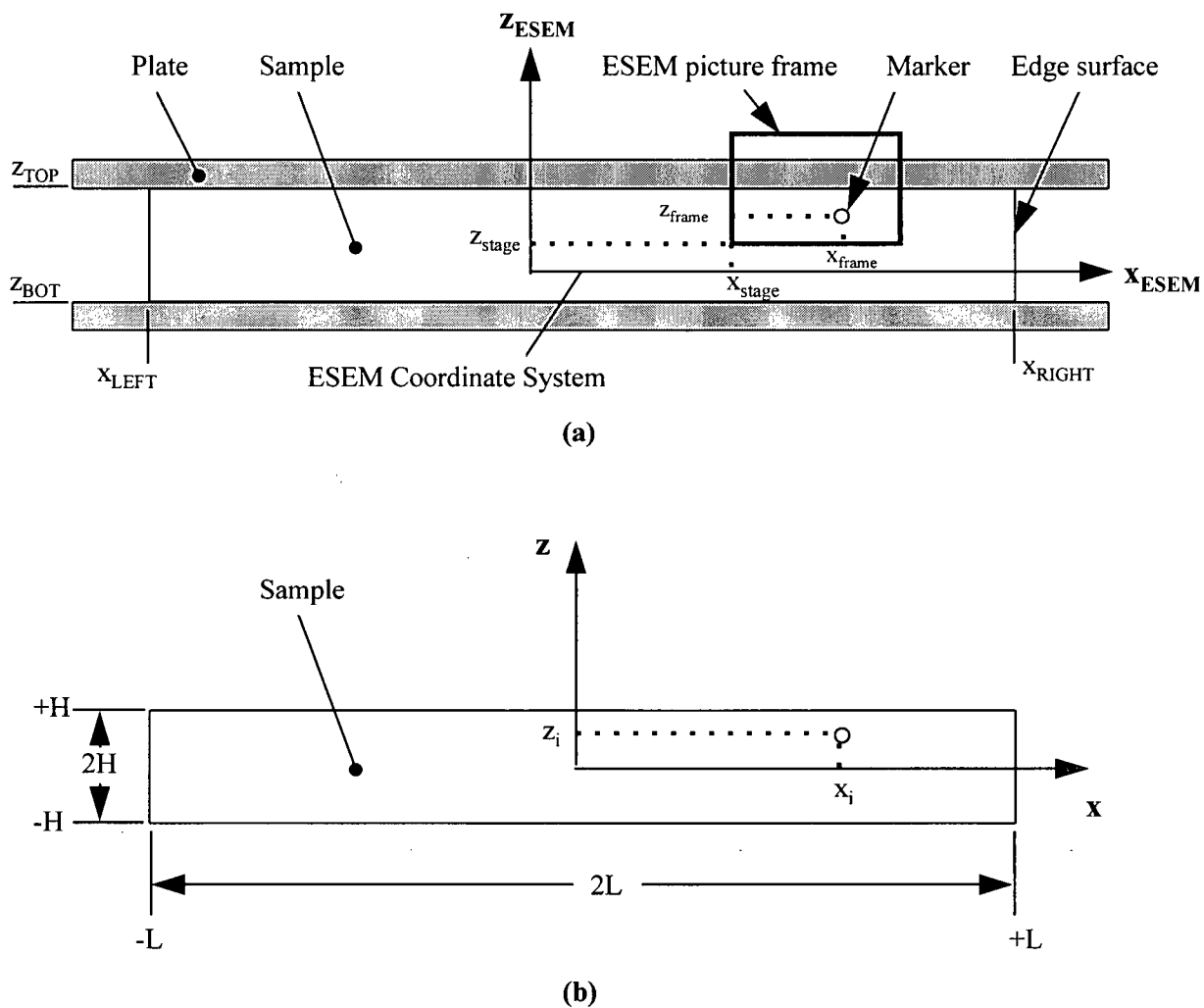


Figure D.1 Coordinate definitions for the computation of the marker position, (a) measurements from the ESEM and (b) marker position definition in the sample coordinate system.

Appendix E Results for Flow Mechanisms Test

The sample dimensions and mass measured before and after the test are presented in Tables E.1-E.4. The dimensions are defined in Figure E.1. From the measurements, the sample strains are calculated using the following relations:

- *in-plane strains*

$$e_x = \frac{1}{2} \left[\left(1 + \frac{L' - L_0}{L_0} \right)^2 - 1 \right] \quad (\text{E.1})$$

$$e_y = \frac{1}{2} \left[\left(1 + \frac{W' - W_0}{W_0} \right)^2 - 1 \right] \quad (\text{E.2})$$

- *volumetric strain*

$$\varepsilon_v = \frac{1}{\rho_r} \frac{(M_0 - M')}{L_0 W_0 H_0} \quad (\text{E.3})$$

From the strains calculated in Table E.1-E.4 the average strains are calculated for the sample tested in similar conditions. The standard variation for the strains is also calculated. The results are presented in Table E.5. The vertical strain contribution from shear flow and percolation flow is calculated using the following equations:

- *shear flow*

$$e_z^s = \frac{-(e_x)}{(1 + e_x)} \quad (\text{E.4})$$

- *percolation flow*

$$e_z^P = \varepsilon_v \quad (E.5)$$

The results are presented in Table E.5. Details on the assumptions for the Equations E.1-E.5 are discussed in Section 6.2.2.

E.1 Tables

Table E.1 Flow mechanism tests, sample measurement results and strains calculated for material A at 100°C.

Sample	Measurements before test				Measurements after test				Strains		
	M ₀ (g)	L ₀ (mm)	W ₀ (mm)	H ₀ (mm)	M'	L'	W'	H'	e _x	e _y	ε _v
[0°]											
4A01	2.28	49.01	25.25	1.29	1.94	49.25	24.64	1.08	0.00	-0.02	-0.17
4A02	2.28	50.80	24.43	1.27	1.93	50.56	24.46	1.07	0.00	0.00	-0.18
4A03	2.20	49.07	24.95	1.29	1.91	49.07	24.53	1.09	0.00	-0.02	-0.14
[90°]											
4A901	2.23	49.98	24.90	1.24	1.92	53.70	24.88	1.04	0.08	0.00	-0.16
4A902	2.22	49.47	24.91	1.27	2.08	52.83	25.25	1.14	0.07	0.01	-0.07
4A903	2.37	50.37	25.07	1.29	1.95	54.32	25.19	0.98	0.08	0.00	-0.20

Table E.2 Flow mechanism tests, sample measurement results and strains calculated for material B at 100°C.

Sample	Measurements before test				Measurements after test				Strains		
	M ₀ (g)	L ₀ (mm)	W ₀ (mm)	H ₀ (mm)	M'	L'	W'	H'	e _x	e _y	ε _v
[0°]											
4B01	2.89	49.61	25.06	1.65	2.81	50.05	24.81	1.47	0.01	-0.01	-0.03
4B02	2.86	48.93	25.21	1.63	2.80	49.17	24.77	1.49	0.00	-0.02	-0.02
4B03	2.79	49.23	25.00	1.61	2.75	50.35	24.67	1.45	0.02	-0.01	-0.02
[90°]											
4B901	2.75	48.17	25.03	1.61	2.69	62.15	25.26	1.19	0.33	0.01	-0.02
4B902	2.79	49.05	24.95	1.63	2.70	62.74	25.14	1.19	0.32	0.01	-0.03
4B903	2.76	48.79	25.49	1.61	2.70	64.97	25.39	1.10	0.39	0.00	-0.02

Table E.3 Flow mechanism tests, sample measurement results and strains calculated for material A at 140°C.

Sample	Measurements before test				Measurements after test				Strains		
	M ₀ (g)	L ₀ (mm)	W ₀ (mm)	H ₀ (mm)	M'	L'	W'	H'	e _x	e _y	e _v
[0°]											
5A01	2.26	48.22	25.18	1.26	1.91	48.29	24.75	1.14	0.00	-0.02	-0.18
5A02	2.22	47.96	24.63	1.27	1.87	48.11	24.41	1.19	0.00	-0.01	-0.18
5A03	2.14	47.33	24.77	1.26	1.78	48.18	24.47	1.14	0.02	-0.01	-0.19
[90°]											
5A901	2.29	48.08	25.32	1.26	2.04	61.98	25.48	1.06	0.33	0.01	-0.13
5A902	2.28	48.31	25.74	1.26	2.02	57.40	25.50	1.10	0.21	-0.01	-0.13
5A903	2.20	48.26	25.54	1.24	1.89	60.40	25.53	0.99	0.28	0.00	-0.16

Table E.4 Flow mechanism tests, sample measurement results and strains calculated for material B at 140°C.

Sample	Measurements before test				Measurements after test				Strains		
	M ₀ (g)	L ₀ (mm)	W ₀ (mm)	H ₀ (mm)	M'	L'	W'	H'	e _x	e _y	e _v
[0°]											
5B01	2.79	49.43	24.73	1.60	2.49	49.62	24.77	1.32	0.00	0.00	-0.12
5B02	2.77	47.80	25.03	1.64	2.55	48.06	24.72	1.45	0.00	-0.01	-0.09
5B03	2.85	48.66	25.05	1.69	2.67	48.82	24.68	1.50	0.00	-0.01	-0.07
[90°]											
5B901	2.93	48.41	25.50	1.66	2.79	62.93	25.53	1.28	0.34	0.00	-0.05
5B902	2.95	49.05	25.63	1.68	2.91	62.83	25.51	1.53	0.32	0.00	-0.01
5B903	2.80	47.99	24.93	1.65	2.59	60.61	25.29	1.42	0.30	0.01	-0.08

Table E.5 Flow mechanism tests, average strains (e_x and ϵ_v) and vertical strains caused by shear flow (e_z^S) and percolation flow (e_z^P).

Test	e_x	ϵ_v	e_z^S	e_z^P
Material A, [0°], 100°C	0.00 (0.00)	-0.16 (0.02)	0.01	-0.15
Material A, [90°], 100°C	0.08 (0.01)	-0.14 (0.07)	-0.08	-0.15
Material B, [0°], 100°C	0.01 (0.01)	-0.02 (0.01)	0.00	-0.01
Material B, [90°], 100°C	0.35 (0.04)	-0.03 (0.01)	-0.26	-0.03
Material A, [0°], 140°C	0.01 (0.01)	-0.19 (0.01)	0.01	-0.18
Material A, [90°], 140°C	0.27 (0.06)	-0.14 (0.02)	-0.21	-0.14
Material B, [0°], 140°C	0.00 (0.00)	-0.09 (0.03)	0.00	-0.08
Material B, [90°], 140°C	0.32 (0.02)	-0.05 (0.03)	-0.25	-0.05

* the standard variation is in parentheses for e_x and ϵ_v

E.2 Figures

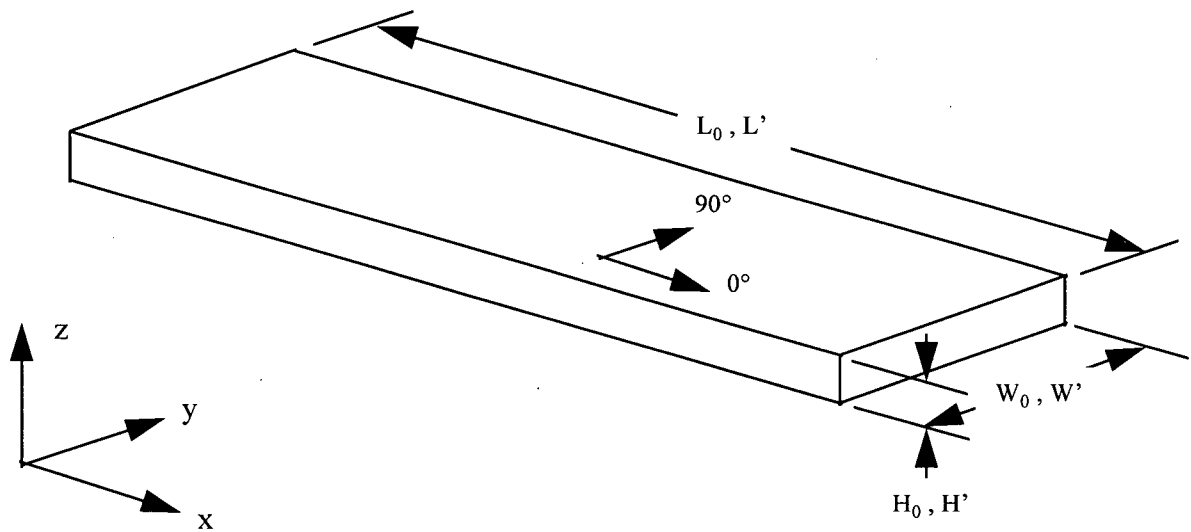


Figure E.1 Flow mechanisms test sample dimensions: before the test (L_0, W_0, H_0) and after the test (L', W', H'). The definition of the fibre orientation direction is also shown.